

Generically Orthogonal Event Decompositions and Measurement Combinations in Standard Model VH ($b\bar{b}$) with the ATLAS Detector

A DISSERTATION PRESENTED
BY
STEPHEN K. CHAN
TO
THE DEPARTMENT OF PHYSICS

IN PARTIAL FULFILLMENT OF THE REQUIREMENTS
FOR THE DEGREE OF
DOCTOR OF PHILOSOPHY
IN THE SUBJECT OF
PHYSICS

HARVARD UNIVERSITY
CAMBRIDGE, MASSACHUSETTS
2018

¹⁸ ©2017 – STEPHEN K. CHAN

¹⁹ ALL RIGHTS RESERVED.

20 **Generically Orthogonal Event Decompositions and**
21 **Measurement Combinations in Standard Model $VH(b\bar{b})$ with**
22 **the ATLAS Detector**

23 **ABSTRACT**

24 This thesis describes variations on the two lepton channel of the Run-2 search for the SM Higgs
25 boson produced in association with a vector boson using different variable sets for multivariate anal-
26 ysis (MVA) training. The three variable sets in question are the set of variables from the fiducial anal-
27 ysis, a set based on the Lorentz Invariants (LI) concept, and a set based on a combination of masses
28 and decay angles derived using the RestFrames (RF) package. Aside from the variable sets used for
29 MVA training and discriminant distributions, the analysis is otherwise identical to the fiducial an-
30 laysis. Both the LI and RF sets perform competitively on the basis of significances, with the RF set
31 showing a $\sim 3.5\%$ improvement in expected fits to Asimov and data, though neither set boosts ob-
32 served significance. Both sets also reduce the observed error on $\hat{\mu}$, with the LI set reducing the error
33 due to systematics by 7.5% and the RF set doing so by 16%.

34 The issue of combining multiple results from different channels and datasets is also examined
35 through the combination of the fiducial Run 1 and Run 2 ATLAS $VH(b\bar{b})$ results, which results in
36 an observed signal strength of $0.90^{+0.18}_{-0.18}(\text{stat.})^{+0.21}_{-0.19}(\text{syst.})$ and an observed (expected) significance
37 of 3.6 (4.0) standard deviations, the first ever evidence of this process.

Contents

38

39	o	INTRODUCTION	I
40	I	THE STANDARD MODEL HIGGS AND COLLIDER EVENT VARIABLES	4
41	1.1	The Standard Model Higgs Boson	5
42	1.2	Higgs Boson Production and Decay at the Large Hadron Collider	8
43	1.3	Collider Events and Event Level Variables	II
44	1.4	Characterization with Event-Level Variables	13
45	1.5	Lorentz Invariants	15
46	1.6	RestFrames Variables	17
47	1.7	Extensions to the ℓ and τ Lepton Channels	19
48	2	THE LARGE HADRON COLLIDER AND THE ATLAS DETECTOR	23
49	2.1	The CERN Accelerator Complex	24
50	2.2	The Large Hadron Collider	24
51	2.3	ATLAS at a Glance	30
52	2.4	The Inner Detector	35
53	2.5	The ATLAS Calorimeters	39
54	2.6	The Muon Spectrometer	47
55	3	DATA AND SIMULATED SAMPLES	53
56	4	SIGNAL AND BACKGROUND MODELING	55
57	4.1	Event Generation In a Nutshell	56
58	4.2	Description of Modeling Uncertainty Categories	58
59	4.3	Process Specific Systematic Summaries	67
60	5	OBJECT AND EVENT RECONSTRUCTION AND SELECTION	77
61	5.1	Triggers	78
62	5.2	Electrons	81
63	5.3	Muons	83
64	5.4	Missing Transverse Energy	85
65	5.5	Jets	85
66	5.6	Flavor Tagging	95
67	5.7	Miscellania and Systematics Summary	106
68	5.8	Event Selection and Analysis Regions	106

69	6 MULTIVARIATE ANALYSIS CONFIGURATION	109
70	6.1 Training Samples and Variable Selection	110
71	6.2 MVA Training	121
72	6.3 Statistics Only BDT Performance	126
73	7 STATISTICAL FIT MODEL AND VALIDATION	132
74	7.1 The Fit Model	133
75	7.2 Fit Inputs	136
76	7.3 Systematic Uncertainties Review	137
77	7.4 The VZ Validation Fit	139
78	7.5 Nuisance Parameter Pulls	143
79	7.6 Postfit Distributions	151
80	7.7 VH Fit Model Validation	158
81	8 FIT RESULTS	173
82	9 MEASUREMENT COMBINATIONS	179
83	9.1 The Combined Fit Model	180
84	9.2 Combined Fit Results	195
85	10 CLOSING THOUGHTS	203
86	APPENDIX A MICROMEGAS TRIGGER PROCESSOR SIMULATION	206
87	A.1 Algorithm Overview	207
88	A.2 Monte Carlo Samples	212
89	A.3 Nominal Performance	212
90	A.4 Fit Quantities	213
91	A.5 Efficiencies	219
92	A.6 Incoherent Background	222
93	A.7 BCID	227
94	A.8 Charge Threshold	227
95	A.9 Misalignments and Corrections	231
96	A.10 Individual Cases	236
97	A.11 $ds \neq 0$	237
98	A.12 $dz \neq 0$	237
99	A.13 $dt \neq 0$	237
100	A.14 $\alpha \neq 0$	238
101	A.15 $\beta \neq 0$	238
102	A.16 $\gamma \neq 0$	238
103	A.17 Simulation Correction of the Algorithm Under Nominal Conditions	241
104	A.18 Translation Misalignments Along the Horizontal Strip Direction (Δs)	244

105	A.19 Translation Misalignments Orthogonal to the Beamline and Horizontal Strip Direction (Δz)	246
106	A.20 Translation Misalignments Parallel to the Beamline (Δt)	248
107	A.21 Chamber Tilts Towards and Away from the IP (γ_s Rotation)	249
108	A.22 Rotation Misalignments Around the Wedge Vertical Axis (β_z)	251
109	A.23 Rotation Misalignments Around the Axis Parallel to the Beamline (α_t)	252
110	A.24 Conclusion	254
112	APPENDIX B TELESCOPING JETS	256
113	B.1 Monte Carlo Simulation	257
114	B.2 Jet Reconstruction and Calibration	258
115	B.3 Event Reconstruction and Selection	259
116	B.4 Validation of Jet Calibration	260
117	B.5 Truth-Level Analysis	265
118	B.6 Errors on Telescoping Significances	268
119	B.7 Counting	268
120	B.8 Multiple Event Interpretations	269
121	B.9 $t(z) = z$	270
122	B.10 $t(z) = \rho_S(z) / \rho_B(z)$	271
123	B.11 Reconstructed-Level Analysis	276
124	B.12 Conclusions and Prospects	282
125	APPENDIX C PROGRESS IN PARTICLE PHYSICS AND EXISTENTIAL THREATS TO THE	
126	AMERICAN WORLD ORDER	283
127	REFERENCES	296

Acknowledgments

¹³⁰ THIS THESIS WOULD NOT HAVE BEEN POSSIBLE without large amounts of espresso.

*Your life has a limit but knowledge has none...if you
understand this and still strive for knowledge, you will
be in danger for certain!*

Zhuangzi

0

131

132

Introduction

133 SINCE THE DISCOVERY of a Standard Model (SM) like Higgs boson at the LHC in 2012⁷⁶, one of
134 the main outstanding physics goals of the LHC has been to observe the primary SM Higgs decay
135 mode, $H \rightarrow b\bar{b}$, with efforts primarily targeted at searching for Higgs bosons produced in associa-
136 tion with a leptonically decaying vector (W or Z , denoted generically as V) boson. As the integrated

¹³⁷ luminosity of data collected at the LHC increases, $H \rightarrow b\bar{b}$ searches will increasingly become limited
¹³⁸ by the ability to constrain systematic uncertainties, with the latest result from ATLAS at $\sqrt{s} = 13$
¹³⁹ TeV using 36.1 fb^{-1} of pp collision data already approaching this regime, having a $VH(b\bar{b})$ signal
¹⁴⁰ strength of $1.20^{+0.24}_{-0.23}(\text{stat.})^{+0.34}_{-0.28}(\text{syst.})$ at $m_H = 125 \text{ GeV}$ ⁴².

¹⁴¹ While this effort will likely require a combination of several different methods at various differ-
¹⁴² ent stages in the analysis chain, one possible avenue forward is to revise the multivariate analysis
¹⁴³ (MVA) discriminant input variables used, as various schemes offer the promise of reducing system-
¹⁴⁴ atic uncertainties through more efficient use of both actual and simulated collision data. This thesis
¹⁴⁵ discusses two such alternate MVA schemes, the RestFrames (RF) and Lorentz Invariants (LI) vari-
¹⁴⁶ ables, in the context of the 2-lepton channel of the Run 2 analysis in⁴² and⁶⁵, henceforth referred to
¹⁴⁷ as the “fiducial analysis,” before a brief discussion of combinations across channels and datasets.

¹⁴⁸ Data and simulation samples used are described in Chapter 3. Signal and background modeling
¹⁴⁹ with accompanying systematics are defined in Chapter 4. Object and event reconstruction definitions
¹⁵⁰ and event selection requirements are outlined in Chapter 5. The multivariate analysis, including a de-
¹⁵¹ scription of the LI and RF variable sets and a summary of performance in the absence of systematic
¹⁵² uncertainties, is described in Section 6. The statistical fit model and systematic uncertainties are de-
¹⁵³ scribed in Section 7, and the fit results may be found in Chapter 8. Combining channels and datasets
¹⁵⁴ at different \sqrt{s} values is discussed in the context of the Run 1 + Run 2 SM $VH(b\bar{b})$ combination in
¹⁵⁵ Chapter 9. Finally, conclusions and closing thoughts are presented in Chapter 10.

¹⁵⁶ Editorial notes:

¹⁵⁷ i. pdf will be *probability distribution* function

- ¹⁵⁸ 2. PDF will be *parton* distribution function
- ¹⁵⁹ 3. Unless otherwise stated, ATLAS and LHC/CERN images are from public available material
- ¹⁶⁰ from experiment webpages. Copyright terms may be found here <https://atlas.cern/>
- ¹⁶¹ **copyright.**

*The relationship between theorists and experimentalists
is like that between a truffle farmer and his pig*

Howard Georgi

1

162

163

The Standard Model Higgs and Collider

164

Event Variables

165 MUCH HAS BEEN SAID about the so-called Standard Model (SM) of particle physics, so only the

166 bare essentials of electroweak symmetry breaking and Higgs production relevant to SM $VH(b\bar{b})$ will

¹⁶⁷ be addressed here. This discussion follows⁶⁶ Chapter II in both content and notation. We then
¹⁶⁸ move onto the treatment of kinematic variables in collider events, including the two novel schemes
¹⁶⁹ considered in this thesis, the Lorentz Invariants (LI) and RestFrames (RF) concepts.

¹⁷⁰ I.I THE STANDARD MODEL HIGGS BOSON

¹⁷¹ The generic scalar Lagrangian potential (the kinetic term will be addressed later) for a scalar in the
¹⁷² SM is:

$$V(\Phi) = m^2 \Phi^\dagger \Phi + \lambda (\Phi^\dagger \Phi)^2 \quad (\text{I.1})$$

¹⁷³ where Φ is the Higgs field, a complex scalar doublet under $SU(2)$. Its four degrees of freedom are
¹⁷⁴ typically decomposed as follows:

$$\Phi = \frac{1}{\sqrt{2}} \begin{pmatrix} \sqrt{2}\phi^+ \\ \phi^0 + i\alpha^0 \end{pmatrix} \quad (\text{I.2})$$

¹⁷⁵ ϕ^+ is the complex charged component of the Higgs doublet, and ϕ^0 and α^0 are the CP-even and
¹⁷⁶ CP-odd neutral components, respectively.

¹⁷⁷ If the sign of $m^2 \Phi^\dagger \Phi$ is negative, Φ acquires a *vacuum expectation value* or VEV:

$$\langle \Phi \rangle = \frac{1}{\sqrt{2}} \begin{pmatrix} 0 \\ \sqrt{\frac{2m^2}{\lambda}} \end{pmatrix} \quad (\text{I.3})$$

¹⁷⁸ with this value typically denoted $v = \sqrt{2m^2/\lambda} = (\sqrt{2}G_F)^{-1/2} \approx 246 \text{ GeV}$ (with the coupling

¹⁷⁹ of the 4-Fermi effective theory of weak interactions measured through experiments involving muon
¹⁸⁰ decay), and ϕ^0 is rewritten as $\phi^0 = H + v$.

¹⁸¹ This non-zero VEV induces spontaneous symmetry breaking in the SM's gauge (local) symme-
¹⁸² try group of $SU(3)_C \times SU(2)_L \times U(1)_Y$ since the VEV does not respect the $SU(2)_L \times U(1)_Y$
¹⁸³ symmetry of the Lagrangian (i.e. $\langle \Phi \rangle$ is not invariant under a gauge transformation of this group).

¹⁸⁴ Three of the four generators of this subgroup are spontaneously broken, which implies the existence
¹⁸⁵ of three massless Goldstone bosons, which are in turn “eaten” by linear combinations of the W^a and
¹⁸⁶ B bosons to form the longitudinal components of the familiar W^\pm and Z bosons, with the last gen-
¹⁸⁷ erator giving rise to the usual, unbroken $U(1)_{EM}$ symmetry and its massless photon, A , as well as
¹⁸⁸ the scalar Higgs boson H . To see this, one starts with the full Higgs SM Lagrangian (kinetic minus
¹⁸⁹ potential only)

$$\mathcal{L}_{Higgs} = (D_\mu \Phi)^\dagger (D_\mu \Phi) - V(\Phi), \quad D_\mu \Phi = (\partial_\mu + ig\sigma^a W_\mu^a + ig' Y B_\mu/2) \Phi \quad (1.4)$$

¹⁹⁰ One simply plugs in the reparametrized Φ with $\phi^0 = H + v$, collects the terms involving v together
¹⁹¹ with the appropriate W and B kinetic terms to extract:

$$M_W^2 = \frac{g^2 v^2}{4}, \quad M_Z^2 = \frac{(g'^2 + g^2) v^2}{4} \quad (1.5)$$

¹⁹² This is left as an exercise for the reader; this exercise also makes manifest that the Higgs couples with
¹⁹³ the W^\pm and Z with strength quadratic in the gauge boson masses. Since the Higgs field also respects

¹⁹⁴ the $SU(3)_C$ color symmetry, the eight gluons are also left massless, and the H is left interacting with
¹⁹⁵ photons and gluons primarily through heavy quark loops (i.e. no tree-level interactions).

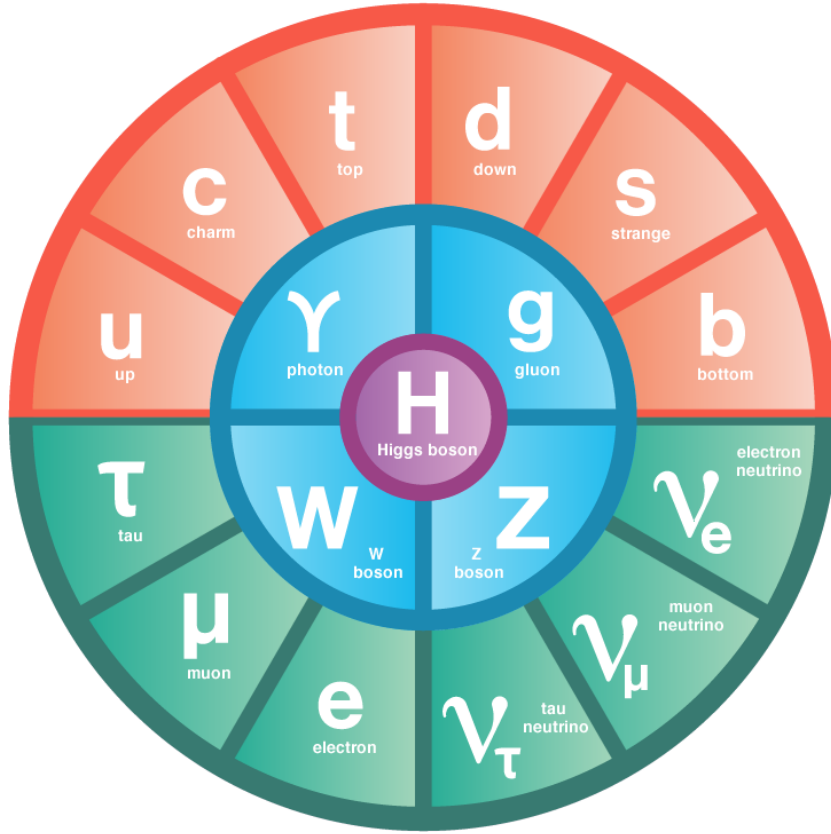


Figure 1.1: The fundamental particles of the Standard Model. IC:⁷⁴

¹⁹⁶ The Higgs is often introduced to the public at large as the mechanism through which fundamen-
¹⁹⁷ tal fermions (enumerated in Figure 1.1) acquire mass—this is through the Yukawa interactions of the
¹⁹⁸ Higgs:

$$\mathcal{L}_{Yukawa} = -\hat{h}_{d_{ij}} \bar{q}_{L_i} \tilde{\Phi} d_{R_j} - \hat{h}_{u_{ij}} \bar{q}_{L_i} \tilde{\Phi} u_{R_j} - \hat{h}_{l_{ij}} \bar{l}_{L_i} \tilde{\Phi} e_{R_j} + h.c. \quad (1.6)$$

¹⁹⁹ where $\tilde{\Phi} = i\sigma_2 \Phi^*$, q_L (l_L) and u_R , d_R (e_R) are the quark (lepton) left-handed doublets and right

200 handed singlets of the weak $SU(2)_L$ group, with each term parametrized by a 3×3 matrix in fam-
201 ily space (also known as the fermion generations). The neutrinos have been purposely omitted since
202 the mechanism that generates their mass is as of yet unknown, though these Yukawa interactions
203 could have a non-zero contribution to neutrino masses. Once the Higgs VEV value is known and
204 the Yukawa interaction matrices \hat{b}_{f_i} ($i, j \in 1, 2, 3$) are diagonalized, the fermion masses can sim-
205 ply be written as $m_{f_i} = b_{f_i} v / \sqrt{2}$. The SM has no motivation for any of these mass values, instead
206 leaving them as empirically determined free parameters.

207 Note that from \mathcal{L}_{Yukawa} , it is easy to see that the Higgs couplings with fermions scale linearly with
208 fermion mass. Higgs self-couplings and beyond the standard model (BSM) Higgs scenarios are be-
209 yond the scope of this thesis.

210 1.2 HIGGS BOSON PRODUCTION AND DECAY AT THE LARGE HADRON COLLIDER

211 The leading order Feynman diagrams for the four dominant modes of Higgs production at the LHC
212 are shown in Figure 1.2, each described briefly in turn. The dominant process, accounting for some
213 87% of Higgs production at the nominal LHC center of mass energy of 14 TeV, is gluon-gluon fu-
214 sion (ggF), shown at top left in Figure 1.2. At high center of mass energies, most of a proton's mo-
215 mentum is predominantly carried by sea gluons (as opposed to the constituent valence quarks asso-
216 ciated with the hadron's identity). This, along with the difficulties associated with high luminosity
217 antiproton beam production, is why the LHC was designed as a proton-proton collider instead of a
218 proton-antiproton collider (like the Tevatron or once planned SSC). As mentioned above, the Higgs
219 does not couple directly to gluons but must instead be produced through the fermion loop shown

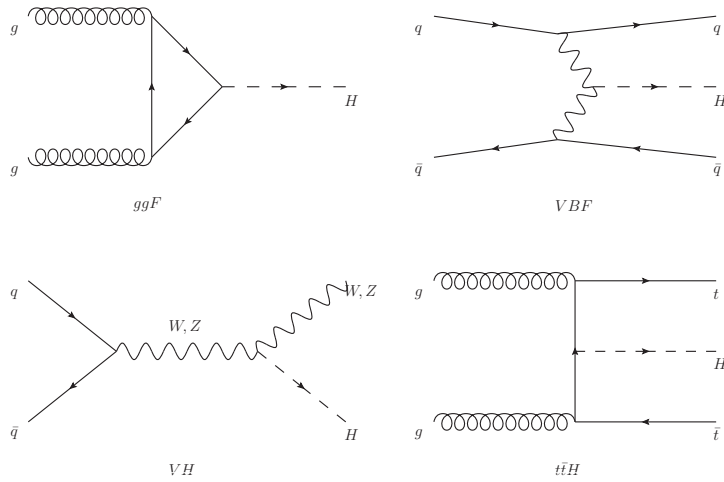


Figure 1.2: Dominant Higgs production modes.

in the figure. The heaviest fundamental fermion by far is the top quark, with $m_t = 173$ GeV, so top loops dominate this process. While not particularly relevant for this thesis, about 14% of events in the 2-lepton channel of the $H \rightarrow b\bar{b}$ analysis are ggF initiated.

The next most prevalent process is vector boson fusion (VBF), where vector bosons (W or Z , denoted generically as V) from quarks in the colliding protons “fuse” to form a Higgs. These quarks typically form jets in the forward region, which provide a unique signature for this process. This process is not relevant for this thesis.

The third leading process is “Higgsstrahlung” or Higgs production in association with a vector boson, often simply VH production. In this process, a quark-antiquark pair in the colliding protons forms an energetic vector boson, which then radiates a Higgs (this is similar to photon emission of accelerating electrons, called “Bremsstrahlung,” hence the name). Some fraction of the time (about 21% of the time for WH and 6.7% of the time for ZH), the energetic V will decay leptonically (i.e.

232 into a decay involving an electron or a muon), which provides a unique and triggerable signature
 233 for this process. Another 20% of the time for ZH production, the Z will decay to neutrinos, which
 234 are not absorbed by detectors and show up as missing transverse energy (\vec{E}_T^{miss}), another triggerable
 235 signature. This ability to trigger on leptons and \vec{E}_T^{miss} and the requirement that this leptonic signa-
 236 ture be consistent with a V allow one to significantly reduce the impact of multijet background (a
 237 very common generic processes at the LHC) on analysis. Hence, this is the process of primary impor-
 238 tance to this thesis.

239 The final important Higgs production process is $t\bar{t}H$ production, the box diagram in the lower
 240 right of Figure 1.2. Again, the top pair provides a useful signature for analysis. This, like VBF, is also
 241 not considered in this thesis.

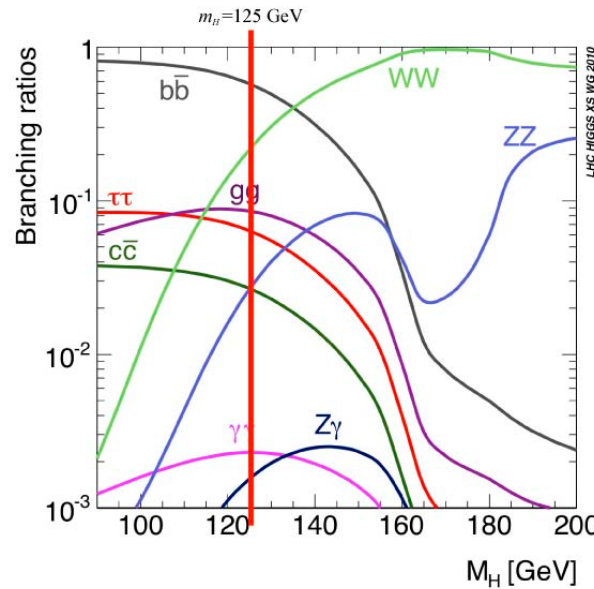


Figure 1.3: Higgs decay modes as a function of its mass; a line has been drawn at the observed Higgs mass of 125 GeV.

242 Once the Higgs has been produced, it can decay in a number of ways, as shown in Figure 1.3. By

243 far the most dominant decay mode of the Higgs is to $b\bar{b}$ at 58% of all decays. This b -quark pair then
 244 hadronizes into two b -jets (for a more thorough discussion of jets and b -jets in particular, see Sec-
 245 tion 5.5). However, many processes at the LHC create pairs of b -jets with invariant masses consistent
 246 with the Higgs and have much higher production rates ($t\bar{t}$ production at the LHC is in the neighbor-
 247 hood of hundreds of pb, compared to Higgs cross sections of a few pb), so a clear process signature
 248 is necessary to study $H \rightarrow b\bar{b}$ production at the LHC. This is why the bulk of search efforts have fo-
 249 cused on VH production. A summary of Higgs production cross sections and simple extrapolations
 250 to raw numbers of Higgs bosons produced for VH for leptonically decaying V is shown in Table 1.1

\sqrt{s} (TeV)	ZH	WH	ggF	total σ	$N_{V \rightarrow \ell^{\pm} H}$
7	$0.34^{+4\%}_{-4\%}$	$0.58^{+3\%}_{-3\%}$	$15.3^{+10\%}_{-10\%}$	17.5	$4.7 \text{ fb}^{-1} \rightarrow 589$
8	$0.42^{+5\%}_{-5\%}$	$0.70^{+3\%}_{-3\%}$	$19.5^{+10\%}_{-11\%}$	22.3	$20.3 \text{ fb}^{-1} \rightarrow 3100$
13	$0.88^{+5\%}_{-5\%}$	$1.37^{+2\%}_{-2\%}$	$44.1^{+11\%}_{-11\%}$	50.6	$36.1 \text{ fb}^{-1} \rightarrow 11100$
14	$0.99^{+5\%}_{-5\%}$	$1.51^{+2\%}_{-2\%}$	$49.7^{+11\%}_{-11\%}$	57.1	$1000 \text{ fb}^{-1} \rightarrow 343000$

Table 1.1: Cross sections (in pb) for processes important to the SM VH ($b\bar{b}$) analysis and the total Higgs cross section as a function of center of mass energy. Also given are the total number of Higgs bosons produced for given luminosities through both WH and ZH processes.

251 1.3 COLLIDER EVENTS AND EVENT LEVEL VARIABLES

252 Collision data in experiments like ATLAS is structured using what is known as the *event data model*.
 253 In this model, one collision corresponds to one event. The raw data, the various tracks, energy de-
 254 posits, and hits in the detector, undergo reconstruction (described at length in Chapter 5) both through
 255 automated, experiment-wide, standardized production and through analysis-specific level selec-
 256 tions, corrections, and calibrations. The result of this considerable effort is a collection of labeled

²⁵⁷ 4-vectors, representing the final state objects. This is shown in Figure 1.4.

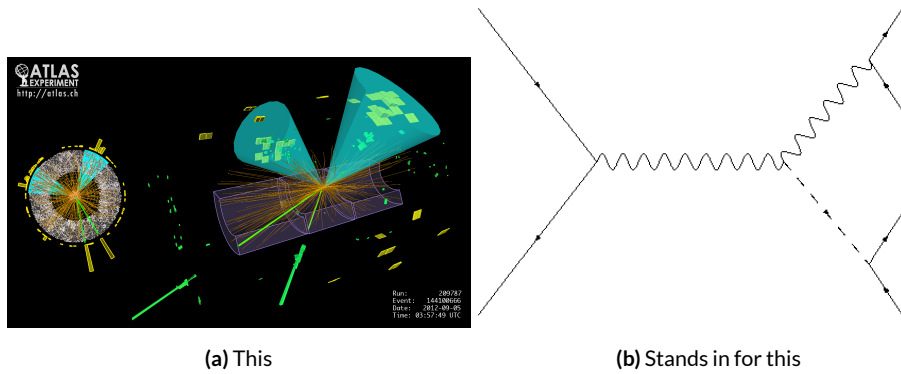


Figure 1.4: Reconstruction in a nutshell

²⁵⁸ In the process that is the focus of this thesis, every event ultimately is condensed into a lepton
²⁵⁹ pair (two electrons or two muons), two or three jets*, all 4-vectors, and a \vec{E}_T^{miss} vector in the trans-
²⁶⁰ verse plane. Further selection then takes place to winnow down events into interesting regions of
²⁶¹ phase space hopefully more rich in signal-like events. Once events are selected in a search like the
²⁶² one in this thesis, one then analyzes the data to test its consistency with some background only hy-
²⁶³ pothesis to produce the usual statistical results. This can be done in various ways, with principal ap-
²⁶⁴ proaches being: a simple counting experiment (often referred to as the “cut and count” approach),
²⁶⁵ a functional fit for excesses over a falling background spectrum (the so-called “bump hunt” used in
²⁶⁶ analyses like the $H \rightarrow \gamma$ discovery channel), or the use of discriminant distributions as PDF’s in a
²⁶⁷ likelihood fit (the approach of this analysis). These distributions can be simple counts (i.e. single bin
²⁶⁸ distributions) in analysis regions, quantities of interest (the distribution of the invariant mass of the

*Sometimes more, though this is a small fraction of events, and the wisdom of this choice may be questioned

269 two b -jets in selected events with the greatest transverse momenta, m_{bb} , is used as a validation), or
270 something more complicated like a multivariate analysis (MVA) discriminant.

271 **I.4 CHARACTERIZATION WITH EVENT-LEVEL VARIABLES**

272 Traditionally, particle physicists have favored the approach of using distributions of physical vari-
273 ables since it is easier to develop “physical intuition” for what these distributions should “look like”
274 during validation, so it is no surprise that as many LHC analyses have transitioned to using MVA
275 techniques that these variables form the basis of many very robust physics results. These variables do
276 quite well summarize many of the main physics features of an event for the signal topology, certainly
277 much better than feeding all 18–22 4-vector components directly into some machine learning algo-
278 rithm. In $ZH \rightarrow \ell\ell b\bar{b}$ events, for example, one wishes to characterize the ZH system by using the
279 lepton pair as a stand-in for the Z and the b -jet pair as a stand-in for the H , and composite variables
280 like m_{bb} and $m_{\ell\ell}$ can be used to check whether events are consistent with these objects. There are
281 also variables like p_T^V that characterize the momentum scale of the event, angles like $\Delta R(b_1, b_2)$ and
282 $\Delta\phi(V, H)$ that can be further used to characterize the overall “shape” of these events, and variables
283 like \vec{E}_T^{miss} that can discriminate against backgrounds like $t\bar{t}$ that do not have a closed topology.

284 Nevertheless, the intuition based approach, with incremental addition of variables as they prove
285 useful in the lifetime of an analysis’s iterations, does beg the question of whether there is a more sys-
286 tematic way to treat this information. There are clearly patterns to which variables are useful: these
287 correspond to important information about the hypothesized physics objects and their relation-
288 ships, and there have been many attempts to systematize the way these variables are found. Such

289 systematic, top-down approaches often promise to increase performance in two ways. The first is by
290 having higher descriptive power, often through some sophisticated treatment of the missing trans-
291 verse energy in an event, \vec{E}_T^{miss} . \vec{E}_T^{miss} is just a single quantity, and if there is just one invisible object
292 in a desired event topology, using \vec{E}_T^{miss} on its own often provides sufficient sensitivity. In more com-
293 plicated topologies with multiple invisible particles in the final state, for example in many supersym-
294 metry searches, a more careful treatment of the missing energy is often necessary.

295 The second means of improvement is through using a more orthogonal basis of description,
296 which allows one to more efficiently use data and simulation samples. A more orthogonal basis im-
297 plies that variables contain less overlapping information with each other and so allow for a more
298 efficient exploration of parameter space. This means one can gain higher sensitivity from equivalent
299 datasets using a more orthogonal basis. To see why this might be the case, take an MVA discrimi-
300 nant for $ZH \rightarrow \ell\ell b\bar{b}$ formed using only the classic variables $\Delta R(b_1, b_2)$ and p_T^V . In the $ZH \rightarrow$
301 $\ell\ell b\bar{b}$ topology, the transverse mass of the Z and H (and hence the lepton pair and jet pair) are equiv-
302 alent. This means that at higher p_T^V the p_T of b -jets will also be higher, which in turn implies that
303 they will have a smaller angle of separation and hence a smaller $\Delta R(b_1, b_2)$. This correlation is not
304 unity—each variable still does have information the other does not—but is still very high. Hence,
305 when training an MVA, which in principle knows nothing about these variables other than some
306 set limits, an undue number of training events will be wasted converging upon relations that could
307 be known *a priori*, and while this might be easy to hard code in for a two variable toy example, the
308 dimensionality of any real discriminant makes this prohibitive. An MVA that uses data (both ac-
309 tual and simulated) more efficiently will also tend to be have lower variance, offering a potential av-

³¹⁰ enue for reduction in the error on quantities of interest due to systematic uncertainties. Details of
³¹¹ how this plays out in a likelihood fit will be deferred to the discussion of the fit model used in the
³¹² $VH(b\bar{b})$ search in Chapter 7.

³¹³ Many of these novel schemes are designed to explicitly address the first issue of invisibles in the
³¹⁴ final state in channels where it is of paramount importance while having the second issue as some-
³¹⁵ thing of a fringe benefit. However, as the amount of data taken at the LHC grows, analyses will in-
³¹⁶ creasingly become systematics limited, so an exploration to the veracity of the second claim has great
³¹⁷ potential for the high luminosity era of the LHC. The $ZH \rightarrow \ell\ell b\bar{b}$ process offers a great setting
³¹⁸ for investigating this issue on its own since its closed topology largely mitigates any improvement
³¹⁹ from more sophisticated treatments of \vec{E}_T^{miss} . We introduce two of these more top-down approaches
³²⁰ to event-level variables below: the “Lorentz Invariant” (LI)⁵³ and “RestFrames inspired” (RF)⁵⁶
³²¹ variable schemes. A broad overview of the concepts behind these schemes will be given here, with
³²² a more in-depth discussion of their implementation deferred until Chapter 6.

³²³ 1.5 LORENTZ INVARIANTS

³²⁴ The LI variables, first put forth by S. Hagebeck and others⁵³, are based upon the fact that once the
³²⁵ 4-vectors of an event are determined, all of the information in an event are encoded into their inner
³²⁶ products (Lorentz invariant quantities, hence the name) and the angles between them. This makes
³²⁷ for 16 quantities in all: the ten inner products of the 4-vectors, the three Euler angles, and the three
³²⁸ parameters specifying the boost of the ZH system. The masses of the four final state objects are not
³²⁹ considered very useful and so can be removed to leave six meaningful inner products (the ${}_4C_2$ com-

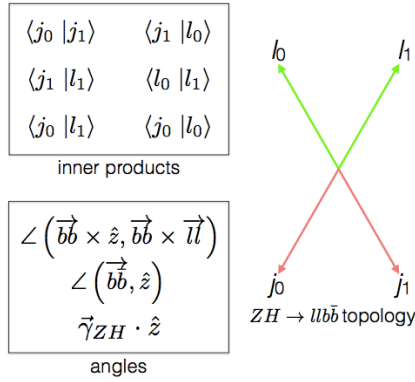


Figure 1.5: Summary of LI variables in the $ZH \rightarrow \ell\ell b\bar{b}$ topology.

binations between distinct final state 4-vectors). Since these inner products can have an ill-defined physical interpretation and in order to help MVA training, each inner product is scaled by:

$$x \rightarrow \frac{x}{x + c} \quad (1.7)$$

where c is the mean of the distribution in the signal MC distribution. These inner products are denoted $x_i_y_j$, where x and y are either j (for jet) or ℓ (for lepton) and the indices are either o (i) for the leading (subleading) object by p_T in the event.

The number of useful angles can be reduced by recognizing some symmetries inherent in the final state. The symmetry around the beam axis eliminates one angle. Furthermore, the boost of the VH system is primarily in the beam direction (z) direction, marginalizing the utility of the transverse boost angles. This leaves the boost in the z direction, denoted `gamma_ZHz`, and two angles chosen to be the angle between the $b\bar{b}$ system and the beam (`angle_bb_z`) and the angle between $(b_1 + b_2) \times \hat{z}$ and $(b_1 + b_2) \times (l_1 + l_2)$ (`angle_bbz_bbll`).

341 These variables do contain a lot of information similar to the usual set: there are mass equivalents
 342 ($j_0 \cdot j_1 \leftrightarrow m_{bb}$, and $l_0 \cdot l_1 \leftrightarrow m_{\ell\ell}$) and angles. Instead of individual final state object scales, there
 343 are the four jet-lepton inner products, though this correspondence (and indeed any physical inter-
 344 pretation) is far from clear. An important advantage of the LI variable set is that all of the variables
 345 are in it are orthogonal in the signal case by construction. A drawback of this framework in a com-
 346 pletely closed final state is that there is no way to treat E_T^{miss} in a Lorentz invariant way.

347 There is also no prescription for any additional jets in the event beyond the two b -tagged jets.
 348 They are simply ignored in these variable calculations since the fiducial analysis requirement of ex-
 349 actly two b -tagged jets eliminates any combinatoric ambiguity, and additional, untagged jets are as-
 350 sumed (not entirely rigorously) to be unrelated to the signal-like hard scatter.

351 I.6 RESTFRAMES VARIABLES

352 The RestFrames variables³⁶, calculated using the software package of the same name, is based upon
 353 the idea that the most natural frame in which to analyze objects of the signal decay tree is in their in-
 354 dividual production (rest) frames. The signal decay tree for $ZH \rightarrow \ell\ell b\bar{b}$ is show in Figure 1.6. Gen-

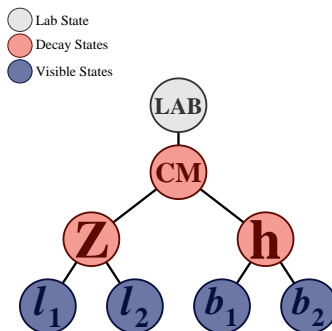


Figure 1.6: The $ZH \rightarrow \ell\ell b\bar{b}$ decay tree.

354 erally, one does not typically have enough information to determine exactly each of the intermediate
 355 rest frames or the boosts between the frames, but in a completely closed final state like $ZH \rightarrow \ell\ell b\bar{b}$,
 356 this can be done in the usual way by adding the 4-vectors of the final state objects and solving the
 357 usual equations from special relativity (`RestFrames` does this automatically for each event).

358 Each frame has associated with it the boost from its immediate parent and a mass scale; that mass
 359 (in this case the correspondence between RF mass variables and standard mass variables is exact) and
 360 the angles between the Euclidean three vector associated with boost and the axis of the decay prod-
 361 ucts provide useful variables. In general, the polar angle (typically given as a cosine) is considered
 362 more useful than the azimuthal angle (typically just a $\Delta\phi$), though this is dependent on the candi-
 363 date decay tree. The Z frame, for example, has `MZ`, which is just the usual $m_{\ell\ell}$, `cosZ`, the cosine of
 364 the polar angle between the lepton momentum axis in their production frame and the boost from
 365 the ZH center of mass (CM) frame, and the angle `dphiCMZ`.

366 In addition to the masses and angles attached to individual object rest frames, energy scales associ-
 367 ated with the CM frame can be used to contextualize other event level quantities. In particular, one
 368 can use the mass of the CM frame as a natural scale to evaluate the momentum of the CM frame,
 369 and the p_T of the CM frame as a natural scale for the event's E_T^{miss} , yielding the variables:

$$R_{p_T} = \frac{p_{T,CM}}{p_{T,CM} + M_{CM}}, \quad R_{p_z} = \frac{p_{z,CM}}{p_{z,CM} + M_{CM}}, \quad R_{met} = \frac{E_T^{miss}}{E_T^{miss} + p_{T,CM}} \quad (1.8)$$

370 denoted `Rpt`, `Rpz`, and `Rmet`. These can be thought of as behaving like significance based variables
 371 in particle physics, like METHT or impact parameter significances, or event level defined versions

372 of the scalings applied to the LI inner products. These are used instead of the final state object scales
373 and standard E_T^{miss} of the standard variable set.

374 Unlike the LI variables, the physical interpretation of RF variables is very clear. Everything has
375 physical units, and these are variables one might have introduced in the usual process of develop-
376 ing an MVA with the traditional mindset. The solution to the issue of additional jets in an event is
377 not immediately clear. In order to keep the two non-standard MVA's on as equal footing as possi-
378 ble, the approach of simply ignoring additional jets is taken in this thesis. Nevertheless, it would be
379 easy enough to redefine the H intermediate frame to have, for example, the two b -tagged jets and the
380 highest p_T untagged jet for any subset of events. This flexibility is not a feature of the Lorentz Invari-
381 ants framework. Of course, `RestFrames` cannot tell you what approach to take, but it is capable of
382 handling more flexible topologies once optimization studies have been completed.

383 I.7 EXTENSIONS TO THE 1 AND 0 LEPTON CHANNELS

384 Both the LI and RF variable concepts are readily extendable to the 1-lepton channel. In this topol-
385 ogy, one of the leptons in the $ZH \rightarrow \ell\ell b\bar{b}$ diagram is replaced by a neutrino, the lone invisible
386 particle in this final state. We can assume that the neutrino has zero mass and transverse momentum
387 equal to the \vec{E}_T^{miss} in the event, leaving one undetermined degree of freedom, the longitudinal mo-
388 mentum of the neutrino, p_z^ν .

389 The LI concept was in fact initially formulated to improve sensitivity in the 1-lepton channel,
390 with the same orthogonality of variables described in the 2-lepton case being the main draw. The LI
391 approach to estimating the neutrino longitudinal momentum is outlined in ³³, which we reproduce

³⁹² here. We first guess the neutrino energy in its rest frame and then boost to the lab frame:

$$\langle E_\nu \rangle = \frac{1}{4} m_{WH} \implies \langle p_z^\nu \rangle = \beta \gamma \langle E_\nu \rangle = \frac{p_z^{WH}}{m_{WH}} \langle E_\nu \rangle = \frac{1}{4} p_z^{WH} \quad (1.9)$$

³⁹³ Finally, assuming energy and momentum in aggregate are equally shared among final state con-

³⁹⁴ stituents, we arrive at

$$\langle p_z^\nu \rangle = \frac{1}{4} \times \frac{4}{3} (p_z^l + p_z^{j0} + p_z^{j1}) \quad (1.10)$$

³⁹⁵ The RF approach for the 1-lepton case amounts to replacing the $Z \rightarrow \ell\ell$ in 1.6 with $W \rightarrow \ell\nu$.

³⁹⁶ As alluded to in the 2-lepton discussion, when there is missing information in the final state from

³⁹⁷ invisible particles and/or combinatoric ambiguities, recursive jigsaw reconstruction (RJR) offers a

³⁹⁸ standard toolkit for deriving estimated boosts between rest frames by analytically minimizing on

³⁹⁹ unknown quantities. While in more exotic final states with multiple invisible particles and com-

⁴⁰⁰ binatoric ambiguities the choice of jigsaw rule can be subjective, the case of W is well-studied and

⁴⁰¹ outlined in detail in Section V.A. of^{s6}. It reproduces the usual transverse mass of the W in place of

⁴⁰² MZ in the 2-lepton case. Not surprisingly, the underlying calculation is also much the same as the LI

⁴⁰³ case (where rest frames and boost were explicitly invoked); again, information is the same, only its

⁴⁰⁴ decomposition is different.

⁴⁰⁵ The 0-lepton channel would appear to present some difficulty as two neutrinos in the final state

⁴⁰⁶ introduce extra degrees of freedom, but both concepts may be extended by treating the invisibly de-

⁴⁰⁷ caying Z as a single invisible particle and requiring the Z to be on-shell. Both of these requirements

⁴⁰⁸ may be folded into the 1-lepton framework to produce similar sets of variables.

Variable	Name	0-lepton	1-lepton	2-lepton
\vec{p}_T^V	pTV		✓	✓
\vec{E}_T^{miss}	MET	✓	✓	✓
\vec{p}_T^{jet1}	pTB ₁	✓	✓	✓
\vec{p}_T^{jet2}	pTB ₂	✓	✓	✓
$\text{MV}_{2\text{C1O}}(\text{jet}_1)^*$	$\text{MV}_{2\text{C1O}}\text{B}_1$	✓	✓	✓
$\text{MV}_{2\text{C1O}}(\text{jet}_2)^*$	$\text{MV}_{2\text{C1O}}\text{B}_2$	✓	✓	✓
m_{jj}	mBB	✓	✓	✓
$\Delta R(\text{jet}_1, \text{jet}_2)$	dRBB	✓	✓	✓
$ \Delta\eta(\text{jet}_1, \text{jet}_2) $	dEtaBB	✓		
$\Delta\phi(V, H)$	dPhiVBB	✓	✓	✓
$\Delta\eta(V, H)$	dEtaVBB			✓
$M_{\text{eff}}(M_{\text{eff}3})$	HT	✓		
$\min(\Delta\phi(\ell, \text{jet}))$	dPhiLBmin		✓	
m_T^W	mTW		✓	
m_{ll}	mLL			✓
$\Delta Y(W, H)$	dYWH		✓	
m_{top}	mTop		✓	
Only in 3 Jet Events				
\vec{p}_T^{jet3}	pTJ ₃	✓	✓	✓
$\text{MV}_{2\text{C1O}}(\text{jet}_3)^*$	$\text{MV}_{2\text{C1O}}\text{B}_3$	✓	✓	✓
m_{jjj}	mBBJ	✓	✓	✓

Table 1.2: Variables used to train the multivariate discriminant. Starred variables (b -tag scores) are not included in current versions of the standard discriminants, but have traditionally been included and most likely will be reintroduced as soon as their accompanying systematics are available.

⁴⁰⁹ While the precise variables that would be included in 0- and 1-lepton LI and RF MVA discrimi-
⁴¹⁰ nants is beyond the scope of this thesis, looking at Table 1.2, we can see the dimensionality and in-
⁴¹¹ puts of the discriminants of the fiducial analysis. The correspondence for LI/RF variables and stan-
⁴¹² dard variables extends nicely to the other lepton channels. The reduction in multiplicity of variables

⁴¹³ owing the lower number of degrees of freedom provided by treating the Z as a single invisible particle in the 0-lepton channel would likely not be an issue, as one would just be able to use a greater fraction of available variables in the MVA discriminant.

⁴¹⁶ *Maybe do the 0-lep calculation and 0/1-lep RF cartoons*

Noli turbare circulos meos

Archimedes

2

417

418 The Large Hadron Collider and the ATLAS

Detector

419

420 THE CERN ACCELERATOR COMPLEX AND ITS EXPERIMENTS stand as a testament to human in-
421 genuity and its commitment to the pursuit of fundamental knowledge. In this chapter, we give a

⁴²² cursory overview of the CERN accelerator complex, including the Large Hadron Collider (LHC),
⁴²³ before moving on to a more detailed review of the ATLAS detector.

⁴²⁴ **2.1 THE CERN ACCELERATOR COMPLEX**

⁴²⁵ The journey of protons from hydrogen canister to high energy collisions through the CERN ac-
⁴²⁶ celerator complex, illustrated in Figure 2.1, is also one through the history of CERN’s accelerator
⁴²⁷ program. After being ionized in an electric field, protons are first accelerated in a linear accelera-
⁴²⁸ tor, LINAC 2^{*}, to a kinetic energy of 50 MeV. From there, they are fed into the Proton Synchotron
⁴²⁹ Booster[†], which further accelerates them to 1.4 GeV and, as its name implies, feeds them to the 628
⁴³⁰ m Proton Synchotron (PS, 1959⁸) and up to 25 GeV. The penultimate stage is the 7 km Super Pro-
⁴³¹ ton Synchotron (SPS, 1976; responsible for the discovery of the W and Z bosons and the 1983 Nobel
⁴³² Prize¹⁰), which accelerates the protons to a kinetic energy of 450 GeV. Finally, these 450 GeV protons
⁴³³ are injected into the LHC¹⁰, a proton-proton collider housed in the 27 km circumference tunnel
⁴³⁴ that housed the Large Electron Positron Collider (LEP) before its operations ceased in 2000.

⁴³⁵ **2.2 THE LARGE HADRON COLLIDER**

⁴³⁶ The LHC was designed to function primarily as a proton-proton collider with a center of mass en-
⁴³⁷ ergy $\sqrt{s} = 14$ TeV and an instantaneous luminosity of $1 \times 10^{34} \text{ cm}^{-2} \cdot \text{s}^{-1}$, though it is also capable
⁴³⁸ of producing heavy ion (Pb-Pb) collisions, which it does for approximately one month in a typical

* 1978’s LINAC 2 is the successor to 1959’s LINAC 1; it will be replaced in 2020 by LINAC 4; LINAC 3 is responsible for ion production.

[†] Protons can be directly from a LINAC into the PS, but the higher injection energy allows for approximately 100 times more protons to be used at once⁹, 1972.

CERN's Accelerator Complex

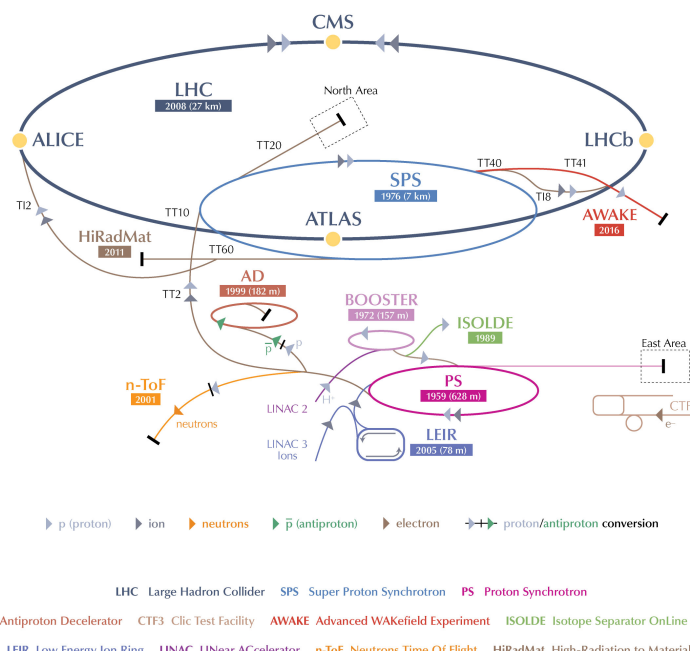


Figure 2.1: The CERN Accelerator Complex⁶⁴

⁴³⁹ year of physics collisions. Owing to an accident at the beginning of the LHC's initial run, the accelerator has operated at center of mass energies of 7, 8, and now 13 TeV.

⁴⁴¹ The limited size of the LEP tunnel (\sim 3.6 m) means that it is impractical to have separate rings
⁴⁴² and magnet systems for each proton beam (proton-antiproton colliders like the Tevatron do not face
⁴⁴³ this complication and can have both beams circulating in the same beam pipe), so the LHC magnets
⁴⁴⁴ are coupled in a "twin bore" design. The LHC magnets make use of superconducting NbTi cables
⁴⁴⁵ and are cooled using superfluid helium to a temperature of 2 K, which allows for operational field
⁴⁴⁶ strengths in excess of 8 T. The layout of an LHC dipole magnet is shown in Figure 2.2. These dipole
⁴⁴⁷ magnets are responsible for bending the LHC's proton beams, and their strength is the principal
⁴⁴⁸ limiting factor in the center of mass energy achievable at a circular collider.

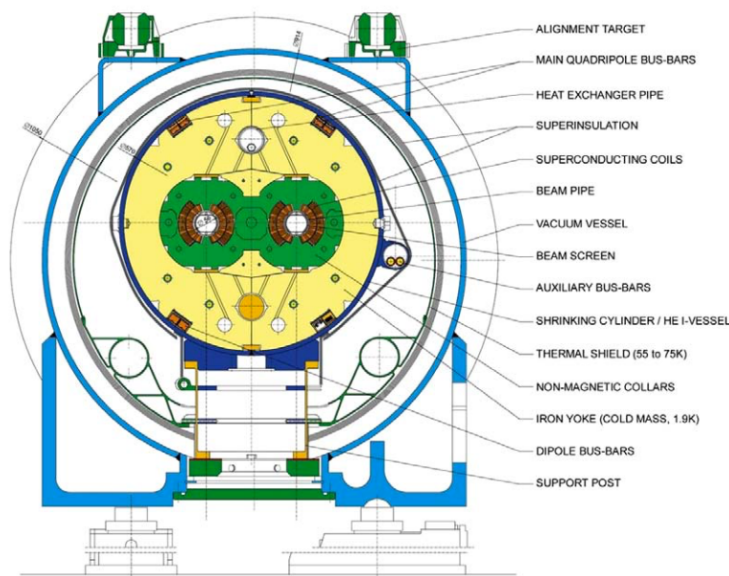


Figure 2.2: Schematic drawing of an LHC dipole magnet and cryogenics system.

⁴⁴⁹ In addition to the dipole magnets, there are quadrupole magnet assemblies in the short straight
⁴⁵⁰ sections (for beam focusing), as well as quadrupole, octupole, and sextupole magnets interspersed
⁴⁵¹ throughout the length of the LHC ring for beam stabilization and other higher order corrections.

⁴⁵² The interior of the LHC beam pipe operates at a nominal pressure of $\sim 10^{-7}$ Pa, famously more
⁴⁵³ rarefied than outer space.

⁴⁵⁴ The LHC ring itself is between 45 m and 170 m below ground and has a 1.4% incline towards Lac
⁴⁵⁵ Léman with eight arcs and eight straight sections. In the middle of each of the eight straight sections,
⁴⁵⁶ there are potential interaction points (each colloquially referred to by its number as “Point N ”),
⁴⁵⁷ with each point housing either accelerator infrastructure or an experiment. A schematic of the con-
⁴⁵⁸ tents of each component, as well as a more detailed view of the infrastructure in the LHC ring, can
⁴⁵⁹ be found in Figure 2.3.

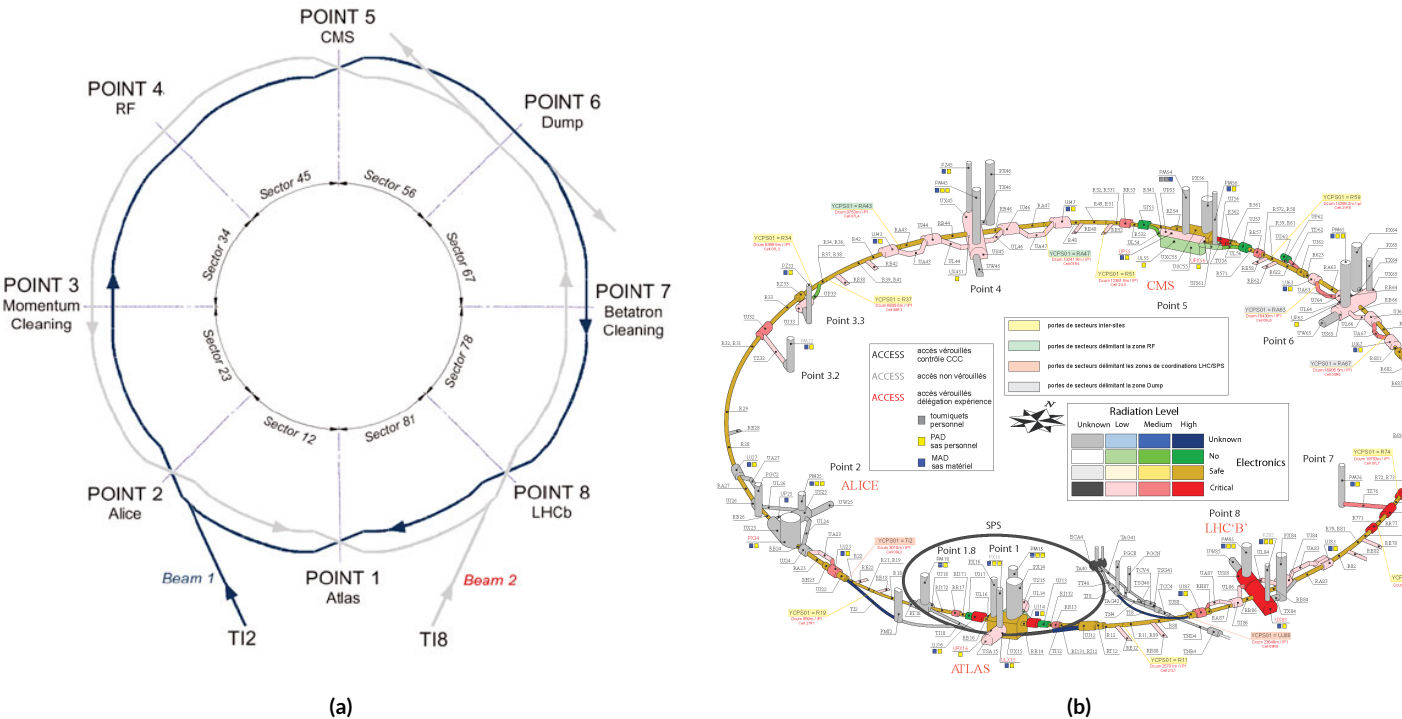


Figure 2.3: Schematic and detailed views of the LHC ring. IC.^{35 72},

460 Points 1, 2, 5, and 8 house the LHC’s experiments, ATLAS (*A Toroidal LHC ApparatuS*, one
461 of the two general purpose detectors, discussed in detail below), ALICE (A Large Ion Collider Ex-
462 periment, a dedicated heavy ion experiment), CMS (Compact Muon Solenoid, the other general
463 purpose detector), and LHCb (LHC beauty, a *B* physics experiment), respectively. Point 3 houses
464 a series of collimators that scatter and absorb particles in the beam with a large momentum devia-
465 tion from other particles in the beam (“momentum cleaning”), while Point 7 has a similar setup to
466 remove particles with large betatron amplitudes (“betatron cleaning”). Betatron amplitudes are re-
467 lated to how well focused beams are and can be thought of as giving a characteristic size for a beam;
468 just as one wants to screen out particles deviating in physical space, one also wants protons in the
469 beam to have nearly identical momentum. Well focused beams in both position and momentum
470 space are crucial to high quality collisions. Point 4 contains the LHC’s RF (radio frequency; 400
471 MHz) acceleration system, responsible for taking protons from their injection energy of 450 GeV to
472 their collision energy of 3.5, 4, 6.5, or 7 TeV. Point 6 is where the energetic ionizing radiation of cir-
473 culating beams can be safely taken out of the collider into a block of absorbing material, either at the
474 end of a data-taking run or in the event of an emergency (in the event of irregular behavior, it is es-
475 sential to do this as quickly as possible to minimize damage to the accelerator and to experiments);
476 this is known as a “beam dump.”

⁴⁷⁷ 2.3 ATLAS AT A GLANCE

⁴⁷⁸ 2.3.1 COORDINATES AND DISTANCES IN THE ATLAS DETECTOR

⁴⁷⁹ *A Toroidal LHC ApparatuS* is one of the two (the other being CMS) general purpose, high lumi-
⁴⁸⁰ nosity detectors at the LHC, located at Interaction Point 1, as described above. With a length of 44
⁴⁸¹ m and a height of 25 m, it is the detector with largest physical dimensions at the LHC.[‡]. While pri-
⁴⁸² marily a high luminosity proton-proton collision detector, ATLAS does collect heavy ion collision
⁴⁸³ data, typically for one month during a year of typical operation.

⁴⁸⁴ The ATLAS coordinate system is shown in Figure 2.4. It is a right-handed coordinate system cen-
⁴⁸⁵ tered at the nominal collision point, with the x axis pointing towards the center of the LHC ring,
⁴⁸⁶ the z axis pointing up, and the y axis completing the right-handed coordinate system.

⁴⁸⁷ While the Cartesian coordinates are useful for specifying the locations of things like detector com-
⁴⁸⁸ ponents and activated calorimeter cells, cylindrical polar coordinates with the same origin, z axis, and
⁴⁸⁹ handedness are often more suitable, with a point in 3-space expressed as (r, ϕ, η) . r is the perpen-
⁴⁹⁰ dicular distance from the beam axis. This differs from the usual spherical ρ , the distance of a point
⁴⁹¹ from the origin, because the ATLAS detector is cylindrical[§], and so detector components are more
⁴⁹² easily located using r instead of ρ . In some contexts, the latter is used, though this is (or should be)
⁴⁹³ made clear. ϕ is the usual (right-handed) azimuthal angle around the beam axis, with 0 at the $+x$
⁴⁹⁴ axis.

[‡]This is the only reason CMS can call itself “compact.”

[§]“toroidal;” the hole is the beam pipe

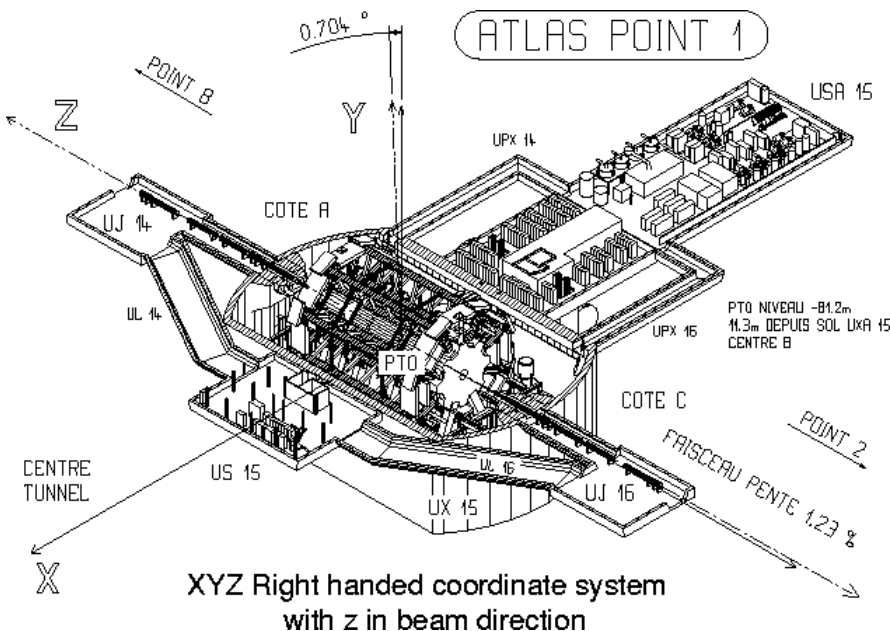


Figure 2.4: The ATLAS coordinate system. "A" side is the airport, and "C" side is "Charlie's," a pub in Saint-Genis, France.

495 In a lepton collider where total momentum is conserved, a useful coordinate is the relativistic

496 rapidity of a particle:

$$y = \frac{1}{2} \ln \left[\frac{E + p_z}{E - p_z} \right] \quad (2.1)$$

497 with E and p_z as the energy and longitudinal momentum of the particle, respectively. The rapidity

498 is the relativistic analog of a rotation angle; boosts can be added in a manner similar to rotations⁴,

499 and differences in rapidity are invariant under boosts. In a hadronic collider, where the participants

500 in the hard scatter are partons inside of the proton of unknown momentum fraction, longitudinal

501 momentum is not conserved. Nevertheless, since the incident momentum is entirely longitudinal,

⁴Generally, one need only insert the appropriate factor of i , the square root of -1 ; this introduces differences in sign and changes all of the trigonometric functions associated with rotations into hyperbolic trigonometric functions.

502 momentum is still conserved in the transverse plane, so quantities like transverse momentum \vec{p}_T
 503 or energy (E_T)^{||} are often very useful in analysis. However, in the massless limit^{**}, we can take $E =$
 504 $\sqrt{\vec{p}_T^2 + p_z^2}$. Hence, with θ taken as the zenith angle and o corresponding to the $+z$ direction, for a
 505 massless particle, $p_z = E \cos \theta$. Using the usual half angle formula $\cos \theta = (1 - \tan^2 \theta) / (1 + \tan^2 \theta)$

506

$$\gamma = \frac{1}{2} \ln \left[\frac{1 + \cos \theta}{1 - \cos \theta} \right] = \frac{1}{2} \ln \left[\frac{(1 + \tan^2(\theta/2)) + (1 - \tan^2(\theta/2))}{(1 + \tan^2(\theta/2)) - (1 - \tan^2(\theta/2))} \right] = -\ln \left(\tan \frac{\theta}{2} \right) \quad (2.2)$$

507 This last expression, denoted η , is known as the pseudorapidity.

$$\eta = -\ln \left(\tan \frac{\theta}{2} \right) \quad (2.3)$$

508 Lower values of $|\eta|$ (1.3) correspond to more central areas of the detector known as the “barrel,”
 509 with the typical layout here being concentric, cylindrical layers. Larger values of $|\eta|$ (to ~ 2.5 for
 510 some systems and up to as much as $\sim 4.5 - 5$ for others) are known as the “end caps,” where ma-
 511 terial is typically arranged as disks of equal radius centered on the beam pipe stacked to ever greater
 512 values of $|z|$. This terminology will be useful when discussing the various subsystems of the ATLAS
 513 detector. Since decay products from a collision propagate radially (in the calorimeter portions of

^{||}Energy is not a vector quantity, but one can take the scalar or vectorial sum of vectors formed from energy deposits with their location as the direction and energy value as magnitude. In practice, primitives are almost always assumed to be massless, so transverse energy and momentum may loosely be thought of as equivalent, with $E_T = |\vec{p}_T| = p_T$

^{**}not a terrible one for most particles depositing energy in the calorimeter; pions have masses of ~ 130 MeV, and typical energies of calorimeter objects are ~ 10 's of GeV, making for a boost of roughly 100.

514 the detector with no magnetic field), the radial coordinate is not so important for composite physics
 515 objects like electrons or jets, which are typically expressed as momentum 4-vectors. Hence, η and ϕ
 516 are often the only useful spatial coordinates. Distances between objects are often expressed not as a
 517 difference in solid angle, but as a distance, ΔR , in the $\eta - \phi$ plane, where

$$\Delta R_{12} = (\eta_1 - \eta_2)^2 + (\phi_1 - \phi_2)^2 \quad (2.4)$$

518 Two important concepts when discussing particles traveling through matter (e.g. particle detec-
 519 tors) are radiation lengths and (nuclear) interaction lengths, which characterize typical lengths for
 520 the energy loss of energetic particles traveling through materials. In general, the energy loss is mod-
 521 eled as an exponential

$$E = E_0 e^{-l/L} \quad (2.5)$$

522 where E_0 is the initial energy, and L is a characteristic length. These lengths depend both on the in-
 523 cident particle and the material through which they pass. In the case of uniform, composite mate-
 524 rials, the length may be found by calculating the reciprocal of the sum of mass fraction weighted
 525 reciprocal characteristic lengths of the components. This formula works quite well for modeling the
 526 very regular behavior of electromagnetic showers (energetic photons convert into electron/positron
 527 pairs, which emit photons...). In this case, L is denoted X_0 ; this is the radiation length. Hadronic
 528 showers are far more complicated, with shower multiplicity and makeup being much more vari-
 529 able^{††}. Nevertheless, a characteristic length can be tabulated for a standard particle type, typically

^{††}Different initial hadrons will shower very differently, and hadronic showers will have phenomena like

530 pions, and is called the nuclear interaction length.

531 2.3.2 GENERAL LAYOUT OF ATLAS

532 The ATLAS detector and its main components are shown in Figure 2.5. ATLAS is designed as a
533 largely hermetic detector, offering full coverage in ϕ and coverage in $|\eta|$ up to 4.7. The multiple sub-
534 systems allow for good characterization of the decay products from collisions in the LHC. The in-
535 nermost system is the inner detector (ID); composed primarily of silicon pixels and strips immersed
536 in a magnetic field, it is designed to reconstruct the curved trajectories of charged particles produced
537 in collisions while taking up as little material as possible.

538 Surrounding the ID is the liquid argon based electromagnetic calorimeter (ECAL), which is de-
539 signed to capture all of the energy of the electromagnetic showers produced by electrons and pho-
540 tons coming from particle collisions. The ECAL is in turn encapsulated by a scintillating tile and
541 liquid argon based hadronic calorimeter (HCAL) that captures any remaining energy from the jets
542 produced by hadronizing quarks and gluons.

543 The outermost layer of ATLAS is the muon spectrometer (MS), which has its own magnetic field
544 produced by toroidal magnets. Muons are highly penetrating particles that escape the calorimeters
545 with most of their initial momentum, so the MS and its magnets are designed to curve these charged
546 particles and measure their trajectories to measure their outgoing momenta. Each of these detector
547 systems has several principal subsystems and performance characteristics, which will be described in
548 turn below.

547 neutral pions converting to photons (which then shower electromagnetically), making them much trickier to
deal with.

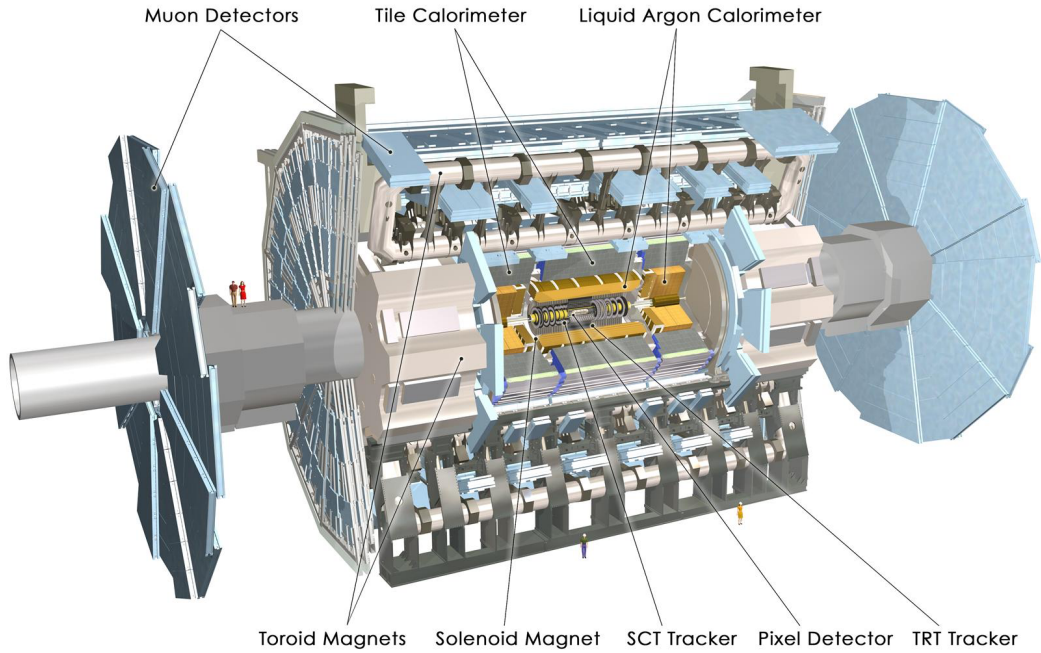


Figure 2.5: The ATLAS detector with principal subsystems shown.

549 2.4 THE INNER DETECTOR

550 ATLAS's inner detector (ID) is surrounded by a 2 T superconducting solenoid that is cryogenically
 551 cooled to a temperature of 4.5 K. The ID uses two silicon detector subsystems (the Pixel and Semi-
 552 Conductor (strip) Tracker (SCT)) to track the curved trajectories of charged particles emanating
 553 from particle collisions and a Transition Radiation Tracker (TRT) composed of gas straw detectors
 554 with filaments for e/π discrimination, as shown in Figure 2.6. The ID offers full coverage in ϕ and
 555 extends to an $|\eta|$ of 2.5.

556 Since the components of the ID do not provide an energy measurement, it is desirable for a track-
 557 ing system to have as small a material budget as possible so that more accurate energy measurements

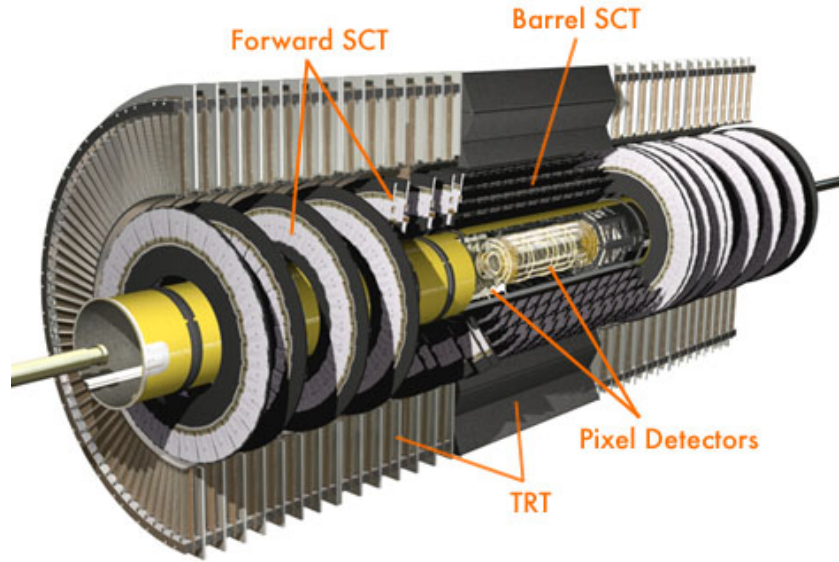


Figure 2.6: The ATLAS inner detector. IC:⁴⁴

558 may be done in the calorimeters. Generally, there are two radiation lengths in the inner detector (the
 559 precise figure varies with η); the full material budget, with the layout of the individual layers in each
 560 subsystem, can be seen in Figure 2.7.

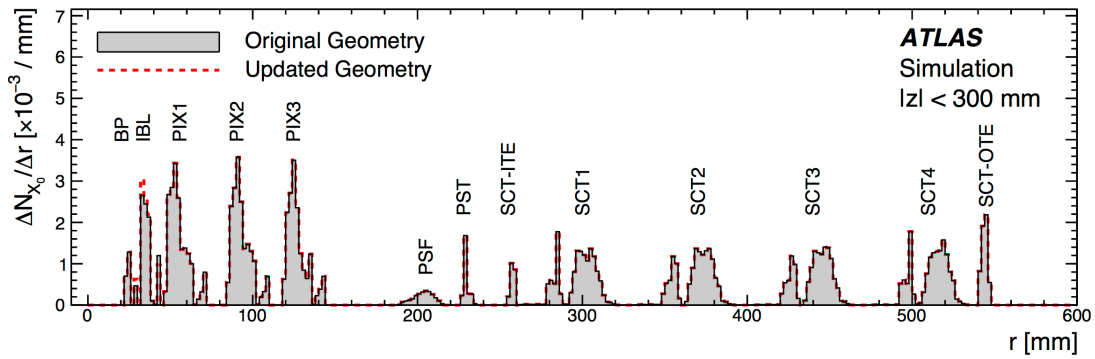


Figure 2.7: The ID material budget. IC:⁴³

561 2.4.I THE PIXEL DETECTOR

562 The innermost part of ATLAS is the Pixel Detector, which, as the name suggests, is comprised of
563 four layers of silicon pixels in the barrel at 32, 51, 89, and 123 mm from the beam pipe, and three lay-
564 ers in the end caps at 495, 580, and 650 mm from the beam pipe, with over 80 million channels total.

565 The innermost layer of pixels, the insertable *B* layer (IBL) was installed during the 2013–14 LHC
566 shutdown. The pixels are cooled to a temperature of $\sim -5^\circ\text{C}$, with N_2 gas and operate at 150–600
567 V. The pixels themselves come in two sizes $50 \times 400(600) \times 250 \mu\text{m}$, with the larger pixels in the
568 outer layers. They provide nominal resolution of $10(115) \mu\text{m}$ resolution in $r - \phi(z)$ direction.

569 In order to improve total coverage in the detector and prevent any gaps, pixels are not installed
570 flush with each other. Pixels in the barrel are tilted at about 20° , with an overlap in $r - \phi$, as shown
571 in Figure 2.8. The disks of the ID end caps are rotated with respect to each other by 3.75° .

572 2.4.2 THE SILICON MICROSTRIP DETECTOR (SCT)

573 The layout of the SCT is similar to that of the Pixel detector, except that, for cost considerations, the
574 SCT uses silicon strips. These strips are also cooled to $\sim -5^\circ\text{C}$ with N_2 gas and operate from 150–
575 350 V. Strip dimensions are $80 \times 6000 \times 285 \mu\text{m}$, and provide nominal $17(580) \mu\text{m}$ resolution in
576 $r - \phi(z)$. Barrel strips feature an 11° tilt and come in four layers at 299, 371, 443, and 514 mm. There
577 are nine end cap disks on each side at z values varying from 934–2720 mm.

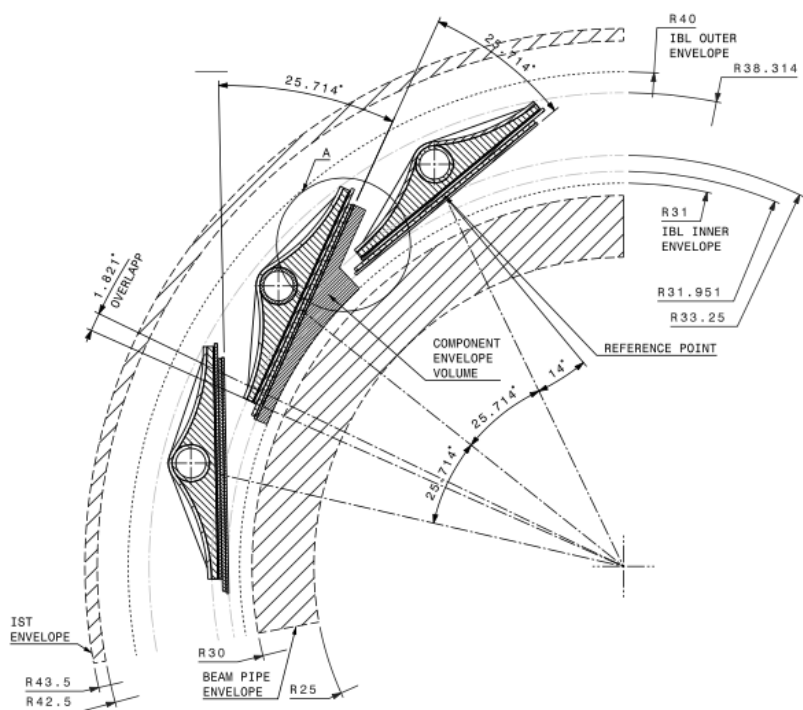


Figure 2.8: Arrangement of pixels in the barrel. IC:³⁴

⁵⁷⁸ 2.4.3 TRANSITION RADIATION TRACKER (TRT)

⁵⁷⁹ The final and outermost subsystem in the ID is the Transition Radiation Tracker (TRT). It provides
⁵⁸⁰ coverage for $|\eta|$ up to 2.0 and is composed of straw detectors with a 4 mm diameter that run the
⁵⁸¹ length of the detector module. The straws provide $130 \mu\text{m}$ resolution, are filled with a Xe-CO₂-O₂
⁵⁸² (70-27-3) gas combination, and operate at -1500 V. The filaments and foil lining inside the straws
⁵⁸³ induce X-ray emission in electrons and pions passing through the TRT as they move from a dielec-
⁵⁸⁴ tric to a gas; this “transition radiation” is the source of the TRT’s name. Since the energy deposited
⁵⁸⁵ due to transition radiation is proportional to the relativistic boost γ , for constant momentum, this
⁵⁸⁶ is inversely proportional to mass. Thus, electrons will have $\sim 130/0.5 = 260\times$ more transition
⁵⁸⁷ radiation than pions, in principle enabling excellent electron/pion discrimination. The TRT will be
⁵⁸⁸ replaced by silicon strips in the Phase II upgrade.

⁵⁸⁹ 2.5 THE ATLAS CALORIMETERS

⁵⁹⁰ ATLAS has four main calorimeter systems: the liquid argon based Electromagnetic Calorimeter
⁵⁹¹ (ECAL), the Hadronic End Cap (HEC), the Forward Calorimeters (FCAL), and the scintillating
⁵⁹² tile based hadronic Tile Calorimeter in the barrel. Their layout and material budget in interaction
⁵⁹³ lengths can be seen in Figure 2.10.

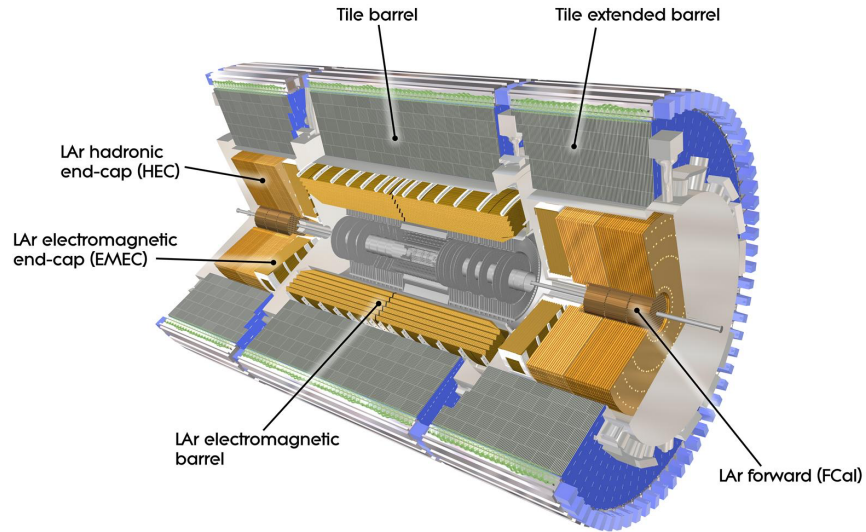


Figure 2.9: The ATLAS calorimeters.

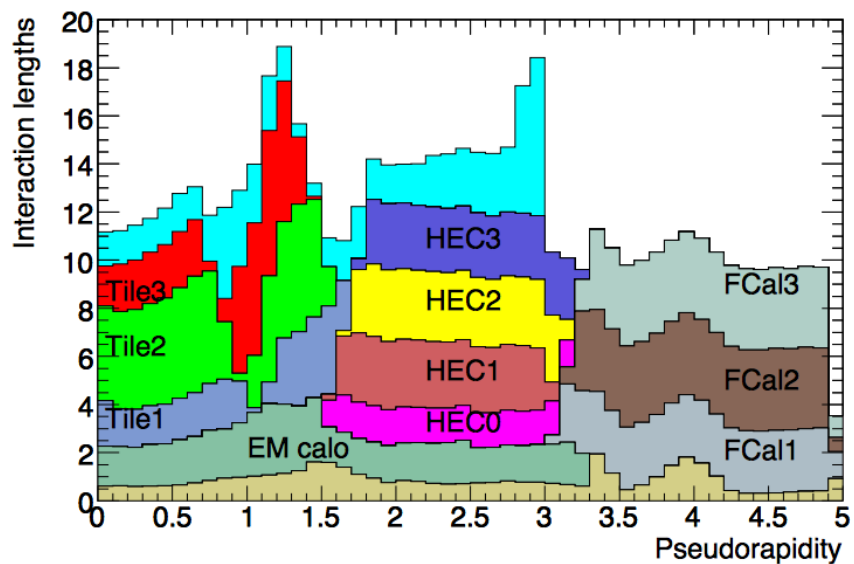


Figure 2.10: Material depth of the ATLAS calorimeters. IC:⁴⁴

594 2.5.1 CALORIMETER RESOLUTION

595 Before diving into the specifics of each of the ATLAS calorimeters, we review some aspects of calorime-
596 ter energy resolution performance. A calorimeter’s relative energy resolution (a ratio) can be broken
597 up into three orthogonal components, as shown in Equation 2.6.

$$\frac{\sigma_E}{E} = \frac{S}{\sqrt{E}} \oplus \frac{N}{E} \oplus C \quad (2.6)$$

598 S is the photoelectron statistics or stochastic term and represents the coefficient to the usual count-
599 ing term (assuming Gaussian statistics); N is a noise term, which is constant per channel (and hence
600 comes in as $1/E$ in the relative energy resolution); and C is a constant “calibration” term, which re-
601 flects how well one intrinsically understands a detector (i.e. mismodelling introduces an irreducible
602 component to the energy resolution). If any detector were perfectly modeled/understood, it’s C
603 term would be zero. $N \sim 0.1 - 0.5$ GeV for a typical calorimeter regardless of type, so S and C
604 are typically quoted.

605 A typical stochastic term scales as $S \sim \text{few\%} \sqrt{d_{\text{active}} [\text{mm}] / f_{\text{samp}}}$, where f_{samp} is the sampling
606 fraction or the ratio of a calorimeter by mass is composed of an active material (i.e. one that regis-
607 ters energy deposits). The tile calorimeter, for example, has a sampling fraction of about 1/36. There
608 are several reasons that this fraction is so low. First, many active volumes have insufficient stopping
609 power; one wants to capture as much energy as possible from electromagnetic and hadronic showers
610 inside the calorimeter, and this simply is not possible for most active media (one notable exception

611 to this is the CMS crystal-based calorimeter; ATLAS is a more conservative design), so well-behaved
612 absorbers like lead or iron are necessary to ensure all the energy is contained within a calorimeter.
613 Another factor is cost; things like liquid argon are expensive. Finally, most active media are unsuit-
614 able for structural support, so sturdy absorbing materials help relieve engineering constraints.

615 **2.5.2 THE ELECTROMAGNETIC CALORIMETER (ECAL)**

616 The ECAL has liquid argon (LAr) as an active material and lead as an absorber. The ECAL barrel
617 extends to $|\eta|$ of 1.475, with three layers at 1150, 1250, and 2050 mm, and its end cap, comprised of
618 two wheels, covers $1.375 < |\eta| < 2.5$, (3.2) for the inner (outer) wheel, with 3 (2) layers out to
619 3100 mm. There is a 1.1 (0.5) cm thick layer of LAr pre-sampler up to $|\eta|$ of 1.8 in the barrel (end cap)
620 of the ECAL, which is designed to aid in correcting for electron and photon energy loss in the ID.

621 The LAr and lead absorber are arranged in alternating, beveled, sawtooth layers in what is known
622 as an “accordion” geometry, shown in Figure 2.11, which shows the layout of a barrel module in the
623 ECAL. The absorber thickness is 1.53 (1.13) mm for $|\eta|$ less (more) than 0.8 to ensure a constant sam-
624 pling fraction. This arrangement helps provide greater coverage in ϕ .

625 The ECAL overall typically covers 2–4 interaction lengths or about 20–40 radiation lengths. Its
626 performance corresponds to resolution coefficients $S = 0.1 \text{ GeV}^{-1/2}$ and $C = 0.002$ with a 450
627 ns drift time. In order to optimize the material budget and overall detector construction, the ECAL
628 barrel infrastructure is integrated with that of the ID’s solenoid. The granularity of the ECAL barrel
629 middle layer, $\Delta\eta \times \Delta\phi$ cells of size 0.025×0.025 , are used to define the granularity of calorimeter
630 cluster reconstruction in ATLAS.

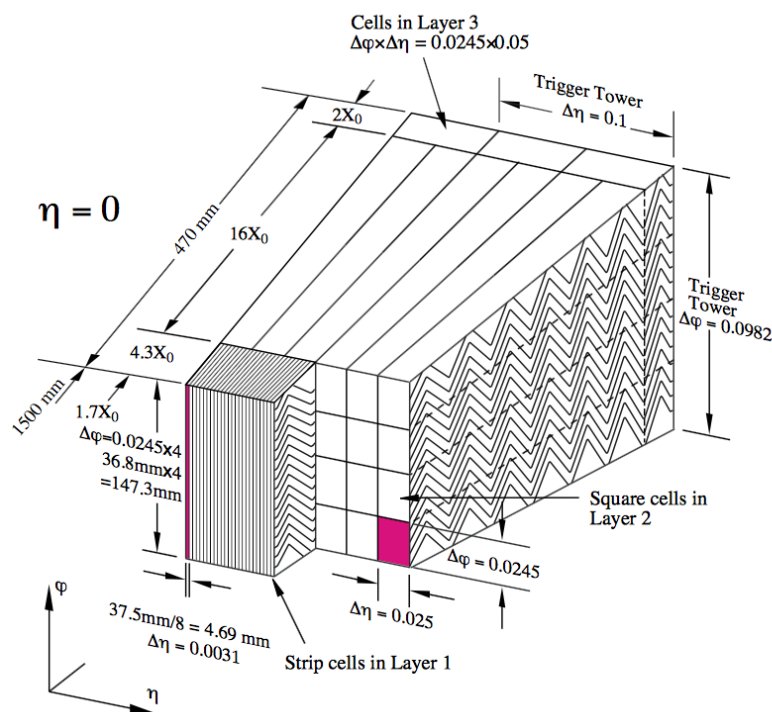


Figure 2.11: The accordion geometry of the LAr electromagnetic calorimeters is prominently shown in this illustration of an ECAL barrel module. IC:⁴⁴

⁶³¹ 2.5.3 HADRONIC END CAPS (HEC)

⁶³² The HEC covers an $|\eta|$ range of 1.5 to 3.2. Like the ECAL end caps, the HEC consists of two identi-
⁶³³ cal wheels out to a distance from the beam axis of 2030 mm; its layout is shown in Figure 2.12. The
⁶³⁴ HEC also has LAr as the active material, but instead has flat copper plates as absorbers for sampling
⁶³⁵ fraction of 4.4% and 2.2% in the first and second wheels, respectively. Its granularity in $\eta - \phi$ is
⁶³⁶ 0.1×0.1 for $|\eta|$ up to 2.5 and 0.2×0.2 in the more forward regions.

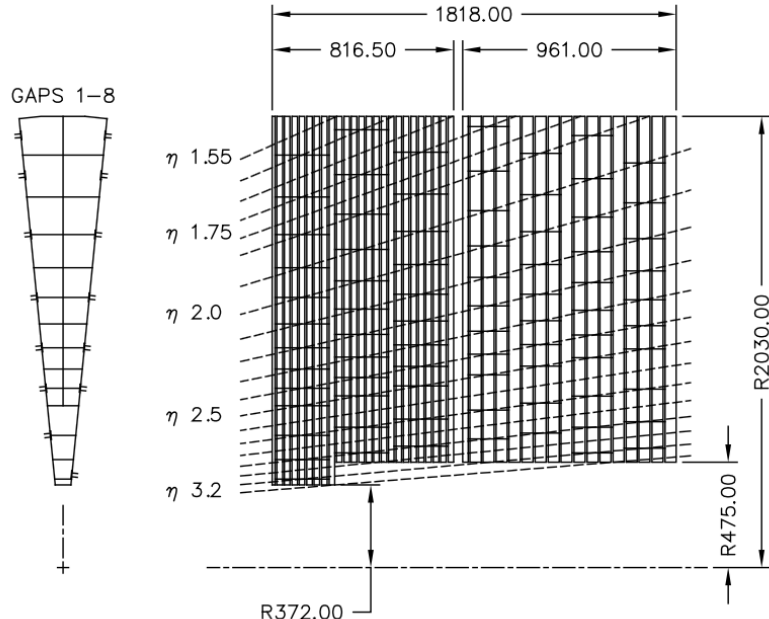


Figure 2.12: The layout of the HEC in $r - \phi$ and $r - z$; dimensions are in millimeters. IC.⁴⁴

⁶³⁷ 2.5.4 THE FORWARD CALORIMETER (FCAL)

⁶³⁸ The FCAL covers an $|\eta|$ range from 3.1 to 4.9, again using LAr as the active material in gaps between
⁶³⁹ rods and tubes in a copper-tungsten matrix, as shown in Figure 2.13. These system has characteris-
⁶⁴⁰ tic performance corresponding to stochastic term of $S \approx 1 \text{ GeV}^{-1/2}$. There are three modules in
⁶⁴¹ the FCAL: one electromagnetic and two hadronic, with the latter two featuring a higher tungsten
⁶⁴² content for a larger absorption length.

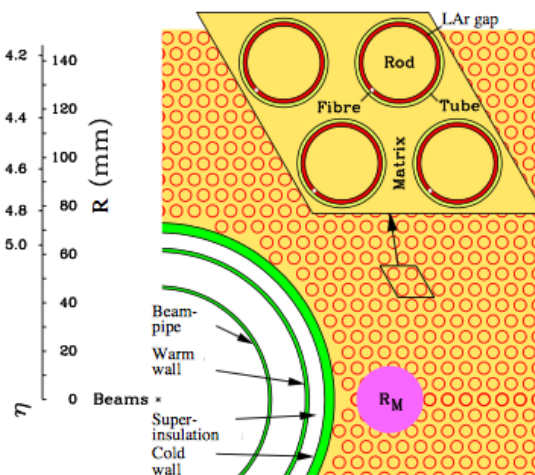


Figure 2.13: The material layout for a typical section of the FCAL in the transverse plane. IC:⁴⁴

⁶⁴³ 2.5.5 THE HADRONIC TILE CALORIMETER

⁶⁴⁴ The tile calorimeter, covering an $|\eta|$ of up to 1.7 is made up of 64 modules in the barrel (each cover-
⁶⁴⁵ ing $\Delta\phi$ of $360/64 = 5.625^\circ$), each with a layout as in Figure 2.14. It is designed to be self-supporting
⁶⁴⁶ for structural reasons, and so is the only calorimeter without LAr as a an active medium, with a stag-
⁶⁴⁷ gered matrix of active scintillating polystyrene and supporting steel. It operates at 1800 V with a 400

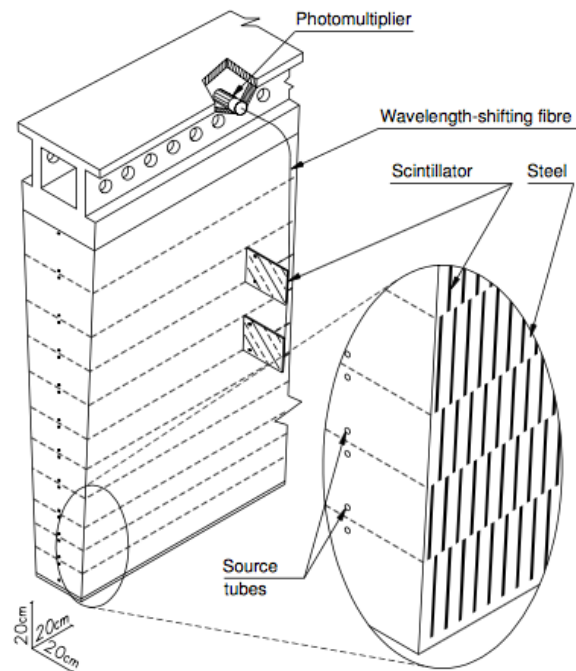


Figure 2.14: The material layout for a typical section of the hadronic tile calorimeter. IC.⁴⁴

648 ns dead time and has a thickness corresponding to 10–20 interaction lengths (2.28–4.25 m). Its cells
 649 have a $\Delta\eta \times \Delta\phi$ granularity of 0.1×0.1 in the first two layers and 0.2×0.1 in the last layer. Its
 650 performance corresponds to $S = 0.5 \text{ GeV}^{-1/2}$ and $C = 0.05$ (0.03 after calibration).

651 2.6 THE MUON SPECTROMETER

652 Since the energy of muons is not captured within the calorimeters, the stations of the ATLAS MS
 653 surround the entire detector and provide tracks of outgoing muons that can be matched to tracks in
 654 the ID. The ATLAS toroids, which provide field strengths of up to 2.5 (3.5) T in the barrel (end cap)
 655 with typical strengths of 0.5–1.0 T, bend the muons, which allows for a muon momentum measure-
 656 ment since the muon mass is known. The relative momentum resolution of a tracker (assuming, as
 657 in ATLAS, that bending primarily happens in the ϕ direction) may be expressed as

$$\frac{\sigma_{p_T}}{p_T} = c_0 \oplus c_1 \cdot p_T \quad (2.7)$$

658 The c_0 term represents a degradation in resolution due to multiple scattering, and is typically 0.5–
 659 2%⁷⁷. The c_1 term describes the phenomenon of, holding magnetic field constant, higher momen-
 660 tum muons curving less. This term has typical values of $10^{-3} - 10^{-4} \text{ GeV}^{-1}$. At very high p_T val-
 661 ues, this is of particular concern since a very small curvature can result in charge misidentification.

662 A cross-sectional view (in $r-z$) of the muon spectrometer with station names, detector types, and
 663 layouts is shown in Figure 2.15. There are three layers of muon detectors in both the barrel (at 5 000,
 664 7 500, and 10 000 mm) and end cap (at 7 000 (11 000), 13 500, and 21 000 mm), with the innermost

665 end cap layer split in two due to the end cap toroid. This corresponds to an $|\eta|$ range up to 2.4 for
 both precision and trigger coverage, and up to 2.7 for precision detection only.^{†‡}

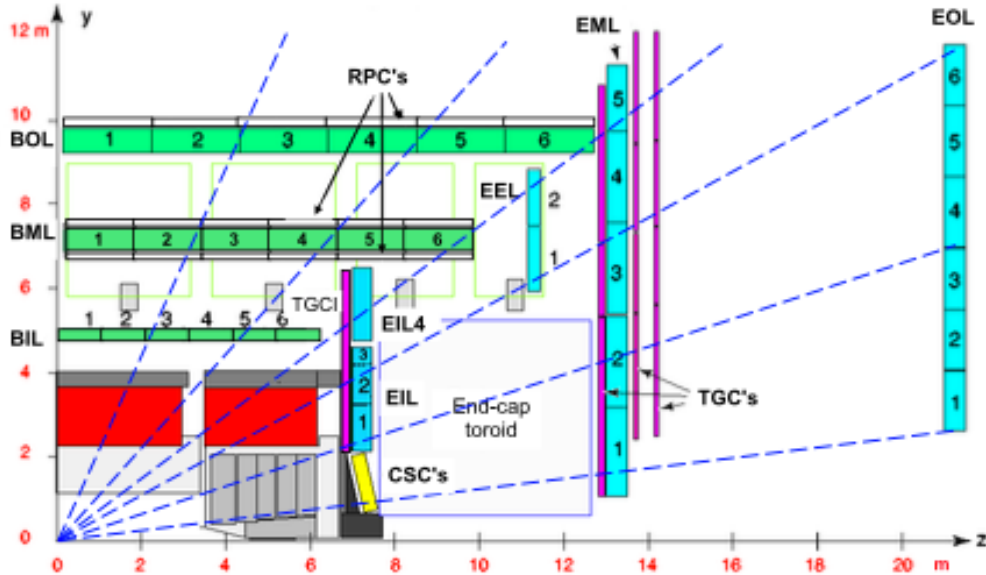


Figure 2.15: The ATLAS muon spectrometer. Naming of the MDT stations obeys the following convention [BE] (barrel or end cap) [IEM0] (inner, inner extended (end cap only), middle, or outer layer) [1-6] (increasing in z (r) for the barrel (end cap)), so EI1 is the station in the inner most end cap layer closest to the beam pipe. IC:⁴⁴

666

667 The MS can reconstruct muons with transverse momenta from 5 GeV up to 3 TeV (with 10% res-
 668 olution at 1 TeV (3% at 100 GeV)). Detectors in the MS fall into two broad headings, precision detec-
 669 tors and trigger detectors, both described below. Nominal performance of the current detector types
 670 in the MS is summarized in Figure 2.16, a table taken from⁴⁴. It should be noted that $|\eta|$ ranges
 671 quoted below, where applicable, do not include the range 0-0.1, where this a gap in the MS to allow
 672 for cabling and other services to the ATLAS detector; for a discussion of compensatory measures in

^{†‡}This will change with the New Small Wheel Phase I Upgrade. cf. Appendix A

⁶⁷³ muon reconstruction, see Chapter 5.

Type	Function	Chamber resolution (RMS) in			Measurements/track		Number of	
		z/R	ϕ	time	barrel	end-cap	chambers	channels
MDT	tracking	35 μm (z)	—	—	20	20	1088 (1150)	339k (354k)
CSC	tracking	40 μm (R)	5 mm	7 ns	—	4	32	30.7k
RPC	trigger	10 mm (z)	10 mm	1.5 ns	6	—	544 (606)	359k (373k)
TGC	trigger	2–6 mm (R)	3–7 mm	4 ns	—	9	3588	318k

Figure 2.16: ATLAS MS detector performance. IC:⁴⁴

⁶⁷⁴ 2.6.1 PRECISION DETECTORS

⁶⁷⁵ The ATLAS MS has two types of precision detectors: Monitored Drift Tubes (MDT's) and Cathode Strip Chambers (CSC's). An MDT is a tube with a 3 cm diameter with length depending on
⁶⁷⁶ the station in which the tube is located. The tube is filled with an Ar/CO₂ gas mixture and has a
⁶⁷⁷ tungsten-rhenium wire at its center that is kept at 3 000 V when operational. The MDT's provide 35
⁶⁷⁸ μm resolution (per chamber) in their cross-sectional dimension (there is no sensitivity along the axis
⁶⁷⁹ of the wire). Resolution of this magnitude requires very precise knowledge of the location of the
⁶⁸⁰ wires within the MDT's; this is generally true for detectors in the MS (trigger as well as precision);
⁶⁸¹ to this end, stations of the MS are aligned using an optical laser system. For a detailed description
⁶⁸² of how misalignment can affect performance, see Appendix A for a detailed discussion of misalign-
⁶⁸³ ment's simulated effects on the performance of the proposed Micromegas trigger processor in the
⁶⁸⁴ New Small Wheel (NSW) of the Phase I upgrade. Their 700 ns dead time, however, precludes their
⁶⁸⁵ use as trigger detectors and also in the region of the small wheel (innermost endcap) closest to the
⁶⁸⁶ beam pipe ($|\eta|$ from 2.0 to 2.7), where rates are highest.
⁶⁸⁷

688 In this region, the precision detectors are the CSC's, which have a much lower dead time of ~ 40
689 ns. These are multiwire proportional chambers with cathode planes that have orthogonal sets of
690 strips, allowing for a measurement in both principal directions. CSC detector sizes also vary by sta-
691 tion, coming in both small and large chambers. The CSC strip pitch is 5.31 (5.56) mm for the large
692 (small) chambers, with position determined from the induced charge distribution in the strips. This
693 corresponds to a nominal resolution of 60 (5 000) μm per plane in the bending (non-bending) direc-
694 tion. These are slated to be replaced by Micromegas detectors in the NSW.

695 **2.6.2 TRIGGER DETECTORS**

696 Trigger detectors have a fundamentally different role than the precision detectors, instead needing to
697 deliver “good enough” approximate values of muon track positions and p_T values. The MS has two
698 types of trigger detectors: Resistive Plate Chambers (RPC’s) in the barrel and Thin Gap Chambers
699 (TGC’s) in the end caps. They collectively cover an $|\eta|$ range to 2.4, and their arrangement is shown
700 in Figure 2.17.

701 The RPC’s are parallel plate detectors with a dead time of 5 ns and a thickness of 2 mm, kept at
702 a potential of 9 800 V; they are deployed in three layers. RPC’s, too, feature strips with orthogonal
703 arrangements on the top and bottom planes, with a strip pitch of 23–35 mm.

704 The TGC’s are multiwire proportional chambers with a dead time of 25 ns. Also, featuring or-
705 thogonal strips, the TGC’s also provide a ϕ measurement to compensate for the lack of MDT sensi-
706 tivity in this direction. There are four layers of TGC’s in the end cap. TGC’s will be supplanted by
707 sTGC’s (small thin gap chambers) in the NSW.

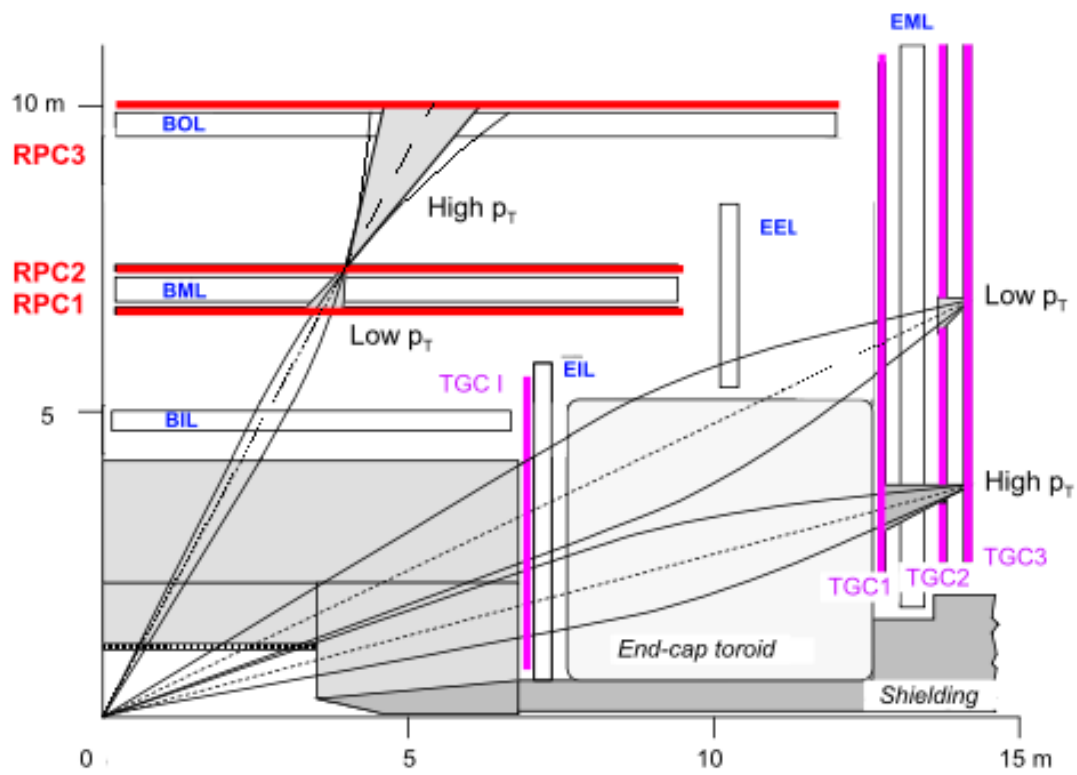


Figure 2.17: ATLAS MS trigger detector arrangement. IC:⁴⁴

708 For more details on how detector level trigger objects work in the ATLAS MS, see Appendix A
709 for details on the Micromegas trigger processor algorithm.

What do you read, my lord?

Words, words, words.

Hamlet, 2:2

3

710

711

Data and Simulated Samples

712 THE DATA AND Monte Carlo simulation (MC) samples used in this thesis are the same as in the fidu-
713 cial analysis. The data corresponds to 36.1 fb^{-1} of pp collision data collected in 2015+16 at the AT-
714 LAS detector at $\sqrt{s} = 13 \text{ TeV}$. Details of the Run 1 analysis referenced in Chapter 9, may be found
715 in ²⁰. Only events recorded with all systems in ATLAS in good working order and passing certain

716 quality requirements, according to a Good Run List (GRL), are analyzed.

717 Details about MC samples may be found in ⁶⁷, and signal and background modeling are discussed
718 in the next. The $ZH \rightarrow \ell\ell b\bar{b}$ process is considered for both multivariate analysis (MVA) optimiza-
719 tion and the final statistical analysis, while $WH \rightarrow \ell\nu b\bar{b}$ and $ZH \rightarrow \nu\nu b\bar{b}$ production are included
720 in the final statistical analysis only. Signal MC samples were generated separately for qq and gg ini-
721 tiated VH processes. $qqVH$ samples were generated with PowHEG MiNLO + PYTHIA8 with the
722 AZNLO tune set and NNPDF3.0 PDF. Nominal $ggZH$ samples were generated using PowHEG for
723 the matrix element (ME) and PYTHIA8 for the parton shower (PS), underlying event (UE), and mul-
724 tiple parton interactions (MPI), again applying the AZNLO tune and NNPDF3.0 PDF set.⁶⁰

725 The background processes considered in these studies are $Z+jets$, $t\bar{t}$, and diboson production for
726 both MVA optimization and the final statistical analysis with single top production and $W+jets$
727 only considered in the final statistical analysis. $V+jets$ samples are generated using SHERPA 2.2.1⁴⁰
728 for both the ME and PS. These samples are generated in different groups, according to the identity
729 of the V , the max (H_T, p_T^V) of events, with further subdivisions according to the flavor of the two
730 leading jets in an event, b , c , or l , for a total of six categories. $t\bar{t}$ samples are generated using PowHEG
731 with the NNPDF3.0 PDF set interfaced with PYTHIA8 using the NNPDF2.3 PDF's and the A14
732 tune⁴⁶. Single top samples use PowHEG with the CT10 PDF's interfaced with PYTHIA6 using the
733 CTEQ6L1 PDF's^{21,57}. Diboson samples are generated with SHERPA 2.2.1 interfaced with the NNPDF3.0
734 NNLO PDF set normalized to NLO cross sections³³.

*There are certain calculations one simply doesn't do in
public.*

Alan Blaer

4

735

736

Signal and Background Modeling

737 THIS CHAPTER summarizes the modeling of the dominant signal and background processes in
738 this analysis, including corrections and systematic uncertainties (systematic uncertainty, also called
739 nuisance parameter (NP), titles are set in this font) related to each process. Further details on the
740 specifics of these topics, including in-depth studies for the derivation and definitions of some of the

⁷⁴¹ quantities cited, may be found in⁶⁷. We start with a general discussion of modeling and associated
⁷⁴² major categories of uncertainties before addressing each of the physics processes.

⁷⁴³ 4.1 EVENT GENERATION IN A NUTSHELL

⁷⁴⁴ Before diving into the specifics of modeling and systematic uncertainties associated with each ma-
⁷⁴⁵ jor set of physics processes considered in this analysis, we review at a schematic level* the problem
⁷⁴⁶ of simulation event generation. Once a physics processes of interest has been determined, how one
⁷⁴⁷ simulates an ensemble of particle collisions to model the process in question. This is illustrated in
⁷⁴⁸ Figure 4.1. Note that the scope of this problem does not include how these generated collision prod-
⁷⁴⁹ ucts propagate through one's detector. This problem is left for Chapter 5.

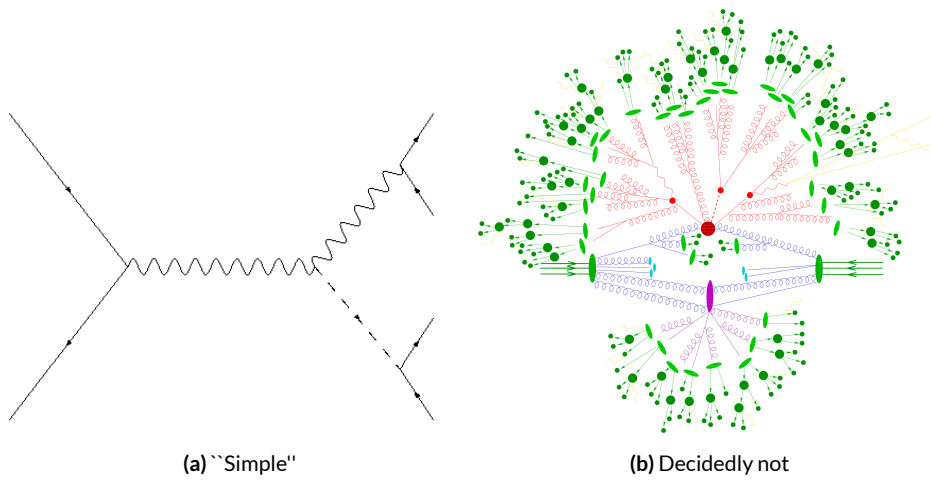


Figure 4.1: The problem here is how to get from (a) to (b).

⁷⁵⁰ The primary source of complication in event generation comes from dealing with hadronic ob-

*i.e. this will not be a technically rigorous discussion. For a more thorough treatment, the reader is di-
rected to the usual references.

jects both in the initial state (the lefthand side of Figure 4.1 (a); the LHC is a hadron collider) and the final state (this analysis searches for Higgs decays to b -jets, the lower righthand side of Figure 4.1).
Common to all hadronic objects, by definition, are the many considerations that go into calculations in quantum chromodynamics (QCD). In calculating the hard scatter process itself, one must make a variety of choices, such as the parton distribution function (PDF) set to use and to what order in perturbation theory to do the calculation (common choices are leading order (LO), (next to) next to leading order ((N)NLO), and (next to) next to leading log (NNLL)). Similar considerations often need to be made for the electroweak parts of an event. These considerations and others will be discussed in more detail below.

The initial state includes not only the hard scatter partons that generate the physics process of interest, but also the rest of the partons in the colliding protons, known as the underlying event (UE). Moreover, the hard scatter partons may not be the only interacting partons in an event, further complicating matters; this phenomenon is known as multiple parton interactions (MPI). Specific to the final state are the kinematic distributions of the final state objects—what their energies and angular distributions will be—in addition to the overall cross section of the process that is measurable by the detector (acceptance effects). Furthermore, one has to model hadronization, the process by which any free (colored) partons in an event transform into colorless hadrons.

Typically, it takes several steps and tools to accomplish this. The hard scatter itself is often modelled with a dedicated event generator like PowHEG⁶⁸ or MADGRAPH²³, with events generated then interfaced with a tool like PYTHIA⁷¹ for the PS, UE, and MPI, though there are exceptions (SHERPA⁵¹, for example, can do both the hard scatter and hadronization/ for some processes).

772 4.2 DESCRIPTION OF MODELING UNCERTAINTY CATEGORIES

773 Each of the steps in event generation described above has associated uncertainties. Some uncertain-
774 ties are inherent in the calculations themselves. The choice of which order in perturbation theory
775 to do a calculation, for example, comes with it an implicitly defined level of precision[†]. Extrapolat-
776 ing from one energy/momentum scale to another also introduces uncertainty. Furthermore, there
777 is no *a priori* correct choice to make at each step in event generation, so each choice (the choice of
778 generator, PDF set, parton shower calculator, all of their configurable parameters, etc.) implies an
779 additional layer of uncertainty.

780 In order to quantify these choices, each source of systematic uncertainty is treated separately and
781 given a unique name. To make this more concrete, take the specific example of the uncertainty asso-
782 ciated with the $H \rightarrow b\bar{b}$ branching ratio of 58%, called `ATLAS_BR_bb`, which encapsulates a num-
783 ber of effects (higher order terms, the mass of the b quark, and choice of α_S). The quoted (in prin-
784 ciple asymmetric) uncertainty on the Higgs BR is not itself a direct input into the analysis model.
785 Instead, the effect of varying the branching ratio up and down by one standard deviation is propa-
786 gated to simulated collision events and recorded (i.e. the analysis is run with the Higgs branching
787 ratio at $\pm 1\sigma$, and the results are recorded alongside the nominal result). The nominal and “up” and
788 “down” variations are then typically taken to define a normally distributed, freely floating param-
789 eter in the statistical fit model. Since these parameters associated with systematic uncertainties are
790 not typically considered interesting quantities, they are often referred to as “nuisance parameters”

789 [†]though this is less well-defined in QCD calculations than for electroweak calculations since they don’t converge

791 (NP's). The terms “systematic,” “systematic uncertainty,” and “nuisance parameter” are often used
792 interchangeably.

793 The specifics of exactly how the effects of variations are saved and propagated to the full fit model
794 are deferred to Chapter 7. The discussion here is confined to how systematic uncertainties for signal
795 and background modeling and their accompanying variations are defined. Modeling systematics are
796 derived separately for each physics process (simulation sample). Sometimes, all of the variation for
797 a given process is encapsulated in a single systematic, but oftentimes the variations from multiple
798 considerations are distinct enough to be treated separately. Furthermore, each of these separate sys-
799 tematics for a given sample/process may be treated in a number of ways (e.g. 0-lepton events may
800 be treated differently from 2-lepton events). An additional subtlety is that a continuous parameter
801 like a branching ratio lends itself quite naturally to defining Gaussian $\pm 1\sigma$ variations, while for dis-
802 crete variations, like choice of PDF set for parton showers, how to proceed is less obvious. This is
803 addressed on a case-by-case basis, as described below.

804 Before enumerating each of the principal physics processes and their systematics, we begin by
805 describing considerations and choices that must be addressed for every physics process in order to
806 make the discussion of individual samples and systematics both clearer and less repetitive.

807 **4.2.1 PHYSICS CONSIDERATIONS**

808 In general, evaluating the uncertainties arising from the many choices in event generation entails
809 producing alternate samples of events, which practically means tuning parameters in the various soft-
810 ware packages and/or using alternate packages/libraries to make new samples. Once these samples

811 have been created, they are compared at truth-level (particle level) using a package called Rivet³⁰ in-
812 stead of using the full ATLAS detector reconstruction for computational considerations. Given the
813 nature of the problem and the tools, there are generally three main categories of physics issues, each
814 described below.

815 **UNDERLYING EVENT AND PARTON SHOWER**

816 The modeling of the underlying event (UE) and parton shower (PS) are usually handled by the same
817 package and so are usually treated together. The typical nominal choice in the fiducial analysis is
818 PYTHIA8. One approach to modeling these uncertainties is simply to see what happens when a
819 different model is used and then compare this alternate set of events to the nominal set, taking the
820 difference as the (implicitly one standard deviation) scale of variation. Another approach is to vary
821 some parameter within a given model, for example, using different tunes in the A14 set for PYTHIA8
822 with their accompanying variations, to characterize the scale of variation.

823 A natural question is how to treat these two approaches on the same footing. When examining
824 a set of potential variations related to the same process or effect, oftentimes the largest single varia-
825 tion in a set is picked as defining the scale for the systematic uncertainty. Another approach is to use
826 the average over a set of variations.[‡] The ATLAS_UEPS_VH_hbb systematic, for example, uses the
827 Pythia8 + A14 tunes approach to determine the scale of UE variation and compares Pythia8 with
828 Herwig7 to characterize the PS variation. Each of the A14 tunes comes with an up and down varia-
829 tion, and the difference between each of these variations and a nominal setup may be expressed as a

[‡]Generally, the maximum is used if it is much larger than other variations, and the average is used if scales are comparable. In general, the historical preference is to be conservative.

830 ratio, R , of total events.

831 As is often done when a physical argument can be made for combining related, but ultimately
832 orthogonal categories/measurements/uncertainties/systematics, the combined UE+PS systematic is
833 taken to be the sum in quadrature of these two effects:

$$\sum_{tunes} \max \left(|R_{up} - R_{down}| \right) \oplus \sigma_{PS} \quad (4.1)$$

834 QCD SCALE

835 The term “QCD scale” in the context of modeling uncertainties refers to the choice of renormal-
836 ization (μ_R) and factorization (μ_F) scales used in QCD calculations. These are typically treated to-
837 gether. Usually, some multiplicative scale factor, f , is chosen, and each scale is varied in concert with
838 the other scale by $1/f$ and $1/f$ (nine total combinations), sometimes with a cap on how large the
839 combined variation can be (so ignoring the (f,f) and $(1/f, 1/f)$ cases). Just as in the UE+PS, the
840 largest variation is usually taken as the systematic uncertainty.

841 PARTON DISTRIBUTION FUNCTIONS AND α_S

842 Finally, separate uncertainties are often made for the choice of parton distribution function (PDF)
843 set and associated choice of strong coupling for QCD (α_S). Much as in the previous two cases, one
844 can vary the parameter α_S and study what samples of simulation events made using different PDF
845 sets relative some nominal setup look like. Similarly, one can take the maximum, average, or sum in
846 quadrature of different variations to characterize a systematic uncertainty.

847 4.2.2 MODELING SYSTEMATIC TYPES

848 With the concept of what type of effect is taken as a single systematic uncertainty and how its varia-
849 tions are generally evaluated, it is now time to turn to the issue of what exactly is being varied.

850 ACCEPTANCE/NORMALIZATION

851 The most basic type of modeling uncertainty is a normalization uncertainty, often called an accep-
852 tance uncertainty. This simply denotes the uncertainty on the number of predicted events for a
853 given process in a given region of phase space (usually delineated by the number of leptons in the
854 final state and sometimes also by the number of and jets the p_T^V [§] of an event) and is usually expressed
855 as a percent.

856 As an example, the uncertainty on the theoretical prediction of the $H \rightarrow b\bar{b}$ branching ratio,
857 denoted ATLAS_BR_bb (it is an ATLAS-wide systematic), is expressed as a normalization system-
858 atic with a value of 1.7%, affecting all VH processes. Now imagine we have an event in a VH sample
859 with weight 1.0. The nominal histograms for this region gets filled with this event's relevant informa-
860 tion with weight 1.0, while the ATLAS_BR_bb__1up (__1do) histograms get filled with weight 1.017
861 (0.983).

[§]This is the transverse mass of the lepton pair for 2-lepton events, the vectorial sum of the single lepton
and \vec{E}_T^{miss} for 1-lepton events, and the \vec{E}_T^{miss} for 0-lepton events.

862 SHAPE SYSTEMATICS

863 In addition to normalization systematics expressed as single numbers attached to different processes
864 in different regions, there are also the so-called “shape systematics” and “shape corrections.” These
865 have the schematic form

$$w_{event} = A_{region} \times f_{region}(event)$$

866 where w_{event} is the simulated event’s weight, A_{region} is the overall normalization (in principle includ-
867 ing any systematics), and $f_{region}(event)$ is some function of event-level variables, usually a single vari-
868 able, like p_T^V or m_{bb} . The purpose of these systematics is to take into account (in the case of a system-
869 atic) or correct (in the case of a correction applied to the event weight) the non-trivial dependence
870 of a normalization on one of these quantities. Some of these are taken from histograms while others
871 are parametric functions (in this analysis, usually linear ones).

872 An example of the former case is the quantity δ_{EW} , the difference between the nominal $qqVH$
873 cross section and the differential cross section as a function of p_T^V at next to leading order (NLO). As
874 a correction, this term is simply used as a correction factor $k_{EW}^{NLO} = (1 + \delta_{EW})$.

875 An example of the latter case is the systematic associated with the m_{bb} dependence of the the
876 $t\bar{t}$ normalization for 2 jet, $p_T^V \in [75, 150]$ GeV, 2 lepton events. In this case, a variety of effects are
877 studied (ME, PS, UE), as shown in Figure 4.3. The top half of the plot is the m_{bb} plot for this re-
878 gion, with the black bars representing the nominal spectrum and spectra generated with different
879 ME, PS, and UE choices. The ratio plot in the bottom half of the figure shows the scale of varia-
880 tion normalized to bin content. From this ratio plot, it is clear that the choice of ME (pink points)

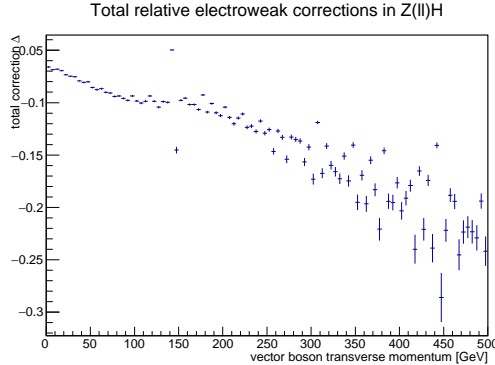


Figure 4.2: The δ_{EW} correction term for 2-lepton $qqZH$.

881 was seen to have the largest effect on normalization. The linear fit in the plot reasonably envelopes
 882 this maximum variation was done, and so is taken as the systematic variation. Hence, in this case,
 883 $f_{\text{region}}(\text{event})$ is a linear function of m_{bb} , with positive (negative) slope for the up (down) variation.

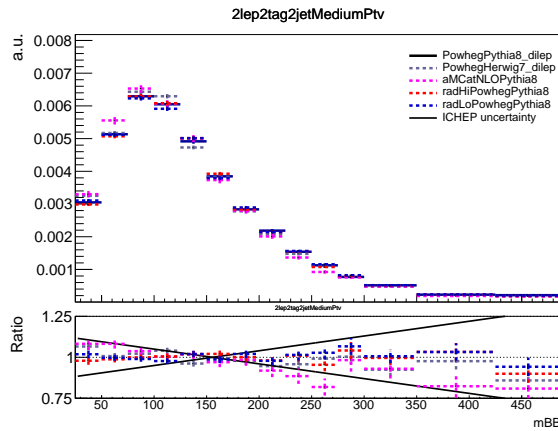


Figure 4.3: The derivation of the 2-lepton $t\bar{t} m_{bb}$ shape systematic.

884 DIVIDING MODELING UNCERTAINTIES: ACCEPTANCE RATIOS

885 In addition to uncertainties on absolute normalizations (both inclusive and region specific), mod-
 886 eling uncertainties are sometimes introduced for the ratio of normalizations between different re-

887 gions. While these can be simple ratios, evaluating a systematic's effect between regions means eval-
 888 uating nominal and alternate choices between regions, so the so-called “double ratio” is often taken
 889 as the scale of variation (plus one). The ATLAS_UEPS_VH_hbb systematic mentioned above, for ex-
 890 ample, has associated with it, ATLAS_UEPS_VH_hbb_32JR. This systematic is evaluated by dividing
 891 the 3 jet to 2 jet ratio in the nominal setup by the same ratio in an alternate setup. Such a ratio generi-
 892 cally looks like:

$$\frac{\text{Acceptance}[\text{Category}_A(\text{nominalMC})]}{\text{Acceptance}[\text{Category}_B(\text{nominalMC})]} \Big/ \frac{\text{Acceptance}[\text{Category}_A(\text{alternativeMC})]}{\text{Acceptance}[\text{Category}_B(\text{alternativeMC})]} \quad (4.3)$$

893 The three main categories are ratios between different flavor regions, ratios between different lep-
 894 ton channels[¶], and ratios between regions with different numbers of jets, n_{jet} . The first category is
 895 only relevant for $V+jets$ systematics and will be treated in that process's dedicated section below. As
 896 this thesis is primarily concerned with the 2-lepton channel, the second category will not be treated
 897 in detail, though the treatment is much the same as other ratio systematics.^{||} In order to discuss the
 898 n_{jet} ratios in systematics (e.g. the ratios in the double ratio example), we must first describe how ex-
 899 clusive n_{jet} cross section calculations are done.

900 THEORETICAL ASIDE: STEWART-TACKMANN A way to calculate uncertainties on processes in re-
 901 gions with different numbers of jets was developed by Stewart and Tackmann and is implicitly used

[¶]e.g. $Z+heavy$ flavor jets (at least one b -jet in the event; often denoted “hf” normalizations in 0- and 2-lepton events

^{||}Such ratios allow for information in one channel to help constrain other channels, particularly for hard to model processes like $Z+hf$. This helps to reduce final overall uncertainties in combined fits. For a discussion of the interplay of nuisance parameters in combined fits, cf. Chapter 9.

902 for most n_{jet} ratio systematics⁷³. The problem is how to calculate the cross section and associated
 903 uncertainty for a process with exclusively N jets in the final state. Generically:

$$\sigma_{\geq N} = \sigma_N + \sigma_{\geq N+1} \quad (4.4)$$

904 The physical interpretation of one parton to one jet is an idealized case. In order to demarcate
 905 between jets, one has some quantity that is used as a cutoff in an integral that defines the border be-
 906 tween jet regions.

$$\sigma_{\geq N} = \int_0^{p_{cut}} \frac{d\sigma_N}{dp} + \int_{p_{cut}} \frac{d\sigma_{\geq N+1}}{dp} \quad (4.5)$$

907 Since these cutoffs (not necessarily constant, etc.) can make calculations more complicated, inclu-
 908 sive cross sections tend to be easier to calculate. Hence, it is usually much easier to evaluate the two
 909 inclusive cross sections and find the uncertainties on these by varying α_S in the usual way (cf. Sec-
 910 tion 4.2.1). One then assumes the inclusive uncertainties are uncorrelated, for a covariance matrix for
 911 $\{\sigma_{\geq N}, \sigma_N, \sigma_{\geq N+1}\}$ of (with Δ_x^2 as the variance associated with x):

$$\Sigma = \begin{pmatrix} \Delta_{\geq N}^2 & \Delta_{\geq N}^2 & 0 \\ \Delta_{\geq N}^2 & \Delta_{\geq N}^2 + \Delta_{\geq N+1}^2 & -\Delta_{\geq N+1}^2 \\ 0 & -\Delta_{\geq N+1}^2 & \Delta_{\geq N+1}^2 \end{pmatrix} \quad (4.6)$$

912 These calculations contain Sudakov double logs of p/Q , where Q corresponds to the scale of the
 913 hard scatter process (m_H), and p_{cut} is usually something like a p_T cutoff. The $N + 1$ term in the co-

914 variance matrix is an uncertainty associated with the cutoff, but the Sudakov double logs will domi-
915 nate any higher order terms. Stewart and Tackmann give the following reasoning:

916 “In the limit $\alpha_S^2 \approx 1$, the fixed-order perturbative expansion breaks down and the logarithmic
917 terms must be resummed to all orders in α_S to obtain a meaningful result. For typical experimental
918 values of p_{cut} fixed-order perturbation theory can still be considered, but the logarithms cause large
919 corrections at each order and dominate the series. This means varying the scale in α_S in Eq. (9) di-
920 rectly tracks the size of the large logarithms and therefore allows one to get some estimate of the size
921 of missing higher-order terms caused by p_{cut} , that correspond to Δ_{cut} . Therefore, we can approxi-
922 mate $\Delta_{cut} = \Delta_{\geq 1}$, where $\Delta_{\geq 1}$ is obtained from the scale variation for $\sigma_{\geq 1}$.”

923 The above considerations are important for this analysis since phase space is separated into 2 and
924 ≥ 3 jet regions, and the uncertainties for these regions are anti-correlated.

925 4.3 PROCESS SPECIFIC SYSTEMATIC SUMMARIES

926 Brief descriptions of modeling systematics, including recapitulations of nominal sample generation,
927 are given in the following sections. The general approach here is to copy the relevant summary tables
928 and describe any major deviations from the general procedures described in the previous section.
929 The dominant backgrounds for the 2-lepton channel are $Z+hf$ and $t\bar{t}$, accounting for well over 90%
930 of all background events. Diboson samples are the next-leading background and are an important
931 validation sample; others are included for completeness. A summary of all the modeling systematics
932 in this analysis are given in Table 4.1.

Process	Systematics
Signal	$H \rightarrow bb$ decay, QCD scale, PDF+ α_S scale, UE+PS (acc, p_T^V , m_{bb} , 3/2 jet ratio)
$Z+jets$	Acc, flavor composition, $p_T^V+m_{bb}$ shape
$t\bar{t}$	Acc, $p_T^V+m_{bb}$ shape
Diboson	Overall acc, UE+PS (acc, p_T^V , m_{bb} , 3/2 jet ratio), QCD scale (acc (2, 3 jet, jet veto), p_T^V , m_{bb})
Single top	Acc, $p_T^V+m_{bb}$ shape

Table 4.1: Summary of modeling systematic uncertainties, with background samples listed in order of importance.

4.3.1 SIGNAL PROCESSES

Nominal signal $q\bar{q}VH$ samples are generated using Powheg with the MiNLO (multiscale improved NLO)⁶² procedure applied interfaced with Pythia8 using the AZNLO tune¹⁹ and NNPDF3.0 PDF set²⁸. For the 2-lepton case, gluon fusion initiated Higgs production is also considered (accounting for $\sim 14\%$ of the total cross section in this channel), with samples generated with Powheg interfaced with Pythia8 using the AZNLO tune. The NNPDF2.3 set²⁷ is used for both the ME and UE+PS.

Alternate samples $q\bar{q}VH$ samples are generated using MADGRAPH5_aMC@NLO²² for the ME and Pythia8 for the UE+PS, hadronization and MPI. The NNPDF2.3 5f FFN PDF sets and the Al4 tune¹³; the latter has variations included. Powheg+MiNLO+Herwig7 were samples were also used for systematics.

The signal systematics categories are $H \rightarrow bb$ decay cross section, QCD scale, PDF+ α_S scale, and UE+PS. Additionally, there is the NLOEWK correction described above. The correction scale factor is derived using the HAWK MC software. To encapsulate NNLOEW effects the maximum of 1%, the square of the correction factor, and the photon induced cross section is used as a systematic.

⁹⁴⁷ Table 4.2, reproduced from ⁶⁷, summarizes the signal cross section systematics, which are applied
⁹⁴⁸ uniformly across the analysis channels (as applicable).

Sys Name	source	Norm. effect	applied to
ATLAS_BR_bb	$H \rightarrow bb$ dec. unc, (HO effects, m_b , α_s)	1.7%	all VH processes
ATLAS_QCDscale_VH	QCD scale uncertainty	0.7%	$qq \rightarrow VH$ processes
ATLAS_QCDscale_ggZH	QCD scale uncertainty	27%	$gg \rightarrow ZH$
ATLAS_pdf_Higgs_VH	PDF+ α_s uncertainty	1.9% 1.6%	$qq \rightarrow WH$ $qq \rightarrow ZH$
ATLAS_pdf_Higgs_ggZH	PDF+ α_s uncertainty	5.0%	$gg \rightarrow ZH$

Table 4.2: Summary of all systematic uncertainties on the VH cross section including their value, source and the corresponding nuisance parameter name.

⁹⁴⁹ The remaining signal systematics are analysis channel specific and are summarized in Table 4.3.
⁹⁵⁰ The methodologies match those described in Section 4.2. The UE+PS systematics were derived us-
⁹⁵¹ ing the alternate samples mentioned above; QCD scale uncertainties were derived by varying scales
⁹⁵² by 1/3 and 3; and PDF uncertainties were derived by comparing the nominal set with the PDF4LHC15_30
⁹⁵³ PDF set²⁹.

⁹⁵⁴ 4.3.2 $V + \text{jets}$

⁹⁵⁵ Nominal $V + \text{jets}$ samples are generated using **SHERPA 2.2.1@NLO**^{** 52} for both the ME and PS, in-
⁹⁵⁶ terfaced with the NNPDF's and using a five quark flavor scheme, and alternative samples are derived
⁹⁵⁷ using **MADGRAPH5** interfaced with **PYTHIA8**. In order to increase statistics in important regions
⁹⁵⁸ of phase space, these samples were separated into kinematic slices based on p_T^V and into bins of jet fla-
⁹⁵⁹ vor. The kinematic slices were in the quantity $\max(H_T, P_T^V)$ and had the intervals [0 – 70, 70 – 140, 140 – 280, 280 – 50
⁹⁶⁰ GeV. The jet flavor slices were made using flavor vetoes and filters:

^{**}SHERPA 2.1 is used for some variations not available in SHERPA 2.2.1.

NP name	oL:		iL:		zL:	
	2j	3j	2j	3j	2j	$\geq 3j$
ATLAS_UEPS_VH_hbb	10.0%	10.0%	12.1%	12.1%	13.9%	13.9%
ATLAS_UEPS_VH_hbb_32JR	–	13.0%	–	12.9%	–	13.4%
ATLAS_UEPS_VH_hbb_VPT	shape only			shape+norm		
ATLAS_UEPS_VH_hbb_MBB	shape only			shape only		
QCDscale_VH_ANA_hbb_J2	6.9%	–	8.8%	–	3.3%	–
QCDscale_VH_ANA_hbb_J3	-7%	+5%	-8.6%	+6.8%	-3.2%	+3.9%
QCDscale_VH_ANA_hbb_JVeto	–	-2.5%	–	3.8%	–	–
QCDscale_VH_ANA_hbb_VPT	shape only			shape+norm		
QCDscale_VH_ANA_hbb_MBB	shape only			shape only		
pdf_HIGGS_VH_ANA_hbb	1.1%	1.1%	1.3%	1.3%	0.5%	0.5%
pdf_VH_ANA_hbb_VPT	shape only			shape+norm		
pdf_VH_ANA_hbb_MBB	shape only			shape only		

Table 4.3: Summary of all systematic uncertainties on the VH acceptance and shapes originating from altering the PDF and α_S uncertainties, including their corresponding nuisance parameter name.

- BFfilter: at least 1 b-hadron with $|\eta| < 4, p_T > 0$ GeV
- CFilterBVeto: at least 1 c-hadron with $|\eta| < 3, p_T > 4$ GeV; veto events which pass the BFfilter
- CVetoBVeto: veto events which pass the BFfilter and/or the CFilterBVeto

These in turn are related to the main flavor regions used in the analysis, based on the flavor of the two leading jets in an event (based on p_T). These five flavors (with up, down, and strange collectively known as “light”) yield six different flavor combinations: bb, bc, bl (these first three collectively known as “heavy flavor” or $V+hf$), cc, cl, ll (or just “light” or l). Ratio systematics are often made with respect to the acceptance in the bb region.

$V+$ jet systematics are derived in several steps. The first is to use double ratios of acceptances between analysis regions and nominal versus alternative MC’s (so $(\text{Region1-nominal}/\text{Region2-nominal})/(\text{Region1-alternate}/\text{Region2-alternate})$). The main region comparisons are 2 jet versus 3 jet ($3+$ jet for 2-lepton)

973 and then 0-lepton versus 2-lepton (1-lepton) for $Z+hf$ ($W+hf^{\dagger\dagger}$). The final uncertainty contains the
 974 sum in quadrature of four effects:

- 975 1. Variation of 0.5 and 2 of QCD scales in the SHERPA sample
 976 2. Sum in quadrature of half the variation from different resummation and CKKW merging
 977 scales ^{††}
 978 3. Maximal variation between nominal setup and SHERPA 2.2.1 with the MMHT_{2014nnlo68cl}
 979 and CT14nnlo PDF sets
 980 4. Difference between the SHERPA and MADGRAPH₅ sets

981 Summaries of the Z +jets uncertainties are provided here; the reader is referred to ⁶⁷ for the W +jets
 982 systematics, as these events are virtually non-existent in the 2-lepton case with which this thesis is al-
 983 most exclusively concerned. In Table 4.4, from ⁶⁷ are the normalization systematics.

Process	Name	prior in region					
		2jet			(\geq)3jets		
		2L: low Vpt	2L: high Vpt	oL	2L: low Vpt	2L high Vpt	oL
$Z+l$	SysZclNorm				18%		
	SysZlNorm				23%		
	norm_Zbb				Floating Normalization		
$Z+hf$	SysZbbNorm_L2_J3	-	-	-	30%	30%	-
	SysZbbNorm_J3	-	-	-	-	-	17%
	SysZbbNorm_OL	-	-	7%	-	-	7%
	SysZbbPTV				effect on each region obtained from shape rw		

Table 4.4: Effect of modelling systematics on Z +jets normalization in the 2lepton regions. For systematic uncertainties implemented with a prior the effect of $1-\sigma$ variation is reported. The uncertainties labelled as Zbb act on the entire $Z+hf$ background.

984 The flavor composition ratio systematics are in Table 4.5, also from ⁶⁷.

^{††}The $W+hf$ CR versus the SR is also considered for $W+hf$

^{‡‡}cf. ⁵⁹, Section 2 for a summary of the CKKW method for different parton multiplicities used in SHERPA

Category	Nuisance Parameter Name	Prior	Applied to
$Z+bc/Z+bb$	SysZbcZbbRatio	40%	$Z+bc$ events (0-Lepton)
		40%	$Z+bc$ events (2-Lepton 2jet)
		30%	$Z+bc$ events (2-Lepton ≥ 3 jet)
$Z+bl/Z+bb$	SysZblZbbRatio	25%	$Z+bl$ events (0-Lepton)
		28%	$Z+bl$ events (2-Lepton 2jet)
		20%	$Z+bl$ events (2-Lepton ≥ 3 jet)
$Z+cc/Z+bb$	SysZccZbbRatio	15%	$Z+cc$ events (0-Lepton)
		16%	$Z+cc$ events (2-Lepton 2jet)
		13%	$Z+cc$ events (2-Lepton ≥ 3 jet)

Table 4.5: The priors on the relative acceptance variations for $Z+hf$. The first column details the flavor components across which the acceptance variation is being considered, the second column lists the names of the corresponding nuisance parameter in the Profile Likelihood Fit, the third contains the value of the prior and the fourth column the processes and categories to which this nuisance parameter is applied.

985 Finally, the p_T^V and m_{bb} shape systematics are derived using control regions in data. The func-
 986 tional form for the p_T^V systematic is $\pm 0.2 \log 10(p_T^V/50\text{GeV})$, and that of the m_{bb} systematic is $\pm 0.0005 \times$
 987 $(m_{jj} - 100\text{ GeV})$.

988 4.3.3 TOP-PAIR PRODUCTION

989 Nominal $t\bar{t}$ samples are produced with Powheg at NLO for the ME calculation using the NNPDF3.0
 990 PDF set interfaced with Pythia8.210 using the A14 tune and the NNPDF2.3 PDF set at LO. The
 991 parameters `hdamp` (nominal value $1.5 m_{top}$, a resummation damping factor for ME/PS matching
 992 that can heuristically thought of as tuning high p_T radiation) in Powheg and `pThard` (nominal
 993 value 0) and `pTdef` (nominal value 2) in Pythia (both control merging with Powheg) are varied
 994 to evaluate certain systematics. Alternative $t\bar{t}$ samples use Powheg+Herwig7, MadGraph5_aMC@NLO-

These use the same selections as the signal regions except for b -tags (0, 1, and 2 tags are studied), with the added requirement in 2tag regions that m_{bb} not be in the range of 110–140GeV.

⁹⁹⁵ +PYTHIA8.2, and the nominal setup with varied tunes and parameter values. Uncertainties are taken
⁹⁹⁶ to cover the largest difference between the nominal and any of these alternate configurations.

⁹⁹⁷ The overall $t\bar{t}$ normalization is a floating normalization, and further systematics attached to the
⁹⁹⁸ ratio of acceptances between regions (3-to-2 jet, SR-to-WhfCR, and 1-to-0 lepton) are defined using
⁹⁹⁹ double ratios; these are summarized in Tables 4.6 and 4.7, taken from⁶⁷.

Systematic	0-lepton		1-lepton			
	2j	3j	WCR 2j	SR 2j	WCR 3j	SR 3j
norm_ttbar	floating normalization					
SysttbarNorm_L0	8%	8%	-	-	-	-
SysttbarNorm_J2	9%	-	9%	9%	-	-
SysttbarNorm_DWhfCR_L1	-	-	25%	-	25%	-

Table 4.6: Effect of modelling systematics on normalization in the 0 and 1-lepton analysis region.

	2jet		≥ 3 jets	
	low Vpt [SR/CR]	high Vpt [SR/CR]	low Vpt [SR/CR]	high Vpt [SR/CR]
norm_ttbar_J2_L2	floating normalization		-	
norm_ttbar_J3_L2	-		floating normalization	
SysTTbarPTV_L2_L2	effect on each region obtained from shape rw			

Table 4.7: Effect of modelling systematics on normalization in the 2lepton regions. The SysTTbarPTV_L2_L2 systematic is implemented as a shape systematic over the full $VpT > 75$ GeV range, and as a result has different acceptance effects in the low and high VpT regions.

¹⁰⁰⁰ Shape systematics for p_T^V and m_{bb} are linear and taken to cover the largest difference reasonably
¹⁰⁰¹ well, as described above in 4.2.2. These are summarized in Table 4.8, again taken from⁶⁷.

The use of a top $e - \mu$ control region helps constrain this.

Analysis region	Uncertainty	Value	Source	Nuisance Parameter
0,1 lepton	p_T^V shape	shape	fit through largest deviation (aMC@NLO+PYTHIA8)	TTbarPTV
2 lepton	p_T^V shape	norm + shape	fit through largest deviation (aMC@NLO+PYTHIA8)	TTbarPTV_L2
0,1 lepton	$m_{b\bar{b}}$ shape	shape only	fit through largest deviation (aMC@NLO+PYTHIA8)	TTbarMBB
2 lepton	$m_{b\bar{b}}$ shape	shape only	fit through largest deviation (aMC@NLO+PYTHIA8)	TTbarMBB_L2

Table 4.8: Summary of all shape uncertainties for the $t\bar{t}$ process with short descriptions and the name of the corresponding nuisance parameters.

1002 4.3.4 DIBOSON PRODUCTION

1003 Three diboson production processes (collectively denoted VV) are important for these analyses: ZZ ,
 1004 WZ , and WW . Nominal samples are created using **SHERPA 2.2.1** using the NNPDF3.0 PDF set. Al-
 1005 ternative samples use PowHEG+PYTHIA8 and PowHEG+HERWIG++. The methodology here is
 1006 similar to that of the $t\bar{t}$ systematics, with both overall acceptance and lepton channel specific uncer-
 1007 tainties, with the exception that UE+PS and QCD scale are treated separately (PDF+ α_s was found
 1008 to be negligible). p_T^V shape systematics are described using linear fits, while $m_{b\bar{b}}$ shape systematics
 1009 are described using hyperbolic tangents (third degree polynomials) in the 2 jet (3 jet) regions. Once
 1010 again, summary tables from⁶⁷ are reproduced here.

Sys Name	source	Norm. effect	applied to
SysWWNorm	overall cross section uncertainty	25%	WW in all regions
SysWZNorm	overall cross section uncertainty	26%	WZ in all regions
SysZZNorm	overall cross section uncertainty	20%	ZZ in all regions

Table 4.9: Summary of all systematic uncertainties on the diboson cross section including their value, source and the corresponding nuisance parameter name.

NP name	oL:		iL:		zL:	
	2j	3j	2j	3j	2j	$\geq 3j$
SysVZ_UEPS_Acc	5.6%	5.6%	3.9%	3.9%	5.8%	5.8%
SysVZ_UEPS_32JR	–	7.3%	–	10.8%	–	3.1%
SysVZ_UEPS_VPT	shape+norm		shape only		shape+norm	
SysVZ_UEPS_MBB	shape only					
SysVZ_QCDscale_J2	10.3%	–	12.7%	–	11.9%	–
SysVZ_QCDscale_J3	-15.2%	+17.4%	-17.7%	+21.2%	-16.4%	+10.1%
SysVZ_QCDscale_JVeto	–	+18.2%	–	+19.0%	–	–
SysVZ_QCDscale_VPT	shape+norm		shape only		shape+norm	
SysVZ_QCDscale_MBB	shape only					

Table 4.10: Summary of the systematic uncertainties on the VH acceptance in each analysis region and on the p_T^V and $m_{b\bar{b}}$ shapes originating from altering the QCD scale, including their nuisance parameter name.

1011 4.3.5 SINGLE TOP PRODUCTION

1012 Single top sample are generated separately for the different production channels (s , t , and Wt) using
 1013 Powheg with the CT10 NLO PDF's interfaced with Pythia6 using the PERUGIA2012 PS tune
 1014 and the corresponding CTEQ6L1 LO PDF's and PHOTOS (TAUOLA) for QED final state (τ) de-
 1015 cays.

Production	Uncertainty	Value	Source	Nuisance Parameter
s -channel	overall normalization	4.6%	sum in quadrature of μ_R , μ_F , α_S and PDF uncertainties	<code>stopNorm</code>
t -channel	overall normalization	4.4%	sum in quadrature of μ_R , μ_F , α_S and PDF uncertainties	<code>stopNorm</code>
t -channel	2 jet region acceptance	17%	sum in quadrature of deviations in alternative generators	<code>stopAcc</code> correlated with overall and 3 jet case
t -channel	3 jet region acceptance	20%	sum in quadrature of deviations in alternative generators	<code>stopAcc</code> correlated with overall and 2 jet case
Wt channel	overall normalization	6.2%	sum in quadrature of μ_R , μ_F , α_S and PDF uncertainties	<code>stopWtNorm</code>
Wt channel	2 jet region normalization	35%	sum in quadrature of deviations in alternative generators	<code>stopWtAcc</code> correlated with overall and 3 jet case
Wt channel	3 jet region normalization	41%	sum in quadrature of deviations in alternative generators	<code>stopWtAcc</code> correlated with overall and 2 jet case
t -channel	p_T^V shape	shape	fit through largest deviation (POWHEG+HERWIG++) $\pm 0.001 \times p_T^V \mp 0.17 + 1$	<code>StopPTV</code>
t -channel	$m_{b\bar{b}}$ shape	shape	fit through largest deviation (POWHEG+PYTHIA6 radHi-radLo) $\pm 0.0008 \times m_{b\bar{b}} \mp 0.12 + 1$	<code>StopMBB</code>
Wt channel	p_T^V shape	shape	fit through largest deviation (POWHEG+PYTHIA6 with diagram subtraction) $\pm 0.003 \times p_T^V \mp 0.69 + 1$	<code>StopWtPTV</code>
Wt channel	$m_{b\bar{b}}$ shape	shape	fit through largest deviation (POWHEG+PYTHIA6 with diagram subtraction) $\pm 0.0036 \times m_{b\bar{b}} \mp 0.52 + 1$ ($m_{b\bar{b}} < 275$ GeV) $\mp 0.47 + 1$ ($m_{b\bar{b}} \geq 275$ GeV)	<code>StopWtMBB</code>

Table 4.11: Summary of all uncertainties for the single top process with short descriptions and the name of the corresponding nuisance parameters, updated for the winter baseline analysis.

“...what would you do first?”

The Master said, “It would have to be rectifying names.”

Confucius, *The Analects*

5

1016

1017

Object and Event Reconstruction and

1018

Selection

1019 IN BREAKING WITH THE STANDARD CONVENTION both object definitions and their associated

1020 experimental systematic uncertainties will be defined in this chapter: the hope is that the proximity

1021 of these descriptions will allow them to elucidate each other. Summary tables are almost exclusively
1022 taken from³¹ or⁶⁵. This analysis, like most typical analyses in ATLAS, use central object definitions
1023 from collaboration combined performance (CP) groups using standard analysis tools and recom-
1024 mendations from these groups for the various objects and their accompanying systematic uncertain-
1025 ties.

1026 Before proceeding to the objects used in this analysis, we begin with a few remarks on uncertain-
1027 ties associated with object reconstruction. Event-level variables and selections are discussed more in
1028 depth in Chapters 1 and 6. As described in Section 4.2, systematics quantify the uncertainty asso-
1029 ciated with certain effects, and are generally treated in an analysis by saving histograms of discrimi-
1030 nating distributions corresponding to the nominal analysis except with the systematic in question
1031 varied by plus and minus one standard deviation each (one histogram each). While for modeling
1032 systematics this only corresponds to different event weights, for experimental systematics like those
1033 described in this chapter (with the exception of flavor tagging and certain trigger systematics), this is
1034 done by varying the parameter in question and re-running reconstruction with the systematic varied
1035 before recomputing all event level quantities and then saving discriminant values in their appropri-
1036 ate distributions. This is, in general, a much more computationally intensive process in the analysis,
1037 which is why an entire software framework, the `CxAODFramework`, was created for this analysis (see
1038 Section 3 of³¹ for more details).

1039 **5.1 TRIGGERS**

1040 Tables of the triggers used with the 2015 and 2016 datasets are given in Tables 5.1 and 5.2.

o lep	i lep	z lep
HLT_xe70	HLT_xe70 HLT_e24_lhmedium_L1EM20VH OR HLT_e60_lhmedium OR HLT_e120_lhloose	HLT_mu20_iloose_L1MU15 OR HLT_mu40 HLT_e24_lhmedium_L1EM20VH OR HLT_e60_lhmedium OR HLT_e120_lhloose

Table 5.1: Summary table of triggers used in 2015 Data.

period	o lep	i lep	z lep
A	HLT_xe90_mht_L1XE50	HLT_xe90_mht_L1XE50 HLT_e26_lhtight_nod0_ivarloose OR HLT_e60_lhmedium_nod0 OR HLT_e60_medium OR HLT_e140_lhloose_nod0	HLT_mu24_ilosse(data) HLT_mu24_ilosse_L1MU15(MC) OR HLT_mu40 HLT_e26_lhtight_nod0_ivarloose OR HLT_e60_lhmedium_nod0 OR HLT_e60_medium OR HLT_e140_lhloose_nod0
B-D ₃	HLT_xe90_mht_L1XE50	HLT_xe90_mht_L1XE50 HLT_e26_lhtight_nod0_ivarloose OR HLT_e60_lhmedium_nod0 OR HLT_e60_medium OR HLT_e140_lhloose_nod0	HLT_mu24_ivarmedium OR HLT_mu50 HLT_e26_lhtight_nod0_ivarloose OR HLT_e60_lhmedium_nod0 OR HLT_e60_medium OR HLT_e140_lhloose_nod0
D ₄ -E ₃	HLT_xe110_mht_L1XE50	HLT_xe110_mht_L1XE50 HLT_e26_lhtight_nod0_ivarloose OR HLT_e60_lhmedium_nod0 OR HLT_e60_medium OR HLT_e140_lhloose_nod0	HLT_mu24_ivarmedium OR HLT_mu50 HLT_e26_lhtight_nod0_ivarloose OR HLT_e60_lhmedium_nod0 OR HLT_e60_medium OR HLT_e140_lhloose_nod0
$\geq F_1$	HLT_xe110_mht_L1XE50	HLT_xe110_mht_L1XE50 HLT_e26_lhtight_nod0_ivarloose OR HLT_e60_lhmedium_nod0 OR HLT_e60_medium OR HLT_e140_lhloose_nod0	HLT_mu26_ivarmedium OR HLT_mu50 HLT_e26_lhtight_nod0_ivarloose OR HLT_e60_lhmedium_nod0 OR HLT_e60_medium OR HLT_e140_lhloose_nod0

Table 5.2: Summary table of triggers used in 2016 Data.

1041 The 0-lepton channel uses a \vec{E}_T^{miss} trigger, while the 2-lepton channel uses single lepton triggers,
 1042 with the 1-lepton analysis using both. Since the 0- and 1-lepton channels are largely beyond the scope
 1043 of this thesis, the discussion here will be limited to the single lepton triggers; the interested reader is
 1044 directed towards ³¹ and its cited sources for an in-depth discussion of the use of the \vec{E}_T^{miss} trigger.

1045 The efficiency of triggers is in general different on simulated datasets than in actual data collected
 1046 in ATLAS, so a scale factor to correct for this difference in efficiency must be applied to simulation
 1047 events. This scale factor is given by the muon CP group for muons for both the 1- and 2-lepton cases
 1048 and from the electron CP group for the 1-lepton case. For the two electron case, this was calculated
 1049 by the analysis team as (details in ³¹):

$$\frac{1 - (1 - \epsilon_{\text{MC}}^{e1} \times \text{SF}^{e1}) \times (1 - \epsilon_{\text{MC}}^{e2} \times \text{SF}^{e2})}{1 - (1 - \epsilon_{\text{MC}}^{e1}) \times (1 - \epsilon_{\text{MC}}^{e2})} \quad (5.1)$$

1050 There are also systematic uncertainties associated with these trigger efficiencies. The single elec-
 1051 tron trigger efficiency systematic uncertainty is encapsulated in a single systematic, `EL_EFF_Trigger_-`
 1052 `Total_1NPCOR_PLUS_UNCOR`, while the single muon trigger efficiency has two components, one
 1053 each for the sample statistics, `MUON_EFF_TrigStatUncertainty`, and systematic uncertainties
 1054 `MUON_EFF_TrigSystUncertainty` associated with that efficiency's measurement.

1055 While the momentum associated with the lowest un-prescaled single lepton triggers changes de-
 1056 pending on data-taking conditions (the numbers associated with the triggers in the tables can be
 1057 thought of as nominal p_T values for trigger level objects), the lowest typical value is ~ 25 GeV. In
 1058 order to maintain this triggering capability on low p_T muons in the higher luminosity environment

¹⁰⁵⁹ of the Run 3 LHC and beyond, trigger-capable detectors will be installed in upgraded New Small
¹⁰⁶⁰ Wheels (NSW) of the ATLAS muon detector during the Phase I upgrade. Detailed studies in sim-
¹⁰⁶¹ ulation of the trigger algorithm performance under nominal and misaligned conditions for the Mi-
¹⁰⁶² cromegas detectors to be installed in the NSW may be found in Appendix A.

¹⁰⁶³ **5.2 ELECTRONS**

¹⁰⁶⁴ Electrons in ATLAS are reconstructed using a combination of the ATLAS electromagnetic calorime-
¹⁰⁶⁵ ter (ECAL) and inner detector (ID). Reconstruction begins by searching for so-called “seed clusters”
¹⁰⁶⁶ in the ECAL. The ECAL is divided into a 200×256 tower grid in the $\eta - \phi$ plane, with each tower
¹⁰⁶⁷ having a size of 0.025 square in η and ϕ , corresponding to the granularity of the ECAL in its middle
¹⁰⁶⁸ layer, with all energy in a tower summed longitudinally. A “sliding window” of 3×5 cells in the
¹⁰⁶⁹ $\eta - \phi$ plane is then used to identify EM clusters associated with electrons based on criteria detailed
¹⁰⁷⁰ in ⁴⁹. This comparatively simple algorithm (in contrast to jet reconstruction detailed below) is effec-
¹⁰⁷¹ tive since electromagnetic showers have a well defined behavior and shape.

¹⁰⁷² Once seed clusters have been formed, they are associated with tracks in the inner detector. Com-
¹⁰⁷³ bined cluster-tracks pairs form electron candidates. In order for a electron candidate to be consid-
¹⁰⁷⁴ ered a suitable electron for analysis, it must pass certain quality requirements, based on a cut on the
¹⁰⁷⁵ value of a likelihood-based (LH) discriminant (cf. ¹⁴ for details). This discriminant is given by:

$$d_{\mathcal{L}} = \frac{\mathcal{L}_S}{\mathcal{L}_S + \mathcal{L}_B}, \quad \mathcal{L}_S(\vec{x}) = \prod_{i=1}^n P_{s,i}(x_i) \quad (5.2)$$

where the s and S (b and B) subscripts refer to distributions in fiducial signal (background) distributions in bins of $|\eta|$ and E_T . The $P(x_i)$ are probability distributions functions (pdf)'s for input variables. Several sets of input variables exist for increasingly stringent quality requirements on electrons; this analysis uses Loose LH electrons as the base for electron selection, with the input variables relating to leakage into the hadronic calorimeter (HCAL), shower and energy deposits in each of the ECAL layers, track quality requirements, TRT hits, and track-cluster matching. This analysis adds a LooseTrackOnly isolation requirement (the p_T sum of tracks within a certain $\eta - \phi$ distance of the candidate track must be below a certain value), impact parameter significance cuts, and an explicit B-layer hit requirement. The ZH -signal electrons must further pass a 27 GeV p_T cut ($1.05 \times p_T^{\text{trigger}}$). These requirements are summarized in Table 5.3.

Electron Selection		η	ID	d_0^{sig}	$ \Delta z_0^{BL} \sin \theta $	Isolation
$VH - \text{loose}$	$>7\text{ GeV}$	$ \eta < 2.47$	LH Loose + B-layer cut	< 5	$< 0.5\text{ mm}$	LooseTrackOnly
$ZH - \text{signal}$	$>27\text{ GeV}$	$ \eta < 2.47$	LH Loose + B-layer cut	< 5	$< 0.5\text{ mm}$	LooseTrackOnly
$WH - \text{signal}$	$>27\text{ GeV}$	$ \eta < 2.47$	LH Tight	< 5	$< 0.5\text{ mm}$	FixedCutHighPtCaloOnly

Table 5.3: Electron selection requirements.

5.2.1 ELECTRON SYSTEMATICS

The electron CP group has tabulated standard systematic uncertainties to be associated with the use of reconstructed electrons in ATLAS analyses in two main categories. The first category is related to efficiency corrections and is broken into three components: identification (`EL_EFF_ID_TotalCorrUncertainty`), reconstruction (`EL_EFF_Reco_TotalCorrUncertainty`), and isolation (`EL_EFF_Iso_TotalCorrUncertainty`). The second category deals with electron energy scale

1092 (roughly, the uncertainty in taking the energy deposits in an EM cluster and turning them into an
1093 electron energy) and energy resolution (the width associated with this). This is in practice a very
1094 complicated procedure, with over 60 systematics associated, but this analysis is not at all sensitive
1095 to these effects and so a simplified model of two systematics, EG_RESOLUTION_ALL and EG_SCALE-
1096 _ALL, is used.

1097 **5.3 MUONS**

1098 This analysis uses the standard CP muon collection in an event, though these muons in ATLAS are
1099 constructed in a variety of ways; for full details see ²⁵ and ¹⁷. Most muons are constructed using tracks
1100 in the chambers of the muon spectrometer (MS), with a variety of algorithms available. MS tracks
1101 are sufficient to reconstruct a muon (a fit on these tracks can be used to point back to an interaction
1102 point for vertex matching, for example) and, in the $|\eta| \in (2.5, 2.7)$ interval where there is no track-
1103 ing, these standalone (SA) muons are the default. The most common and robust form of muon
1104 reconstruction combines tracks in the MS with tracks in the ID (more precisely, a global refit with
1105 hits from both subsystems is typically done) to form combined (CB) muons. CB and SA muons
1106 automatically pass the loose reconstruction requirements for the Loose muons used in this analy-
1107 sis. Additionally, since there is a gap in the $|\eta| < 0.1$ range in the MS to make room for cabling and
1108 other detector services, there are two further muon types used in this range: the segment tagged (ST)
1109 muons that match ID tracks to segments in the MDT or CSC chambers and the calorimeter tagged
1110 (CT) muons that match ID tracks to calorimeter clusters consistent with minimum ionizing parti-
1111 cles (which muons in ATLAS generally are).

1112 Further quality requirements are imposed on Loose muons for the different muon categories
 1113 used in this analysis. Isolation requirements similar to the electrons in corresponding categories are
 1114 imposed, and impact parameter requirements are also imposed. The ZH signal muons also have a
 1115 p_T cut at 27 GeV and a requirement that the muon fall within the $|\eta|$ range of the ID.

Muon Selection		η	ID	d_0^{sig}	$ \Delta z_0^{\text{BL}} \sin \theta $	Isolation
$VH - \text{loose}$	$> 7 \text{ GeV}$	$ \eta < 2.7$	Loose quality	< 3	$< 0.5 \text{ mm}$	LooseTrackOnly
$ZH - \text{signal}$	$> 27 \text{ GeV}$	$ \eta < 2.5$	Loose quality	< 3	$< 0.5 \text{ mm}$	LooseTrackOnly
$WH - \text{signal}$	$> 25 \text{ GeV}$	$ \eta < 2.5$	Medium quality	< 3	$< 0.5 \text{ mm}$	FixedCutHighPtTrackOnly

Table 5.4: Muon selection requirements.

1116 5.3.1 MUON SYSTEMATICS

1117 Similar to the treatment of systematic uncertainties associated with the electrons, muons have CP de-
 1118 fined systematics. The muon momentum scale and resolution systematics are divided into three cat-
 1119 egories associated one for uncertainties related to ID tracks (`MUONS_ID`), one for MS tracks (`MUONS-`
 1120 `_MS`), one for the overall scale (`MUONS_SCALE`), and two for charge dependent momentum scales
 1121 (`MUON_SAGITTA_RHO` and `MUON_SAGITTA_RESBIAS`). The remaining systematics have a STAT and
 1122 SYS component corresponding to the sample statistics and systematic uncertainties for their individ-
 1123 ual components. Efficiency scale factors use different standard candles in different p_T ranges (J/ψ 's
 1124 (Z 's) below (above) 15 GeV), and so these systematics are broken up into two categories (`MUON_EFF-`
 1125 `_STAT` and `MUON_EFF_SYS`; `MUON_EFF_STAT_LOWPT` and `MUON_EFF_SYS_LOWPT`). There are also
 1126 isolation systematics (`MUON_ISO_STAT`, `MUON_ISO_SYS`) and track to vertex association systematics
 1127 (`MUON_TTVA_STAT`, `MUON_TTVA_SYS`).

¹¹²⁸ **5.4 MISSING TRANSVERSE ENERGY**

¹¹²⁹ High precision performance of \vec{E}_T^{miss} is not so crucial to the 2-lepton analysis (though it is very im-
¹¹³⁰ portant to the other channels), so the interested reader is referred to²⁶. \vec{E}_T^{miss} in ATLAS is the neg-
¹¹³¹ ative vectoral sum of physics objects (in this analysis just jets and leptons, though in principle also
¹¹³² including τ 's and γ 's) and a so-called track based soft term (TST). The TST is comprised of valid
¹¹³³ ID tracks not associated with any physics objects in an event. These tracks must be associated to an
¹¹³⁴ event's primary vertex, have a $p_T > 0.4$ GeV, and pass other quality requirements.

¹¹³⁵ The \vec{E}_T^{miss} systematic uncertainties relevant to this analysis are related to track based energy scale
¹¹³⁶ and resolutions in both the soft term and in the jets and are: MET_SoftTrk_ResoPara, MET_Soft-
¹¹³⁷ Trk_ResoPerp, MET_SoftTrk_ScaleDown, MET_SoftTrk_ScaleUp, MET_JetTrk_Scale-
¹¹³⁸ Down , and MET_JetTrk_ScaleUp.

¹¹³⁹ **5.5 JETS**

¹¹⁴⁰ Unlike leptons, all analyses considered in this thesis are sensitive to factors regarding jet reconstruc-
¹¹⁴¹ tion and associated systematic uncertainties. A general discussion of jets precedes jet reconstruction
¹¹⁴² in ATLAS and associated systematics relevant to this thesis.

¹¹⁴³ **5.5.1 JET ALGORITHMS**

¹¹⁴⁴ The hadronic nature of jets makes jet reconstruction a lot more complicated than electron or photon
¹¹⁴⁵ reconstruction, where a regular shower shape and track matching (or lack thereof in the case of the

1146 chargeless photon) provide a fairly straightforward and robust approach. The interested reader is

1147 referred to⁷⁰ for an excellent survey, from which this discussion is greatly abbreviated.

1148 Looking at an event like the one in Figure 5.1, unambiguous individual jets are particularly easy to

1149 identify, more or less popping out of the $\eta - \phi$ plane plot, but this is not always the case.

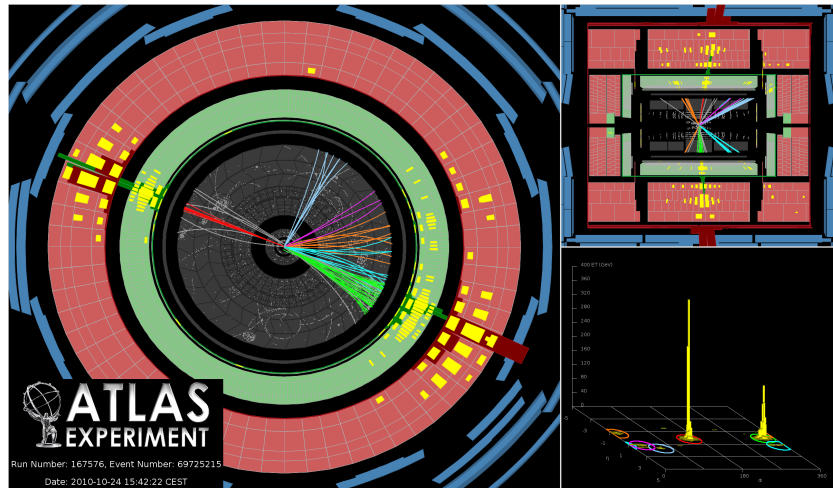


Figure 5.1: A clean ATLAS dijet event.

1150 Two general methods of turning particles/calorimeter towers into jets exist: cone-based and se-

1151 quential recombination. The general theme of the former is to find a hard (energetic) particle and

1152 draw a circle around it in the $\eta - \phi$ plane in an intelligent manner, while the theme of the latter

1153 is to find some metric of distance between particles and then to cluster pairs based on this distance

1154 into jets in an intelligent way. Cone-based algorithms are simple (and therefore generally quite fast)

1155 but generally lack some properties of the sequentially recombined jets (though there are notable ex-

1156 ceptions like SISCone). Cone algorithm reconstructed jets are important for trigger level objects in

1157 ATLAS, though since no jet triggers are used in this analysis, they will not be discussed any further

1158 here.

1159 The general drawback of cone-based algorithms is that they are not infrared and collinear (IRC)
1160 safe. That is, neither the emission of a soft (IR) quark or gluon during hadronization nor the collinear
1161 splitting of hard particles during hadronization should not change the final jet collection in an event.
1162 These are fairly common edge cases and can lead to certain pathologies in QCD calculations. In-
1163frared and collinear safety are diagrammed schematically in Figures 5.2 (a) and (b), taken from⁷⁰.

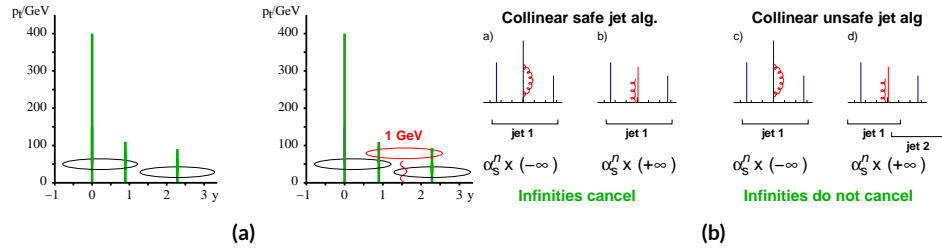


Figure 5.2: Infrared (a) and collinear (b) safety.

1164 Sequential recombination algorithms are generally safe from these effects, as these edge cases are
1165 very “close” to each other by construction. A sequential recombination algorithm proceeds as fol-
1166lows

- 1167 1. Evaluate the set of distances d_{ij} (for pairs of objects) and d_{iB} (the “beam distance” for each
1168 individual object)

$$d_{ij} = \min \left(p_{Ti}^{2p}, p_{Tj}^{2p} \right) \frac{\Delta R_{ij}^2}{R^2}, \quad d_{iB} = p_{Ti}^{2p} \quad (5.3)$$

- 1169 2. Find the minimum distance
1170 3. If the minimum distance is:

- 1171 • A d_{ij} : cluster these objects together, and go to step 1
- 1172 • A d_{iB} : call the i^{th} object a jet, remove it from the set of objects to be clustered, and go to
1173 step 1

1174 4. Repeat until all objects are clustered into jets

1175 The choices one must make in sequential recombination are the size parameter R , akin to a cone

1176 radius in cone-based algorithms, and the momentum power p . Common choices and their trade-offs

1177 are:

- 1178 • +1: the k_t algorithm; favors the softer particles in an event, so the cluster sequence gives a his-
1179 tory of hadronization, but jet shapes are irregular (i.e. not circular in the $\eta - \phi$ plane)
- 1180 • 0: the Cambridge-Aachen algorithm: a pure distance metric; less substructure but jets tend to
1181 be more circular
- 1182 • -1: the anti- k_t algorithm: clustering begins with hardest particles in an event; regular, localized
1183 jet shapes, but virtually no substructure in clustering history

1184 Jet reconstruction using all three algorithms on the same event, as well as SISCone, are shown in

1185 Figure 5.3.

1186 All three algorithms have uses for different applications in ATLAS, with anti- $k_t R = 0.4$ jets

1187 being the default jet collection.* These are the jets used in this analysis.

1188 If the choice of jet algorithm seems a little arbitrary, it is. There is no one-size-fits-all jet collection

1189 perfect for every application, and analyzers have to make these choices for themselves. One interest-

1190 ing choice is the jet size parameter, R . A large R jet will contain more of the radiation coming from a

1191 final state object, but its large size makes it susceptible to contamination from the underlying event

1192 and pileup (as well as other analysis objects if R is sufficiently large or objects sufficiently boosted),

1193 with small R jets having the opposite features. $R = 0.4$ is a fairly middle-of-the-road choice. A natu-

1194 ral question to ask is whether there needs to be just one jet collection in an analysis. Might there not

*The other collections find their primary uses in jet substructure techniques. For an example, cf. the discussion of jet trimming in Appendix B.

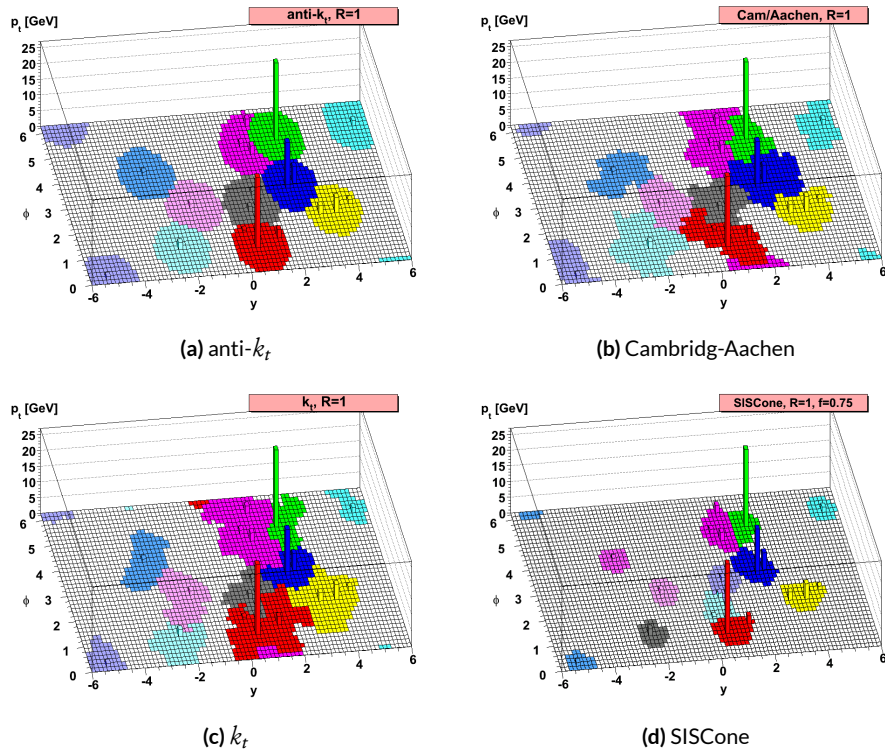


Figure 5.3: Different jet algorithms used on the same event. IC:⁷⁰

₁₁₉₅ be more information to be gained from looking at more jet sizes or clusterings? Preliminary studies
₁₁₉₆ point to this answer being yes and are addressed in Appendix B.

₁₁₉₇ 5.5.2 STANDARD ATLAS HBB JETS

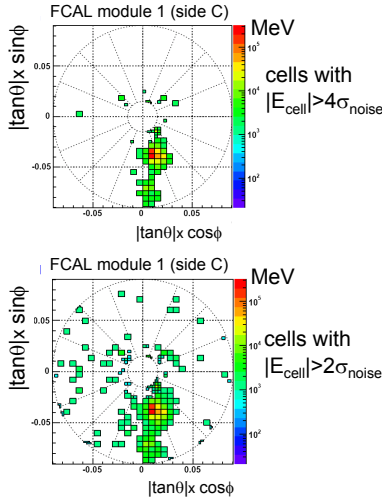
₁₁₉₈ There are a few considerations that arise with jets in physical detectors. The first is what type of ob-
₁₁₉₉ ject to use as the stand in for “particles” since ATLAS measures energy deposits, not pions. The
₁₂₀₀ approach ATLAS has settled upon are calorimeter topological clusters (or CaloTopoClusters for
₁₂₀₁ short)⁵⁸. Unlike the sliding window algorithm used for electron clusters, CaloTopoClusters use a
₁₂₀₂ noise significance based approach in the “4-2-0” algorithm. Each cell in the electromagnetic and
₁₂₀₃ hadronic calorimeters (ECAL and HCAL, respectively) has associated with it a characteristic noise
₁₂₀₄ level (N in Equation 2.6), with this noise level in each channel, it is possible to construct a “signifi-
₁₂₀₅ cance” for the registered energy deposit in a given channel for a given event by dividing the measured
₁₂₀₆ value by its characteristic noise. Groups of cells having a significance of 4 are taken as the centers of
₁₂₀₇ clusters in the $\eta - \phi$ plane. The second layer in a cluster includes all neighboring cells to the central
₁₂₀₈ layer with significance of at least 2, and the final layer includes all the nearest neighbors to the second
₁₂₀₉ layer. This is described in Figure 5.4 from⁶¹.

₁₂₁₀ Once CaloTopoClusters have been formed and clustered into jets, they are calibrated using the
₁₂₁₁ electromagnetic (EM) scale (the scale for clusters coming form EM showers). Further details may be
₁₂₁₂ found in¹⁶.

₁₂₁₃ Jets in this analysis fall into two categories, “signal” and “forward” jets, and are required to pass
₁₂₁₄ certain quality requirements, described in Table 5.5. All jets must pass a series of jet cleaning require-

Local Hadronic Calibration: Clusters

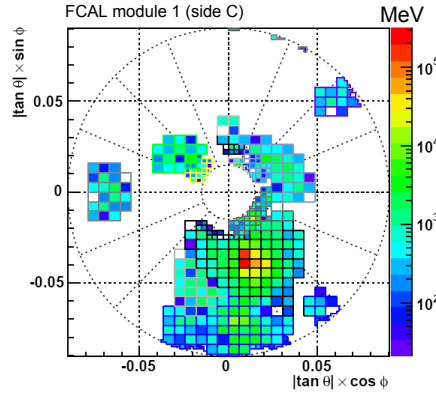
Sven Menke



□ Topological clustering

❖ 4,2,0 clusters in FCal

➢ jets with $p_T > 50 \text{ GeV}$



3rd Hadronic Calibration Workshop, Milan, Italy, 26-27 April, 2007

M. Lefebvre, P. Loch

33

Figure 5.4: A description of the 4-2-0 clustering algorithm.

1215 ments using calorimeter level variables to eliminate jets coming from problematic calorimeter cells
 1216 and certain backgrounds. Some signal jet candidates also make use of a Jet Vertex Tagger (JVT) that
 1217 uses primary vertex and jet and track p_T information to decide whether certain soft jets are likely to
 1218 have come from the the primary (hard scatter) vertex in an event or are to be considered pileup. Fur-
 1219 ther details on JVT may be found in ²⁴. Jets are further corrected using standard CP tools and a dedi-
 1220 cated PtReco correction, all outlined in Section 7.3 of ³¹.

1221 Overlap removal in this analysis is done according to the following precedence, taken from ³¹ with
 1222 further steps only taken into account if an object survives previous steps:

- 1223 • tau-electron: If $(\tau, e) < 0.2$, the τ lepton is removed.
- 1224 • tau-muon: If $(\tau, \mu) < 0.2$, the τ lepton is removed, with the exception that if the τ lepton has

Jet Category	Selection Requirements
Forward Jets	jet cleaning $p_T > 30 \text{ GeV}$ $2.5 \leq \eta < 4.5$
Signal Jets	$p_T > 20 \text{ GeV}$ and $ \eta < 2.5$ jet cleaning $\text{JVT} \geq 0.59$ if ($p_T < 60 \text{ GeV}$ and $ \eta < 2.4$)

Table 5.5: `AntiKt4EMTopoJets` selection requirements. The jet cleaning is applied via the `JetCleaningTool`, that removes events in regions corresponding to hot calorimeter cells.

- 1225 $> 50 \text{ GeV}$ and the muon is not a combined muon, then the τ lepton is not removed.
- 1226 • electron-muon: If a combined muon shares an ID track with an electron, the electron is re-
- 1227 moved.
- 1228 If a calo-tagged muon shares an ID track with an electron, the muon is removed.
- 1229 • electron-jet: If $(\text{jet}, e) < 0.2$ the jet is removed.
- 1230 For any surviving jets, if $(\text{jet}, e) < \min(0.4, 0.04 + 10 \text{ GeV}/e)$, the electron is removed.
- 1231 • muon-jet If $(\text{jet}, \mu) < 0.2$ or the muon ID track is ghost associated to the jet, then the jet is re-
- 1232 moved if the jet has less than three associated tracks with $> 500 \text{ MeV}$ ($\text{NumTrkPt500PV}^{\text{jet}} < 3$) or
- 1233 both of the following conditions are met: the ratio of the muon and jet is larger than 0.5 ($\mu/\text{jet} >$
- 1234 0.5) and the ratio of the muon to the sum of tracks with $> 500 \text{ MeV}$ associated to the jet is
- 1235 larger than 0.7 ($\text{muon}/\text{SumPtTrkPt500PV}^{\text{jet}} > 0.7$).
- 1236 For any surviving jets, if $(\text{jet}, \mu) < \min(0.4, 0.04 + 10 \text{ GeV}/\mu)$, the muon is removed.
- 1237 • tau-jet: If $(\tau, \text{jet}) < 0.2$, the jet is removed.
- 1238 • electron-fat jet: If $(e, \text{fat jet}) < 1.2$, the fat jet is removed.

1239 Jets are corrected using a muon-in-jet correction and then a kinematic fitter (Appendix D of⁶⁵)
1240 for the 2-lepton case (PtReco correction for the 0- and 1- lepton case). The muon-in-jet correction
1241 is designed for b -jets. Since the decay of a b -quark to a c -quark and finally to a light quark (these are
1242 the multiple vertices for which JetFitter in Section 5.6.1 searches) involves two weak decays, there are
1243 two W -bosons involved in the decay. Some of these will decay semileptonically, and, while electron
1244 and τ energy will be captured by the calorimeters, semileptonic μ 's will only be registered in the MS,
1245 which occurs in some 44% of all decays from a theoretical standpoint, which amounts to about 12%
1246 in practice (due to track isolation requirements for the leptons). This value is about 1–2% for elec-
1247 trons, which deposit their energy in the calorimeter and so require no correction; any jet with a valid
1248 lepton associated to it is deemed semileptonic (all others are called hadronic). Any jet with muons
1249 associated with it has the closest muon's 4-vector (in the $\eta - \phi$ plane) added to it.

1250 The PtReco correction is a scale factor on the muon-in-jet corrected jet's 4-vector based on the
1251 jet's p_T and whether the jet is hadronic or semileptonic. This correction factor is based on particle
1252 level studies done on a TruthWZ sample. As the 0- and 1-lepton cases are not the focus of this thesis,
1253 the interested reader is directed to Section 7.3 of³¹.

1254 The kinematic fitter used in 2-lepton events with two or three jets takes as its input 12 fit parame-
1255 ters,

- 1256 • energies of 2 electron or of 2 muons
- 1257 • energies of 2 b -jets
- 1258 • η, ϕ of 2 leptons and 2 jets
- 1259 • p_X and p_Y of $\ell\ell b\bar{b}$ system.

1260 • $m_{\ell\ell}$

1261 and 3 constraints for the variation of these parameters,

- 1262 • parameters : Gaussian (b-jet energy : Transfer Functions (TF); these are denoted L , with an
1263 L_{truth} as a prior) (the ϕ parameters)
- 1264 • p_X and p_Y of $\ell\ell b\bar{b}$ system : zero with a width of 9 GeV obtained from ZH signal MC.
- 1265 • m_{ll} : Breit-Wigner (BW) distribution of Z boson (final term, leptons denoted Ω)

1266 which leads to test statistic from the usual likelihood formalism to be minimized in each event:

$$-2 \ln \mathcal{L} = \sum_{i=j} \left(\frac{(\phi_i^n - \phi_i^0)^2}{\sigma_\phi^2} \right) + \left(\frac{(\Omega_l^n - \Omega_l^0)^2}{\sigma_\Omega^2} \right) - 2 \ln(L^j) - 2 \ln(L_{truth}^j)$$

1267 $+ \sum_{i=x,y} \frac{(\sum p_i^n - \sum p_i^0)^2}{\sigma_{\sum p_i}^2} + 2 \ln((m_{\ell\ell} - M_X^2)^2 + M_X^2 \Gamma^2) \quad (5.4)$

1268 5.5.3 JET SYSTEMATICS

1269 As with the electron systematics, jet energy scale (JES) and resolution (JER) are the two principal
1270 considerations for systematic uncertainties, with even more standard. JER, as with the electron en-
1271 ergy resolution, is a single systematic uncertainty, `JET_JER_SINGLE_NP`. There is also a single JVT
1272 efficiency `JET_JvtEfficiency` systematic uncertainty. There are 88 nominal JES systematics, and
1273 this analysis is sufficiently sensitive to these variations that a single systematic is grossly insufficient.
1274 Nevertheless, some simplification is possible, with the 75 of these nuisance parameters (mostly statis-

1275 tical uncertainties related to the Z +jet and γ +jet calibrations) being reduced to 8, and several explic-
1276 itly named nuisance parameter. These remaining named NP's are: 3 NP's related to the η intercali-
1277 bration used to extrapolate standard calibrations to other jet η regions, 4 NP's related to the flavor
1278 composition of principle background samples (W/Z +jets, top, and diboson), 4 pileup systematics, a
1279 single NP for the b -jet energy scale, a high p_T jet energy scale systematic, and one for jets that punch
1280 through the HCAL to leave energy deposits in the MS. These are listed explicitly in Table 5.7.

1281 5.6 FLAVOR TAGGING

1282 Given that the final state in this analysis involves pairs of jets originating from b -quarks, deploying
1283 effective flavor tagging algorithms is imperative. While flavor tagging in general can be used to isolate
1284 any flavor (b , c , or light (u , d , s , or gluon-initiated jets)), this analysis exclusively looks for b -jets, so
1285 this disucssion will focus on b 's. At truth-level in sumlation, this is fairly straightforward: one need
1286 only look at the particles contained within a jet and seeing if any include a b -quark (sometimes a B
1287 hadron) in the decay chain.

1288 5.6.1 DIRECT TAGGING

1289 One of the most distinctive features of b -jets is the presence of secondary vertices, as illustrated in Fig-
1290 ure 5.5. While most partons created in particle collisions will hadronize promptly, b -quarks will first
1291 hadronize into B -hadrons, which have lifetimes of about a picosecond. This small but finite lifetime
1292 means that these particles will travel about half a millimeter or so before decaying into a jet in much
1293 the usual way, and the tracks from this decay will point back to this displaced, secondary vertex.

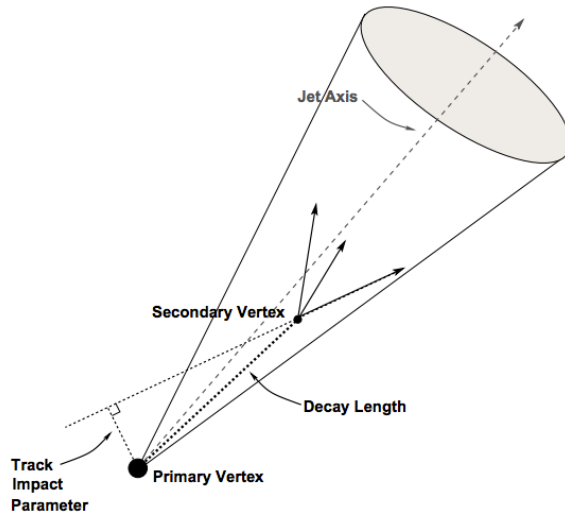


Figure 5.5: An illustration of a secondary vertex in a b -jet. Image credit: ⁵⁴

¹²⁹⁴ There are various secondary vertex algorithms used as inputs to the nominal b -tagging algorithm¹⁵,

¹²⁹⁵ with three main types of algorithms used as inputs

- ¹²⁹⁶ 1. Track impact parameter based algorithms: I₂PD (signed transverse only; more pileup ro-
¹²⁹⁷ bust), I₃PD (signed transverse and longitudinal)
- ¹²⁹⁸ 2. Inclusive secondary vertex reconstruction: SV1 (start with two track vertex pairs and con-
¹²⁹⁹ struct a secondary vertex)
- ¹³⁰⁰ 3. Multiple vertex reconstruction (decay chain): JetFitter (PV $\rightarrow b \rightarrow c$ decay chain using Kalman
¹³⁰¹ filter)

¹³⁰² All of these are combined into a boosted decision tree (BDT) and trained on five million $t\bar{t}$ events

¹³⁰³ with an 90%/10% light/ c jet background to form the MV_{2c10} algorithm, with 10 referring to the per-

¹³⁰⁴ centage of charm events in the training background. The 10% charm ratio was found to be a good

¹³⁰⁵ balance between increased charm rejection capability (as opposed to MV_{2c00}, which has no charm

1306 in the background training samples) and loss in light jet rejection (compared to MV2c20, which has
1307 20% charm events in background training samples).

1308 ANALYSIS SPECIFIC CONCERNS AND SYSTEMATIC UNCERTAINTIES In addition to specifying
1309 the tagging algorithm, the working point efficiency must be specified. As with selection algorithms
1310 in general, there is a trade off between efficiency/recall (identifying all the b -jets, minimizing type
1311 II error) and purity/precision (making sure all jets positively identified are in fact b -jets, minimiz-
1312 ing type I error). Nominal efficiency working points have been calibrated by the flavor tagging CP
1313 group and are outlined in Table 5.6.

name	MV2c10 weight cut	b -tagging efficiency [%]	c RR	light RR
FixedCutBEff_60	0.9349	60.03	34.54	1538.78
FixedCutBEff_70	0.8244	69.97	12.17	381.32
FixedCutBEff_77	0.6459	76.97	6.21	134.34
FixedCutBEff_85	0.1758	84.95	3.10	33.53

Table 5.6: b -tagging working points available for MV2c10 for AntiKt4EMTopoJets. RR is the rejection rate (the inverse of efficiency).

1314 These values are aggregate figures, as both the jet's p_T and η are inputs to the MV2c10 discrim-
1315 inant. The working point chosen for this analysis is the 70% **FixedCutBEff_70** working point,
1316 with "fixed cut" referring to the fact that this particular usage of the MV2c10 BDT value is a simple
1317 cut value.

1318 Just as with the trigger and lepton identification efficiencies, flavor tagging efficiencies differ from
1319 their nominal values somewhat depending on what simulation or data sample is being used. To
1320 account for this difference, just as in the other cases, scale factors are applied to simulation event

1321 weights. It is through these event weights, as with the modeling systematics, that the flavor tagging
1322 systematic uncertainties are applied. Given that there are 24 input variables to MV2c10 and that fla-
1323 vor tagging is in general a very difficult problem, it is not surprising that, as with the JES, there are
1324 very many systematic uncertainties associated with flavor tagging. However, as with JES, the CP
1325 group has compacted the full systematic set into a reduced set of 13 systematic uncertainties: 3 each
1326 associated with c and light jets, 5 for b -jets (with the naming convention FT_EFF_Eigen_(B|C|Light)N),
1327 one for the extrapolation of scale factors to different jet p_T regimes (FT_EFF_Eigen_extrapolation),
1328 and one for the charm to bottom extrapolation (FT_EFF_Eigen_extrapolation_from_charm)⁷⁹.
1329 This schematic is a middle-of-the-road “Medium” set of systematics.

1330 5.6.2 TRUTH TAGGING

1331 Since imposing a 2 b -tag requirement overwhelmingly rejects events dominated by c - and light jets,
1332 statistics in such MC samples are very low. In order to circumvent this problem and restore full MC
1333 statistics, the tag rate function, or “truth-tagging” procedure (in contrast to the standard or “direct
1334 tagging” procedure) is applied, in which all events are kept but given a weight that preserves the over-
1335 all shape and normalization of underlying distributions. Intuitively, this is done by giving events with
1336 real b -jets in MC a much higher weight than events having only c - or light jets. Truth-tagging is ap-
1337 plied to all samples when conducting MVA training in order to maximize statistics and reduce the
1338 risk of overtraining. Truth-tagging is also used for data-MC comparison plots in 2-tag regions and
1339 for $V + cc$, $V + c\ell$, $V + \ell$, and WW samples used in the final likelihood fit. A detailed description of
1340 the truth-tagging process is provided below.

1341 Each jet in a given event has associated with it a b -tagging efficiency, denoted ε , that is a function
 1342 of its p_T , η , and real flavor (b , c , or light) from truth-level information in MC. Intuitively, this effi-
 1343 ciency can be thought of as the likelihood that a given jet will be b -tagged. Hence, b -jets have a much
 1344 higher b -tagging efficiency than c -jets, which in turn have a higher b -tagging efficiency than light jets.
 1345 We define a truth-tag weight for a given combination of tagged and untagged jets as the product of
 1346 the efficiencies of the tagged jets times the product of the complement of the efficiencies of the un-
 1347 tagged jets. For example, for an event with three jets, labeled 1, 2, and 3, if jets 1 and 2 are tagged, and
 1348 jet 3 is untagged, the truth-tag weight associated with this combination is

$$\varepsilon_1 \varepsilon_2 (1 - \varepsilon_3) \quad (5.5)$$

1349 In order to obtain a truth-tag weight for an event, one takes the sum of the weights for each pos-
 1350 sible tag combination. The current analysis requires that all events have exactly two b -tagged jets, so
 1351 the truth-tag weight is the sum of all the weights of all possible pairs of tagged jets (events with fewer
 1352 than two jets are discarded). Going back to the three jet example, one has the possible combinations:
 1353 jets 1+2 as tagged and jet 3 as untagged; jets 1+3 as tagged and jet 2 as untagged; and finally jets 2+3 as
 1354 tagged and jet 1 as untagged, which yields a total event weight of

$$w_{tot} = \varepsilon_1 \varepsilon_2 (1 - \varepsilon_3) + \varepsilon_1 \varepsilon_3 (1 - \varepsilon_2) + \varepsilon_2 \varepsilon_3 (1 - \varepsilon_1) \quad (5.6)$$

1355 For some applications (e.g. in order to use variables like pTB1, the p_T of the harder b -tagged jet in

1356 an event, in MVA training), it is necessary to choose a combination of jets in an event as “tagged.”

1357 This combination is chosen randomly, with the probability for a given combination to be chosen

1358 being proportional to its truth-tag weight. In the three jet example, the probability of tagging jets

1359 1+2 is:

$$\frac{\varepsilon_1 \varepsilon_2 (1 - \varepsilon_3)}{w_{tot}} = \frac{\varepsilon_1 \varepsilon_2 (1 - \varepsilon_3)}{\varepsilon_1 \varepsilon_2 (1 - \varepsilon_3) + \varepsilon_1 \varepsilon_3 (1 - \varepsilon_2) + \varepsilon_2 \varepsilon_3 (1 - \varepsilon_1)} \quad (5.7)$$

1360 Though not used in the current analysis, functionality exists for generic truth-tagging require-

1361 ments (i.e. an arbitrary number of tags on an arbitrary number of jets) through the logical combina-

1362 toric extension and for so-called “pseudo-continuous tagging,” where a b -tag score is generated for

1363 each jet in a given event. Since a random combination of jets is set by hand to pass the b -tagging cuts

1364 regardless of its b -tag score, a new score must be generated if this information is to be used in further

1365 analysis. Under current settings, jets that are tagged are assigned a random b -tag score that is sampled

1366 from the MV2C10 cumulative distribution above the 70% efficiency working point cut. All other

1367 jets in the event are assigned a random b -tag score below the 70% working point cut. Since these dis-

1368 tributions are discrete, the scores are not truly continuous (cf. example distributions in Figure 5.6),

1369 hence the “pseudo-continuous” nomenclature.

1370 A number of closure tests were performed on both the nominal and several systematics cases. In

1371 the plots that follow, truth (solid) and direct (dashed) tagging distributions for m_{bb} and $\Delta R(b_1, b_2)$

1372 in different p_T^V regimes for 2 lepton, 2 jet events. Agreement between the truth and direct tagging

1373 cases is generally very good, an example of which can be seen in Figure 5.7 for a signal qqZllH125

1374 sample, and the overall benefit of truth-tagging can be somewhat dramatically seen in the corre-

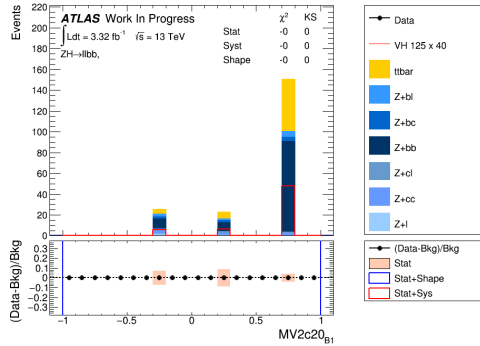


Figure 5.6: An example of a pseudo-continuous b -tagging distribution

sponding plots $Z+\ell$ samples in Figure 5.8. At high p_T^V ($p_T^V > 200$ GeV), however, in events with two
 real b -jets, there is a much greater likelihood that the b -jets will merge into a single jet, which render
 the naïve assumption that jets remain discrete invalid. While this does not appear to be a problem in
 most samples (cf. $t\bar{t}$ in Figure 5.9), there is a mismodelling effect at low m_{bb} and low $\Delta R(b_1, b_2)$ at
 $p_T^V > 200$ GeV for $W/Z + bb$ samples where truth-tagging overestimates the number of events in
 this merged regime, as can be seen in Figure 5.10

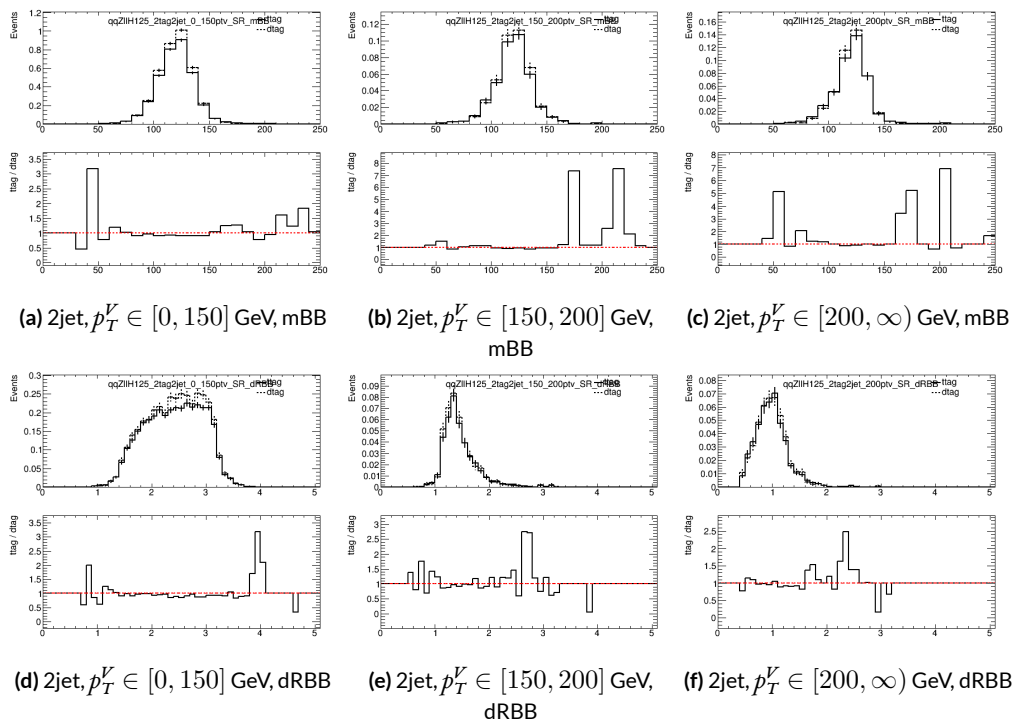


Figure 5.7: Truth-tagging closure tests for 2 lepton, 2 jet qqZIIH125 samples in three different p_T^V regions.

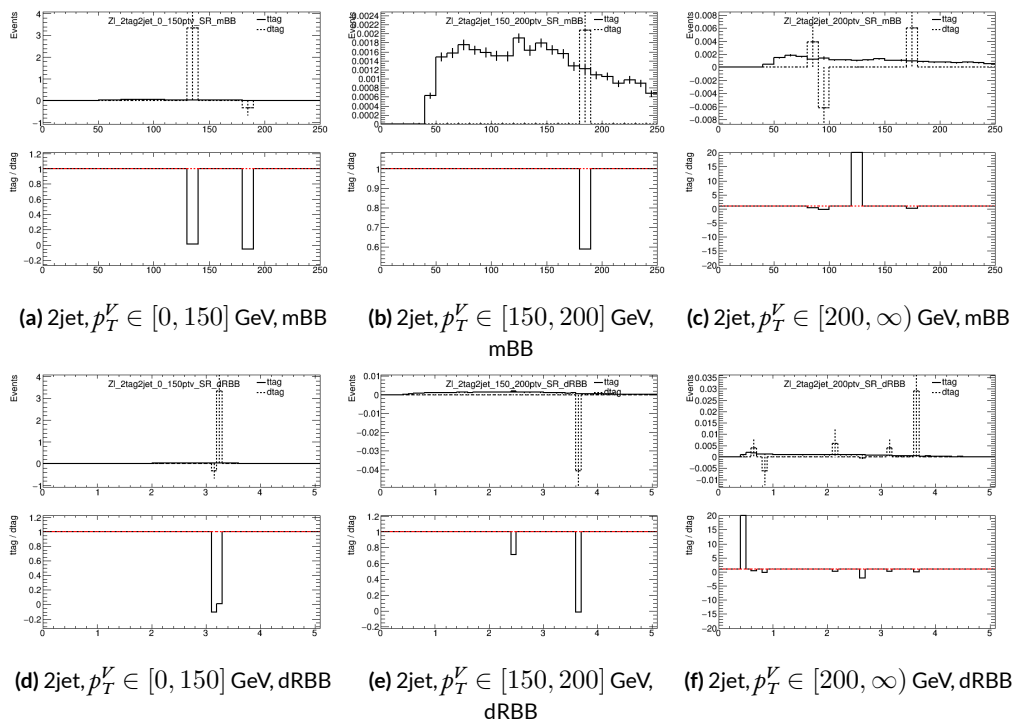


Figure 5.8: Truth-tagging closure tests for 2 lepton, 2 jet $Z + \ell$ samples in three different p_T^V regions.

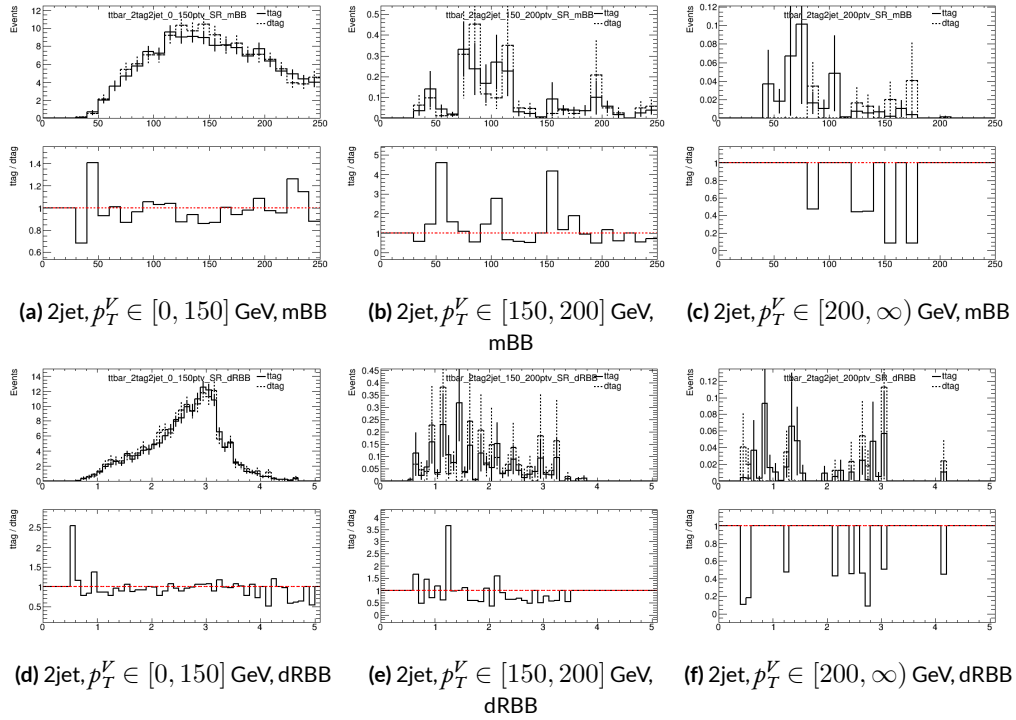


Figure 5.9: Truth-tagging closure tests for 2 lepton, 2 jet $t\bar{t}$ samples in three different p_T^V regions.

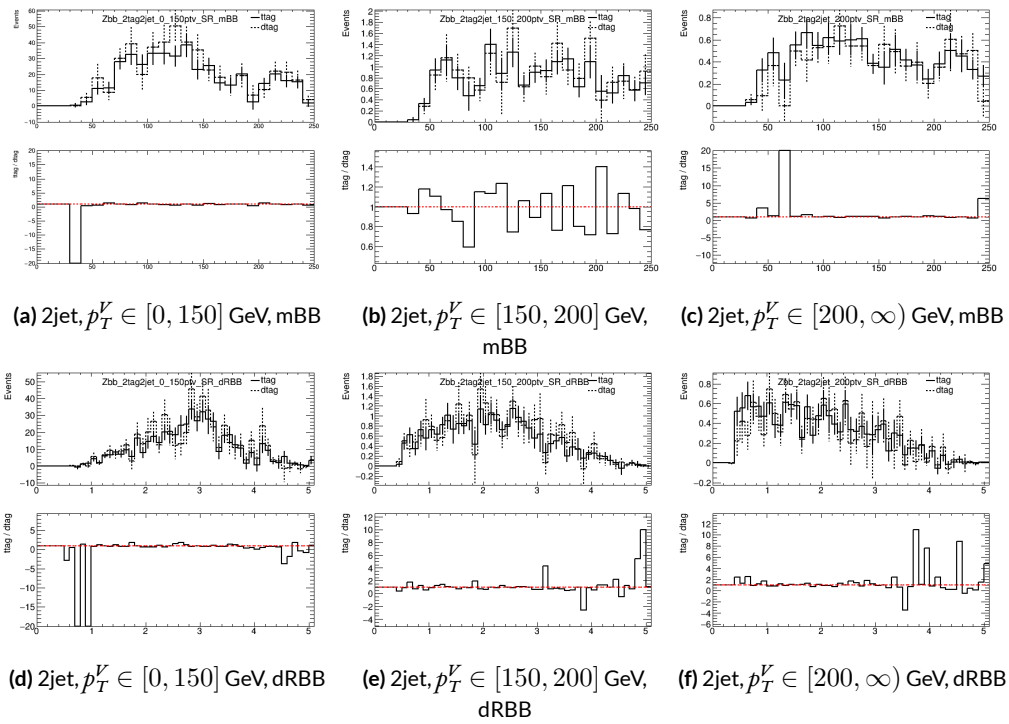


Figure 5.10: Truth-tagging closure tests for 2 lepton, 2 jet $Z + bb$ samples in three different p_T^V regions.

1381 5.7 MISCELLANIA AND SYSTEMATICS SUMMARY

1382 A summary of all experimental systematics, taken from^{6s}, may be found below. In addition to the
1383 systematics discussed above, there are also two further systematics, on the total integrated luminosity
1384 and on the event reweighting factor used to account for pileup, both included in Table 5.7.

1385 5.8 EVENT SELECTION AND ANALYSIS REGIONS

1386 With object and event reconstruction described, it is now time to address which events are actually
1387 selected for use in analysis. This analysis focuses specifically on the 2-lepton channel of the fiducial
1388 analysis, with the event selection and analysis region definitions being identical. Common to all
1389 lepton channels in the fiducial analysis is the set of requirements on the jets in a given event. There
1390 must be at least two central jets and exactly two signal jets that have been “*b*-tagged” according to the
1391 MV2c10 algorithm¹⁵, with at least one of these *b*-jets having $p_T > 45$ GeV. For MVA training and
1392 certain background samples, a process known as “truth-tagging” is applied instead of the standard *b*-
1393 tagging to boost sample statistics and stabilize training/fits (cf.^{6s} Section 4.2 for details). After event
1394 selection, the *muon-in-jet* and *PtReco* corrections, described in^{3t} 6.3.3-4, are applied to the *b*-jets.

1395 In addition to the common selections, there are 2-lepton specific selections. All events are re-
1396 quired to pass an un-prescaled single lepton trigger, a full list of which may be found in Tables 5
1397 and 6 of^{3t} with the requirement that one of the two selected leptons in the event must have fired
1398 the trigger. There must be 2 VH-loose leptons, and at least one of these must be a ZH-signal lepton
1399 (cf. Tables 5.3 and 5.4 for definitions). This lepton pair must have an invariant mass between 81 and

Systematic uncertainty	Short description	Reference
Event		
Luminosity	uncertainty on total integrated luminosity	Section 11.1 in Ref. ³¹
Pileup Reweighting	uncertainty on pileup reweighting	Section 11.1 in Ref. ³¹
	Electrons	
EL_EFF_Trigger_Total_iNPCOR_PLUS_UNCOR	trigger efficiency uncertainty	Section 11.2.2. in Ref. ³¹
EL_EFF_Reco_Total_iNPCOR_PLUS_UNCOR	reconstruction efficiency uncertainty	Section 11.3.1. in Ref. ³¹
EL_EFF_ID_Total_iNPCOR_PLUS_UNCOR	ID efficiency uncertainty	Section 11.3.1. in Ref. ³¹
EL_EFF_Iso_Total_iNPCOR_PLUS_UNCOR	isolation efficiency uncertainty	Section 11.3.1. in Ref. ³¹
EG_SCALE_ALL	energy scale uncertainty	Section 11.3.2. in Ref. ³¹
EG_RESOLUTION_ALL	energy resolution uncertainty	Section 11.3.2. in Ref. ³¹
	Muons	
MUON_EFF_TrigStatUncertainty	trigger efficiency uncertainty	Section 11.2.2. in Ref. ³¹
MUON_EFF_TrigSystUncertainty		
MUON_EFF_STAT	reconstruction and ID efficiency uncertainty for muons with > 15 GeV	Section 11.4.1. in Ref. ³¹
MUON_EFF_SYS	reconstruction and ID efficiency uncertainty for muons with < 15 GeV	Section 11.4.1. in Ref. ³¹
MUON_EFF_STAT_LOWPT		
MUON_EFF_SYST_LOWPT		
MUON_ISO_STAT	isolation efficiency uncertainty	Section 11.4.1. in Ref. ³¹
MUON_ISO_SYS		
MUON_TTVA_STAT	track-to-vertex association efficiency uncertainty	Section 11.4.1. in Ref. ³¹
MUON_TTVA_SYS		
MUON_ID	momentum resolution uncertainty from inner detector	Section 11.4.2. in Ref. ³¹
MUON_MS	momentum resolution uncertainty from muon system	Section 11.4.2. in Ref. ³¹
MUON_SCALE	momentum scale uncertainty	Section 11.4.2. in Ref. ³¹
MUON_SAGITTA_RHO		
MUON_SAGITTA_RESBIAS	charge dependent momentum scale uncertainty	Section 11.4.2 in Ref. ³¹
	Jets	
JET_2iNP_JET_EffectiveNP_1	energy scale uncertainty from the in situ analyses splits into 8 components	Section 11.5.1. in Ref. ³¹
JET_2iNP_JET_EffectiveNP_2	energy scale uncertainty from the in situ analyses splits into 8 components	Section 11.5.1. in Ref. ³¹
JET_2iNP_JET_EffectiveNP_3	energy scale uncertainty from the in situ analyses splits into 8 components	Section 11.5.1. in Ref. ³¹
JET_2iNP_JET_EffectiveNP_4	energy scale uncertainty from the in situ analyses splits into 8 components	Section 11.5.1. in Ref. ³¹
JET_2iNP_JET_EffectiveNP_5	energy scale uncertainty from the in situ analyses splits into 8 components	Section 11.5.1. in Ref. ³¹
JET_2iNP_JET_EffectiveNP_6	energy scale uncertainty from the in situ analyses splits into 8 components	Section 11.5.1. in Ref. ³¹
JET_2iNP_JET_EffectiveNP_7	energy scale uncertainty from the in situ analyses splits into 8 components	Section 11.5.1. in Ref. ³¹
JET_2iNP_JET_EffectiveNP_8restTerm	energy scale uncertainty from the in situ analyses splits into 8 components	Section 11.5.1. in Ref. ³¹
JET_2iNP_JET_EtaIntercalibration_Modeling	energy scale uncertainty on eta-intercalibration (modeling)	Section 11.5.1. in Ref. ³¹
JET_2iNP_JET_EtaIntercalibration_TotalStat	energy scale uncertainty on eta-intercalibrations (statistics/method)	Section 11.5.1. in Ref. ³¹
JET_2iNP_JET_EtaIntercalibration_NonClosure	energy scale uncertainty on eta-intercalibrations (non-closure)	Section 11.5.1. in Ref. ³¹
JET_2iNP_JET_Pileup_OffsetMu	energy scale uncertainty on pile-up (mu dependent)	Section 11.5.1. in Ref. ³¹
JET_2iNP_JET_Pileup_OffsetNPV	energy scale uncertainty on pile-up (NPV dependent)	Section 11.5.1. in Ref. ³¹
JET_2iNP_JET_Pileup_PtTerm	energy scale uncertainty on pile-up (pt term)	Section 11.5.1. in Ref. ³¹
JET_2iNP_JET_Pileup_RhoTopology	energy scale uncertainty on pile-up (density ρ)	Section 11.5.1. in Ref. ³¹
JET_2iNP_JET_Flavor_Composition_Zjets	energy scale uncertainty on $Z+jets$ sample's flavour composition	Section 11.5.1. in Ref. ³¹
JET_2iNP_JET_Flavor_Composition_Wjets	energy scale uncertainty on $W+jets$ sample's flavour composition	Section 11.5.1. in Ref. ³¹
JET_2iNP_JET_Flavor_Composition_top	energy scale uncertainty on top sample's flavour composition	Section 11.5.1. in Ref. ³¹
JET_2iNP_JET_Flavor_Composition	energy scale uncertainty on VV and VH sample's flavour composition	Section 11.5.1. in Ref. ³¹
JET_2iNP_JET_Flavor_Response	energy scale uncertainty on samples' flavour response	Section 11.5.1. in Ref. ³¹
JET_2iNP_JET_BJES_Response	energy scale uncertainty on b-jets	Section 11.5.1. in Ref. ³¹
JET_2iNP_JET_PunchThrough_MC15	energy scale uncertainty for punch-through jets	Section 11.5.1. in Ref. ³¹
JET_2iNP_JET_SingleParticle_HighPt	energy scale uncertainty from the behaviour of high-pT jets	Section 11.5.1. in Ref. ³¹
JET_JER_SINGLE_NP	energy resolution uncertainty	Section 11.5.1. in Ref. ³¹
JET_JvtEfficiency	JVT efficiency uncertainty	Section 11.5.1 in Ref. ³¹
FT_EFF_Eigen_B	b -tagging efficiency uncertainties ("BTAG_MEDIUM"): 3 components for b jets, 3 for c jets and 5 for light jets	Section 11.7. in Ref. ³¹
FT_EFF_Eigen_C		
FT_EFF_Eigen_L		
FT_EFF_Eigen_extrapolation	b -tagging efficiency uncertainty on the extrapolation to high- jets	Section 11.7. in Ref. ³¹
FT_EFF_Eigen_extrapolation_from_charm	b -tagging efficiency uncertainty on tau jets	Section 11.7. in Ref. ³¹
	MET	
METTrigStat	trigger efficiency uncertainty	Section 11.2.1. in Ref. ³¹
METTrigTop/Z		
MET_SoftTrk_ResoPara	track-based soft term related longitudinal resolution uncertainty	Section 11.6. in Ref. ³¹
MET_SoftTrk_ResoPerp	track-based soft term related transverse resolution uncertainty	Section 11.6. in Ref. ³¹
MET_SoftTrk_Scale	track-based soft term related longitudinal scale uncertainty	Section 11.6. in Ref. ³¹
MET_JetTrk_Scale	track MET scale uncertainty due to tracks in jets	Section 11.6. in Ref. ³¹

Table 5.7: Summary of the experimental systematic uncertainties considered. Details on the individual systematic uncertainties can be found in the given Sections of Ref. ³¹.

¹⁴⁰⁰ 101 GeV. In addition to the jet corrections described above, a kinematic fitter is applied to the leptons
¹⁴⁰¹ and two leading corrected jets in an event with three or fewer jets[†] to take advantage of the fact that
¹⁴⁰² the 2-lepton final state is closed (cf. ²⁰); these objects are only used for MVA training/fit inputs.

¹⁴⁰³ In order to increase analysis sensitivity, the analysis is split into orthogonal regions based on the
¹⁴⁰⁴ number of jets and the transverse momentum of the Z candidate (the vectoral sum of the lepton
¹⁴⁰⁵ pair; this p_T is denoted p_T^V): 2 and ≥ 3 jets; p_T^V in $[75, 150), [150, \infty)$ GeV. In addition to the signal
¹⁴⁰⁶ regions where the leptons are required to be the same flavor (e or μ), there are top $e - \mu$ control
¹⁴⁰⁷ regions used to constrain the top backgrounds.

¹⁴⁰⁸ All of these requirements are summarized in 5.8.

Category	Requirement
Trigger	un-prescaled, single lepton
Jets	≥ 2 central jets; 2 b -tagged signal jets, harder jet with $p_T > 45$ GeV
Leptons	2 VH-loose leptons (≥ 1 ZH-signal lepton); same (opp) flavor for SR (CR)
$m_{\ell\ell}$	$m_{\ell\ell} \in (81, 101)$ GeV
p_T^V regions (GeV)	$[75, 150), [150, \infty)$

Table 5.8: Event selection requirements

¹⁴⁰⁹ It should be noted that the use of ≥ 3 jet events is a 2-lepton specific selection. These regions are
¹⁴¹⁰ exclusive 3 jet regions in the 0- and 1-lepton channels, but the fiducial 2-lepton analysis was found to
¹⁴¹¹ see a $\sim 4\%$ gain in sensitivity in studies by including ≥ 4 jet events⁶⁹.

[†]The gain from using the kinematic fitter is found to be smeared out in events with higher jet multiplicities.

猛き者も遂には滅びぬ、
偏に風の前の塵に同じ。

Heike monogatari

6

1412

1413

Multivariate Analysis Configuration

1414 IN ORDER TO fully leverage the descriptive power of the 13 TeV dataset, this analysis makes use of a
1415 multivariate (MVA) discriminant. Where traditionally event counts or single discriminating vari-
1416 ables per region of phase space have been fed to fits, MVA discriminants seek to integrate additional
1417 information not captured in the conventional phase space cuts plus dijet invariant mass distribu-

1418 tions. Formulating the MVA discriminant is an exercise in supervised learning to construct a binary
1419 classifier, where one uses labeled “signal” and “background” MC events to optimize the parameters
1420 of a statistical model—in this case a boosted decision tree (BDT) with some set of physically moti-
1421 vated variables (or “factors”). The interested reader is directed to the standard references on machine
1422 learning for further details. Sample and variable selection, including variables derived using the the
1423 RestFrames and Lorentz Invariants concepts introduced in Sections 1.5–1.7, are discussed in Section
1424 6.1; MVA training is treated in Section 6.2; and the data statistics only (no systematics) performance
1425 of the three MVA discriminants is explored in Section 6.3.

1426 6.1 TRAINING SAMPLES AND VARIABLE SELECTION

1427 A subset of samples described in Chapter 3 is used for multivariate analysis training, with $qqZH \rightarrow$
1428 $\ell\ell b\bar{b}$ and $ggZH \rightarrow \ell\ell b\bar{b}$ used as signal samples and $Z+jets$, $t\bar{t}$, and VV used as background samples.
1429 Truth-tagging (Section 5.6.2) is used on all samples in MVA training to improve training statistics
1430 and stability. All figures quoted in this section scale distributions to a luminosity of 36.1 fb^{-1} .

1431 6.1.1 STANDARD VARIABLES

1432 The standard set of variables taken as a baseline is the same as used in the fiducial analysis. The vari-
1433 ables fall into several main categories: energy/momenta scales of composite objects (m_{bb} , m_{bbj} ,
1434 p_T^V , $m_{\ell\ell}$), angles ($\Delta R(b_1, b_2)$, $\Delta\phi(V, H)$, $\Delta\eta(V, H)$), transverse momenta of the jets in the event
1435 ($p_T^{b_1}$, $p_T^{b_2}$, $p_T^{j_3}$), and E_T^{miss} . Input distributions for these variables in all the 2 (≥ 3 jet) analysis signal
1436 regions may be found in Figure 6.1 (6.2). The “kf” at the end of variable names denotes that these

are derived using 4-vectors that are the result of the kinematic fitter. The distributions in the figure

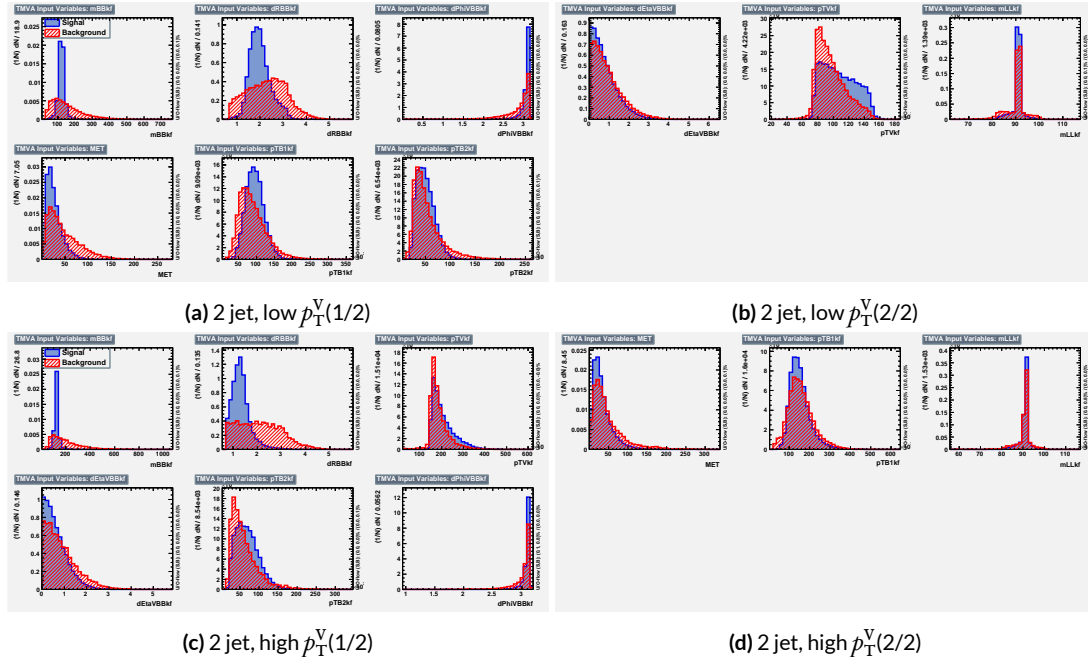


Figure 6.1: Input variables in 2 jet signal regions for the standard variable set. Signal distributions are in red, and background distributions are in blue.

1437

1438 are used as inputs for one of the two k-folded final discriminants, and the order of the distributions
 1439 is the hyperparameter optimized order for feeding into the BDT; what precisely this means will be
 1440 discussed in following sections. While variables in the analysis regions are generally similar, there are
 1441 some notable exceptions. p_T^V and the correlated $\Delta R(b_1, b_2)$ have different shapes, by construction
 1442 for the former and by correlation for the latter, at low and high p_T^V . * The ≥ 3 jet regions also have
 1443 variables that are not applicable to the 2 jet regions; the inclusion of m_{BBJ} (the invariant mass of the
 1444 two b -jets and leading untagged jet) in particular is of note and suggests a potential avenue forward

*Recall that higher p_T^V means, in a balanced final state like $ZH \rightarrow \ell\ell b\bar{b}$, the b -jet pair will have higher p_T and hence be more collimated (lower $\Delta R(b_1, b_2)$); this is not necessarily the case for background events, as the distributions show.

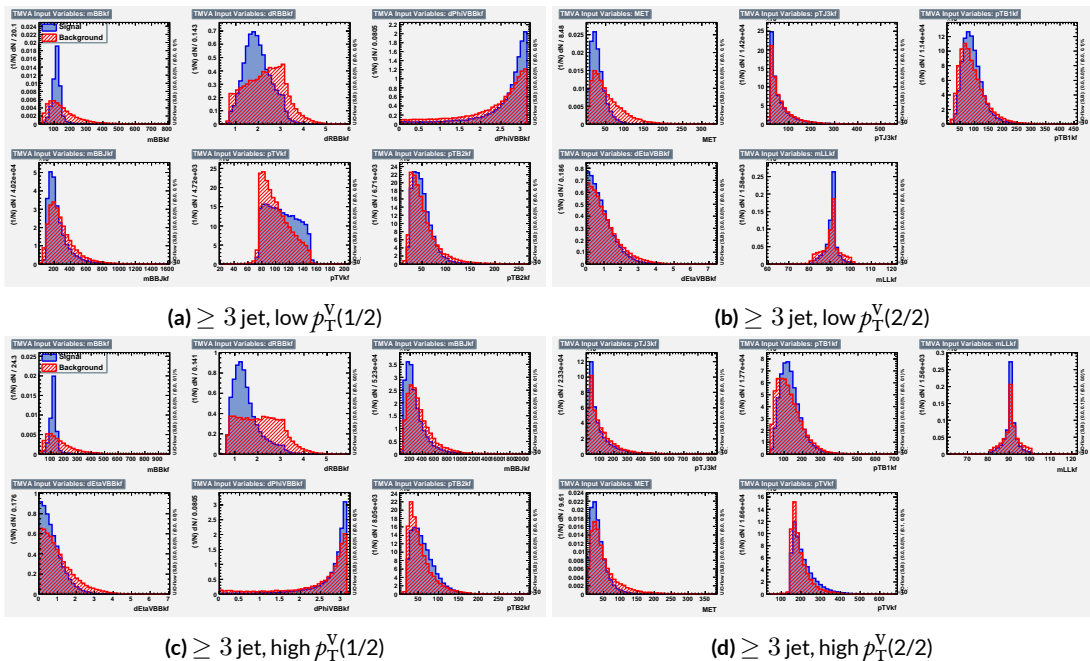


Figure 6.2: Input variables in ≥ 3 jet signal regions for the standard variable set. Signal distributions are in red, and background distributions are in blue.

1445 for refinements of the non-standard variables.

1446 Looking at the correlation matrices for the standard variables in Figure 6.3, it is easy to see that

there are large number of non-trivial correlations

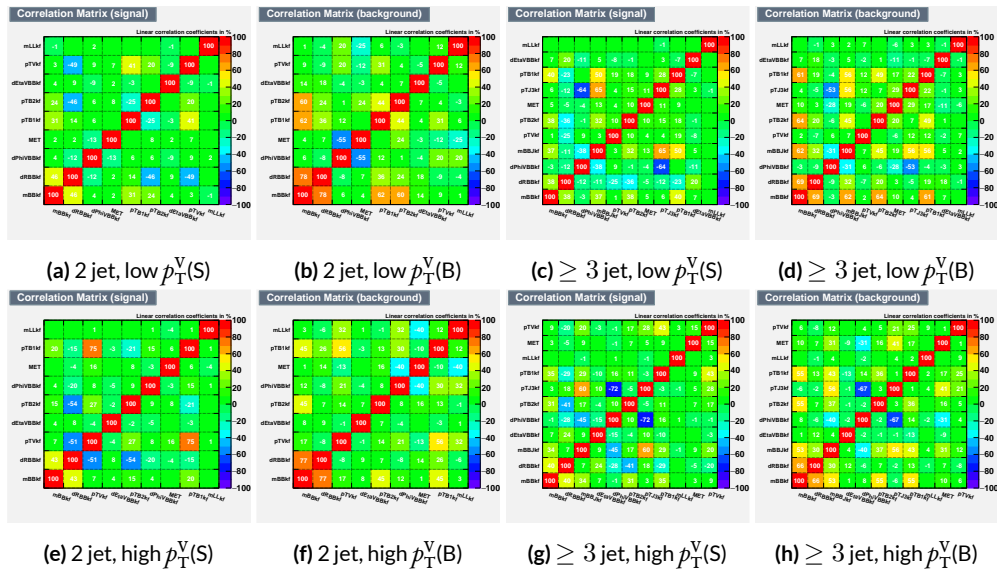


Figure 6.3: Signal and background variable correlations for the standard variable set.

1447

1448 6.1.2 LORENTZ INVARIANTS

1449 In choosing the set of variables used for a set of Lorentz Invariants based discriminants, we decided
 1450 to use S. Hagebeck's set from⁵³ and related studies. Distributions of these variables in the same ar-
 rangement as with the standard variables may be seen in Figures 6.4 and 6.5. One thing to note

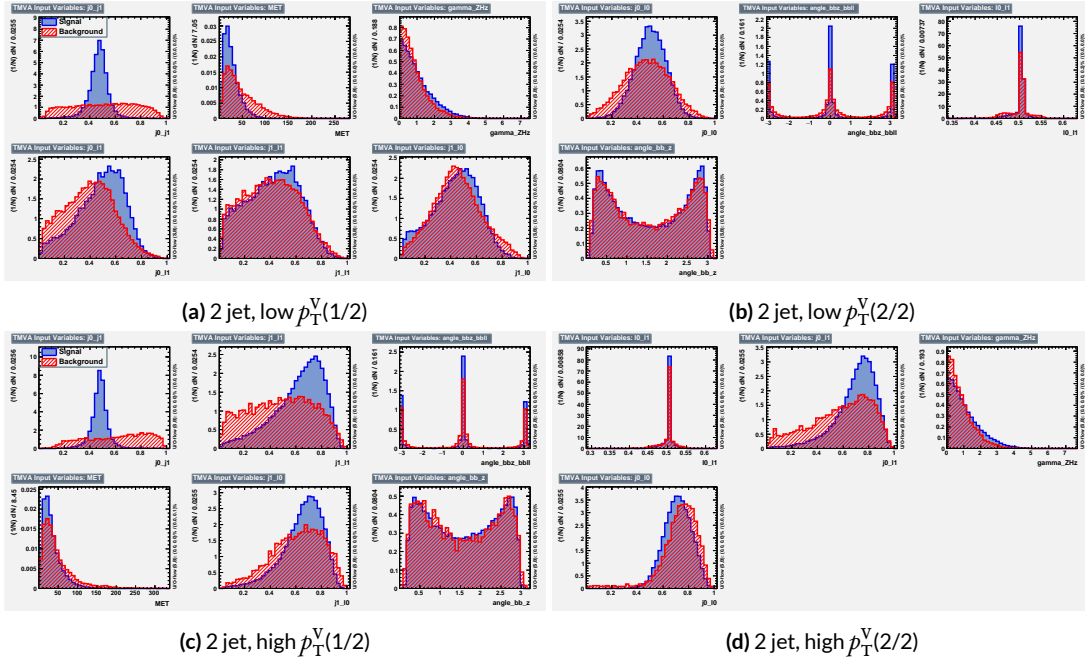


Figure 6.4: Input variables in 2 jet signal regions for the LI variable set. Signal distributions are in red, and background distributions are in blue.

1451

1452 about the variable set chosen here is that \vec{E}_T^{miss} has been added to the standard LI set. Since the LI
 1453 construction assumes that this quantity is zero, there is no obvious way to include it. Nevertheless,
 1454 as the correlation matrices for the LI variables show in Figure 6.6, there is actually very little corre-
 1455 lation between \vec{E}_T^{miss} and the other variables (with this being slightly less the case for the background
 1456 correlations, as to be expected since $t\bar{t}$, a principal background, is \vec{E}_T^{miss} -rich). Hence, if including

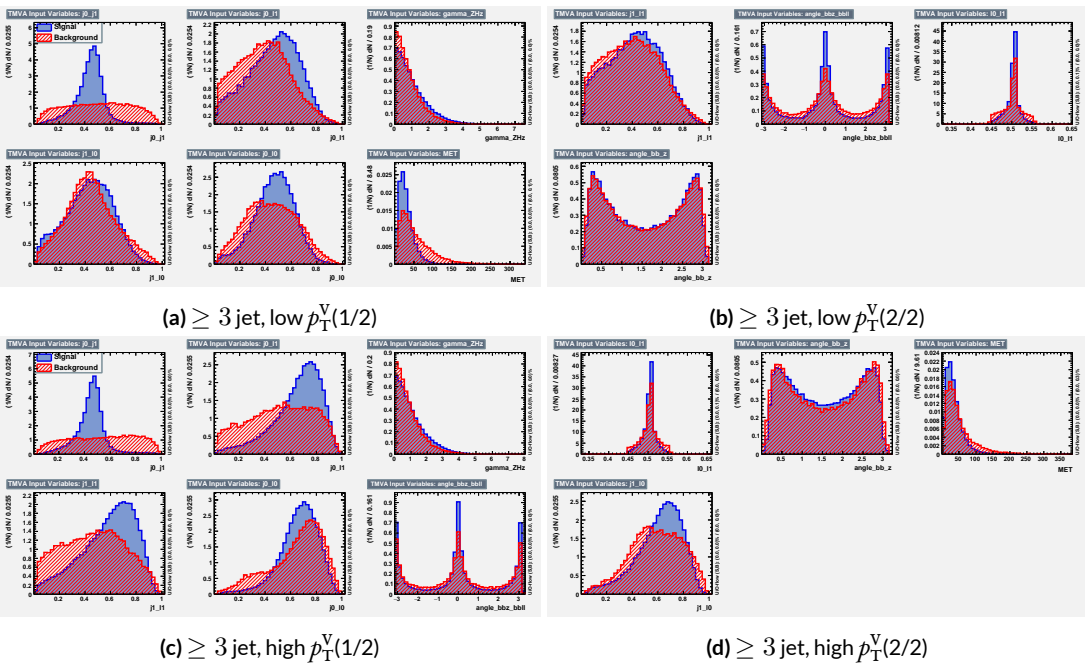


Figure 6.5: Input variables in ≥ 3 jet signal regions for the LI variable set. Signal distributions are in red, and background distributions are in blue.

1457 \vec{E}_T^{miss} violates the spirit somewhat of the LI variables, it does not break terribly much with the aim of having a more orthogonal set.

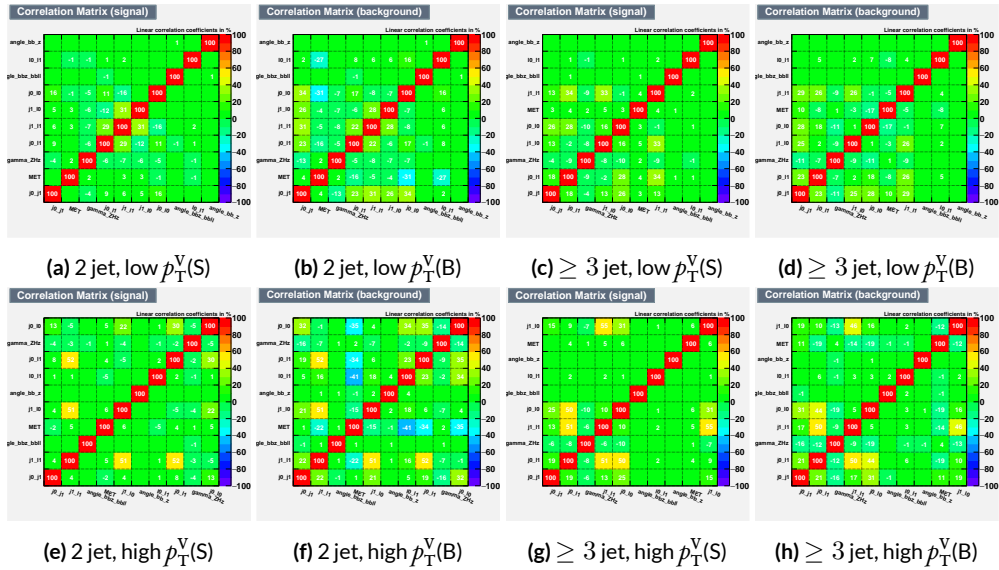


Figure 6.6: Signal and background variable correlations for the LI variable set.

1459 6.1.3 RESTFRAMES VARIABLES

1460 There is no precedent for using the RestFrames variables in the $ZH \rightarrow \ell\ell b\bar{b}$ analysis, so a subset
1461 of possible RF variables had to be selected as the basis of a discriminant. The masses and cosines of
1462 boost angles from parent frames for the CM, Z , and H frames gives six variables, and it was decided
1463 that it would be good to match the LI in terms of variable number and treatment (i.e. no special
1464 treatment of the third jet), which leaves four more variables. In addition to the cosines, there are
1465 also the $\Delta\phi$ angles. Furthermore, there are the event-by-event scaled momentum ratios, both lon-
1466 gitudinal and transverse. There is also both a $\Delta\phi$ and an CM-scaled ratio for the \vec{E}_T^{miss} . All of these
1467 variables were included in a ranking using slightly different training settings as the main hyperpa-
1468 rameter optimization variable ranking described below. The goal of this study was not to develop a
1469 discriminant, as the number of variables is too high, but rather to see which ones are generally use-
1470 ful. Table 6.1 shows the results of this study. Percent gains (losses) at each step by adding the variable
1471 with biggest gain (smallest loss) are shown in green (red). The final row shows an aggregate rank-
1472 ing, calculated simply by adding up a variables ranks in all bins and ordering the variables smallest
1473 to greatest. This simple aggregation does not take into account which regions are potentially more
1474 sensitive and so where taken simply to give an idea of how variables generally performed. With this
1475 in mind, the RF variables were chosen to be the masses M_{CM} , M_H , and M_Z , the angles $\cos CM$, \cosh ,
1476 $\cos Z$, $\cos \phi CMH$, and the ratios R_{pt} , R_{pz} , and R_{met} . Their distributions may be seen in Figures 6.7
1477 and 6.8.

1478 Correlations for the chosen RF variables are shown in Figure 6.9. These correlations are much

Region	Variable Chain
2jet pTVbin1	Rpt (65.8%), Rpz (29.0%), cosZ (11.4%), MZ (-1.75%), dphiCMH (7.26%), cosCM (3.95%), cosH (0.142%), MCM (2.18%), dphiCMZ (-2.3%), dphiCMMet (-0.236%), dphiLABCM (0.404%), Rmet (-4.04%)
3jet pTVbin1	Rpt (50.8%), Rpz (15.6%), MZ (14.8%), cosZ (3.08%), MCM (3.79%), dphiCMH (3.24%), cosH (0.755%), dphiCMMet (1.04%), Rmet (-1.03%), cosCM (5.31%), dphiCMZ (-1.27%), dphiLABCM (-2.88%), pTJ3 (-1.27%)
2jet pTVbin2	Rpt (52.0%), Rpz (13.8%), cosZ (16.9%), cosH (6.49%), MCM (1.71%), cosCM (6.21%), Rmet (4.25%), dphiCMMet (-1.53%), dphiLABCM (-0.757%), dphiCMH (0.213%), MZ (-0.788%), dphiCMZ (-2.39%)
3jet pTVbin2	Rpt (31.5%), Rpz (21.6%), cosH (8.97%), cosZ (1.42%), cosCM (11.3%), dphiCMZ (-2.84%), MCM (8.17%), dphiCMH (-0.841%), dphiLABCM (-0.00318%), dphiCMMet (-2.6%), pTJ3 (-3.21%), MZ (-1.8%), Rmet (-6.29%)
Aggregate	Rpt (o,o,o,o), Rpz (i,i,i,i), cosZ (2,3,2,3), cosH (6,6,3,2), MCM (7,4,4,6), MZ (3,2,10,11), dphiCMH (4,5,9,7), cosCM (5,9,5,4), dphiCMMet (9,7,7,9), dphiCMZ (8,10,11,5), Rmet (11,8,6,12), dphiLABCM (10,11,8,8)

Table 6.1: Full RF variable ranking study summary. Green (red) percentages represent gains (losses) in a validation significance at each step.

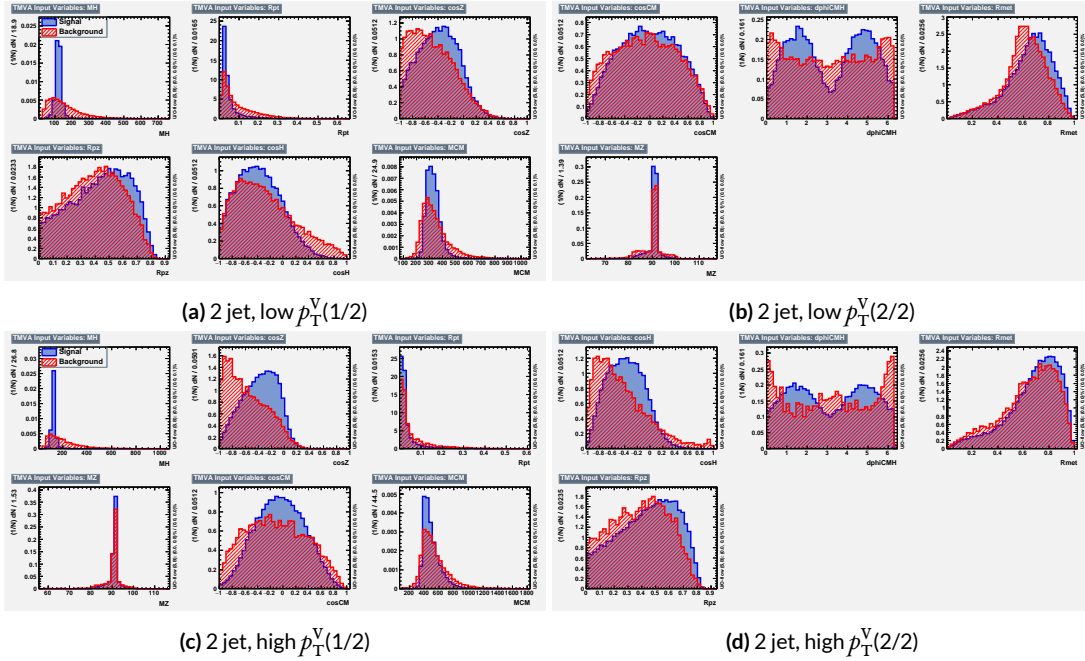


Figure 6.7: Input variables in 2 jet signal regions for the RF variable set. Signal distributions are in red, and background distributions are in blue.

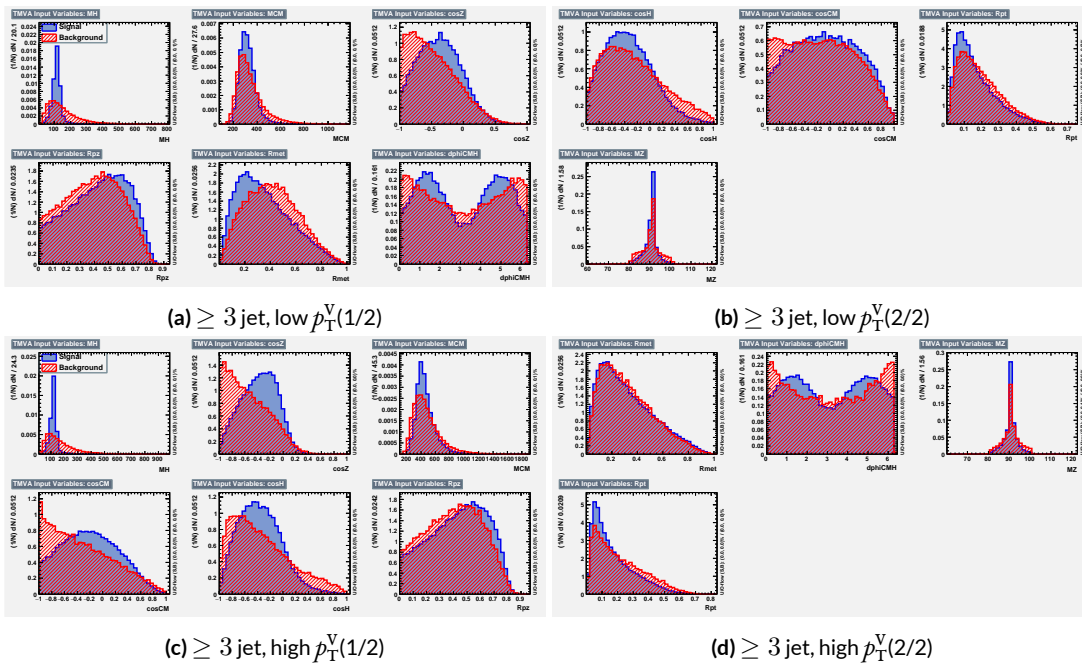


Figure 6.8: Input variables in ≥ 3 jet signal regions for the RF variable set. Signal distributions are in red, and background distributions are in blue.

1479 lower than for the standard case but still slightly higher than for the LI case. Notably, many strong
 1480 correlations that exist for signal events do not exist in background events and vice versa, so what is
 1481 lost in orthogonality may very well be recuperated in greater separation[†]. Given the generally better
 1482 performance of the RF sets, as we shall see in following sections and chapters, this slight tradeoff is
 1483 likely an aesthetic one, with the main benefits of a more orthogonal basis likely realized at this level
 1484 of correlation.

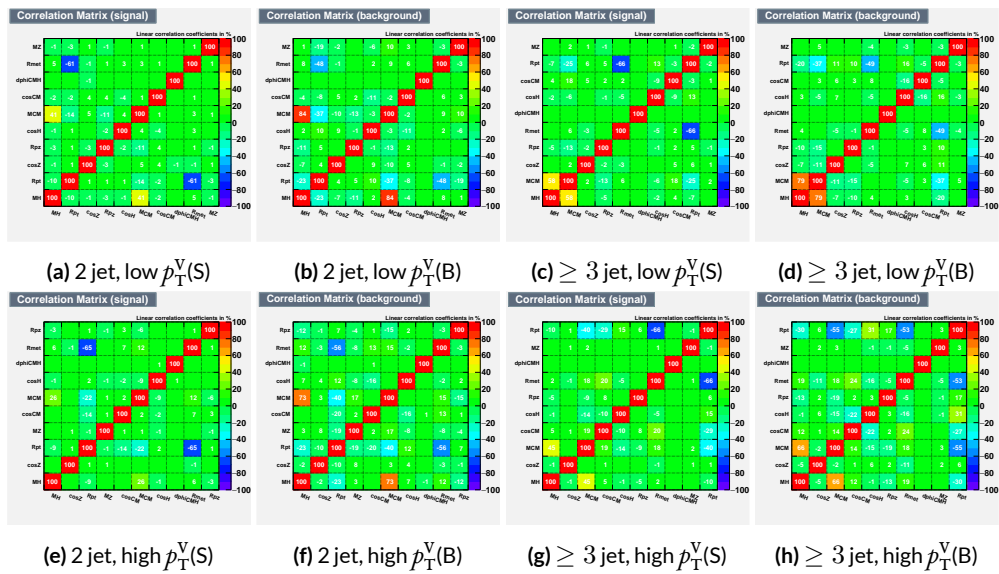


Figure 6.9: Signal and background variable correlations for the RF variable set.

1485 A summary of the variables used in the three cases is given in 6.2.

[†]It is very hard to say for certain whether this is the case for MVA discriminants, and such dedicated studies might make worthwhile future studies.

Variable Set	Variables
Standard	mBB, mLL, (mBBJ), pTV, pTB1, pTB2, (pTJ3), dRBB, dPhiVBB, dEtaVBB, MET 9(11) vars
Lorentz Invariants	j0_j1, j0_l1, l0_l1, j1_l1, j0_l0, j1_l0, gamma_ZHz, angle_bbz_bbll angle_bb_z, MET 10 vars
RestFrames	MH, MCM, MZ, cosH, cosCM, cosZ, Rpz, Rpt, dphiCMH, Rmet 10 vars

Table 6.2: Variables used in MVA training. Variables in parentheses are only used in the ≥ 3 jet regions.

1486 6.2 MVA TRAINING

1487 With variables chosen, the MVA discriminants must be trained and optimized. MVA training and
 1488 hyperparameter optimization (in this case, just the order in which variables are fed into the MVA) is
 1489 conducted using the “holdout” method. In this scheme, events are divided into three equal portions
 1490 (in this case using `EventNumber%3`), with the first third (the “training” set) being used for the initial
 1491 training, the second third (the “validation” set) being used for hyperparameter optimization, and
 1492 the final third (the “testing” set) used to evaluate the performance of the final discriminants in each
 1493 analysis region.

1494 The MVA discriminant used is a boosted decision tree (BDT). Training is done in TMVA using
 1495 the training settings of the fiducial analysis^{65‡}. For the purposes of hyperparameterization and test-
 1496 ing, transformation D with $z_s = z_b = 10$ is applied to the BDT distributions, and the cumulative
 1497 sum of the significance $S/\sqrt{S + B}$ in each bin is calculated for each pair of distributions.

1498 Transformation D is a histogram transformation, developed during the Run 1 SM $VH(b\bar{b})$ search,

[‡]Namely, !H:!V:BoostType=AdaBoost:AdaBoostBeta=0.15:SeparationType=GiniIndex:-PruneMethod=NoPruning:NTrees=200:MaxDepth=4:nCuts=100:nEventsMin=5%

1499 designed to reduce the number of bins in final BDT distributions and thereby mitigate the effect of
 1500 statistical fluctuations in data while also maintaining sensitivity. Such an arbitrary transformation
 1501 may be expressed as:

$$Z(I[k, l]) = Z(z_s, n_s(I[k, l]), N_s, z_b, n_b(I[k, l]), N_b) \quad (6.1)$$

1502 where

- 1503 • $I[k, l]$ is an interval of the histograms, containing the bins between bin k and bin l ;
- 1504 • N_s is the total number of signal events in the histogram;
- 1505 • N_b is the total number of background events in the histogram;
- 1506 • $n_s(I[k, l])$ is the total number of signal events in the interval $I[k, l]$;
- 1507 • $n_b(I[k, l])$ is the total number of background events in the interval $I[k, l]$;
- 1508 • z_s and z_b are parameters used to tune the algorithm.

1509 Transformation D uses:

$$Z = z_s \frac{n_s}{N_s} + z_b \frac{n_b}{N_b} \quad (6.2)$$

1510 Rebinning occurs as follow:

- 1511 1. Begin with the highest valued bin in the original pair of distributions. Call this the “last” bin
1512 and use it as l , and have k be this bin as well.
- 1513 2. Calculate $Z(I[k, l])$
- 1514 3. If $Z \leq 1$, set $k \rightarrow k - 1$ and return to step 2. If not, rebin bins $k-l$ into a single bin and name
1515 $k - 1$ the new “last” bin l .
- 1516 4. Continue until all bins have been iterated through; if $Z \leq 1$ for any remaining n of the
1517 lowest-valued bins (as is often the case), simply rebin these as a single bin.

1518 Variable ranking is done iteratively (greedily) in each analysis region. In each set, the validation
 1519 significance of a BDT using an initial subset of variables is calculated ($dRBB$ and mBB for the stan-
 1520 dard set; $j_0_j_1$ for the LI set; and MH for the RF set). Each of the remaining unranked variables
 1521 are then added separately, one at a time, to the BDT. The variable yielding the highest validation
 1522 significance is then added to the set list of ranked variables and removed from the list of unranked
 1523 variables. This process is repeated until no variables remain. These rankings are shown in Figures
 1524 6.10–6.12. Rankings tend to be fairly stable.

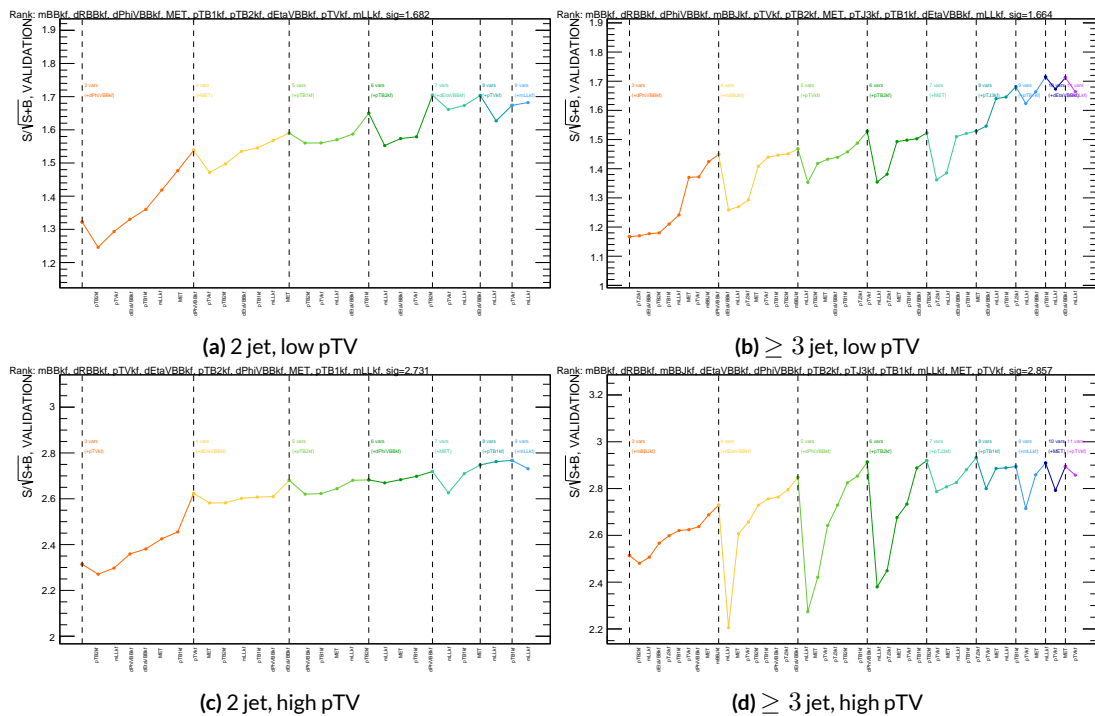


Figure 6.10: Rankings for the standard variable set.

1525 Once variables have been ranked, the BDT may be used both to evaluate performance in a simpli-
 1526 fied analysis scenario in the absence of systematic uncertainties (described below in Section 6.3) and

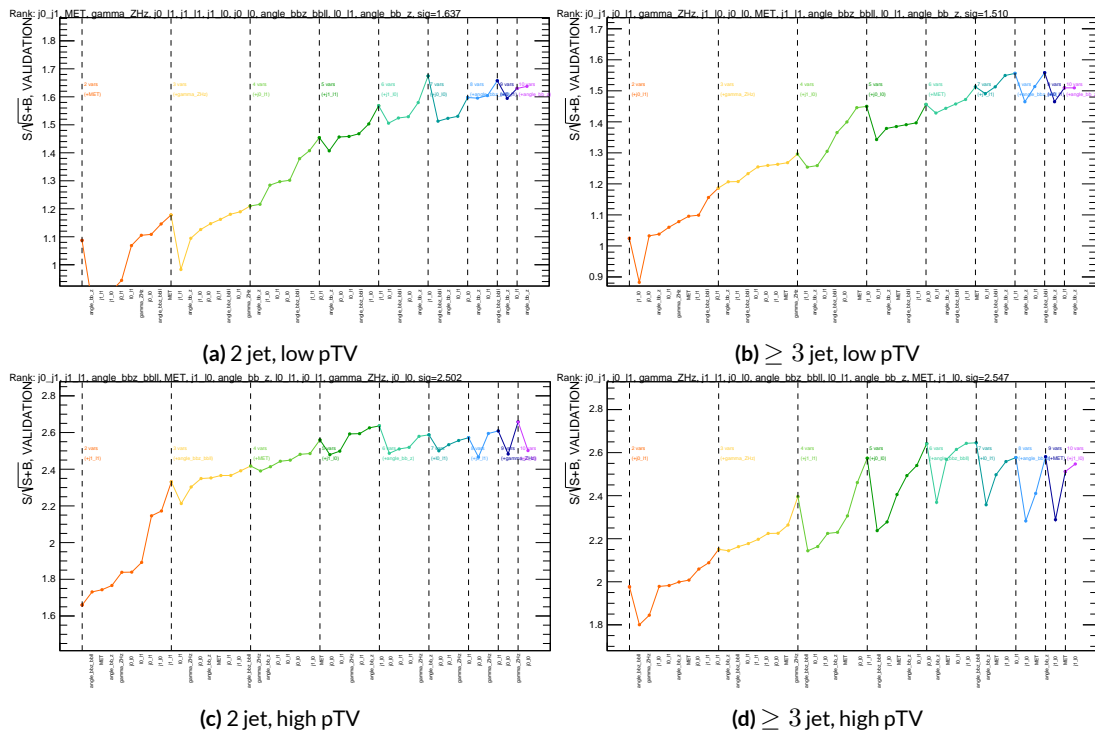


Figure 6.11: Rankings for the L1 variable set.

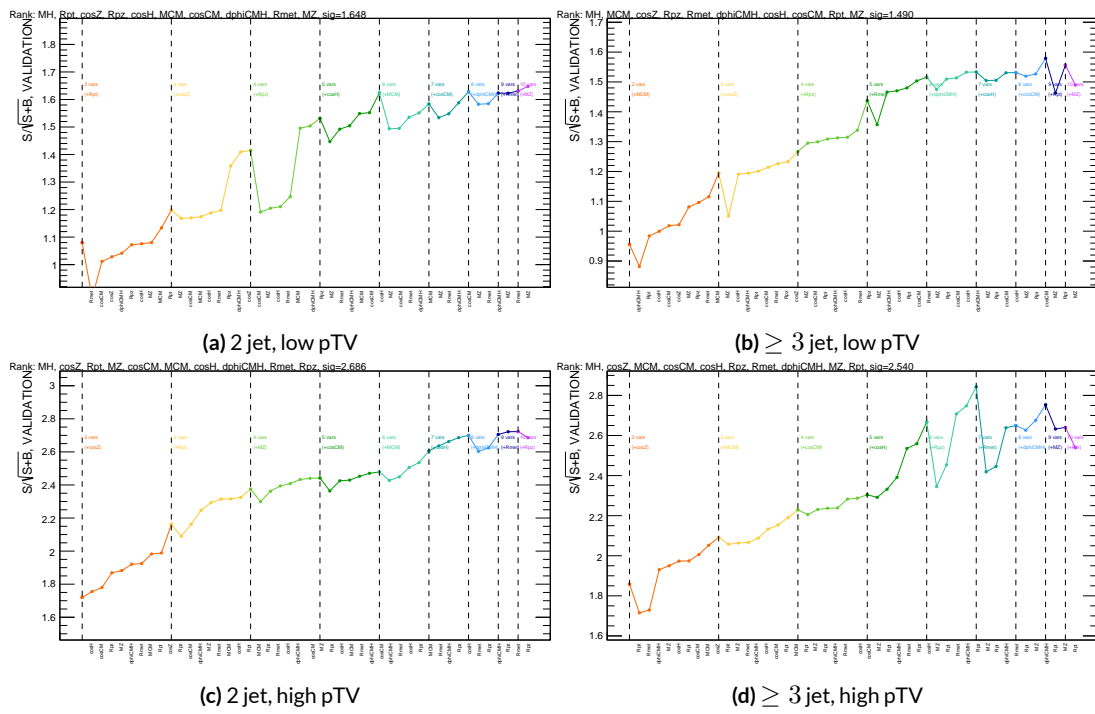


Figure 6.12: Rankings for the RF variable set.

1527 to create xml files for the production of fit inputs for an analysis including systematics. Following
1528 the approach taken in the fiducial analysis, BDT discriminants using two “k-folds” are produced to
1529 prevent overtraining, since the samples used for training are the same as those used to produce in-
1530 puts for the full profile likelihood fit. In this scheme, a BDT trained on events with an even (odd)
1531 `EventNumber` are used to evaluate events with an odd (even) `EventNumber`.

1532 6.3 STATISTICS ONLY BDT PERFORMANCE

1533 As described above, cumulative significances can be extracted from pairs of signal and background
1534 BDT output distributions in a given region. In order to evaluate performance of variable sets in the
1535 absence of systematic uncertainties, such pairs can be constructed by evaluating BDT score on the
1536 testing set of events using the optimal variable rankings in each region. We show two versions of
1537 each testing distribution for each variable set in each signal region in Figures 6.13–6.15. The training
1538 distribution is always shown as points. The plots with block histograms with numbers of bins that
1539 match (do not match) the training distribution do not (do) have transformation D applied. Trans-
1540 formation D histograms are included to show the distributions actually used for significance evalu-
1541 ation, while the untransformed histograms are included to illustrate that the level of overtraining is
1542 not too terrible[§]. For better comparison of the distributions, all histograms have been scaled to have
1543 the same normalization.

1544 As can be seen in the summary of cumulative significances for each of these analysis regions and
1545 variable sets in Figure 6.16, the performance of each of the variable sets is quite similar. The standard

[§]The raw distributions include a K-S test statistic for signal (background) distributions.

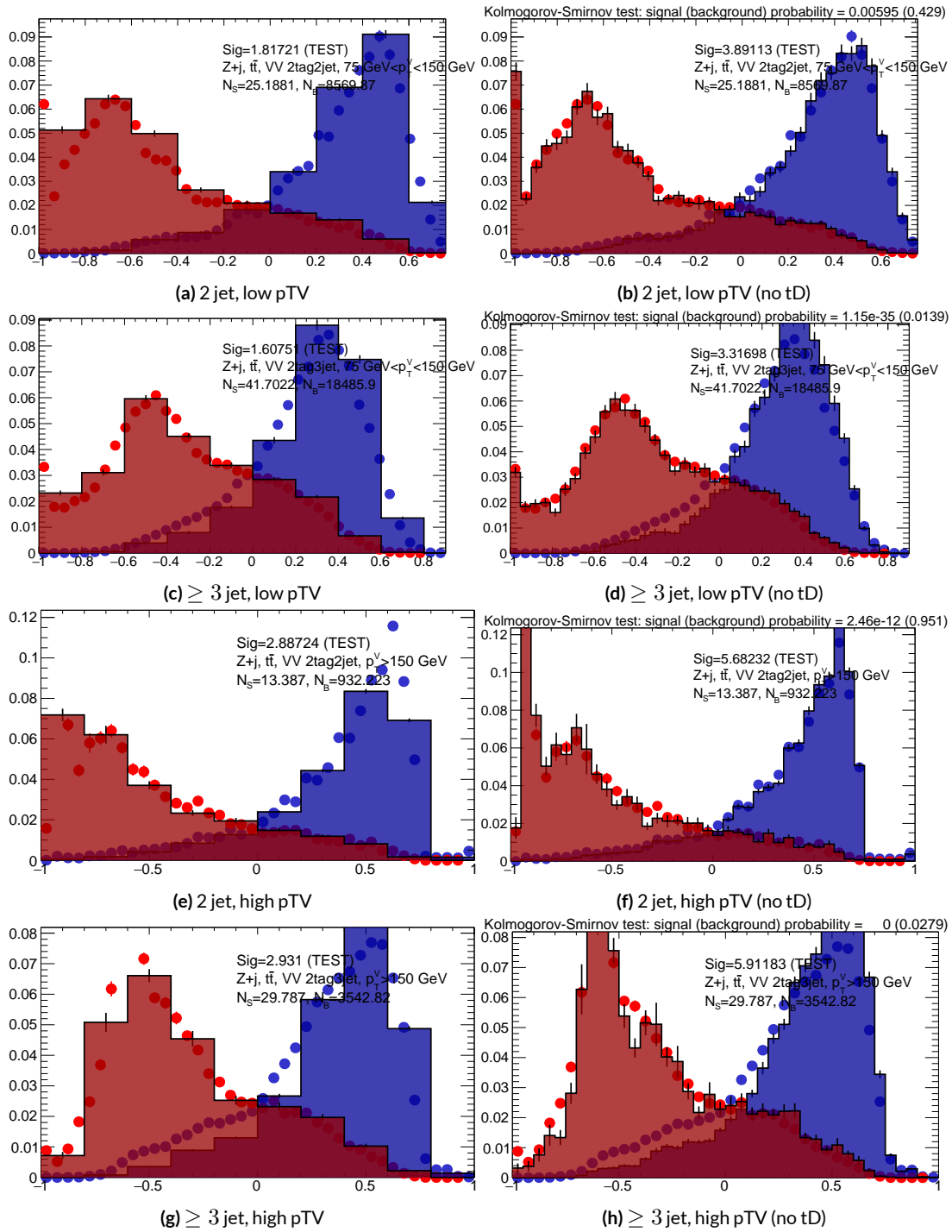


Figure 6.13: Training (points) and testing (block histogram) MVA distributions used for stat only testing for the standard variable set.

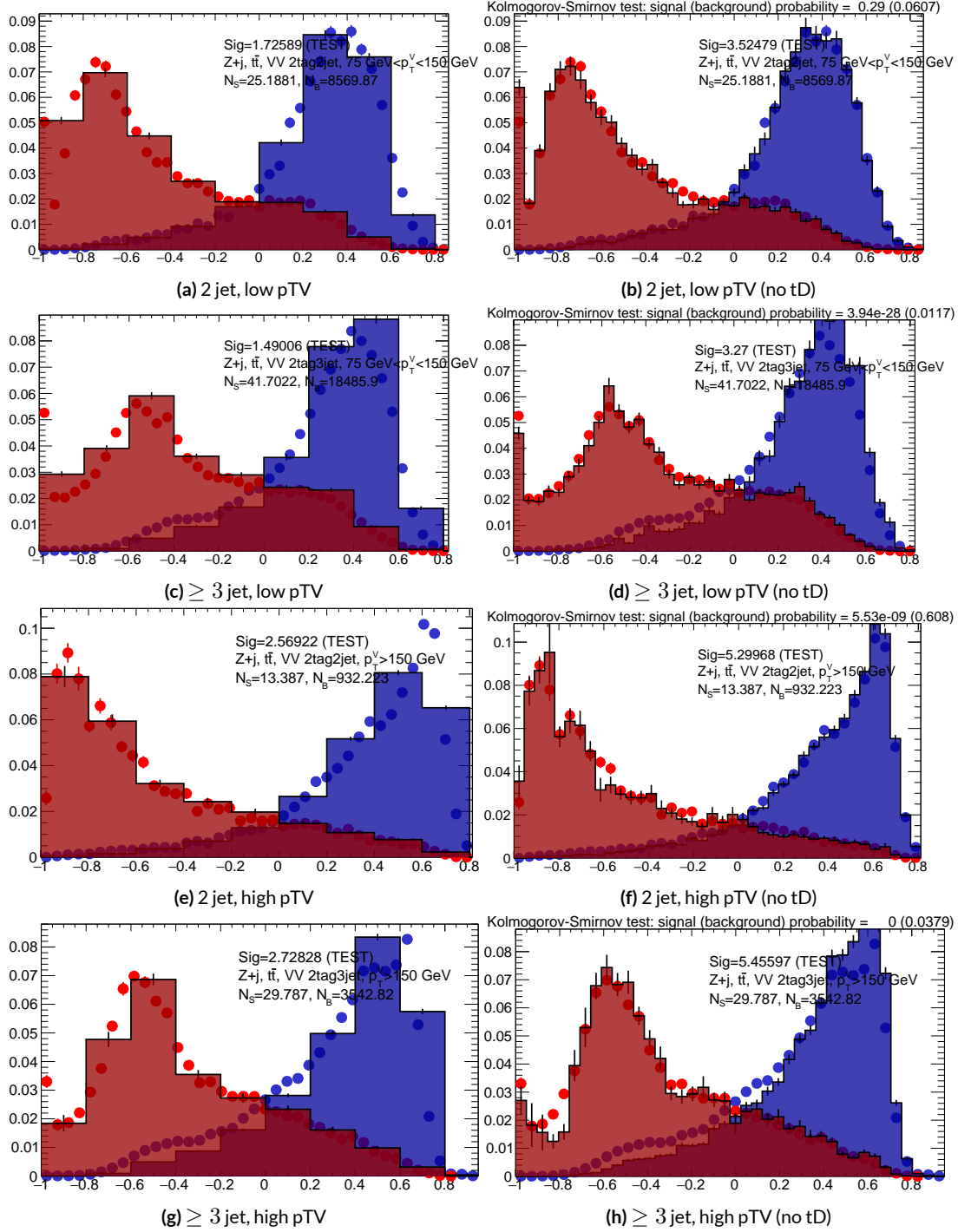


Figure 6.14: Training (points) and testing (block histogram) MVA distributions used for stat only testing for the LI variable set.

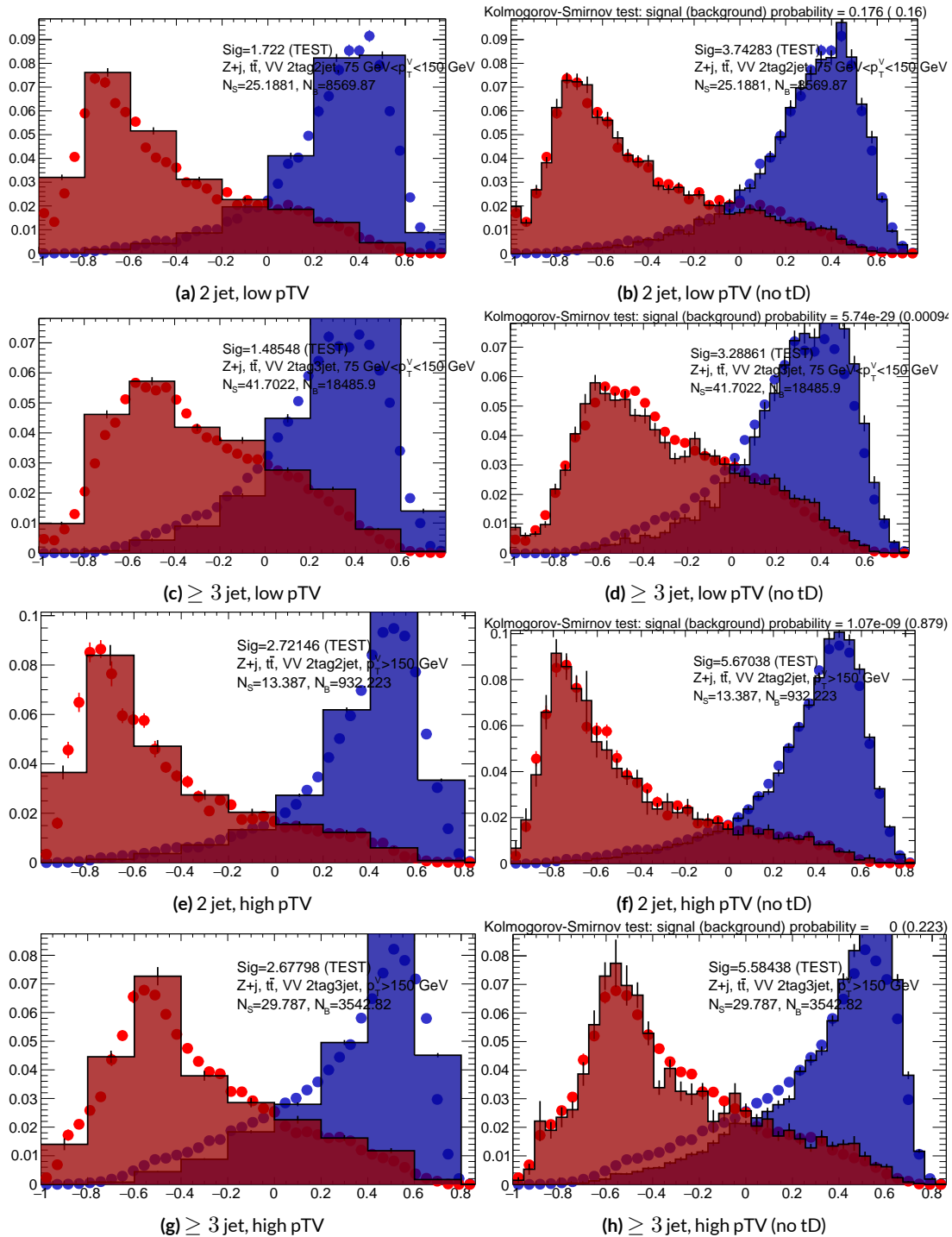


Figure 6.15: Training (points) and testing (block histogram) MVA distributions used for stat only testing for the RF variable set.

1546 set performs best, with the LI (RF) set having a cumulative significance that is 7.9% (6.9%) lower.
 1547 This suggests that the LI and RF variables, in the $ZH \rightarrow \ell\ell b\bar{b}$ closed final state, have no more in-
 1548 trinsic descriptive power than the standard set. That these figures are all relatively high (~ 4.5) is
 1549 due largely to the absence of systematics and possibly in part due to the fact that many of the most
 1550 significant bins occur at high values of the BDT output, which, as can be seen in any of the testing
 distributions, contain a small fraction of background events. An interesting feature to note in Fig-

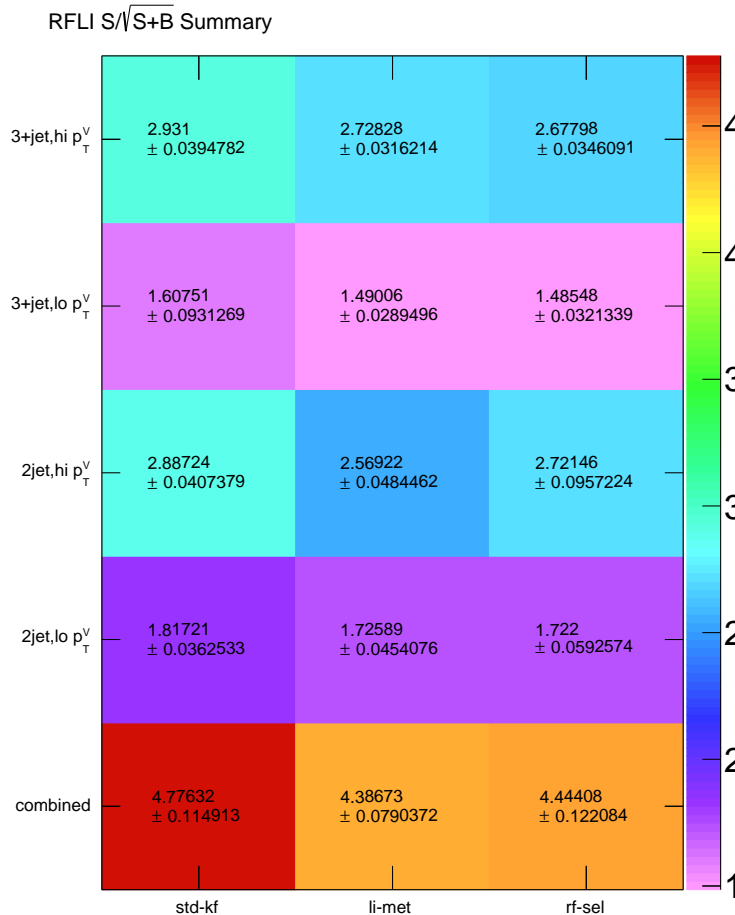


Figure 6.16: Results of testing significances sorted by analysis region and variable set.

1551

1552 ure 6.16 is that while the standard set does perform better in all regions, the gap is larger in the ≥ 3
1553 jet regions, suggesting that further optimization in the ≥ 3 jet case could be useful. Moreover, as
1554 discussed at the end of Chapter 5, the choice of ≥ 3 jet and not exclusive 3 jet regions is a 2-lepton
1555 specific choice and may not be justified for the non-standard variable sets.

Multivac picked you as most representative this year.

Not the smartest, or the strongest, or the luckiest, but

just the most representative. Now we don't question

Multivac, do we?

Isaac Asimov, "Franchise"

1556

7

1557

Statistical Fit Model and Validation

1558 THE ULTIMATE GOAL of an analysis like the search for SM $VH(b\bar{b})$ decay is to say with as much
1559 justified precision as possible with the ATLAS collision data whether or not the SM-like Higgs ob-
1560 served in other decay modes also decays to b -quarks and, if so, whether this rate is consistent with
1561 the SM prediction. In the limit of perfect modeling of both background processes and detector/reconstruction,

1562 the only free parameter is this production rate, referred to typically as a “signal strength,” denoted μ ,
1563 with $\mu = 1$ corresponding to the SM prediction and $\mu = 0$ corresponding to the SM with no
1564 Higgs.

1565 To get a better sense of what this might look like, take a look at the example discriminant distri-
1566 bution in Figure 7.1. The black points are data (with statistical error bars), and the colored block
1567 histograms have size corresponding to the number of predicted events for each process in each bin of
1568 the final BDT. In the limit of perfect understanding, a fit would correspond to a constant scale fac-
1569 tor on the red, signal histogram, where one would choose a best fit μ value, denoted $\hat{\mu}$, that would
1570 minimize the sum in quadrature of differences between the number of observed data events and
1571 $\mu s_i + b_i$, where s_i and b_i are the predicted number of signal and background events in each bin.

1572 The only source of uncertainty would be due to data statistics, so for an infinitely large dataset with
1573 perfect understanding, μ could be fitted to arbitrary precision. This, of course, is not the case since
1574 there is a finite amount of data and very many sources of systematic uncertainty, discussed in pre-
1575 vious chapters. This chapter will first describe how systematic uncertainties are integrated into the
1576 statistical fit of this analysis before describing two sets of cross checks on both a validation VZ fit and
1577 on the fit for the VH fit of interest.

1578 7.1 THE FIT MODEL

1579 In order to derive the strength of the signal process $ZH \rightarrow \ell\ell b\bar{b}$ and other quantities of interest
1580 while taking into account systematic uncertainties or nuisance parameters (NP’s, collectively de-
1581 noted θ), a binned likelihood function is constructed as the product over bins of Poisson distribu-

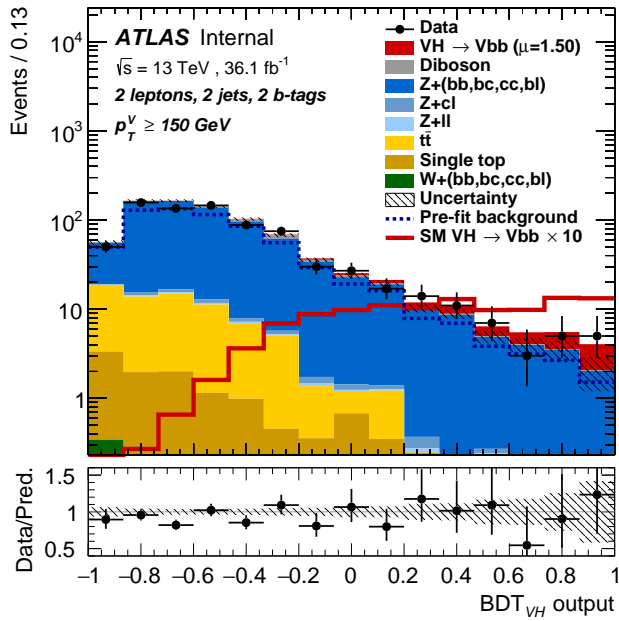


Figure 7.1: An example postfit distribution. The reason this looks different from postfit distributions later in this chapter is that this is a log plot.

1582 tions:

$$\mathcal{L}(\mu, \theta) = \text{Pois}(n | \mu S + B) \left[\prod_{i \in \text{bins}} \frac{\mu s_i + b_i}{\mu S + B} \right] \prod_{j \in \text{NP's}} \mathcal{N}_{\theta_j}(\theta_j, \sigma_j^2 | 0, 1) \quad (7.1)$$

1583 where n is the total number of events observed, s_i and b_i are the number of expected signal and back-

1584 ground events in each bin, and S and B are the total expected signal and background events. The

1585 signal and background expectations generally are functions of the NP's θ . NP's related to the nor-

1586 malization of signal and background processes fall into two categories. The first set is left to float

1587 freely like μ while the second set are parametrized as log-normally distributed to prevent negative

1588 predicted values. All other NP's are parametrized with Gaussian priors. This results in a “penalty”

1589 on the NLL discussed below of $(\hat{\alpha} - \mu_\alpha)^2 / \sigma_\alpha^2$, for NP α , normally parametrized with mean μ_α

1590 (corresponding to the nominal prediction) and variance σ_α^2 (derived as discussed in Chapters 4 and

1591 5) for an MLE of $\hat{\alpha}$.

1592 One can maximize^{*} the likelihood in Equation 7.1 for a fixed value of μ to derive estimators for
1593 the NP's θ ; values of θ so derived are denoted $\hat{\theta}_\mu$ to emphasize that these are likelihood maximizing
1594 for a given μ . The profile likelihood technique finds the likelihood function's maximum by compar-
1595 ing the values of the likelihood over all possible values of μ using these "profiles" and picking the
1596 one with the greatest $\mathcal{L}(\mu, \hat{\theta}_\mu)$ value; these values of μ and θ are denoted $\hat{\mu}$ and $\hat{\theta}$. The profile like-
1597 lihood can further be used to construct a test statistic[†]

$$q_\mu = -2 \left(\log \mathcal{L}(\mu, \hat{\theta}_\mu) - \log \mathcal{L}(\hat{\mu}, \hat{\theta}) \right) \quad (7.2)$$

1598 This statistic can be used to derive the usual significance (p value), by setting $\mu = 0$ to find the com-
1599 patability with the background-only hypothesis⁴⁵. If there is insufficient evidence for the signal hy-
1600 pothesis, the CL_s method can be used to set limits¹⁸.

1601 In order to both validate the fit model and study the behavior of fits independent of a given dataset,
1602 a so-called "Asimov"[‡] dataset can be constructed for a given fit model; this dataset has each bin equal
1603 to its expectation value for assumed values of the NP's and a given μ value (in this case, $\mu = 1$, the
1604 SM prediction).

^{*}Maximization is mathematically identical to finding the minimum of the negative logarithm of the likelihood, which is numerically an easier problem.

[†]The factor of -2 is added so that this statistic gives, in the asymptotic limit of large N , a χ^2 distribution.

[‡]A reference to the short story quoted at the beginning of this chapter in which a computer picks a single voter to stand in for the views of the entire American electorate.

1605 7.2 FIT INPUTS

1606 Inputs to the binned likelihood are distributions of the BDT outputs described in Chapter 6 for the
1607 signal regions and of m_{bb} for the top $e - \mu$ control regions. These regions split events according
1608 to their p_T^V and number of jets. All events are required to have two b -tagged jets, as well as pass the
1609 other event selection requirements summarized in Table 5.8; the only difference between the signal
1610 and control region selections is that the same flavor requirement (i.e. leptons both be electrons or
1611 muons) is flipped so that events in the control region have exactly one electron and one muon. The
1612 BDT outputs are binned using transformation D, while the m_{bb} distributions have 50 GeV bins,
1613 with the exception of the 2 jet, high p_T^V region, where a single bin is used due to low statistics.

1614 Input distributions in MC are further divided according to their physics process. The signal pro-
1615 cesses are divided based on both the identity of associated V and the number of leptons in the final
1616 state; $ZH \rightarrow \ell\ell b\bar{b}$ events are further separated into distributions for qq and gg initiated processes.
1617 $V+jets$ events are split according to V identity and into the jet flavor bins described in Chapter 3.
1618 Due to the effectiveness of the 2 b -tag requirement suppressing the presence of both c and l jets,
1619 truth-tagging is used to boost MC statistics in the cc , cl , and ll distributions.[§] For top backgrounds,
1620 single top production is split according to production mode (s , t , and Wt), with $t\bar{t}$ as single category.
1621 Diboson background distributions are also split according to the identity of the V 's (ZZ , WZ , and
1622 WW). Fit input segmentation is summarized in Table 7.1.

1622 [§]Since WW is not an important contribution to the already small total diboson background, no truth-tagging was applied here, in contrast to the fiducial analysis.

Category	Bins
# of Jets	2, 3+
p_T^V Regions (GeV)	$[75, 150], [150, \infty)$
Sample	data, signal $[(W, qqZ, ggZ)] \times n_{lep}$, $V+jets [(W, Z)] \times (bb, bc, bl, cc, cl, ll)]$, $t\bar{t}$, diboson (ZZ, WW, WZ), single top (s, t, Wt)

Table 7.1: Fit input segmentation.

1623 7.3 SYSTEMATIC UNCERTAINTIES REVIEW

1624 Tables 7.2 and 7.3 summarize modeling (Chapter 4) and experimental (Chapter 5) systematic uncer-
 1625 tainties considered in this analysis, respectively. In addition to these, simulation statistics uncertain-
 1626 ties (“MC stat errors”) are also included in the fit model. There is one distribution per systematic
 1627 (one each for up and down) per sample per region. The $\pm 1\sigma$ variation for a systematic is calculated
 1628 as the difference in the integrals between the nominal and up/down varied distributions.

Process	Systematics
Signal	$H \rightarrow bb$ decay, QCD scale, PDF+ α_S scale, UE+PS (acc, p_T^V , m_{bb} , 3/2 jet ratio)
$Z+jets$	Acc, flavor composition, $p_T^V+m_{bb}$ shape
$t\bar{t}$	Acc, $p_T^V+m_{bb}$ shape
Single top	Acc, $p_T^V+m_{bb}$ shape
Diboson	Overall acc, UE+PS (acc, p_T^V , m_{bb} , 3/2 jet ratio), QCD scale (acc (2, 3 jet, jet veto), p_T^V , m_{bb})

Table 7.2: Summary of modeling systematic uncertainties.

1629 The systematics distributions undergo processes known as “smoothing” and “pruning” before
 1630 being combined into the final likelihood used in minimization.
 1631 The difference between systematics varied distributions and nominal distributions approaches

Process	Systematics
Jets	21 NP scheme for JES, JER as single NP
E_T^{miss}	trigger efficiency, track-based soft terms, scale uncertainty due to jet tracks
Flavor Tagging	Eigen parameter scheme (CDI File: 2016-20_7-13TeV-MC15-CDI-2017-06-07_v2)
Electrons	trigger eff, reco/ID eff, isolation eff, energy scale/resoltuion
Muons	trigger eff, reco/ID eff, isolation eff, track to vertex association, momentum resolution/scale
Event	total luminosity, pileup reweighting

Table 7.3: Summary of experimental systematic uncertainties.

1632 some stable value in the limit of large simulation statistics, but if the fluctuations due to simulation
 1633 statistics in a distribution are large compared to the actual physical effect (whether this is because
 1634 the actual effect is small or if the actual distribution is derived from a small number of simulation
 1635 events), then systematic uncertainty will be overestimated by, in effect, counting the MC stat error
 1636 multiple times. Smoothing is designed to mitigate these effects by merging adjacent bins in some
 1637 input distributions. Smoothing happens in two steps (the full details of smoothing algorithms may
 1638 be found in ⁶⁵ and in the `WSMaker` code):
 1639 1. Merge bins iteratively where bin differences are smallest in input distributions until no local
 1640 extrema remain (obviously, a single peak or valley is allowed to remain)
 1641 2. Sequentially merge bins (highest to lowest, like transformation D) until the statistical uncer-
 1642 tainty in a given bin is smaller than 5% of merged bin content
 1643 Not all systematic uncertainties defined are included in the final fit. Systematics are subject “prun-
 1644 ing” (individually in each region/sample: there are two histograms per systematic (up/down) per
 1645 region per sample, so pruning just consists of removing the histograms from the set of distributions
 1646 included in the likelihood) if they are do not have a significant impact, defined as follows:

- Normalization/acceptance systematics are pruned away if either:
 - The variation is less than 0.5%
 - Both up and down variations have the same sign

- Shape systematics pruned away if either:
 - Not one single bin has a deviation over 0.5% after the overall normalisation is removed
 - If only the up or the down variation is non-zero

- Shape+Normalisation systematics are pruned away if the associated sample is less than 2% of the total background and either:
 - If the predicted signal is < 2% of the total background in all bins and the shape and normalisation error are each < 0.5% of the total background
 - If instead at least one bin has a signal contribution > 2% of the total background, and only in each of these bins, the shape and normalisation error are each < 2% of the signal yield

1660 7.4 THE VZ VALIDATION FIT

1661 One of the primary validation cross-checks for the fiducial analysis was a *VZ* fit—that is, conducting
 1662 the entire analysis but looking for $Z \rightarrow b\bar{b}$ decays instead of the Higgs. The idea here is that the
 1663 Z is very well understood and so “rediscovering” Z decay to b 's is taken as a benchmark of analysis
 1664 reliability since the complexity of the fit model precludes the use of orthogonal control regions for
 1665 validation as is done in other analyses (generally, if there is a good control region, one prefers to use it

1666 to constrain backgrounds and improve the fit model). To do this, a new MVA discriminant is made
 1667 by keeping all hyperparameter configurations the same (e.g. variable ranking) but using diboson
 1668 samples as signal. For the 2-lepton case, this means using $ZZ \rightarrow \ell\ell b\bar{b}$ as the signal sample. This
 1669 new MVA is used to make the inputs described in Section 7.2, and the fit is then run as for the VH
 1670 fit (again, with ZZ as signal). VH samples are considered background in these diboson fits.

1671 The VZ fit sensitivities for the standard, LI, and RF fits are summarized in Table 7.4. The ex-
 1672 pected significances are all fairly comparable and about what was the case in the fiducial analysis.
 1673 The observed significance for the standard set matches fairly well with the expected value on data,
 1674 but the LI and RF observed significances are quite a bit lower.

	Standard	LI	RF
Expected (Asimov)	3.83	3.67	3.72
Expected (data)	3.00	2.95	3.11
Observed (data)	3.17	1.80	2.09

Table 7.4: Expected (for both data and Asimov) and observed $VZ \rightarrow \ell\ell b\bar{b}$ sensitivities for the standard, LI, and RF variable sets.

1675 These values, however, are consistent with the observed signal strength values, which can be seen
 1676 in Figure 7.2 (b), with both the LI and RF fits showing a deficit of signal events with respect to the
 1677 SM expectation, though not by much more than one standard deviation (a possible explanation is
 1678 explored in the following section). Just as in the VH fits, errors arising systematic uncertainties are
 1679 lower in the fits to the observed dataset. That the effect is not noticeable in Asimov fits is not too
 1680 surprising, since this analysis (and these variable configurations in particular), is not optimized for
 1681 VZ .

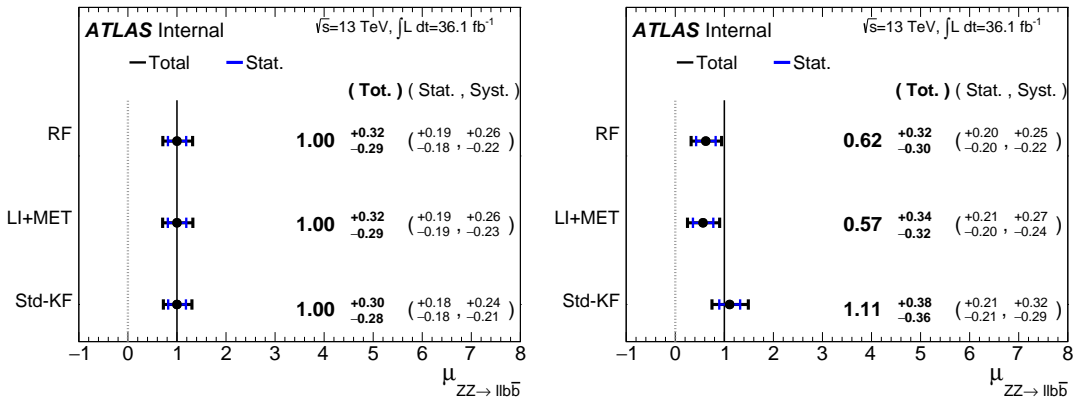


Figure 7.2: μ summary plots for the standard, LI, and RF variable sets. The Asimov case (with $\mu = 1$ by construction) is in (a), and $\hat{\mu}$ best fit values and error summary are in (b).

1682 7.4.I 2 AND ≥ 3 JET FITS

1683 While the treatment of simply ignoring any additional jets in the event seems adequate for the VH
 1684 analysis (discussed below), the potential shortcoming of this treatment appears in the VZ analysis
 1685 when the 2 and ≥ 3 jet cases are fit separately⁴, as can be seen in Figure 7.3. Compared to the stan-
 1686 dard fit, the LI and RF fits have lower $\hat{\mu}_{\geq 3 \text{ jet}}$ values, consistent with the interpretation that the ad-
 1687 ditional information from the third jet in the ≥ 3 jet regions for the standard case is important for
 1688 characterizing events in these regions for VZ fits.

1689 A natural question to ask is why this would be an issue for the VZ but not the VH case. One
 1690 potential answer is that at high transverse boosts, there is a greater probability for final state
 1691 radiation in the hadronically decaying Z , so there are more events where the third jet should be in-
 1692 cluded in the calculation of variables like $m_{b\bar{b}}$ or for angles involving the $b\bar{b}$ system (e.g. $\cos\theta$ in the
 1693 RF case). While the absolute scale at which the low and high p_T^V regions are separated remains the

⁴standalone fits, with half the regions each, not 2 POI fits

same does not change from the VH to the VZ analysis, 150 GeV, the implicit cutoff on the transverse boost of the hadronically decaying boson does. For the Higgs, with a mass of 125 GeV, the p_T^V cutoff corresponds to $\gamma \sim 1.56 - 6.74$, but for the Z , with a mass of 91 GeV, this is $\gamma \sim 1.93 - 9.21$, about 23–37% higher.

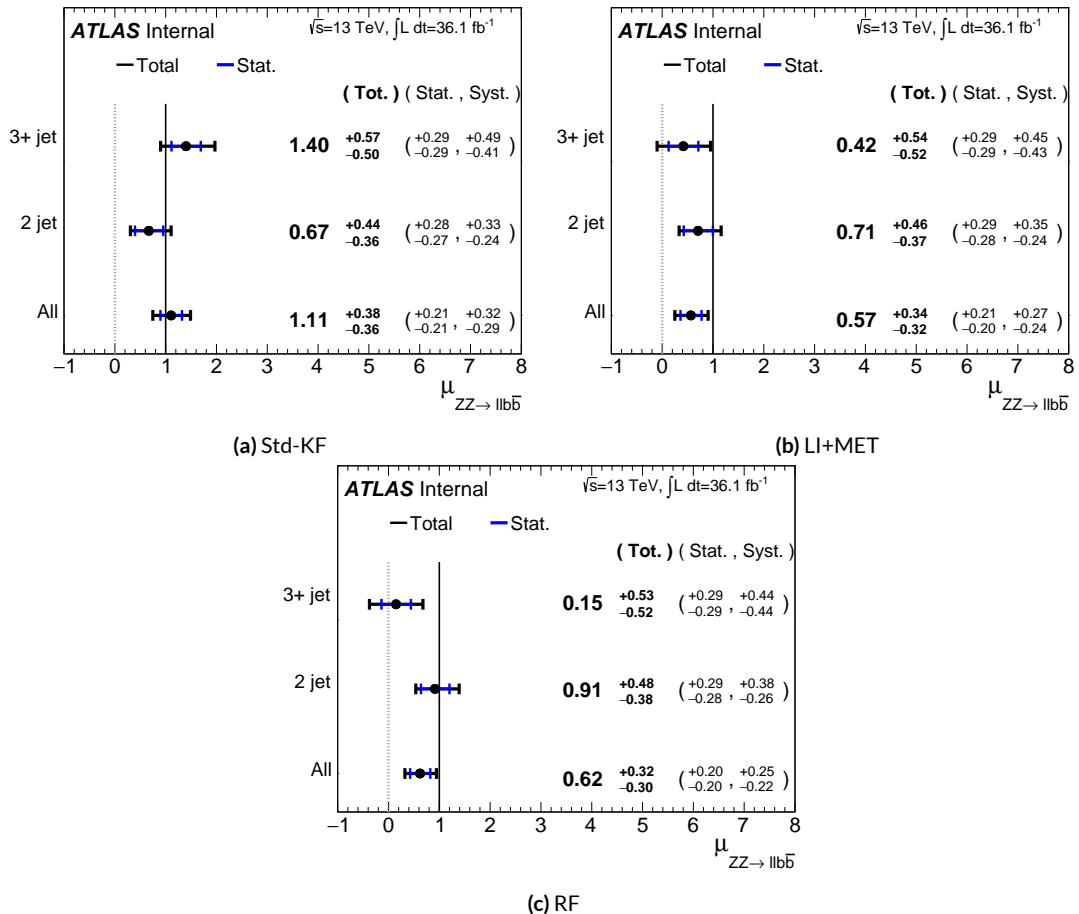


Figure 7.3: $\hat{\mu}$ summary plots with standalone fits for the different n_{jet} regions for the standard, LI, and RF variable sets.

If either the LI or RF schemes were to be used in a mainstream analysis, these validation fits suggest that the third jet ought to be included in variable schemes (e.g. by adding the third jet to the

1700 Higgs in the high p_T^V case). On the issue of whether or not ≥ 4 jet events should be included, the
1701 RF set shows very little sensitivity to this change (a 2 jet and 3 jet only fit moves $\hat{\mu}$ to 0.64, while
1702 doing so for the LI set moves it to 0.40), so this, like the addition of the third jet into the variable
1703 sets, would have to be addressed individually. Nevertheless, this optimization is beyond the scope of
1704 this thesis, which aims to preserve as much of the fiducial analysis as possible for as straightforward a
1705 comparison as possible.

1706 For completeness, we include the full set of fit validation results for the VZ fit, explaining them in
1707 turn.

1708 7.5 NUISANCE PARAMETER PULLS

1709 The first set of plots statistical fit experts will want to look at are the “pulls” and “pull comparisons.”
1710 In these plots, the best fit (nominal) values and one standard deviation error bars are shown for ob-
1711 served (Asimov) pull plots, with the green and yellow bands corresponding to $\pm 1, 2\sigma$, respectively.
1712 These plots are divided by NP category for readability. [¶] In pull comparisons, these pulls are over-
1713 layed and color-coded. Pull comparisons here have the following color code: black is the standard
1714 variable set, red is the LI set, and blue is the RF set.

1715 A well-behaved fit has pulls close to nominal values (“closeness” should be interpreted in the
1716 context of pull value divided by pull error). As can be seen in Figures 7.4–7.8, the fits for the three
1717 different variable sets are fairly similar from a NP pull perspective, though the $Z+{\rm jets}$ m_{bb} and p_T^V

1718 [¶]Over 100 non-MC stat NP’s survive pruning in these 2-lepton only Run 2 fits; well over 500 survive in the Run 1+Run 2 combined fit.

1718 NP's and the jet energy resolution NP are heavily pulled (a handful of poorly behaved pulls is not
 1719 uncommon, though typically warrants further investigation). As a general note, these pull plots cal-
 1720 culate pulls using a simultaneous HESSE matrix inversion, which is fine for relatively small fits, but
 1721 the more reliable MINOS result, which calculates the impact of each NP on its own, should be cross-
 1722 checked for significant pulls**. The ranking plots below do this.

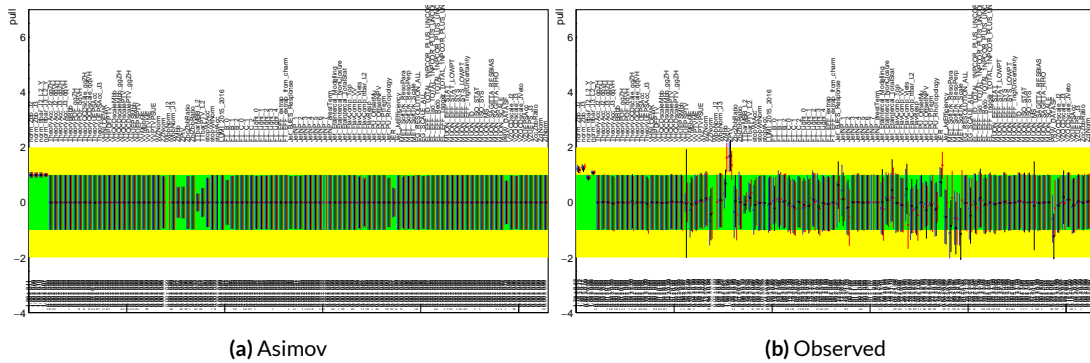


Figure 7.4: Pull comparison for all NP's but MC stats.

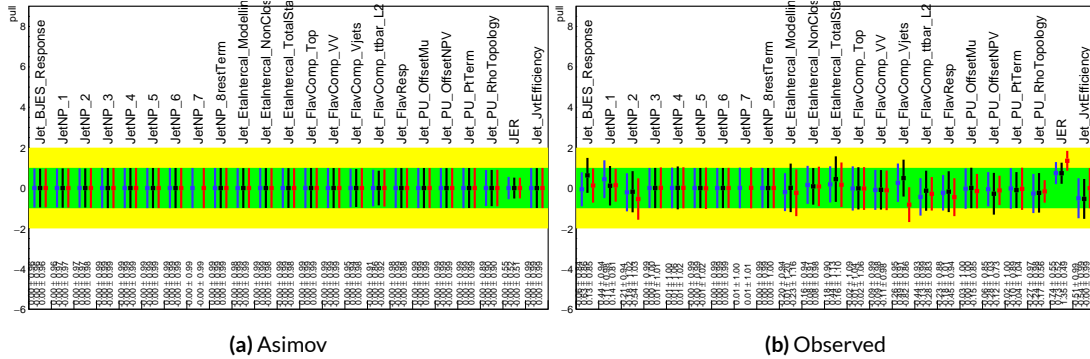


Figure 7.5: Pull comparison for jet NP's.

1723 Nuisance parameter correlation matrices (for correlations with magnitude at least 0.25) for all
 1724 three variable set fits can be found in Figures 7.10–7.12. These are useful for seeing which NP's move

**This becomes more of an issue for very large fits, like the full Run 1 + Run 2 combined fits in Chapter 9.

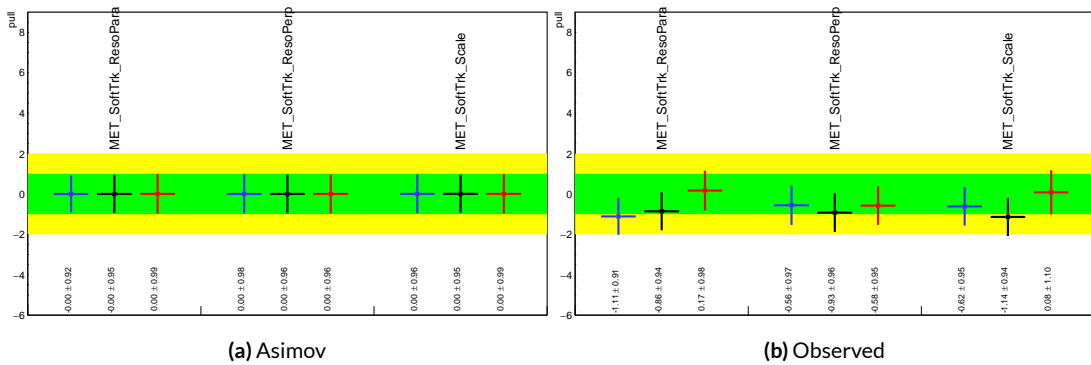


Figure 7.6: Pull comparison for MET NP's.

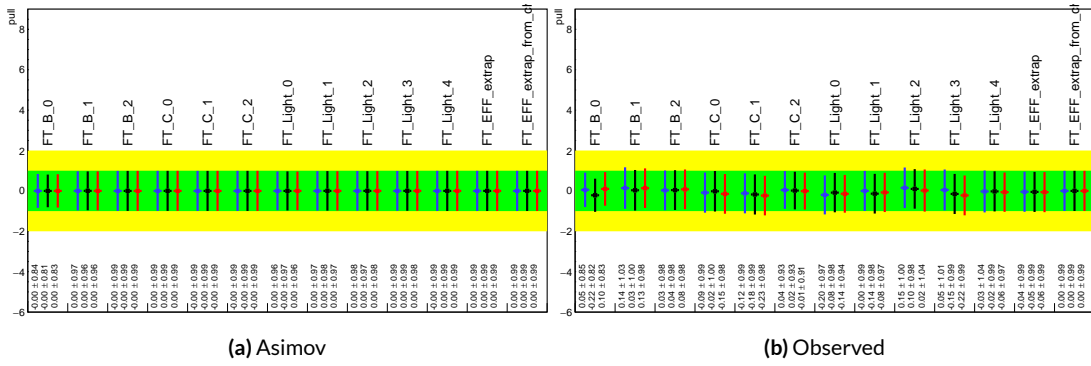


Figure 7.7: Pull comparison for Flavour Tagging NP's.

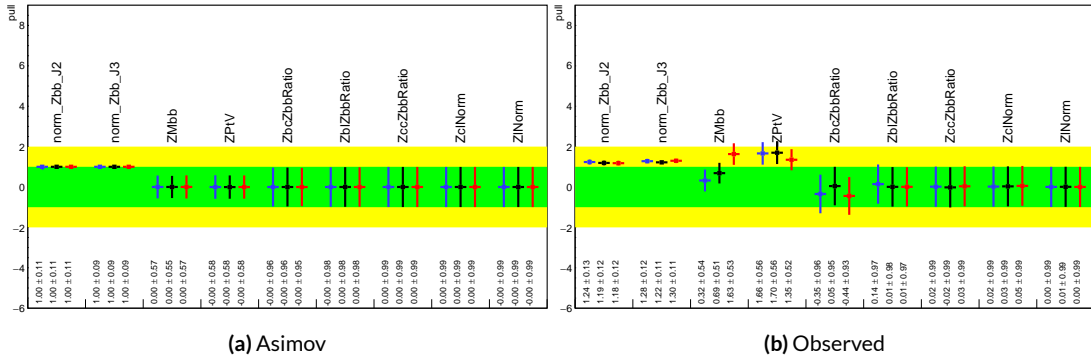


Figure 7.8: Pull comparison for Z +jets NP's.

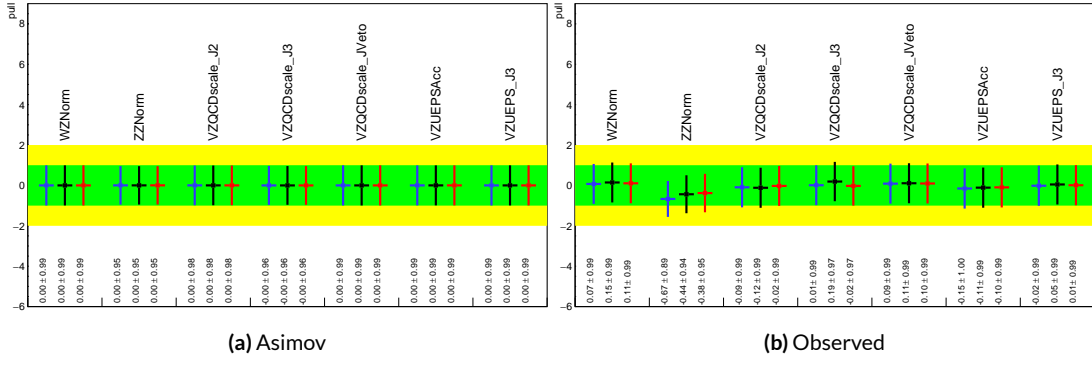


Figure 7.9: Pull comparison for signal process modeling NP's.

1725 together (if there is no physical argument for them to do so, this is a potential indicator that further

1726 investigation is warranted).

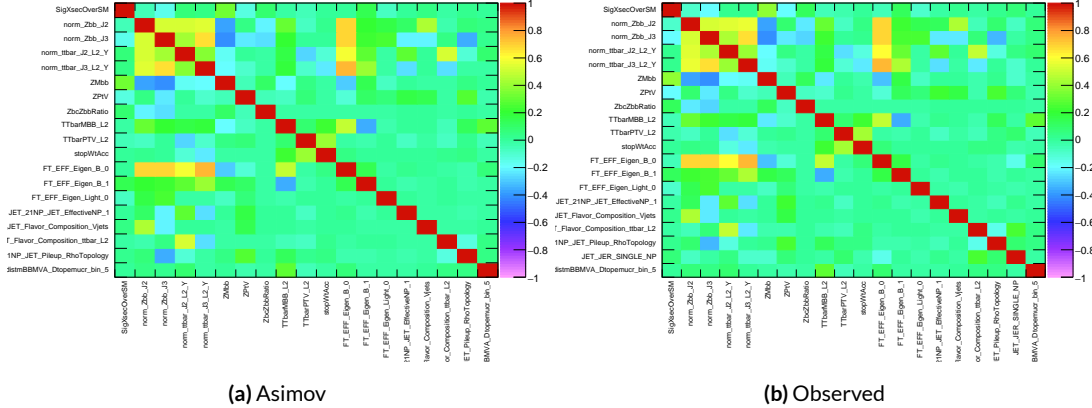


Figure 7.10: NP correlations for standard variable fits.

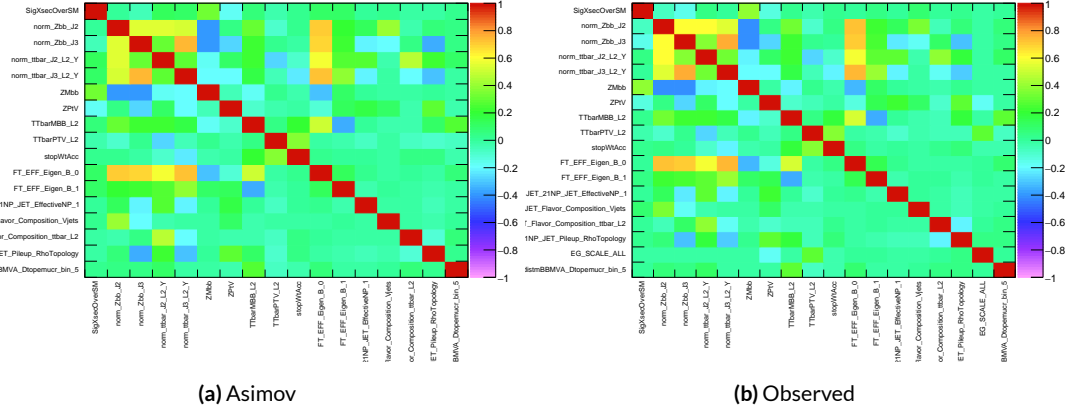


Figure 7.11: NP correlations for LI variable fits.

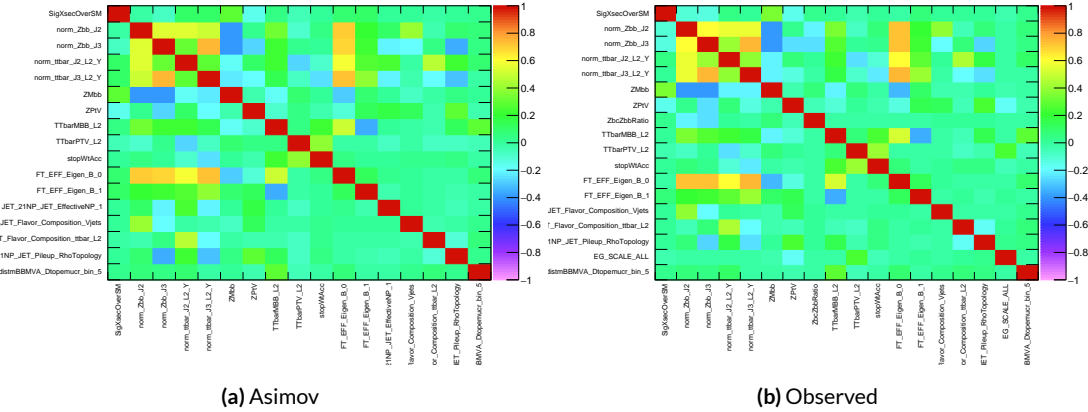


Figure 7.12: NP correlations for RF variable fits.

1727 7.5.1 NUISANCE PARAMETER RANKING PLOTS AND BREAKDOWNS

1728 The next set of fit results that is used to diagnose the quality of a fit is the impact of different nui-
 1729 sance parameters on the total error on μ , both individually and as categories. Figure 7.13 shows the
 1730 top 25 nuisance parameters ranked by their postfit impact on $\hat{\mu}$; these plots use the aforementioned,
 1731 more reliable MINOS approach. This set of rankings is fairly similar, with $Z+jets$ systematics being
 1732 particularly prominent. The advantage of seeing individual nuisance parameter rankings, as op-
 1733 posed to impacts of categories in aggregate, is that particularly pathological NP's are easier to see;
 1734 in particular, jet energy resolution and $Z+jets p_T^V$ systematic from the pull comparison plots show
 up with high rankings. Yellow bands are pre-fit impact on μ .

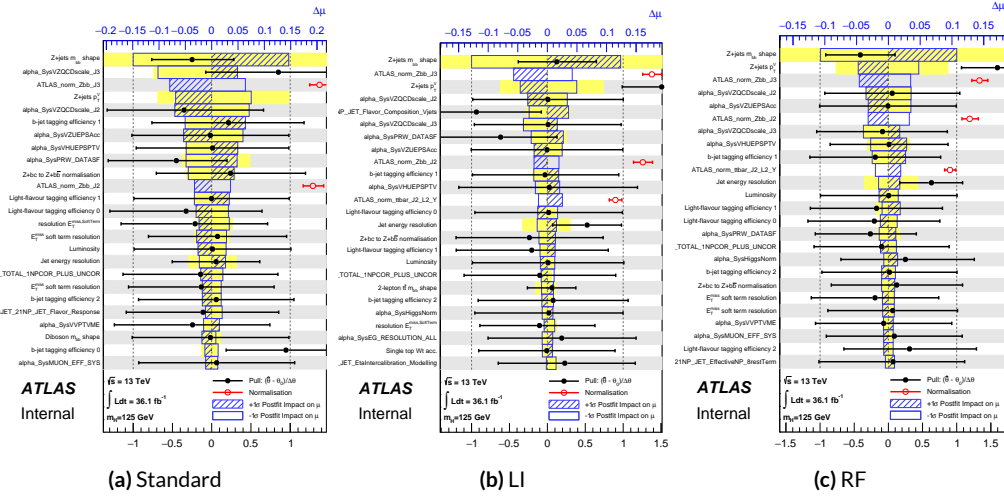


Figure 7.13: Plots for the top 25 nuisance parameters according to their postfit impact on $\hat{\mu}$ for the standard (a), LI (b), and RF (c) variable sets.

1735

1736 This is consistent with the picture of NP's taken in aggregate categories in Tables 7.5 and 7.6,
 1737 known as “breakdowns,” with $Z+jets$ in particular featuring prominently. Of particular interest

¹⁷³⁸ is also the lower impact of MC stats in the observed fit.

	Std-KF	LI+MET	RF
Total	+0.305 / -0.277	+0.324 / -0.292	+0.319 / -0.288
DataStat	+0.183 / -0.179	+0.190 / -0.186	+0.188 / -0.184
FullSyst	+0.244 / -0.212	+0.262 / -0.226	+0.258 / -0.221
Floating normalizations	+0.092 / -0.084	+0.098 / -0.079	+0.094 / -0.076
All normalizations	+0.093 / -0.084	+0.098 / -0.079	+0.094 / -0.076
All but normalizations	+0.214 / -0.179	+0.229 / -0.188	+0.224 / -0.182
Jets, MET	+0.052 / -0.043	+0.041 / -0.034	+0.047 / -0.037
Jets	+0.034 / -0.029	+0.033 / -0.028	+0.032 / -0.026
MET	+0.035 / -0.027	+0.015 / -0.012	+0.020 / -0.016
BTag	+0.064 / -0.051	+0.063 / -0.031	+0.059 / -0.032
BTag b	+0.053 / -0.041	+0.061 / -0.028	+0.055 / -0.025
BTag c	+0.011 / -0.010	+0.006 / -0.005	+0.007 / -0.006
BTag light	+0.030 / -0.027	+0.016 / -0.013	+0.022 / -0.019
Leptons	+0.021 / -0.012	+0.022 / -0.014	+0.023 / -0.014
Luminosity	+0.039 / -0.022	+0.039 / -0.022	+0.040 / -0.022
Diboson	+0.049 / -0.028	+0.047 / -0.026	+0.047 / -0.026
Model Zjets	+0.106 / -0.105	+0.113 / -0.110	+0.102 / -0.099
Zjets flt. norm.	+0.039 / -0.053	+0.024 / -0.029	+0.021 / -0.031
Model Wjets	+0.000 / -0.000	+0.000 / -0.000	+0.000 / -0.000
Wjets flt. norm.	+0.000 / -0.000	+0.000 / -0.000	+0.000 / -0.000
Model ttbar	+0.015 / -0.013	+0.032 / -0.017	+0.030 / -0.016
Model Single Top	+0.004 / -0.003	+0.009 / -0.008	+0.005 / -0.004
Model Multi Jet	+0.000 / -0.000	+0.000 / -0.000	+0.000 / -0.000
Signal Systematics	+0.003 / -0.003	+0.003 / -0.003	+0.003 / -0.003
MC stat	+0.097 / -0.094	+0.108 / -0.103	+0.107 / -0.104

Table 7.5: Summary of impact of various nuisance parameter categories on the error on μ for Asimov fits for the standard, LI, and RF variable sets.

	Std-KF	LI+MET	RF
$\hat{\mu}$	1.1079	0.5651	0.6218
Total	+0.381 / -0.360	+0.339 / -0.316	+0.322 / -0.299
DataStat	+0.214 / -0.211	+0.210 / -0.205	+0.201 / -0.197
FullSyst	+0.315 / -0.292	+0.267 / -0.241	+0.252 / -0.225
Floating normalizations	+0.120 / -0.122	+0.095 / -0.089	+0.082 / -0.079
All normalizations	+0.121 / -0.123	+0.095 / -0.090	+0.082 / -0.079
All but normalizations	+0.279 / -0.254	+0.228 / -0.200	+0.213 / -0.184
Jets, MET	+0.076 / -0.065	+0.045 / -0.043	+0.038 / -0.033
Jets	+0.047 / -0.040	+0.044 / -0.041	+0.027 / -0.024
MET	+0.055 / -0.046	+0.015 / -0.015	+0.012 / -0.010
BTag	+0.083 / -0.079	+0.041 / -0.031	+0.041 / -0.035
BTag b	+0.063 / -0.059	+0.032 / -0.022	+0.031 / -0.026
BTag c	+0.018 / -0.017	+0.008 / -0.007	+0.010 / -0.009
BTag light	+0.051 / -0.046	+0.024 / -0.021	+0.025 / -0.022
Leptons	+0.022 / -0.011	+0.015 / -0.008	+0.019 / -0.008
Luminosity	+0.044 / -0.022	+0.026 / -0.006	+0.027 / -0.008
Diboson	+0.049 / -0.026	+0.025 / -0.013	+0.027 / -0.017
Model Zjets	+0.156 / -0.162	+0.133 / -0.133	+0.115 / -0.117
Zjets flt. norm.	+0.061 / -0.089	+0.041 / -0.064	+0.028 / -0.056
Model Wjets	+0.000 / -0.001	+0.000 / -0.001	+0.000 / -0.001
Wjets flt. norm.	+0.000 / -0.001	+0.000 / -0.001	+0.000 / -0.001
Model ttbar	+0.015 / -0.024	+0.018 / -0.005	+0.017 / -0.009
Model Single Top	+0.005 / -0.003	+0.010 / -0.008	+0.007 / -0.004
Model Multi Jet	+0.000 / -0.001	+0.000 / -0.001	+0.000 / -0.001
Signal Systematics	+0.005 / -0.004	+0.009 / -0.006	+0.005 / -0.006
MC stat	+0.140 / -0.143	+0.132 / -0.131	+0.128 / -0.129

Table 7.6: Summary of impact of various nuisance parameter categories on the error on $\hat{\mu}$ for observed fits for the standard, LI, and RF variable sets.

1739 7.6 POSTFIT DISTRIBUTIONS

1740 Finally, postfit distributions for the MVA discriminant (m_{bb}) distribution in the signal (top $e - \mu$
1741 control) region for the standard, Lorentz Invariant, and RestFrames variable sets are shown. It is
1742 generally considered good practice to check the actual postfit distributions of discriminating quan-
1743 tities used to make sure there is good agreement. ^{††} It should be noted that agreement is not always
1744 great when “eyeballing” a distribution, as fits are messy and $V+hf$ modeling is notoriously hard.
1745 This is particularly true in the VZ fit since normalizations for $Z+hf$ in particular are derived using
1746 VH optimized sidebands. This is also why a lot of these plots are presented as log plots (which hide
1747 disagreement better; the general argument goes that one has the ratio plots on the bottom and log
1748 plots allow one to see rare backgrounds in plots).

^{††}Sometimes distributions of input variables (MC histograms scaled by their postfit normalizations) are also used.

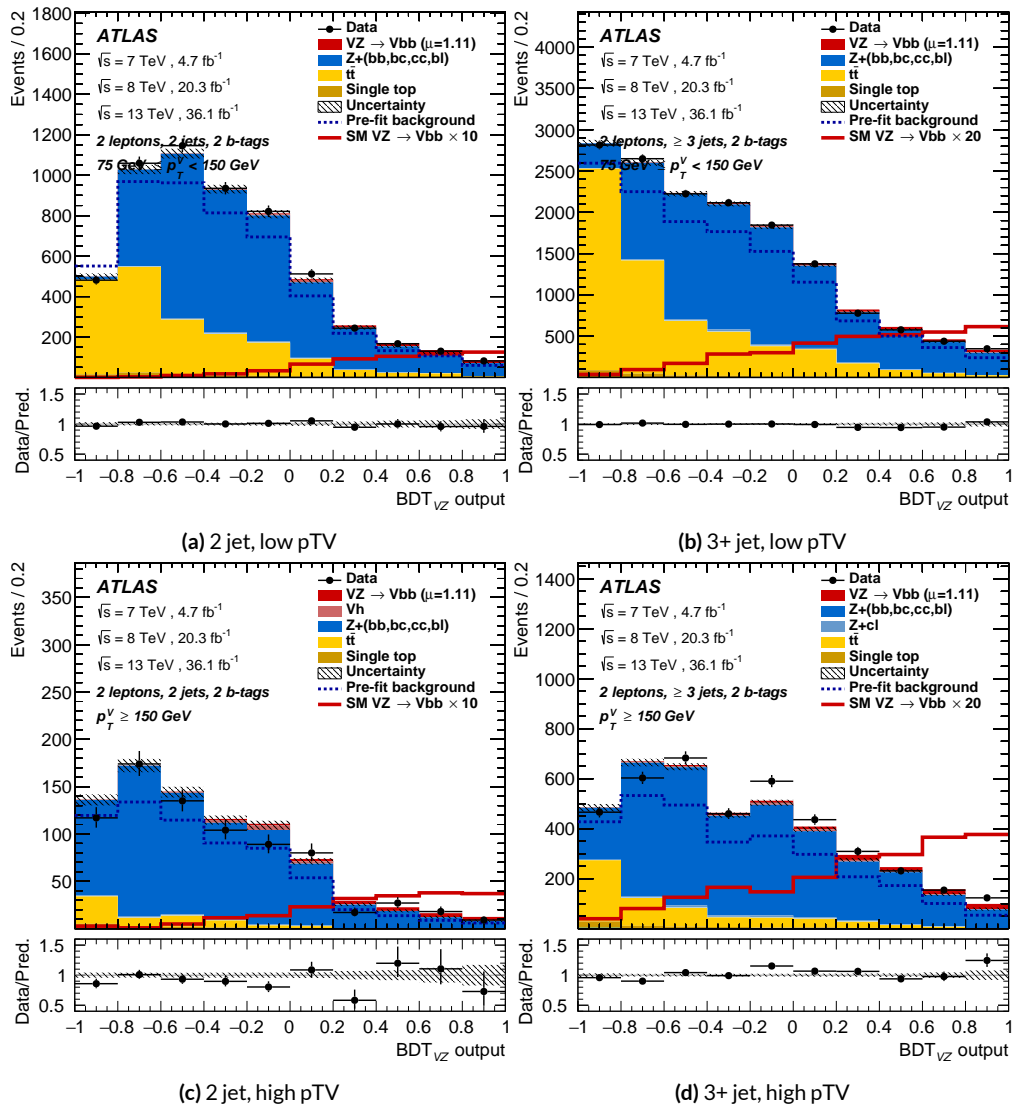


Figure 7.14: Postfit BDT_{VZ} plots in the signal region for the standard variable set.

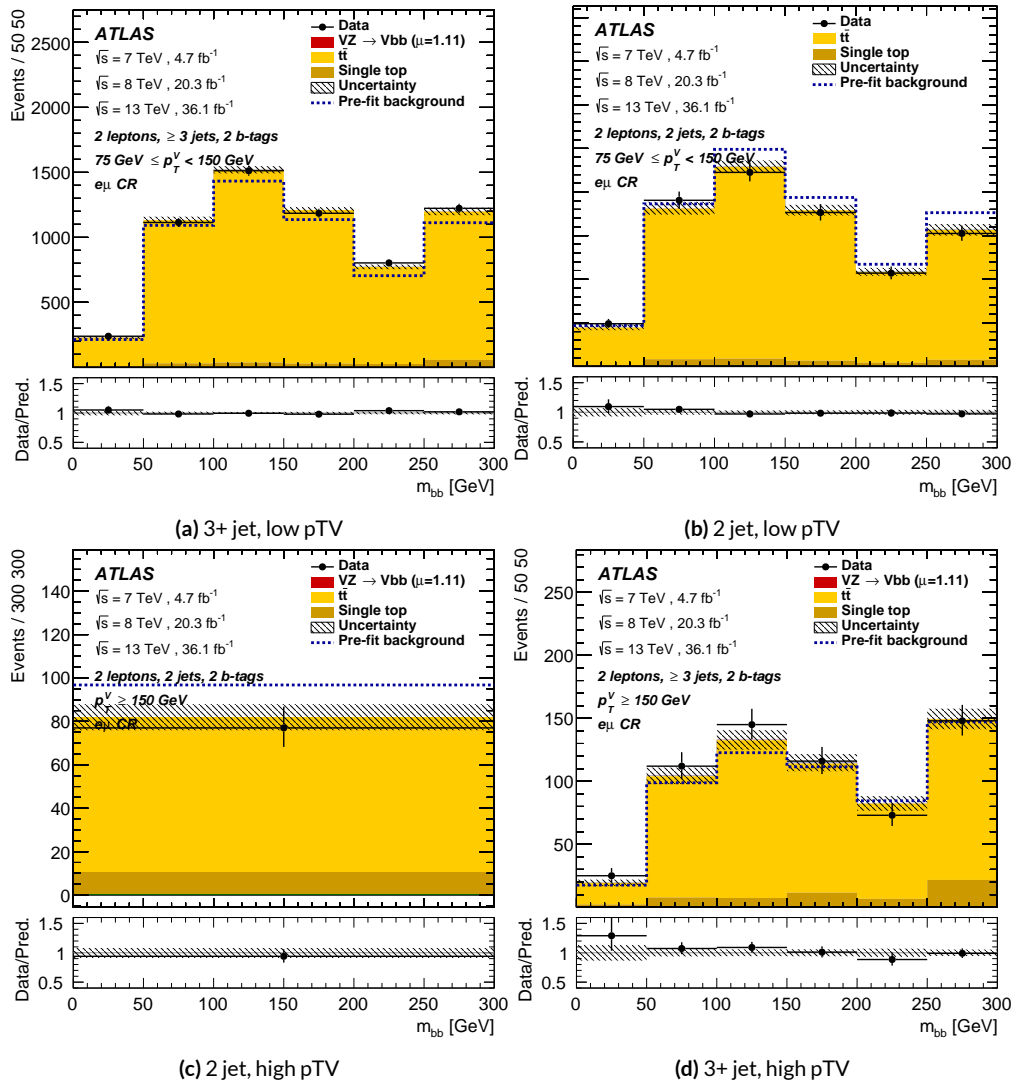


Figure 7.15: Postfit m_{bb} plots in the top $e - \mu$ CR for the standard variable set.

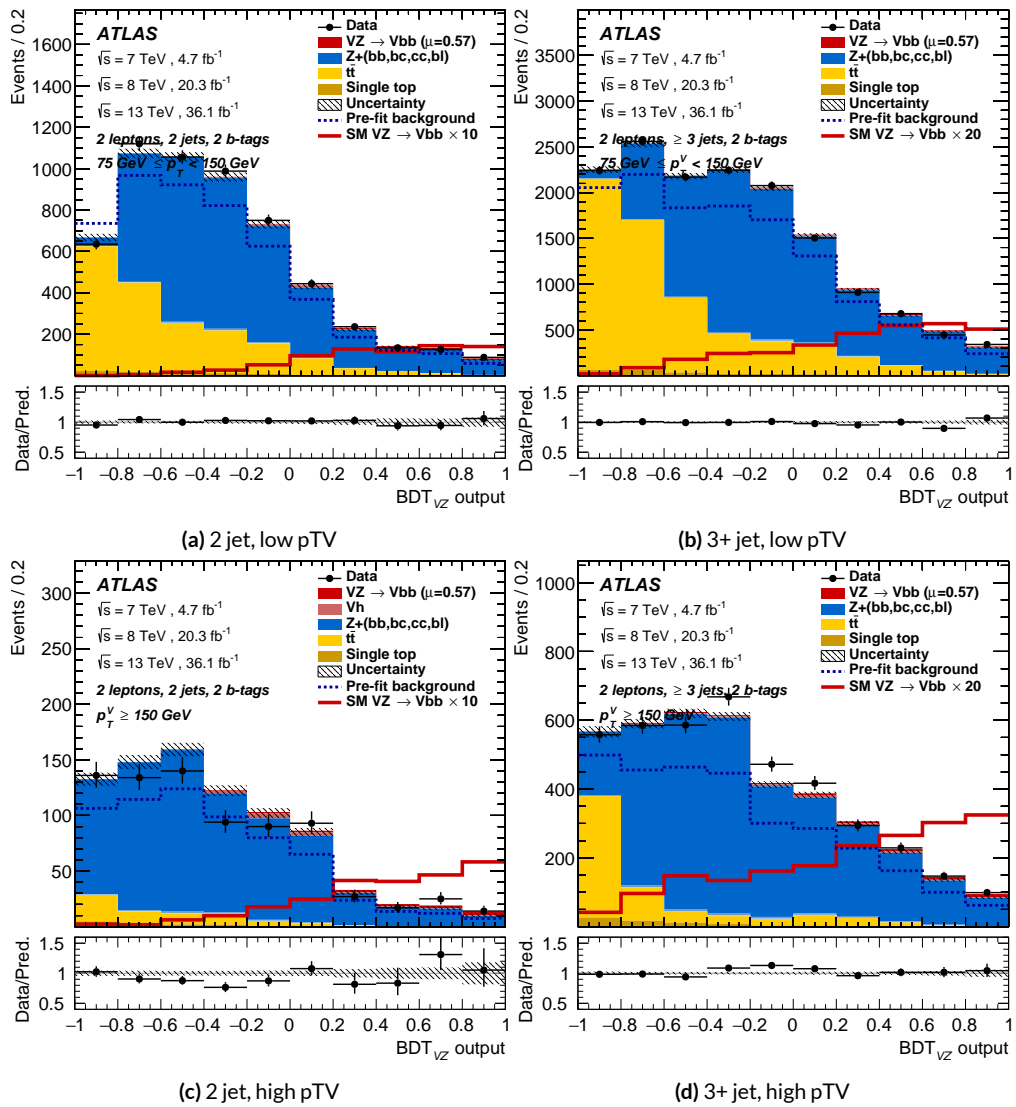


Figure 7.16: Postfit BDT_{VZ} plots in the signal region for the LI variable set.

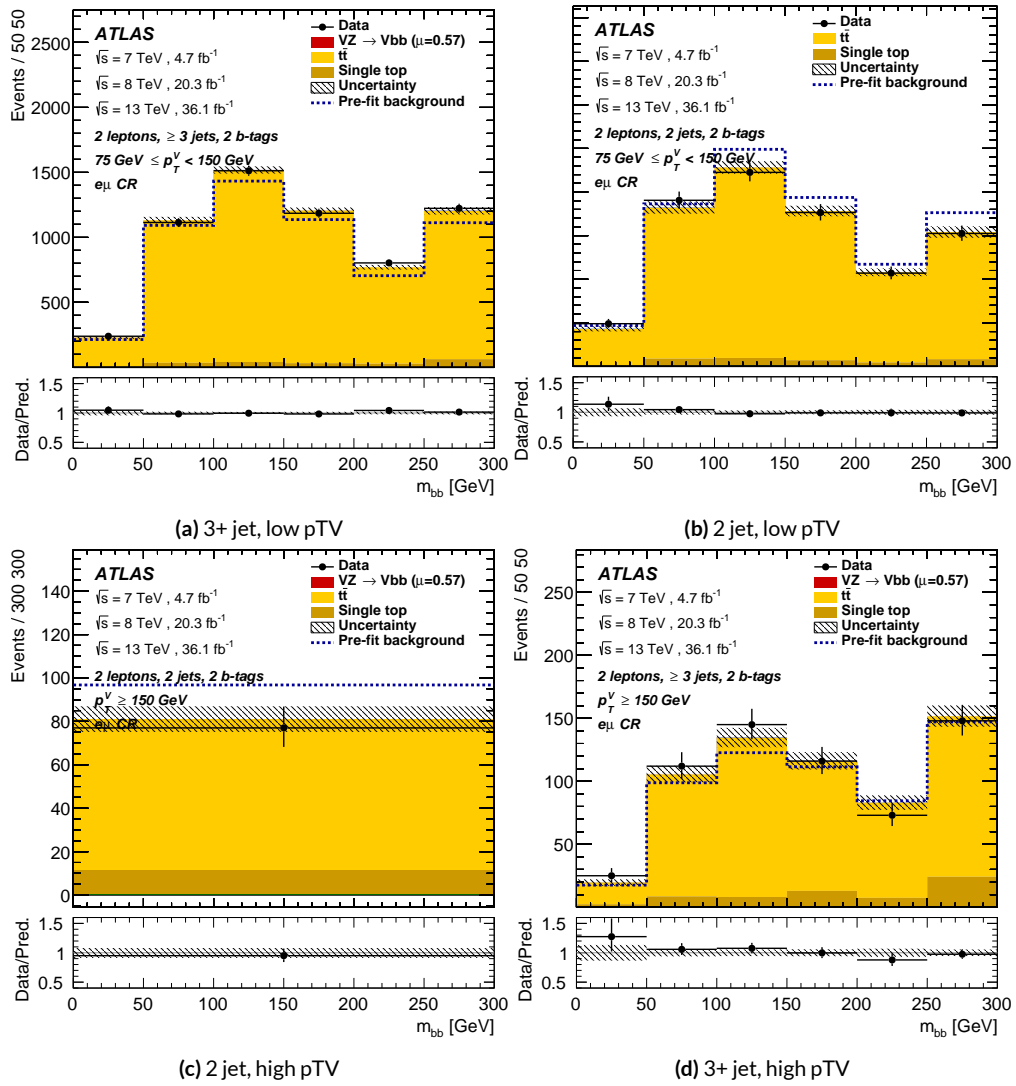


Figure 7.17: Postfit m_{bb} plots in the top $e - \mu$ CR for the LI variable set.

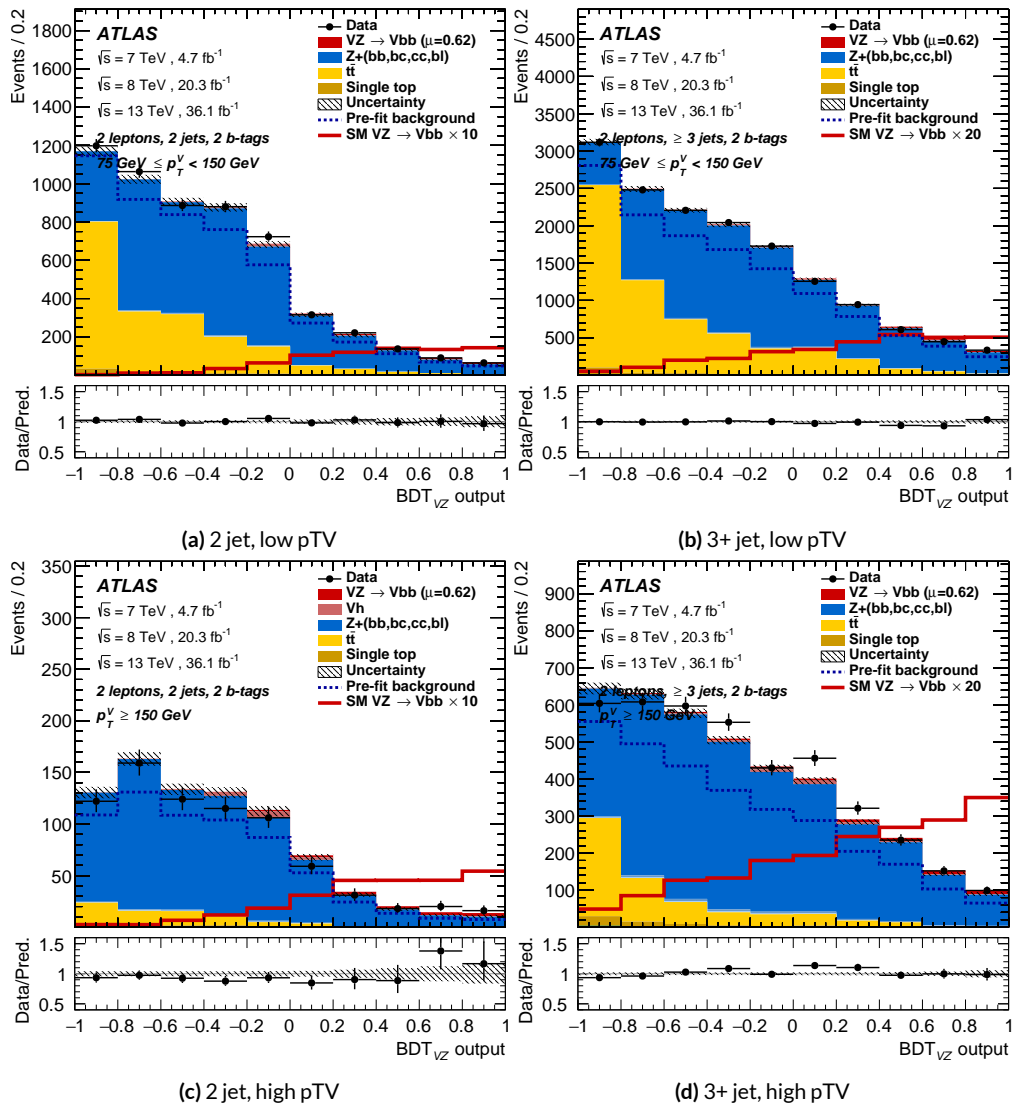


Figure 7.18: Postfit BDT_{VZ} plots in the signal region for the RF variable set.

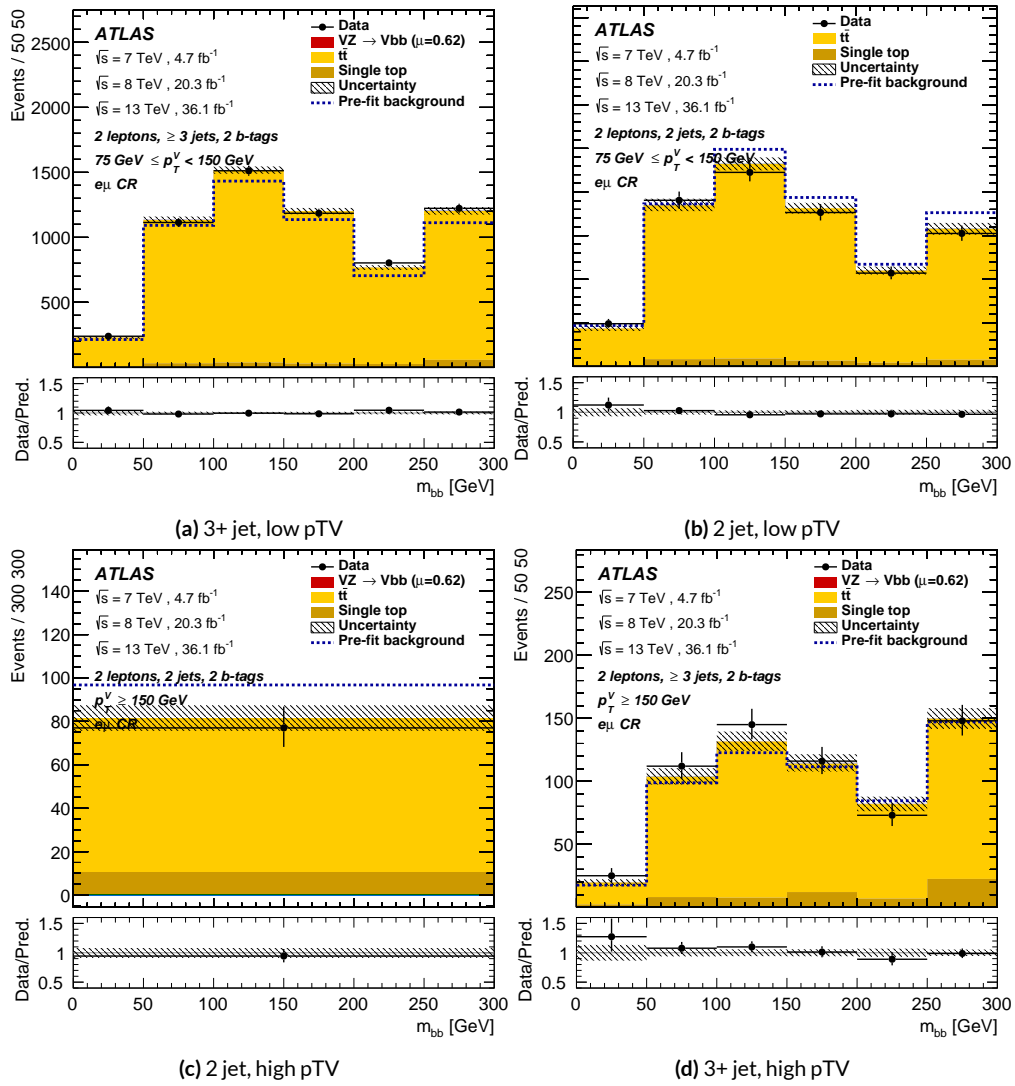


Figure 7.19: Postfit m_{bb} plots in the top $e - \mu$ CR for the RF variable set.

1749 7.7 VH FIT MODEL VALIDATION

We now move onto the fit validation distributions and numbers for the VH fit of interest.

1751 7.7.1 NUISANCE PARAMETER PULLS

As can be seen in Figures 7.20–7.24, the fits for the three different variable sets are fairly similar from a NP pull perspective. Again, black is the standard variable set, red is the LI set, and blue is the RF set. The possible exception is the signal UE+PS p_T^V systematic, which looks very different for all three cases (underconstrained for the standard, but overconstrained for the novel variable cases), though this difference goes away in the ranking plot, meaning this is almost certainly an unphysical artifice of the faster HESSE inversion used to produce the pull comparison plots.

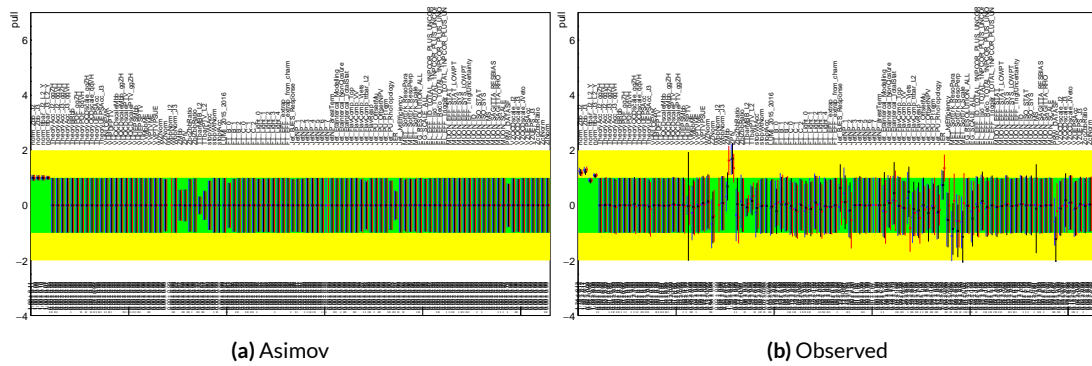


Figure 7.20: Pull comparison for all NP's but MC stats.

1758 Nuisance parameter correlation matrices (for correlations with magnitude at least 0.25) for all
1759 three variable set fits can be found in Figures 7.26–7.28.

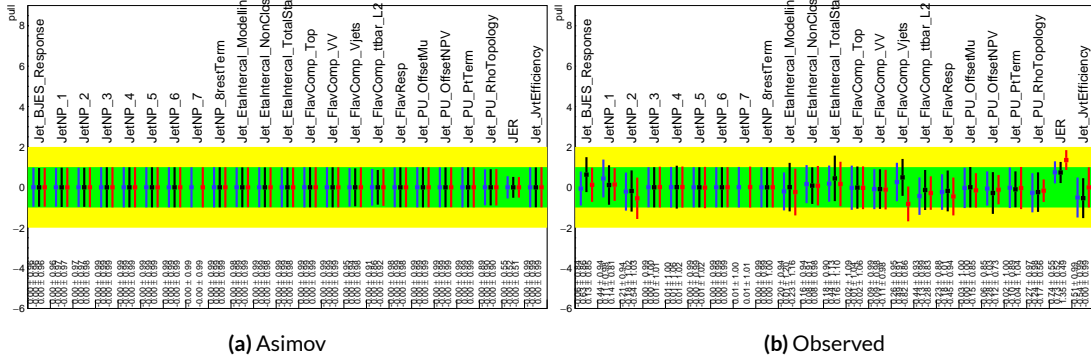


Figure 7.21: Pull comparison for jet NP's.

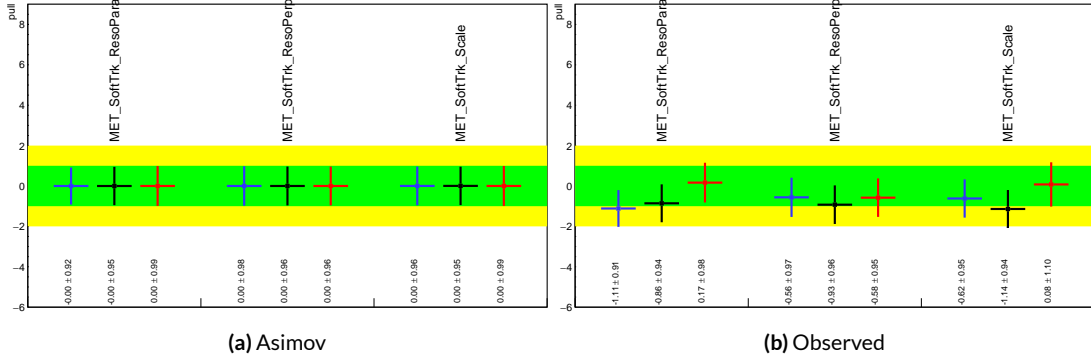


Figure 7.22: Pull comparison for MET NP's.

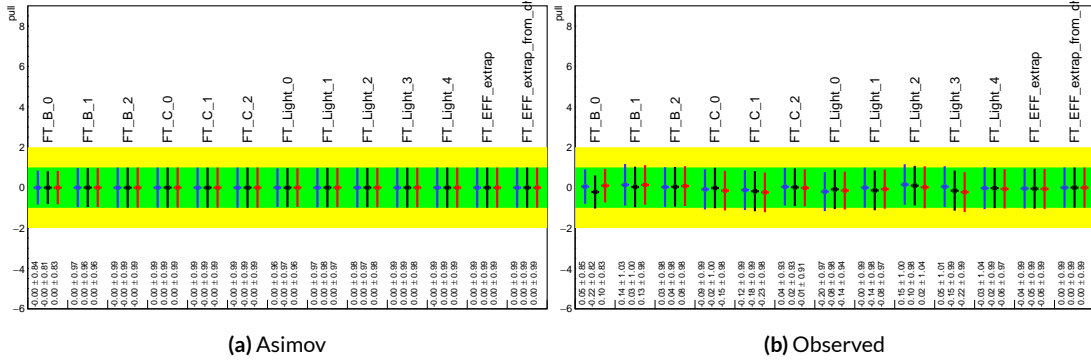


Figure 7.23: Pull comparison for Flavour Tagging NP's.

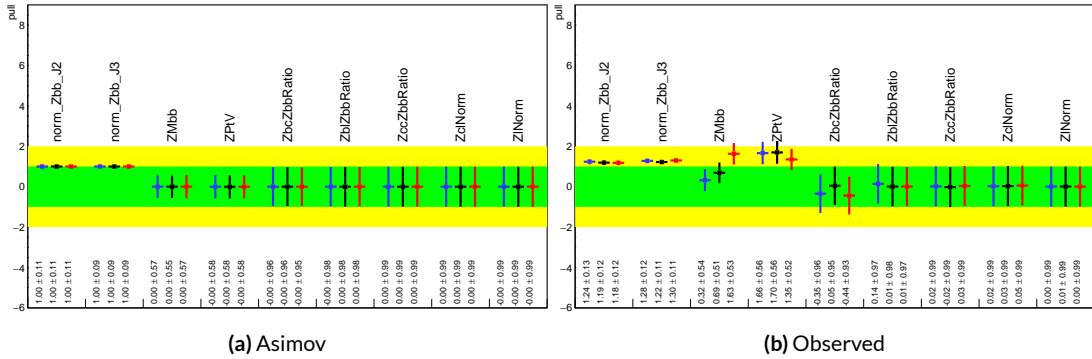


Figure 7.24: Pull comparison for $Z + \text{jets}$ NP's.

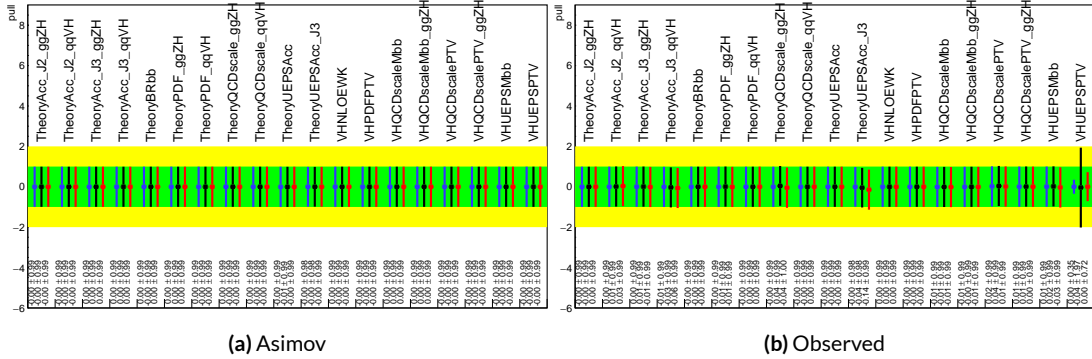


Figure 7.25: Pull comparison for signal process modeling NP's.

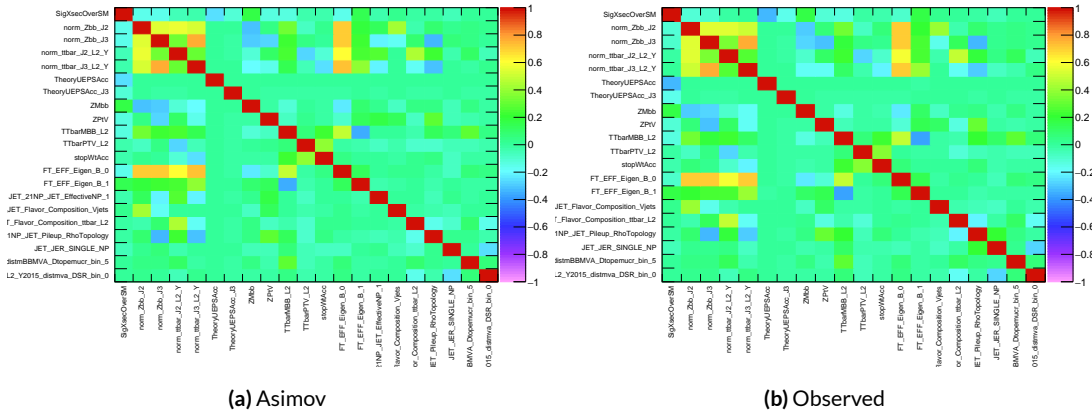


Figure 7.26: NP correlations for standard variable fits.

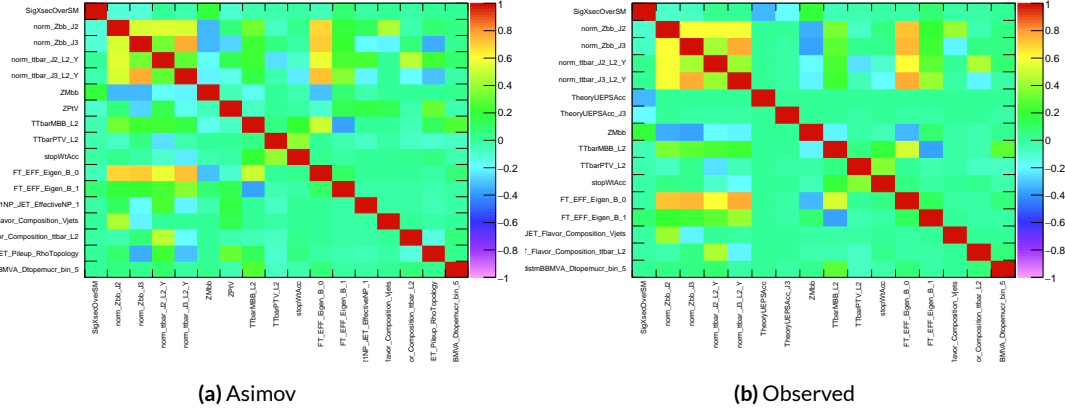


Figure 7.27: NP correlations for LI variable fits.

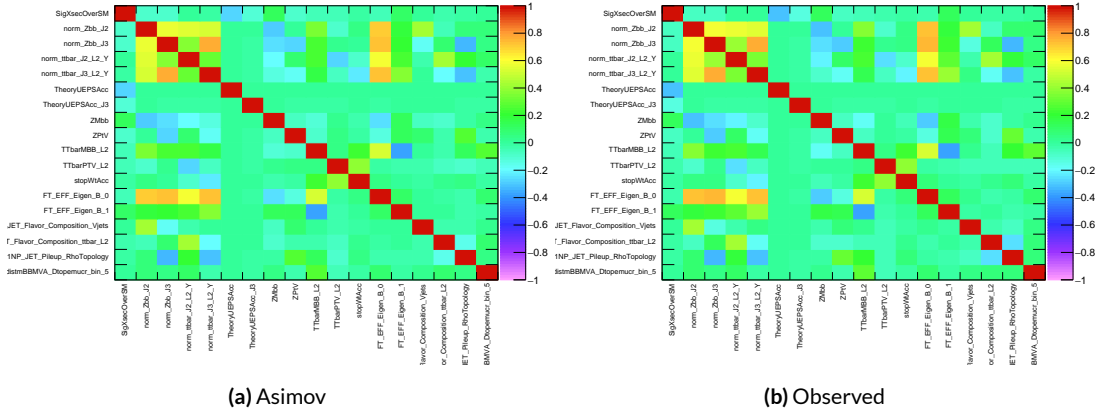


Figure 7.28: NP correlations for RF variable fits.

1760 7.7.2 FULL BREAKDOWN OF ERRORS

1761 A postfit ranking of nuisance parameters according to their impact on $\hat{\mu}$ for the different variable
 1762 sets may be found in Figure 7.29, with rankings being fairly similar. In particular, the signal UE+PS
 1763 p_T^V systematic is top-ranked for all three variable sets and also looks very similar, unlike in the pull
 1764 comparison plot, reiterating the importance of evaluating individually the impact of highly ranked
 1765 NP's. The $Z+jets p_T^V$ is highly pulled in all three cases, though this is less severe for the non-standard
 1766 set (it is off the scale for the standard variable ranking). The RF discriminant mitigates the effect of
 1767 poorly modeled jet energy resolution better than the other sets.

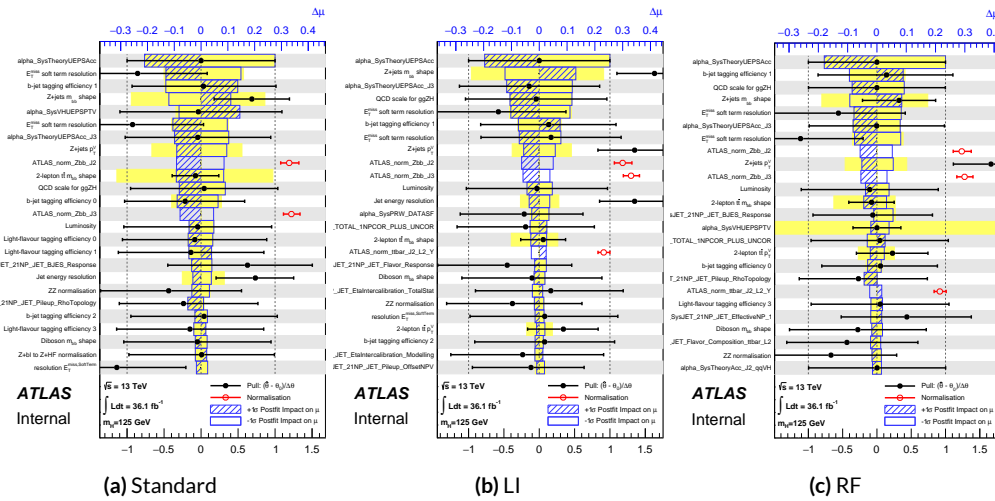


Figure 7.29: Plots for the top 25 nuisance parameters according to their postfit impact on $\hat{\mu}$ for the standard (a), LI (b), and RF (c) variable sets.

1768 The Asimov (Table 7.7) and observed (Table 7.8) breakdowns both consistently suggest that the
 1769 LI variable set does a better job of constraining systematic uncertainties than the standard set and
 1770 that the RF set does better still. It is also not surprising that the gain is more substantial in the ob-

¹⁷⁷¹ served fit than in the Asimov fits, as in the latter there are the “penalty” terms from pulls in addition
¹⁷⁷² to the overall broadening in the likelihood.

	Std-KF	LI+MET	RF
Total	+0.608 / -0.511	+0.632 / -0.539	+0.600 / -0.494
DataStat	+0.420 / -0.401	+0.453 / -0.434	+0.424 / -0.404
FullSyst	+0.440 / -0.318	+0.441 / -0.319	+0.425 / -0.284
Floating normalizations	+0.122 / -0.125	+0.110 / -0.111	+0.093 / -0.089
All normalizations	+0.128 / -0.129	+0.112 / -0.112	+0.099 / -0.092
All but normalizations	+0.403 / -0.274	+0.387 / -0.250	+0.382 / -0.227
Jets, MET	+0.180 / -0.097	+0.146 / -0.079	+0.122 / -0.083
Jets	+0.051 / -0.030	+0.044 / -0.035	+0.025 / -0.042
MET	+0.173 / -0.091	+0.140 / -0.074	+0.117 / -0.063
BTag	+0.138 / -0.136	+0.069 / -0.071	+0.076 / -0.078
BTag b	+0.125 / -0.125	+0.067 / -0.070	+0.073 / -0.075
BTag c	+0.018 / -0.016	+0.004 / -0.004	+0.005 / -0.005
BTag light	+0.057 / -0.051	+0.020 / -0.014	+0.009 / -0.018
Leptons	+0.013 / -0.012	+0.029 / -0.026	+0.012 / -0.023
Luminosity	+0.052 / -0.020	+0.050 / -0.016	+0.050 / -0.019
Diboson	+0.043 / -0.039	+0.035 / -0.031	+0.038 / -0.029
Model Zjets	+0.119 / -0.117	+0.124 / -0.127	+0.095 / -0.086
Zjets flt. norm.	+0.080 / -0.106	+0.052 / -0.092	+0.026 / -0.072
Model Wjets	+0.001 / -0.001	+0.001 / -0.001	+0.000 / -0.001
Wjets flt. norm.	+0.000 / -0.000	+0.000 / -0.000	+0.000 / -0.000
Model ttbar	+0.076 / -0.080	+0.025 / -0.035	+0.025 / -0.040
Model Single Top	+0.015 / -0.015	+0.002 / -0.004	+0.021 / -0.007
Model Multi Jet	+0.000 / -0.000	+0.000 / -0.000	+0.000 / -0.000
Signal Systematics	+0.262 / -0.087	+0.272 / -0.082	+0.290 / -0.088
MC stat	+0.149 / -0.136	+0.168 / -0.154	+0.153 / -0.136

Table 7.7: Expected error breakdowns for the standard, LI, and RF variable sets

	Std-KF	LI+MET	RF
$\hat{\mu}$	1.7458	1.6467	1.5019
Total	+0.811 / -0.662	+0.778 / -0.641	+0.731 / -0.612
DataStat	+0.502 / -0.484	+0.507 / -0.489	+0.500 / -0.481
FullSyst	+0.637 / -0.451	+0.591 / -0.415	+0.533 / -0.378
Floating normalizations	+0.153 / -0.143	+0.128 / -0.118	+0.110 / -0.109
All normalizations	+0.158 / -0.147	+0.130 / -0.119	+0.112 / -0.110
All but normalizations	+0.599 / -0.402	+0.544 / -0.354	+0.486 / -0.318
Jets, MET	+0.218 / -0.145	+0.198 / -0.113	+0.167 / -0.106
Jets	+0.071 / -0.059	+0.065 / -0.047	+0.036 / -0.051
MET	+0.209 / -0.130	+0.190 / -0.102	+0.152 / -0.077
BTAG	+0.162 / -0.166	+0.093 / -0.070	+0.115 / -0.099
BTAG b	+0.142 / -0.147	+0.090 / -0.066	+0.110 / -0.094
BTAG c	+0.022 / -0.021	+0.006 / -0.006	+0.007 / -0.007
BTAG light	+0.074 / -0.072	+0.025 / -0.022	+0.031 / -0.029
Leptons	+0.039 / -0.029	+0.035 / -0.031	+0.034 / -0.030
Luminosity	+0.079 / -0.039	+0.073 / -0.034	+0.069 / -0.032
Diboson	+0.047 / -0.043	+0.031 / -0.028	+0.029 / -0.028
Model Zjets	+0.164 / -0.152	+0.141 / -0.143	+0.101 / -0.105
Zjets flt. norm.	+0.070 / -0.109	+0.041 / -0.086	+0.033 / -0.083
Model Wjets	+0.001 / -0.001	+0.001 / -0.000	+0.001 / -0.001
Wjets flt. norm.	+0.000 / -0.000	+0.000 / -0.000	+0.000 / -0.000
Model ttbar	+0.067 / -0.102	+0.029 / -0.040	+0.040 / -0.048
Model Single Top	+0.015 / -0.020	+0.001 / -0.005	+0.004 / -0.006
Model Multi Jet	+0.000 / -0.000	+0.000 / -0.000	+0.000 / -0.000
Signal Systematics	+0.434 / -0.183	+0.418 / -0.190	+0.364 / -0.152
MC stat	+0.226 / -0.201	+0.221 / -0.200	+0.212 / -0.189

Table 7.8: Observed signal strengths, and error breakdowns for the standard, LI, and RF variable sets

1773 7.7.3 POSTFIT DISTRIBUTIONS AND S/B PLOTS

1774 Postfit distributions for the MVA discriminant (m_{bb}) distribution in the signal (top $e - \mu$ control)
1775 region for the standard, Lorentz Invariant, and RestFrames variable sets are found in Figures 7.30–
1776 7.35. Here, as in the VZ fit, agreement is reasonable. In a combined fit with all three channels, $Z+hf$
1777 normalizations in particular would be correlated across the 0- and 2-lepton channels, which might
1778 help to better constrain this mismodeling (and perhaps as a result some of the $Z+jets$ systematics as
1779 well).

1780 One final type of plot presented as a result is the binned $\log_{10} (S/B)$ in signal regions distribu-
1781 tions may be found in Figure 7.36. For these plots, one fills a histogram with the $\log_{10} (S/B)$ ratio in
1782 each postfit distribution bin weighted by the total number of events. In this case, a log plot is help-
1783 ful because the highest bins would be invisible on a linear plot. These distributions are allegedly use-
1784 ful for seeing where most of one's sensitivity lies. Practically, it is problematic if the pull (from the
1785 null hypothesis) is higher at lower S/B values, which may indicate a poorly optimized discriminant.

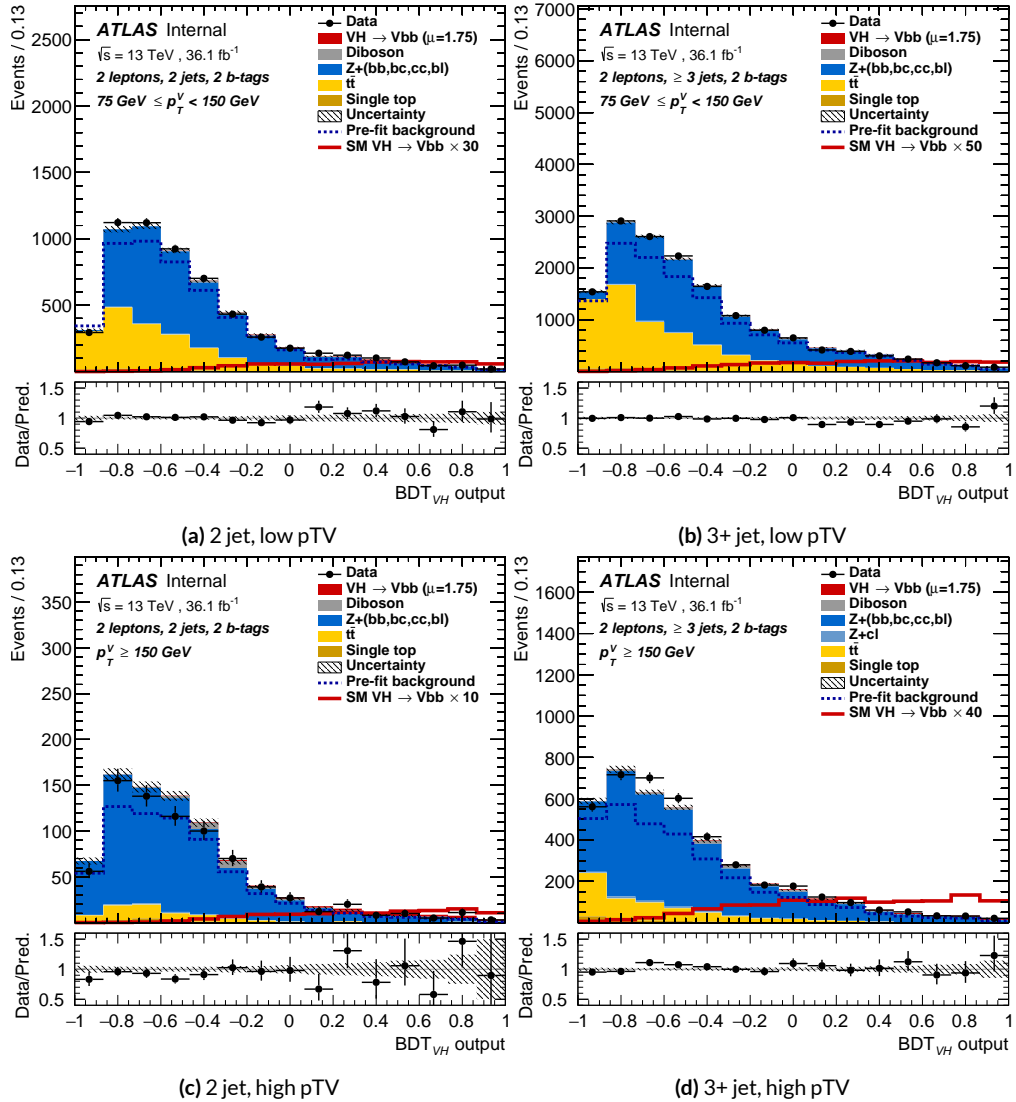


Figure 7.30: Postfit BDT_{VH} plots in the signal region for the standard variable set.

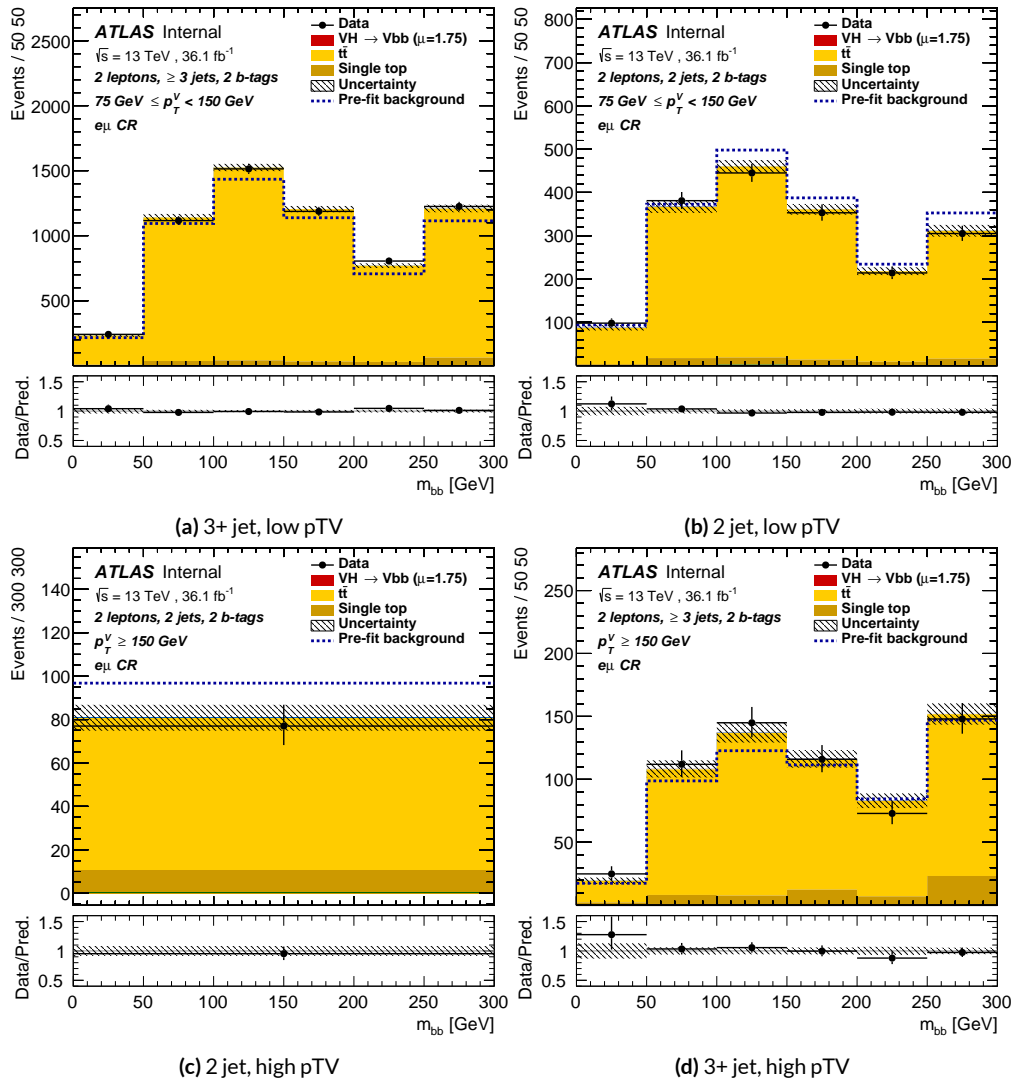


Figure 7.31: Postfit m_{bb} plots in the top $e - \mu$ CR for the standard variable set.

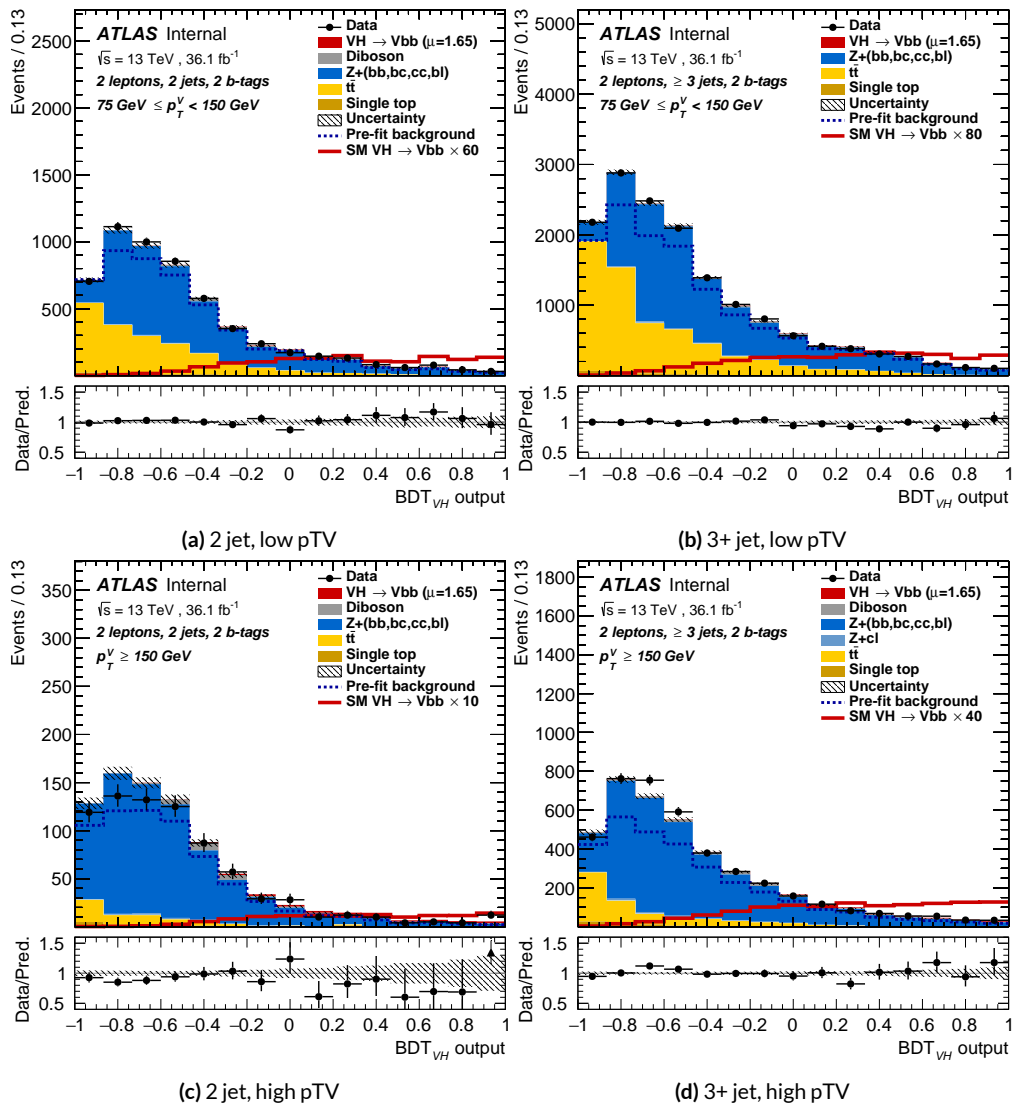


Figure 7.32: Postfit BDT_{VH} plots in the signal region for the LI variable set.

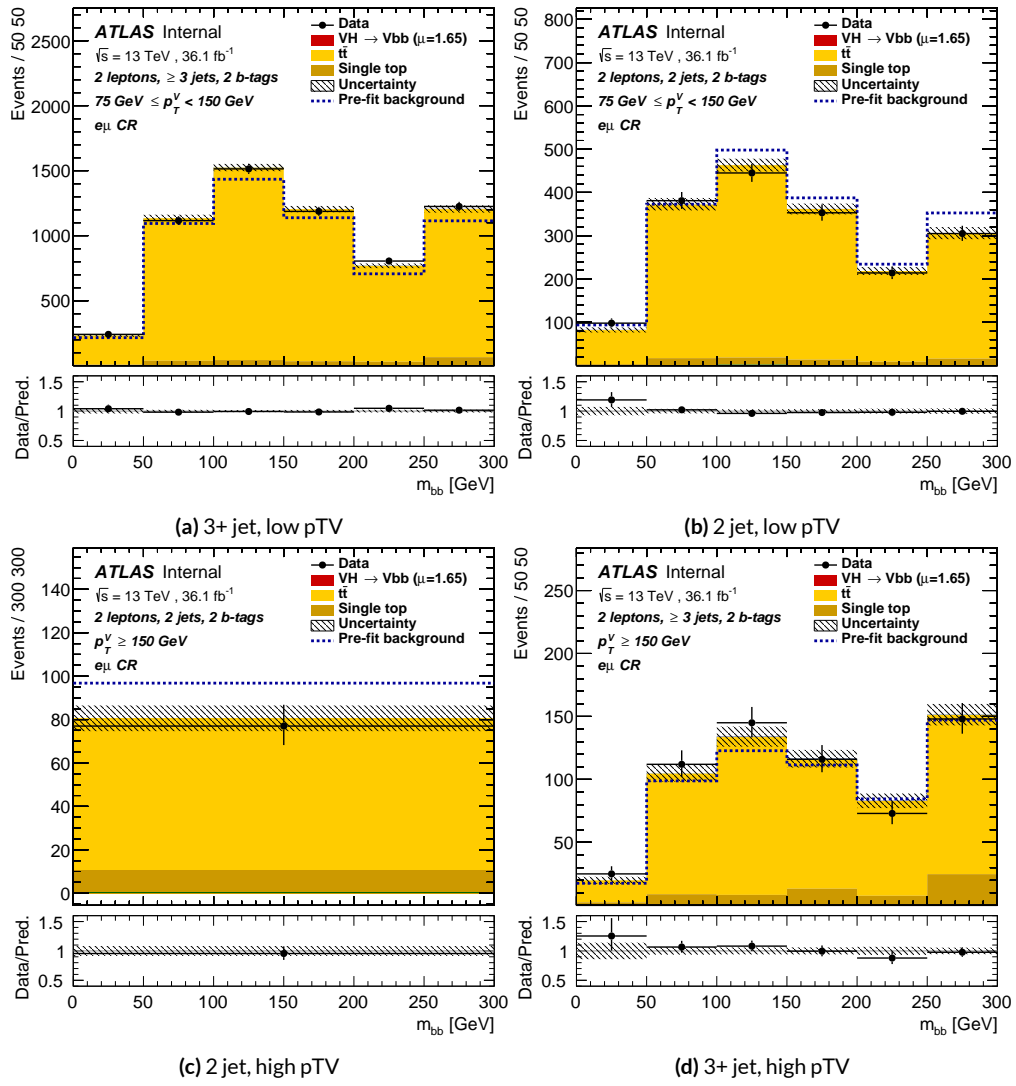


Figure 7.33: Postfit m_{bb} plots in the top $e - \mu$ CR for the LI variable set.

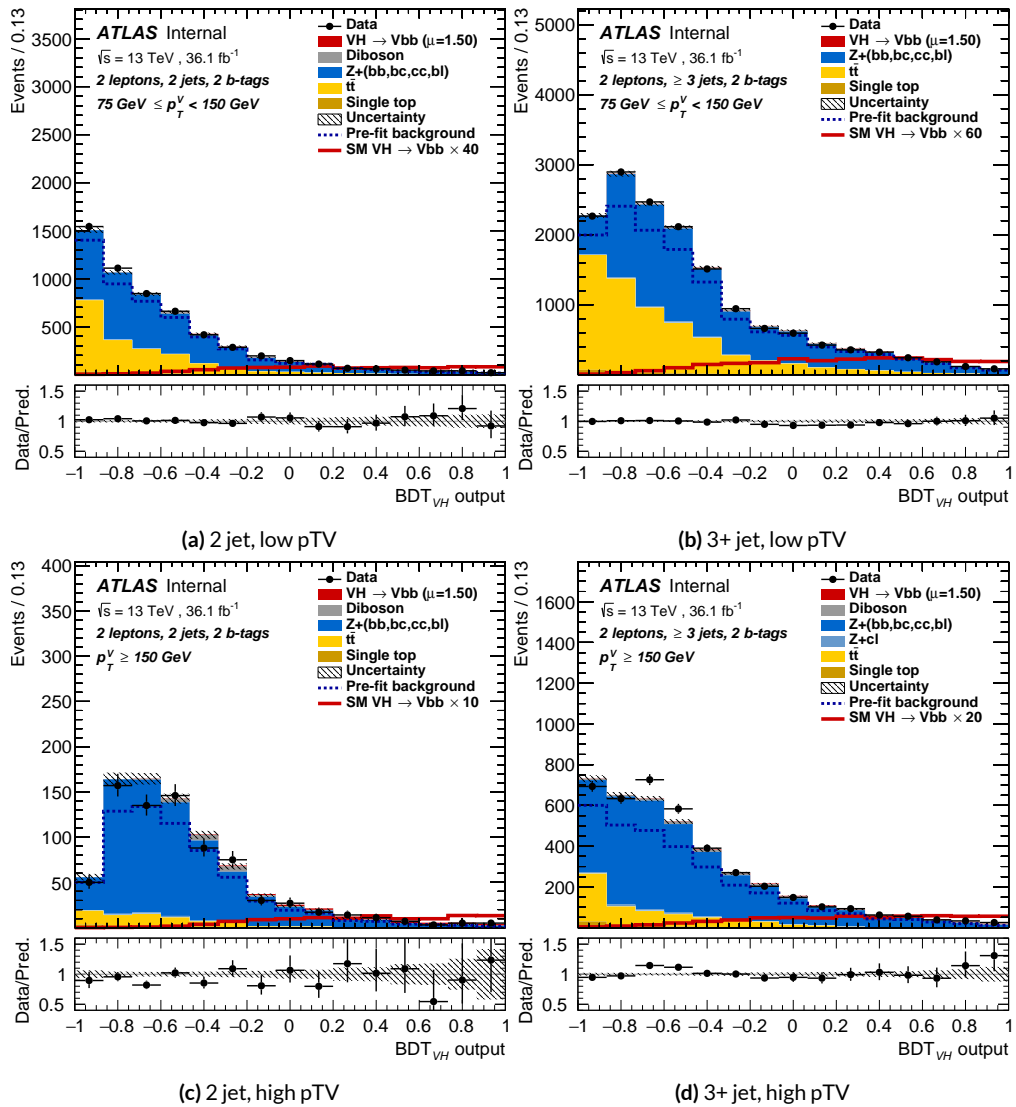


Figure 7.34: Postfit BDT_{VH} plots in the signal region for the RF variable set.

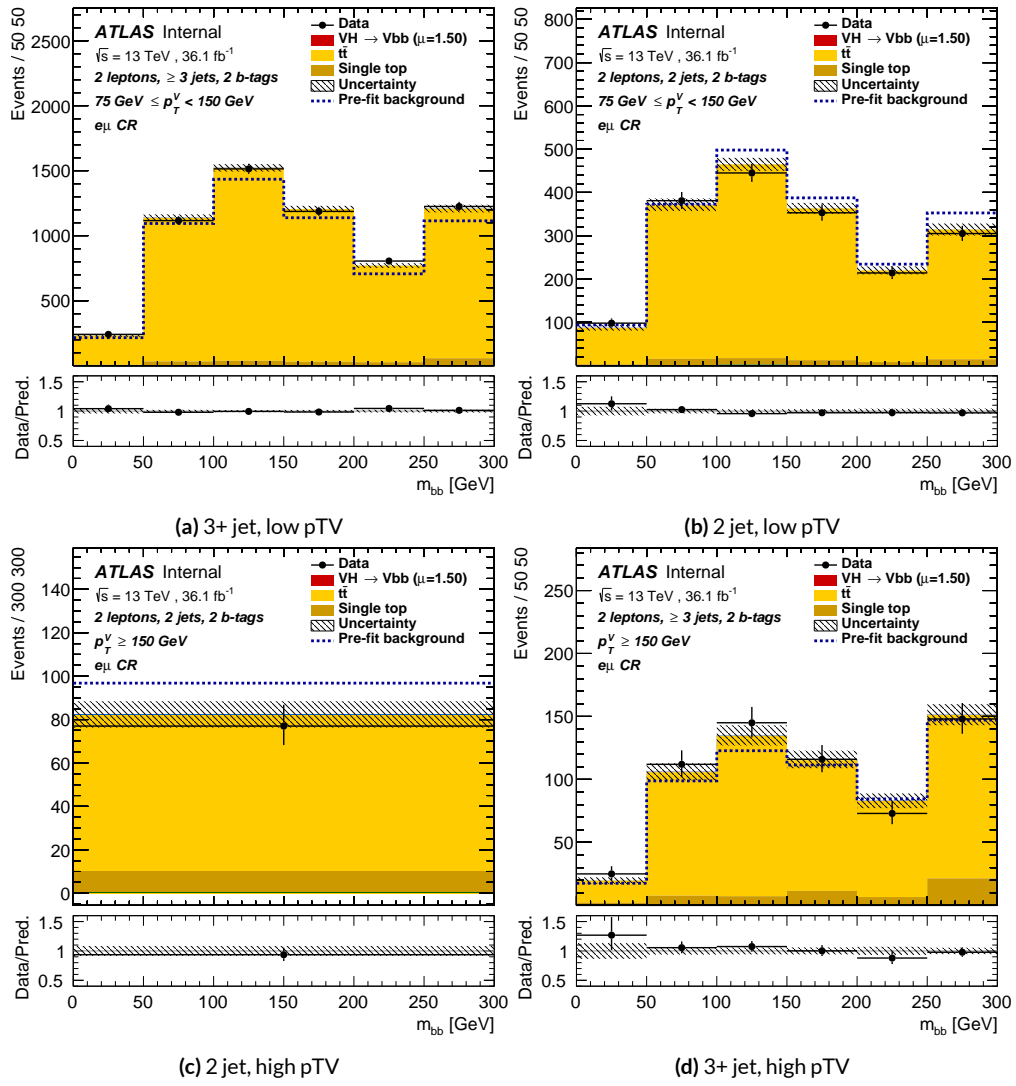


Figure 7.35: Postfit m_{bb} plots in the top $e - \mu$ CR for the RF variable set.

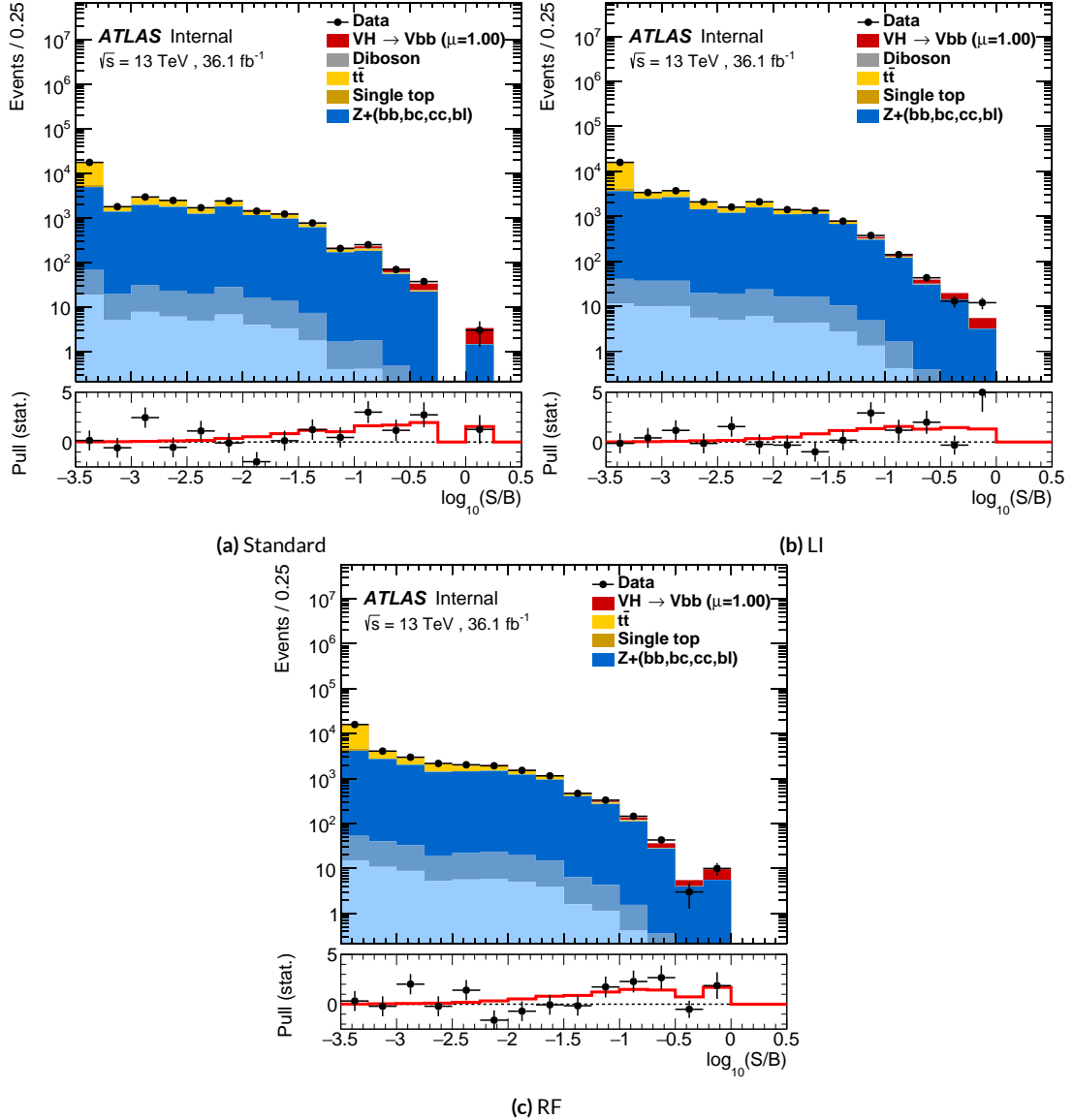


Figure 7.36: Binned S/B plots for the standard (a), LI (b), and RF (c) variable sets. Signal is weighted to $\mu = 1$ for comparison to the SM prediction.

*Kein Operationsplan reicht mit einiger Sicherheit
über das erste Zusammentreffen mit der feindlichen
Hauptmacht hinaus.*

Helmuth von Moltke

8

1786

Fit Results

1787

1788 THE RESULTS IN THIS CHAPTER were first reported in³⁷ and describe how the three different fit
1789 models detailed and validated Chapter 7, corresponding to the standard, RF, and LI variable sets
1790 described in Chapter 6 perform on actual VH fits. In particular sensitivities, nuisance parameter
1791 impacts, and signal strengths on expected fits to Asimov datasets and both expected and observed

1792 fits on the actual dataset are compared.

1793 Expected and observed sensitivities for the different variable sets may be found in Table 8.1. The
1794 RF fits feature the highest expected sensitivities, outperforming the standard set by 3.5% and 3.4%
1795 for fits to Asimov and observed datasets, respectively. The LI variable has a lower significance than
1796 both for expected fits to both Asimov and data with a 6.7% (1.7%) significance than the standard set
1797 for the Asimov (observed) dataset. While the fit using standard variables does have a higher observed
1798 significance than both the LI and RF fits, by 2.8% and 8.6%, respectively, these numbers should be
1799 viewed in the context of the best fit $\hat{\mu}$ values, discussed below. That is, the standard set may yield the
1800 highest sensitivity for this particular dataset, but this is not necessarily (and likely is not) the case for
1801 any given dataset.

	Standard	LI	RF
Expected (Asimov)	2.06	1.92	2.13
Expected (data)	1.76	1.73	1.80
Observed (data)	2.87	2.79	2.62

Table 8.1: Expected (for both data and Asimov) and observed significances for the standard, LI, and RF variable sets.

1802 A summary of fitted signal strengths and errors for both the Asimov (a) and observed (b) datasets
1803 are shown in Figure 8.1.* A summary of error breakdowns is given in Tables 8.2 (Asimov) and 8.3
1804 (observed) for total error, data statistics contributions, total systematic error contributions, and cat-
1805 egories for which the total impact is ≥ 0.1 for the standard fit. As is to be expected for both the
1806 Asimov and observed dataset fits, the contribution to the total error on μ arising from data statistics

*For reference, the standalone 2-lepton fit from the fiducial analysis is $2.11^{+0.50}_{-0.48}$ (stat.) $^{+0.64}_{-0.47}$ (syst.)

¹⁸⁰⁷ is nearly identical, since each set of fits uses the same selections and data.[†]

	Std-KF	LI+MET	RF
Total	+0.608 / -0.511	+0.632 / -0.539	+0.600 / -0.494
DataStat	+0.420 / -0.401	+0.453 / -0.434	+0.424 / -0.404
FullSyst	+0.440 / -0.318	+0.441 / -0.319	+0.425 / -0.284
Signal Systematics	+0.262 / -0.087	+0.272 / -0.082	+0.290 / -0.088
MET	+0.173 / -0.091	+0.140 / -0.074	+0.117 / -0.063
Flavor Tagging	+0.138 / -0.136	+0.069 / -0.071	+0.076 / -0.078
Model Zjets	+0.119 / -0.117	+0.124 / -0.127	+0.095 / -0.086

Table 8.2: Summary of error impacts on total μ error for principal categories in the Asimov standard, LI, and RF fits.

	Std-KF	LI+MET	RF
Total	+0.811 / -0.662	+0.778 / -0.641	+0.731 / -0.612
DataStat	+0.502 / -0.484	+0.507 / -0.489	+0.500 / -0.481
FullSyst	+0.637 / -0.451	+0.591 / -0.415	+0.533 / -0.378
Signal Systematics	+0.434 / -0.183	+0.418 / -0.190	+0.364 / -0.152
MET	+0.209 / -0.130	+0.190 / -0.102	+0.152 / -0.077
Flavor Tagging	+0.162 / -0.166	+0.093 / -0.070	+0.115 / -0.099
Model Zjets	+0.164 / -0.152	+0.141 / -0.143	+0.101 / -0.105

Table 8.3: Summary of error impacts on total $\hat{\mu}$ error for principal categories in the observed standard, LI, and RF fits.

¹⁸⁰⁸ The contribution from systematic uncertainties, however, does vary considerably across the vari-
¹⁸⁰⁹ able sets. The Asimov fits are a best case scenario in the sense that, by construction, all NP's are equal
¹⁸¹⁰ to their predicted values (and so no "penalty" is paid for pulls on Gaussian NP's). The systematics er-
¹⁸¹¹ ror from the LI fit is slightly higher (subpercent) than that from the standard fit, and 4.6% higher er-
¹⁸¹² ror overall due to differences in data stats. The RF Asimov fit, however, has a 6.5% lower total error

[†]Though not exactly identical. Since the BDT's are different for the different variable sets, the binning (as determined by transformation D) and bin contents in each set are generally different, leading to slightly different data statistics errors.

1813 from systematics than the standard Asimov fit (and a 2.2% lower error overall). Moreover, for both
 1814 the LI and RF sets, errors are markedly smaller for the MET and Flavor Tagging categories, with the
 1815 RF fit also featuring a smaller errors on Z +jets modeling; the only notable exception to this trend in
 1816 Asimov fits are the signal systematics.

1817 These trends are more pronounced in the observed fits. As can be seen in Table 8.3, both the LI
 1818 and RF fits have smaller errors from systematic uncertainties, both overall and in all principal cate-
 1819 gories, with the LI and RF fits having 7.5% (3.7%) and 16% (8.8%) lower systematics (total) error on
 1820 $\hat{\mu}$, respectively.

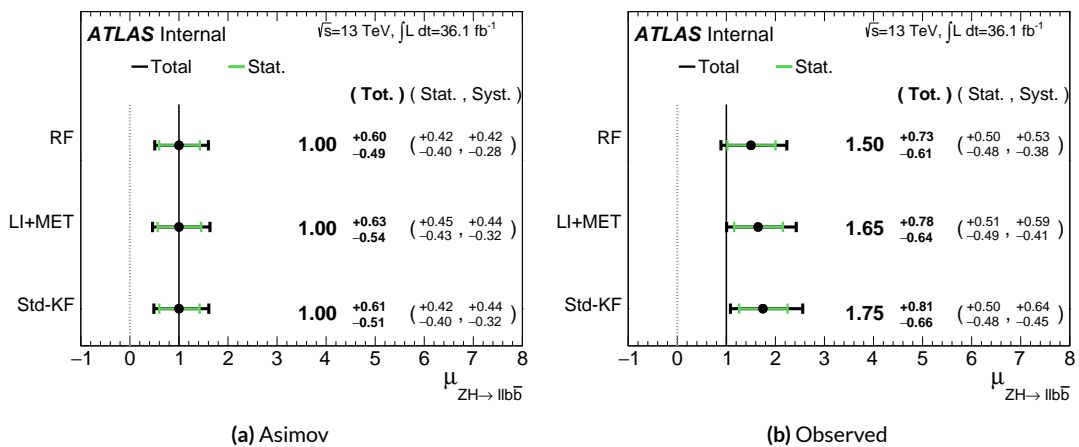


Figure 8.1: μ summary plots for the standard, LI, and RF variable sets. The Asimov case (with $\mu = 1$ by construction) is in (a), and $\hat{\mu}$ best fit values and error summary are in (b).

1821 Studying the performance of the Lorentz Invariant and RestFrames variable sets at both a data
 1822 statistics only context and with the full fit model in the $ZH \rightarrow \ell\ell b\bar{b}$ channel of the $VH(b\bar{b})$ anal-
 1823 ysis suggests that these variables may offer a potential method for better constraining systematic un-
 1824 certainties in $VH(b\bar{b})$ searches as more orthogonal bases in describing the information in collision

1825 events.

1826 The marginally worse performance of the LI and RF variables (7.9% and 6.9%, respectively) with
1827 respect to the standard variable at a stats only level illustrates that neither variable set has greater
1828 intrinsic descriptive power in the absence of systematics in this closed final state. Hence, any gains
1829 from either of these variable sets in a full fit come from improved treatment of systematic uncertain-
1830 ties.

1831 With full systematics, the LI variable set narrows the sensitivity gap somewhat, with lower signif-
1832 icances by 6.7% (1.7%) on expected fits to Asimov (data) and by 2.8% on observed significances. The
1833 RF variable set outperforms the standard set in expected fits with 3.5% (3.4%) higher significance
1834 on Asimov (data), but has an 8.6% lower observed significance, though the observed significances
1835 should be viewed in the context of observed $\hat{\mu}$ values.

1836 Moreover, the LI and RF variable sets generally perform better in the context of the error on μ .
1837 The LI fit is comparable to the standard set on Asimov data and has a 7.5% lower total systematics er-
1838 ror on $\hat{\mu}$ on observed data, while the RF fit is lower in both cases, with systematics error being 6.5%
1839 (16%) lower on Asimov (observed) data.

1840 These figures of merit suggest that both the LI and RF variables are more orthogonal than the
1841 standard variable set used in the fiducial analysis. Moreover, the RF variable set does seem to con-
1842 sistently perform better than the LI set. Furthermore, both variable sets have straightforward exten-
1843 sions to the other lepton channels in the $VH(b\bar{b})$ analysis. The magnitude of any gain from the
1844 more sophisticated treatment of E_T^{miss} in these extensions is beyond the scope of these studies, but
1845 the performance in this closed final state do suggest that there is some value to be had in these non-

¹⁸⁴⁶ standard descriptions independent of these considerations.

*If I have seen further, it is by standing on ye shoulders of
giants.*

Isaac Newton

9

1847

1848

Measurement Combinations

1849 WHILE THE DISCUSSION thus far has focused on improvements looking towards future in just the
1850 $ZH \rightarrow \ell\ell b\bar{b}$ channel, any actual result for SM $VH(b\bar{b})$ combines all channels and all available
1851 datasets. Using additional channels at a given center of mass energy is straightforward since the fit
1852 model is designed with this combination in mind. Combining dataset results (known as “workspaces”)

1853 from different center of mass energies is not so simple an exercise since both the underlying physics
1854 (and its associated modeling) and the treatment of key experimental considerations, like flavor tag-
1855 ging, and their associated systematics change from dataset to dataset. A combined fit model must
1856 take these considerations into account, and the formulation of the fit model combining the Run
1857 1 ($\sqrt{s} = 7$ TeV with 4.7 fb^{-1} of data, and $\sqrt{s} = 8$ TeV with 20.3 fb^{-1} of data) and Run 2 ($\sqrt{s} = 13$
1858 TeV with) SM $VH(b\bar{b})$ results is the topic of Section 9.1. Its results, as reported in ⁴², are given in
1859 9.2.

1860 9.1 THE COMBINED FIT MODEL

1861 It is clear the signal strength parameter of interest should be fully correlated among the different
1862 datasets. Some signal modeling systematics were left unchanged from Run 1 through Run 2 and/or
1863 were designed to be explicitly correlated. Beyond these two special cases, it is not immediately clear
1864 what level of correlation should be imposed. The general methodology for settling upon a correla-
1865 tion scheme is as follows:

- 1866 1. Identify which NP categories have significant impacts on μ
- 1867 2. Of these NP's, identify which have one-to-one correspondences or established correlation
1868 schemes among \sqrt{s} values
- 1869 3. Test whether correlation has a sizeable impact on expected fit quantities

1870 The only two sizeable experimental NP categories are jet energy scale (JES) and flavor tagging sys-
1871 tematics. Correlation schemes of varying degrees of completeness exist for these categories, so ex-
1872 plicit NP correlations can be tested for these two categories. As these studies were conducted before

1873 unblinding, “sizeable impact” was judged by comparing fit results (sensitivities, pull comparisons,
1874 and breakdowns) on combined workspaces using the unblinded and public $\mu = 0.51$ result for
1875 Run 1 and Asimov data for the Run 2 result. These are treated in Sections 9.1.1 and 9.1.2. Modeling
1876 systematics require a slightly different treatment, and are explored in 9.1.3.

1877 As noted in Chapter 7 when looking at pull comparison plots for combined workspaces, the error
1878 bars in these plots are calculated using a simultaneous HESSE matrix inversion, which can fail to give
1879 sensible values for high dimensional models (the combined workspaces have well over 500 NP’s).
1880 This is not true of the nuisance parameter ranking plots, which use a MINOS based approach to test
1881 the effect of each NP individually. This is much slower but much more rigorous, which is why only
1882 ranking plots appear outside of supporting material and pull comparisons are considered “diagno-
1883 tic” plots.

1884 9.1.1 JET ENERGY SCALE SYSTEMATICS

1885 Fortunately for the case of jet energy scale systematics, the JetEtMiss group provides two recom-
1886 mended “strong” and “weak” correlation schemes between Run 1 and Run 2. These were used as
1887 a point of departure for the JES combination correlation scheme. However, the JES NP’s in both
1888 the Run 1 and Run 2 workspaces are a reduced set of NP’s, with some 56 (75) NP’s reduced to 6 (8)
1889 for Run 1 (2). In order to restore the full set of JES NP’s, the effective NP’s in each workspace are un-
1890 folded using maps detailing the linear combinations of unfolded NP’s that form the effective NP’s.

The linear combinations used to unfold the effective JES NP's were calculated as follows:

$$NP_{i,eff} = \frac{\sum_j A_{ij} |NP_{j,unf}| NP_{j,unf}}{\sqrt{\sum_j A_{ij}^2 |NP_{j,unf}|^2}} \quad (9.1)$$

- 1892 where *eff* and *unf* are for effective and unfolded NP's, respectively, the A_{ij} 's are scalar coefficients
 1893 taken from raw maps, and $|NP_{j,unf}|$ are the amplitudes of the unfolded NP's. The raw A_{ij} and scaled
 1894 maps for Run 1 and Run 2 may be found in Figure 9.1

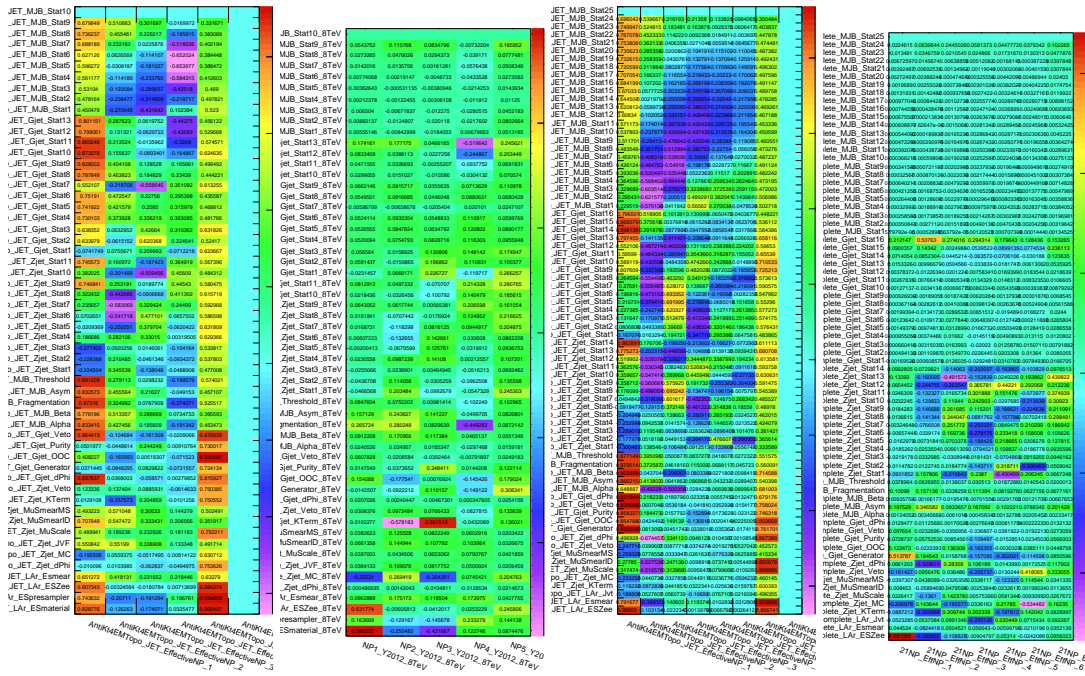


Figure 9.1: The raw and scaled coefficients for unfolding Run 1 (a and b) and Run 2 (c and d), respectively

Unfolding was found to have very little effect on both expected sensitivities and errors, as can be

- 1896 seen in Tables 9.1– 9.4.

	R ₁ Unfold	R ₁ Eff	R ₂ Unfold	R ₂ Eff	Comb Unfold	Comb Eff
Exp. Sig.	2.604	2.606	3.014	3.014	4.005	3.998
Obs. Sig.	1.369	1.374	3.53	3.53	3.581	3.571
Exp. Limit	0.755 ^{+0.296} _{-0.211}	0.755 ^{+0.296} _{-0.211}	0.732 ^{+0.287} _{-0.205}	0.732 ^{+0.287} _{-0.205}	0.512 ^{+0.201} _{-0.143}	0.51 ^{+0.2} _{-0.143}
Obs. Limit	1.21	1.21	1.94	1.94	1.36	1.37

Table 9.1: Expected and observed sensitivities for Run 1, Run 2, and combined workspaces with effective and unfolded JES NP's.

	R ₁ Unfold	R ₁ Eff
$ \Delta\hat{\mu} $		0.0018
$\hat{\mu}$	0.5064	0.5082
Total	+0.400 / -0.373	+0.401 / -0.373
DataStat	+0.312 / -0.301	+0.312 / -0.301
FullSyst	+0.250 / -0.220	+0.251 / -0.220
Jets	+0.060 / -0.051	+0.060 / -0.052
BTag	+0.094 / -0.079	+0.095 / -0.079
	+0.119 / -0.106	+0.119 / -0.106
	+0.076 / -0.076	+0.077 / -0.076

Table 9.2: Error on signal strength breakdowns for Run 1 workspaces with effective and unfolded JES NP's.

	R ₂ Unfold	R ₂ Eff
$ \Delta\hat{\mu} $		0.0
$\hat{\mu}$	1.2051	1.2052
Total	+0.421 / -0.366	+0.421 / -0.366
DataStat	+0.239 / -0.234	+0.239 / -0.234
FullSyst	+0.346 / -0.282	+0.346 / -0.282
Jets	+0.066 / -0.047	+0.066 / -0.047
BTag	+0.119 / -0.106	+0.119 / -0.106

Table 9.3: Error on signal strength breakdowns for Run 2 workspaces with effective and unfolded JES NP's.

	Comb Unfold	Comb Eff
$ \Delta\hat{\mu} $	0.0006	
$\hat{\mu}$	0.8992	0.8985
Total	+0.278 / -0.261	+0.278 / -0.261
DataStat	+0.185 / -0.181	+0.185 / -0.181
FullSyst	+0.208 / -0.187	+0.208 / -0.188
Jets	+0.040 / -0.044	+0.041 / -0.036
BTag	+0.076 / -0.076	+0.077 / -0.076

Table 9.4: Error on signal strength breakdowns for combined workspaces with effective and unfolded JES NP's.

1897 It was also found that fit sensitivities and breakdowns were similarly indifferent to the use of ei-

1898 ther the strong or weak JES correlation schemes, as shown in Tables 9.5 and 9.6.

	JES Weak Unfold	JES Weak Eff	JES Strong Unfold	JES Strong Eff
Exp. Sig.	3.57	3.57	3.59	3.59
Exp. Limit	$0.493^{+0.193}_{-0.138}$	$0.494^{+0.193}_{-0.138}$	$0.493^{+0.193}_{-0.138}$	$0.493^{+0.193}_{-0.138}$

Table 9.5: Expected sensitivities for both effective and unfolded combined workspaces using the strong and weak JES correlation schemes.

	Comb Unfold	Comb Eff	Strong Unfold	Strong Eff
$\Delta\hat{\mu}$	0.0009		0.0025	
Total	+0.269 -0.254	+0.27 -0.255	+0.27 -0.255	+0.27 -0.255
DataStat	+0.181 -0.177	+0.181 -0.177	+0.181 -0.177	+0.181 -0.178
FullSyst	+0.199 -0.183	+0.2 -0.183	+0.2 -0.183	+0.201 -0.183
Jets	+0.0387 -0.032	+0.041 -0.0337	+0.0425 -0.0329	+0.0432 -0.0338
BTag	+0.0975 -0.0933	+0.098 -0.0936	+0.0979 -0.0935	+0.098 -0.0936

Table 9.6: Error on signal strength breakdowns for both effective and unfolded combined workspaces using the strong and weak JES correlation schemes.

1899 Comparisons of top ranked nuisance parameters in Figures 9.2–9.4 and for the complete JES pull

1900 comparisons in Figures 9.5–9.8 also show very little difference with respect to correlation scheme
 1901 (except obviously for the number of JES NP's). Constrained pulls in pull comparisons should once
 again be taken as a shortcoming of HESSE and not the fit model.

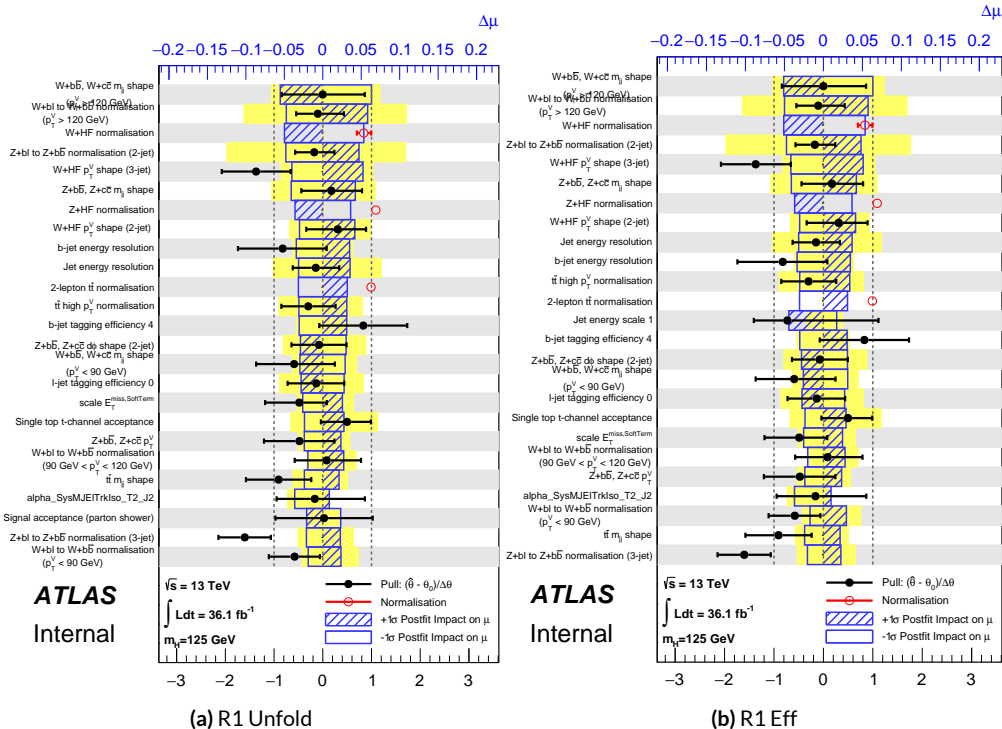


Figure 9.2: Ranks for the effective and unfolded JES NP Run1 combined workspaces.

1902
 1903 As a result of these studies, the weak JES correlation scheme with uncorrelated effective JES NP's
 1904 (i.e. just the b -jet energy scale NP) has been chosen as the treatment of JES in the Run 1 + Run 2
 1905 combined fit.

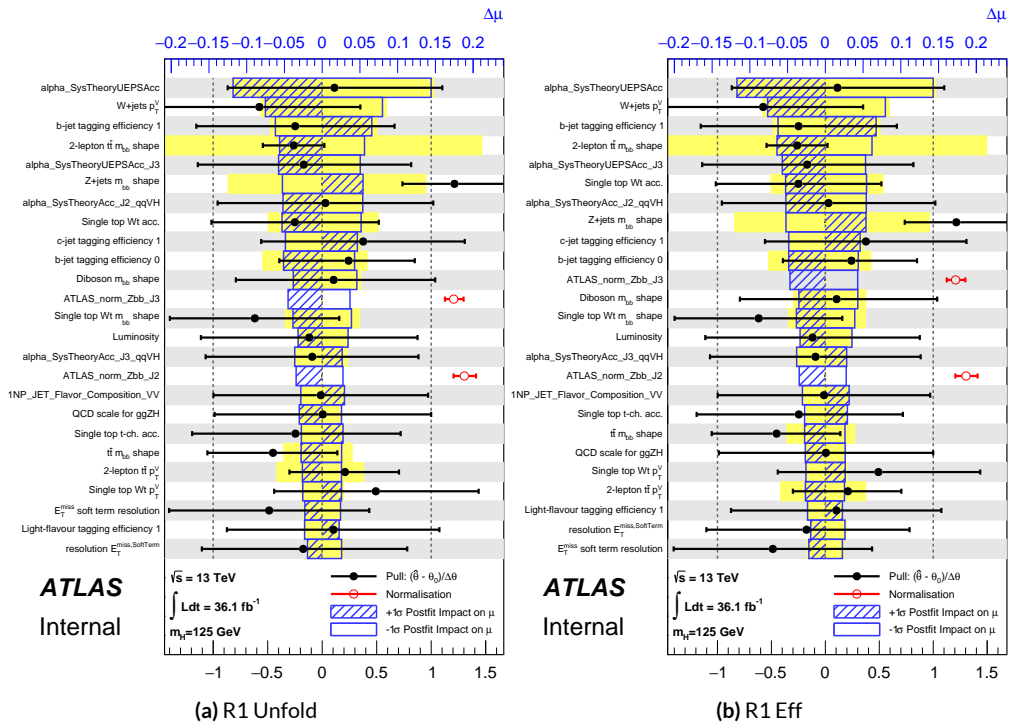


Figure 9.3: Ranks for the effective and unfolded JES NP Run2 combined workspaces.

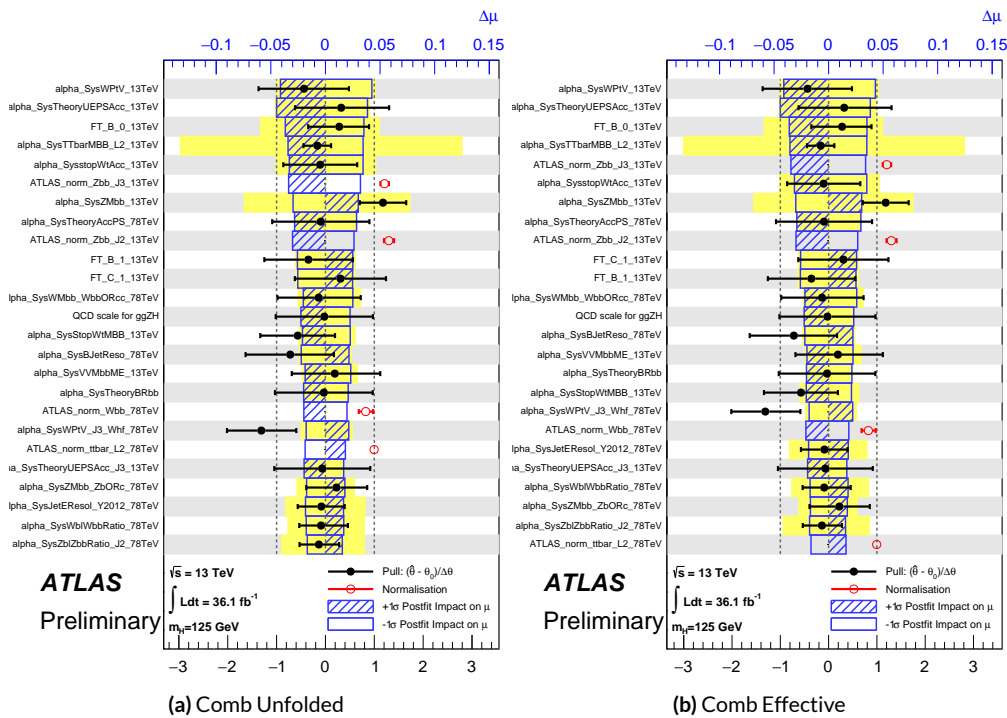


Figure 9.4: Ranks for the effective and unfolded JES NP Run1+Run2 combined workspaces.

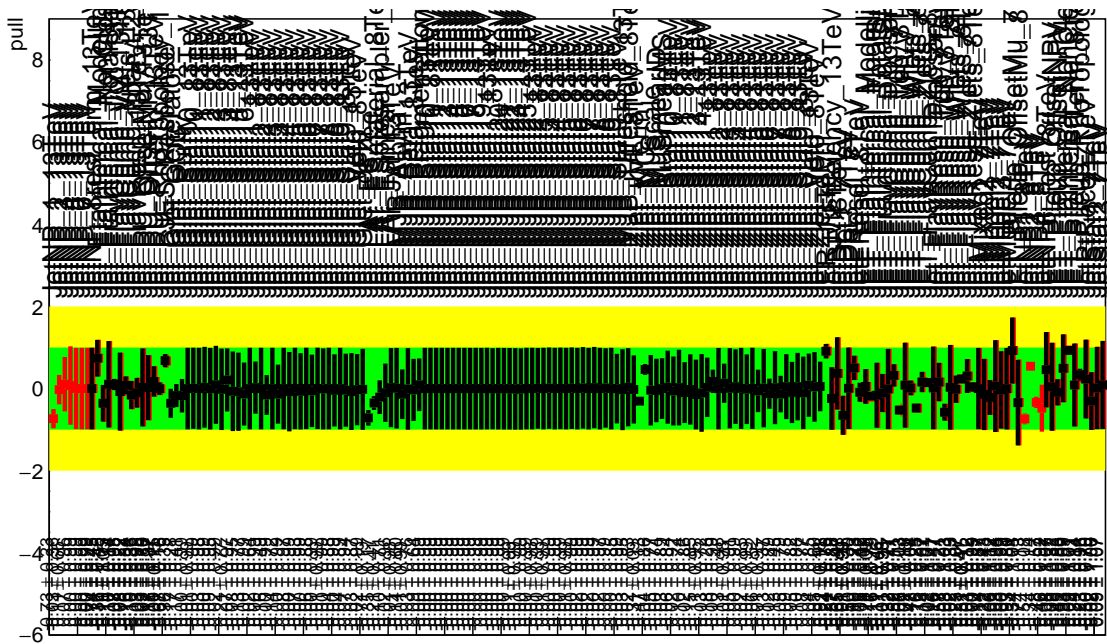


Figure 9.5: Pull Comparisons: jesu---Jet Comb Unfold, Comb Eff, Strong Unfold, Strong Eff

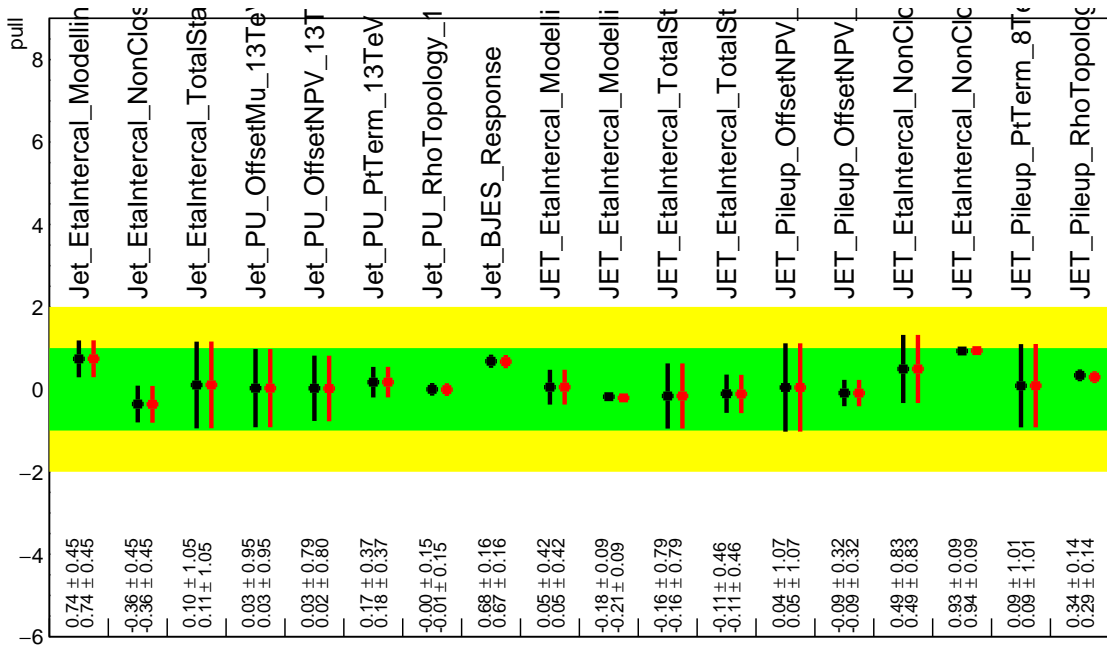


Figure 9.6: Pull Comparisons: jesu---JetMatched Comb Unfold, Comb Eff, Strong Unfold, Strong Eff

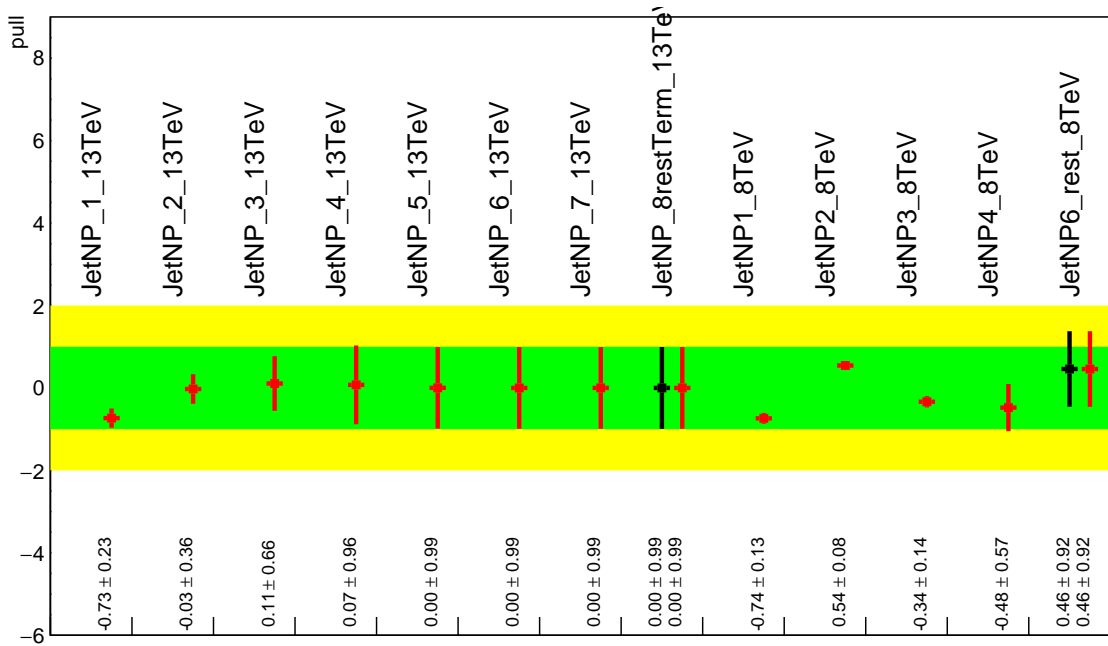


Figure 9.7: Pull Comparisons: jesu---JetEff Comb Unfold, **Comb Eff**, Strong Unfold, **Strong Eff**

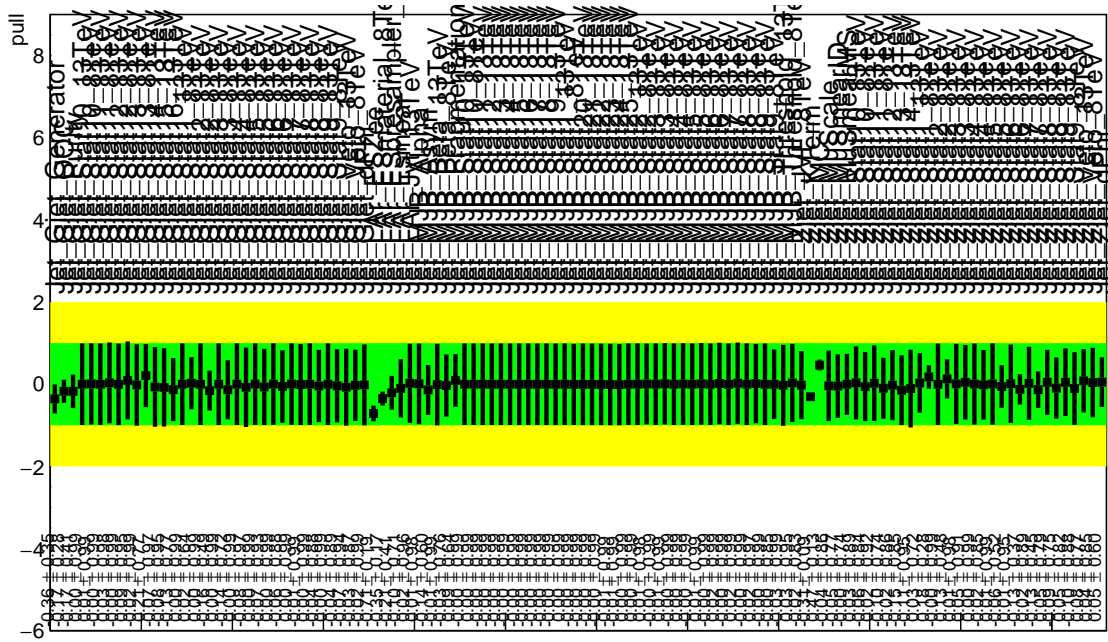


Figure 9.8: Pull Comparisons: jesu---JetUnfold Comb Unfold, **Comb Eff**, Strong Unfold, **Strong Eff**

1906 9.1.2 FLAVOR TAGGING

1907 Unfortunately, the ATLAS Flavor Tagging group did not provide any recommendations for corre-
1908 lating Run 1 and Run 2 NP's, though given the high ranking of these NP's in the Run 2, result, per-
1909 forming at least some studies was deemed crucial. Nevertheless, great improvements and changes to
1910 the treatment of flavor tagging between Run 1 and Run 2 does weaken the argument for any strong
1911 flavor tagging correlation scheme.

1912 Given that c -tagging changed significantly between Run 1 and Run 2 and that light tagging NP's
1913 are very lowly ranked, these sets of NP's are left uncorrelated. Moreover, the change in the physical
1914 meaning of the effective b -tagging NP's means a full correlation of such NP's (insomuch as they exist
1915 in each result) is one of limited utility. Hence, it was decided to leave flavor tagging NP's uncorre-
1916 lated. However, since the meaning of the leading b -tagging NP's is approximately constant across
1917 years and since Run 2 b -tagging NP's are very highly ranked in both the Run 2 only and combined
1918 fits, tests correlating these NP's were conducted, the results of which can be seen below. It should be
1919 noted that the leading B NP at 8 TeV, `SysBTagB0Effic_Y2012_8TeV`, has an opposite effect on $t\bar{t}$
1920 normalization than the 7 and 13 TeV NP's, and so must be flipped using a similar strategy as for JES
1921 unfolding. Initial studies of flavor tagging correlations did not flip this NP, and so results for this
1922 scheme (labeled "Bo 8TeV Not Flipped") have also been included for comparison.

1923 It is clear from these results that correlating the leading effective Eigen NP associated with b 's can
1924 have a noticeable effect on final fit results and that the 8 TeV Bo NP is the most important compo-
1925 nent of a combined Bo NP. It is also not so surprising that the 8 TeV result should drive the com-

	Comb Eff	BTag Bo	Bo 8TeV Flipped
Exp. Sig.	3.998	4.127	3.921
Obs. Sig.	3.571	3.859	3.418
Exp. Limit	0.51 ^{+0.2} _{-0.143}	0.5 ^{+0.196} _{-0.14}	0.517 ^{+0.202} _{-0.144}
Obs. Limit	1.37	1.41	1.35

Table 9.7: Expected and observed sensitivities for a combination featuring the weak JES scheme, combination with the weak JES scheme + leading b NP's correlated, and the b correlation with the 8 TeV NP with sign unflipped.

	Comb Eff	BTag Bo	Bo 8TeV Not Flipped
$ \Delta\hat{\mu} $	—	0.0446	0.0268
$\hat{\mu}$	0.8985	0.9431	0.8717
Total	+0.278 / -0.261	+0.275 / -0.256	+0.282 / -0.263
DataStat	+0.185 / -0.181	+0.180 / -0.177	+0.189 / -0.186
FullSyst	+0.208 / -0.188	+0.207 / -0.186	+0.209 / -0.186
BTag	+0.077 / -0.076	+0.071 / -0.068	+0.079 / -0.075
BTag b	+0.062 / -0.059	+0.055 / -0.049	+0.064 / -0.060

Table 9.8: Breakdowns of the impact of different NP sets on total error on \hat{m}_{ll} for a combination featuring the weak JES scheme and a combination with the weak JES scheme + leading b NP's correlated.

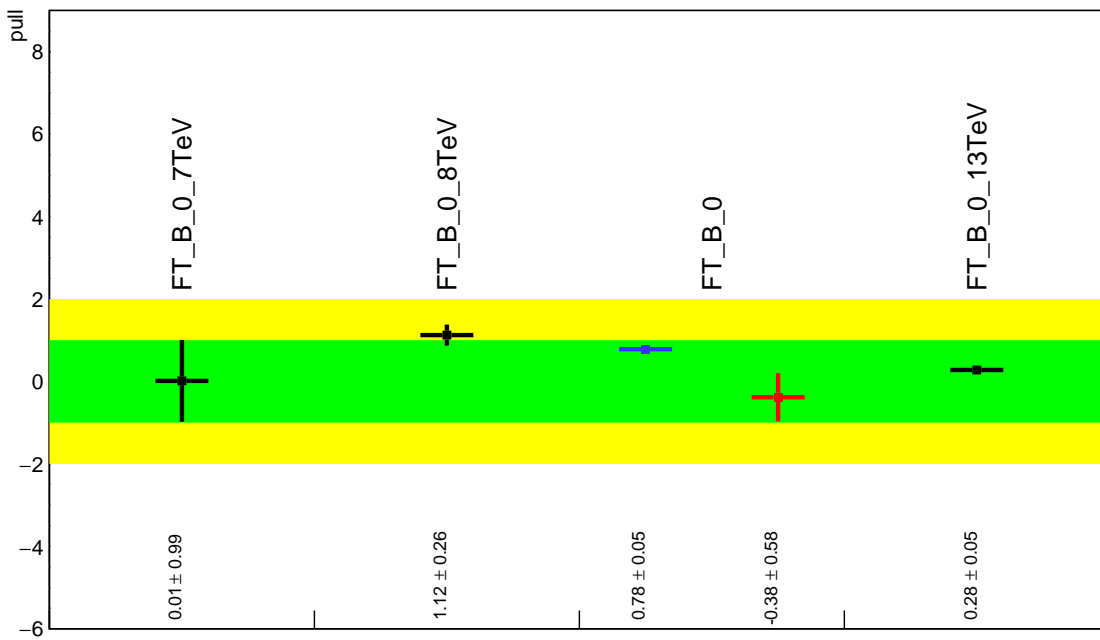


Figure 9.9: Pull Comparisons: btag-b---BTagBO Comb Eff, BTag BO

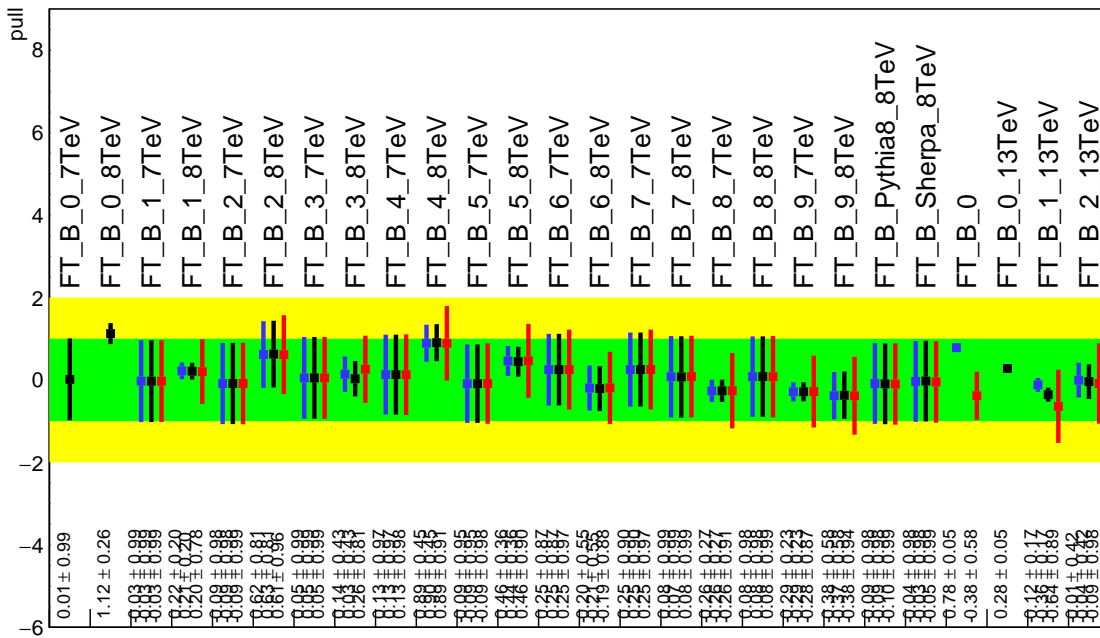


Figure 9.10: Pull Comparisons: btag-b---BTagB Comb Eff, BTag BO

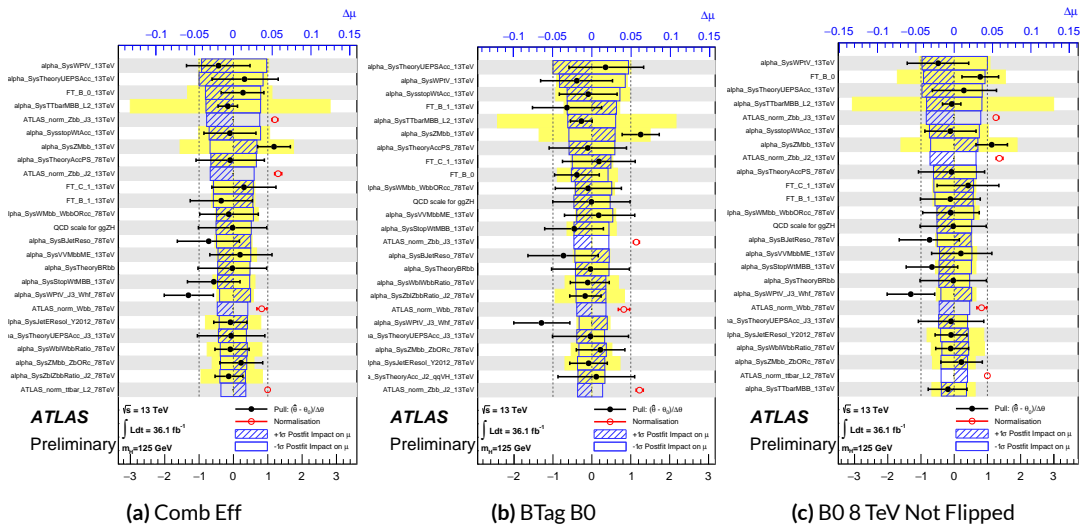


Figure 9.11: NP rankings for a combination featuring the weak JES scheme and a combination with the weak JES scheme + leading b NP's correlated.

1926 bined nuisance parameter since it is the only result to make use of both pseudocontinuous tagging-
 1927 based and b -tag regions into the final fit, implicitly yielding much more information about b 's. The
 1928 13 TeV fit has neither of these regions. What is less clear is whether there are sufficient grounds for
 1929 implementing this correlation (i.e. does the correspondence of these NP's across years warrant a full
 1930 correlation). While there are no current plans to do so, this matter warrants careful scrutiny if Run 1
 1931 is to be combined with future results.

1932 9.1.3 MODELING SYSTEMATICS

1933 Another principal systematic category is modeling uncertainties. The effect of correlating groups
 1934 of systematics was estimated using the same strategy employed by the ATLAS/CMS SM $VH(b\bar{b})$
 1935 combination for Run 1. This extrapolation can be used to estimate the impact of correlations on
 1936 the estimated signal strength, the total error on the signal strength, and the χ^2 of the result. The

¹⁹³⁷ impact of such correlations is no more than a few percent effect, as the following tables demonstrate,
¹⁹³⁸ beginning with the category with the greatest shift, W+jets modeling, in Table 9.9.

	$ \Delta\mu $	σ	$ \Delta\sigma $	χ^2
$\rho=-1$	0.0024	0.2448	0.011 (4.3%)	0.95
$\rho=-0.6$	0.0015	0.2493	0.00654 (2.55%)	0.9804
$\rho=-0.3$	0.0008	0.2526	0.00325 (1.27%)	1.0045
$\rho=0$	—	0.2558	—	1.0298
$\rho=0.3$	0.0008	0.259	0.0032 (1.25%)	1.0564
$\rho=0.6$	0.0017	0.2622	0.00636 (2.49%)	1.0844
$\rho=1$	0.0029	0.2664	0.0105 (4.11%)	1.1242

Table 9.9: Run 1 + Run 2 W+jets modeling correlation projections

¹⁹³⁹ 9.1.4 FINAL CORRELATION SCHEME

¹⁹⁴⁰ The final Run 1 + Run 2 correlation scheme is shown in Table 9.10. As detailed above, neither JES
¹⁹⁴¹ nor modeling systematics had any demonstrable effect on combined fit results. Hence, only signal
¹⁹⁴² NP's and the b -jet energy scale are correlated (the weak JES scheme without unfolding). While the
¹⁹⁴³ effect of flavor tagging correlations is less clear, the result physical arguments for correlation are less
¹⁹⁴⁴ strong; the size of effect was discovered rather late in the analysis process; and no nuisance parameter
¹⁹⁴⁵ unfolding maps exist for flavor tagging as they do for JES, so it was decided to leave these uncorre-
¹⁹⁴⁶ lated as well.

7 TeV NP	8 TeV NP	13 TeV NP
	ATLAS_BR_bb	SysTheoryBRbb
	SysTheoryQCDscale_ggZH	SysTheoryQCDscale_ggZH
	SysTheoryQCDscale_qqVH	SysTheoryQCDscale_qqVH
—	SysTheoryPDF_ggZH_8TeV	SysTheoryPDF_ggZH
—	SysTheoryPDF_qqVH_8TeV	SysTheoryPDF_qqVH
—	SysTheoryVHPt_8TeV	SysVHNLOEWK
SysJetFlavB_7TeV	SysJetFlavB_8TeV	SysJET_21NP_JET_BJES_Response

Table 9.10: A summary of correlated nuisance parameters among the 7, 8, and 13 TeV datasets.

1947 9.2 COMBINED FIT RESULTS

1948 9.2.1 COMBINED FIT MODEL VALIDATION

1949 Before moving onto the final results, we present the rest of the validation for the Run 1 + Run 2
 1950 combined fits, beginning with impacts of ranked individual nuisance parameters in Figure 9.12 and
 1951 for all nuisance parameter categories in Table 9.11. Both of these sets of results point to the most im-
 1952 portant nuisance parameters being signal systematics, b -tagging, and V +jets modeling systematics,
 1953 with Run 2 NP's generally being higher ranked. That some NP's are strongly pulled is not unusual
 1954 as the fit model has so many NP's; V +jets modeling in particular has been historically difficult.

1955 In addition to looking at the behaviors of nuisance parameters to gauge fit model performance
 1956 and stability, fits are conducted using multiple parameters of interest. Typical divisions are Run 1
 1957 vs. Run 2, lepton channels, and WH vs ZH . As mentioned in Chapter 7, the profile likelihood test
 1958 statistic given in Equation 7.2 is, in the limit of large sample statistics, a χ^2 distribution with degrees
 1959 of freedom equal to the number of parameters of interest plus number of nuisance parameters.
 1960 Thus, changing the number of interest parameters and leaving the rest of the fit model unchanged

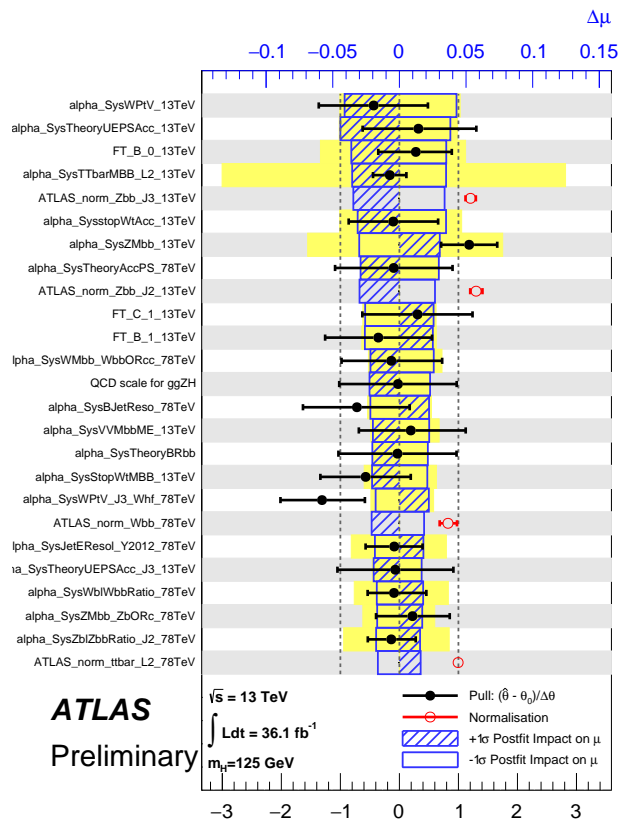


Figure 9.12: Ranked nuisance parameters for the Run1+Run2 combination.

Total	+0.278 / -0.261
DataStat	+0.185 / -0.181
FullSyst	+0.208 / -0.188
Floating normalizations	+0.055 / -0.056
All normalizations	+0.068 / -0.069
All but normalizations	+0.192 / -0.172
Jets, MET	+0.046 / -0.040
Jets	+0.041 / -0.036
MET	+0.023 / -0.018
BTag	+0.077 / -0.076
BTag b	+0.062 / -0.059
BTag c	+0.033 / -0.032
BTag light	+0.028 / -0.028
Leptons	+0.008 / -0.008
Luminosity	+0.026 / -0.014
Diboson	+0.030 / -0.027
Model Zjets	+0.049 / -0.050
Zjets flt. norm.	+0.032 / -0.040
Model Wjets	+0.082 / -0.083
Wjets flt. norm.	+0.031 / -0.027
Model ttbar	+0.047 / -0.046
ttbar flt. norm.	+0.025 / -0.026
Model Single Top	+0.047 / -0.045
Model Multi Jet	+0.027 / -0.038
Signal Systematics	+0.098 / -0.052
MC stat	+0.080 / -0.084

Table 9.11: Summary of the impact of different nuisance parameter categories on the total error on $\hat{\mu}$ for the combined Run1+Run2 fit.

¹⁹⁶¹ means that the difference between the nominal fit and a fit with more parameters of interest ought
¹⁹⁶² to also be distributed as a χ^2 distribution with degrees of freedom equivalent to the number of extra
¹⁹⁶³ parameters of interest. This difference can then be interpreted as a compatibility between the two
¹⁹⁶⁴ results using the standard tables for this distribution, giving another gauge of fit performance. These
¹⁹⁶⁵ are shown in Table 9.12.

Fit	Compatibility
Leptons (3 POI)	1.49%
WH/ZH (2 POI)	34.2%
Run 1/Run 2 (2 POI)	20.8%
Run 1/Run 2 \times Leptons (6 POI)	7.10%
Run 1/Run 2 \times WH/ZH (4 POI)	34.6%

Table 9.12: Summary of multiple POI compatabilities. The well-known Run 1 7 TeV 0-lepton deficit is responsible for the low compatibility with the 6 and 3 POI fits.

¹⁹⁶⁶ The low compatabilities associated with treating the lepton channels as separate parameters of
¹⁹⁶⁷ interest are a symptom of the low signal strengths associated with the Run 1 0-lepton channel, in par-
¹⁹⁶⁸ ticular the 7 TeV result. Given the relatively small amount of data associated with the 7 TeV result,
¹⁹⁶⁹ this should not be a cause for alarm. Signal strength summary plots for the fits treating Run 1 and
¹⁹⁷⁰ Run 2 separately are shown in Figures 9.13-9.15, where the effect of the Run 1 parameters can be seen
¹⁹⁷¹ graphically.

¹⁹⁷² 9.2.2 FINAL RESULTS

¹⁹⁷³ The combined results yields an observed (expected) significance of 3.57 (4.00) and an observed (ex-
¹⁹⁷⁴ pected) limit of 1.37 ($0.510^{+0.200}_{-0.143}$), with a signal strength of $\hat{\mu} = 0.898^{+0.278}_{-0.261}$.

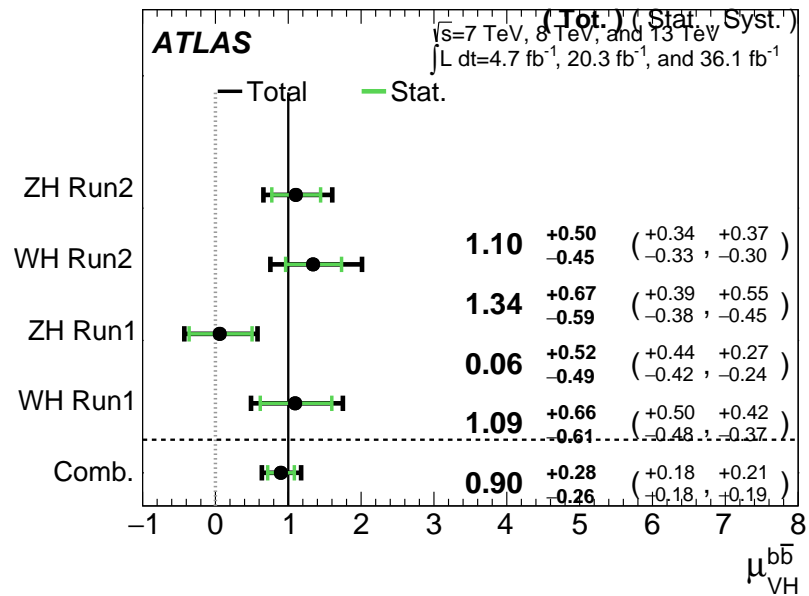


Figure 9.13: $\hat{\mu}$ summary plot for a four parameter of interest fit.

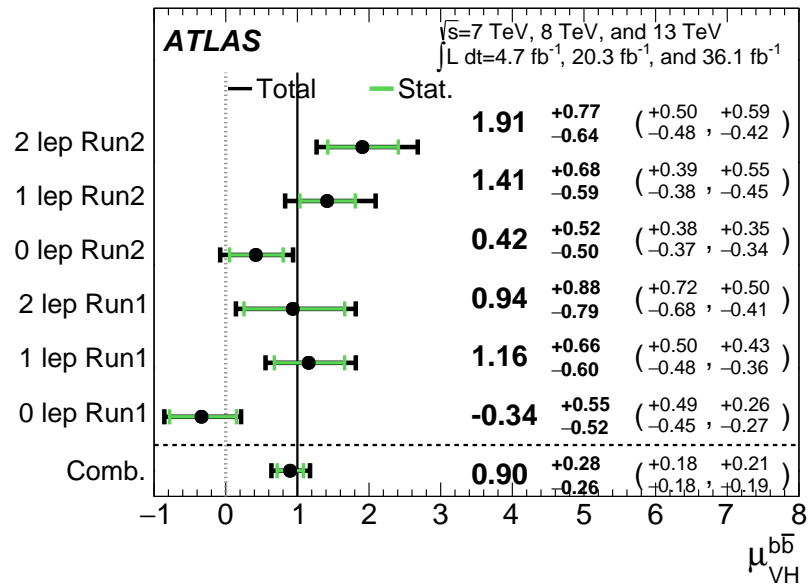


Figure 9.14: $\hat{\mu}$ summary plot for a six parameter of interest fit.

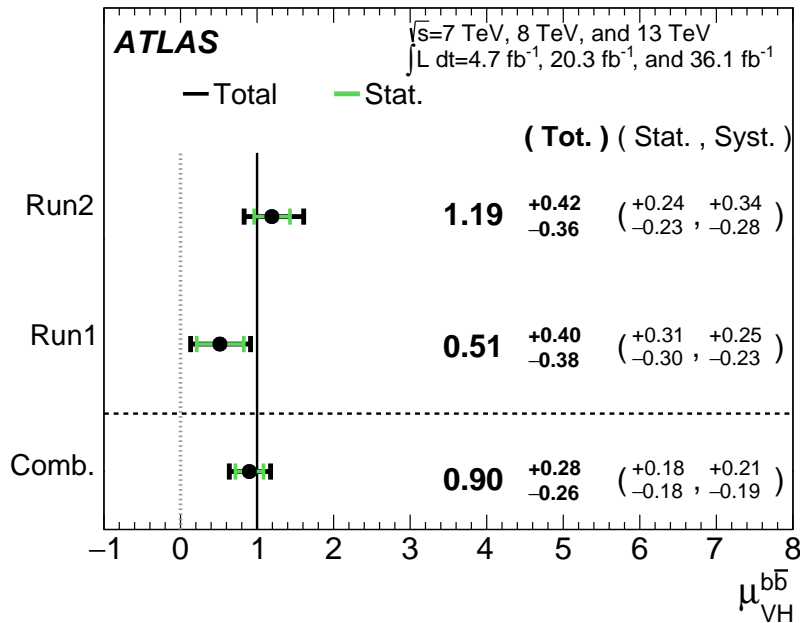


Figure 9.15: $\hat{\mu}$ summary plot for a two parameter of interest (Run 1 and Run 2) values.

1975 The two and three parameter of interest fit signal strength summary plots, as well as a summary
 1976 of the historical values of the 7, 8, and 13 TeV results may be found in Figures 9.16-9.18. The main
 1977 results for Run 1, Run 2, and the combination may be found in Table 9.13. These results were collec-
 1978 tively noted as the first ever experimental evidence for SM $VH(b\bar{b})$ in ⁴².

Dataset	$\hat{\mu}$	Total Error in $\hat{\mu}$	Obs. (Exp.) Significance
Run 1	0.51	$+0.40 / -0.37$	1.4 (2.6)
Run 2	1.20	$+0.42 / -0.36$	3.54 (3.03)
Combined	0.90	$+0.28 / -0.26$	3.57 (4.00)

Table 9.13: A summary of main results for the Run 1, Run 2, and combined fits.

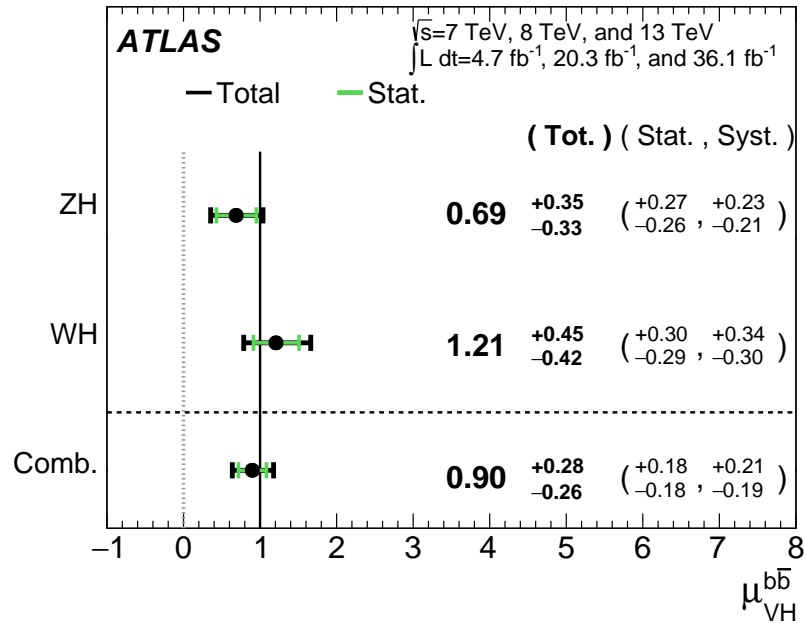


Figure 9.16: $\hat{\mu}$ summary plot for a two parameter of interest fit.

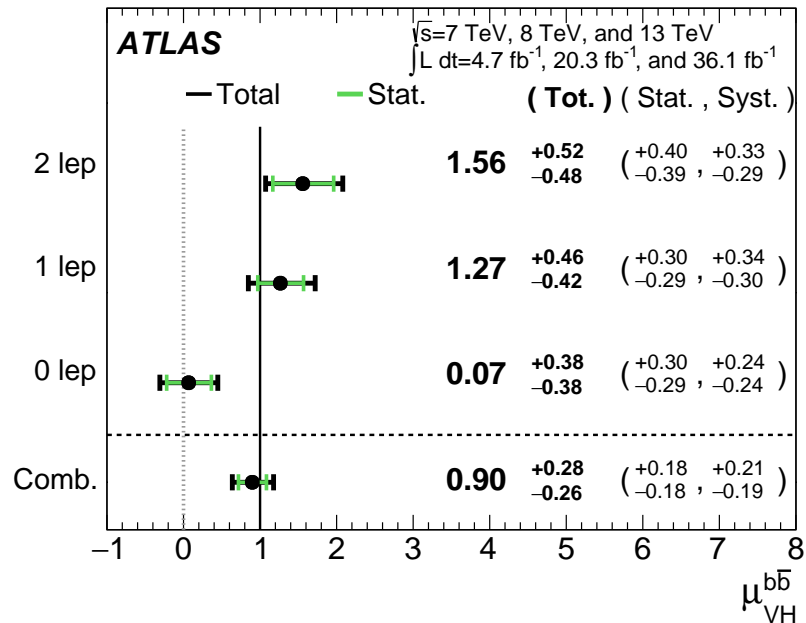


Figure 9.17: $\hat{\mu}$ summary plot for a three parameter of interest fit.

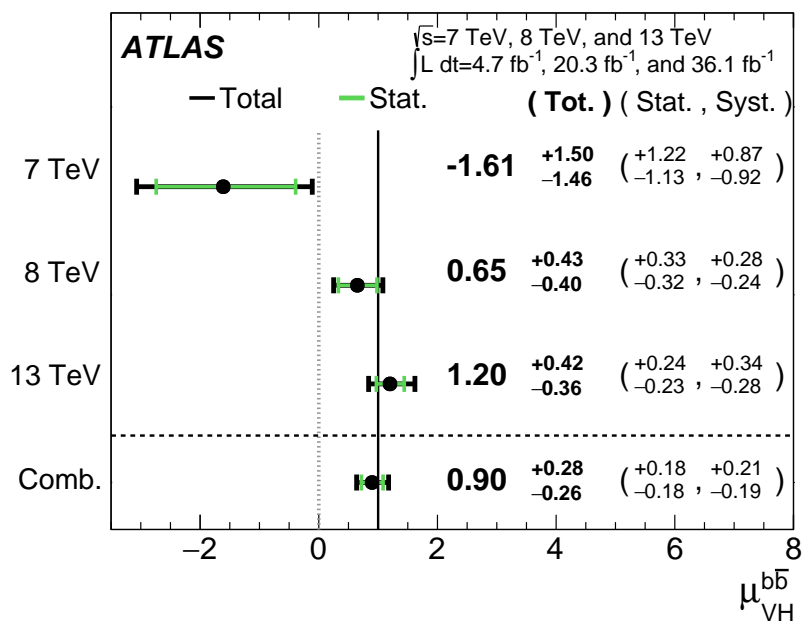


Figure 9.18: $\hat{\mu}$ summary plot for different \sqrt{s} values.

Vanitas vanitatum, omnis vanitas

Ecclesiastes 1:2

1979

10

1980

Closing Thoughts

1981 SINCE BOTH THE LHC and ATLAS are performing very well, it is only a matter of time before the
1982 evidence for SM $VH(b\bar{b})$ passes the 5 Gaussian standard deviation threshold necessary for discovery.
1983 Official discovery may come less than a year after reports of first evidence and may not even require
1984 a combination with the Run 1 result, depending on the latter two years of ATLAS Run 2 data (2017

1985 and 2018).

1986 It is entirely natural to ask, then, how essential the techniques and results described in this thesis
1987 will prove to be moving forward. Neither the LI/RF multivariate techniques nor combination with
1988 Run 1 datasets and their accompanying low signal strength values are necessary for discovery, and
1989 the latter may not even be essential to timely^{*} discovery of SM $VH(b\bar{b})$. Nevertheless, both sets of
1990 results hold great potential as key parts of a concerted ensemble of efforts towards precision Higgs
1991 physics.

1992 With the perhaps final major center of mass energy increase at the energy frontier ever complete,
1993 analyses must rely on increased integrated luminosity. Hence, it is becoming increasingly likely that
1994 any new fundamental physics at colliders will require the use of results of systematics limited analy-
1995 ses. This is the regime where the techniques described in this thesis will be most useful.

1996 As the LHC and its experiments undergo successive stages of upgrades and operate in evermore
1997 extreme environments, the statistical fit models used to describe LHC data will continue to evolve in
1998 complexity and diverge from their predecessors. The techniques described in Chapter 9 will become
1999 increasingly more vital to producing the best physics results possible. The improvement in precision
2000 from $\hat{\mu}_{VH} = 1.20^{+0.24}_{-0.23}(\text{stat.})^{+0.34}_{-0.28}(\text{syst.})$ to $\hat{\mu}_{VH} = 0.90^{+0.18}_{-0.18}(\text{stat.})^{+0.21}_{-0.19}(\text{syst.})$ is just the begin-
2001 ning.

2002 The best methods for reduction of systematic uncertainties will naturally depend in part on the
2003 state of the art for both fundamental physics process and detector modeling, but techniques that
2004 can reduce systematic uncertainties independent of fit model, dataset, and physics process provide

*i.e. before or coincident with CMS

2005 a promising avenue forward. The improvements in systematic uncertainties using the Lorentz In-
 2006 variant and RestFrames variable techniques in the $ZH \rightarrow \ell\ell b\bar{b}$ analysis, summarized in Table 10.1,
 2007 show that a smarter and more orthogonal decomposition of information in a collision event pro-
 2008 vides benefits independent of any clever treatment of \vec{E}_T^{miss} (which both schemes also provide). Both
 2009 techniques are readily extendible to other analysis channels, with the RestFrames concept demon-
 2010 strating stronger performance and greater flexibility to nearly completely generic final states.

	Standard	LI	RF
$\hat{\mu}$	$1.75^{+0.50, 0.64}_{-0.48, 0.45})$	$1.65^{+0.51, 0.59}_{-0.49, 0.41}$	$1.50^{+0.50, 0.53}_{-0.48, 0.36}$
Asi. $\Delta err(\mu)$	—	< 1%, +4.6%	-6.5%, -2.2%
Obs. $\Delta err(\hat{\mu})$	—	-7.5%, -3.7%	-16%, -8.8%
Stat only sig.	4.78	4.39 (-7.9%)	4.44 (-6.9%)
Exp. (Asi.) sig.	2.06	1.92 (-6.7%)	2.13 (+3.5%)
Exp. (data) sig.	1.76	1.73 (-1.7%)	1.80 (+3.4%)
Obs. (data) sig.	2.87	2.79 (-2.8%)	2.62 (-8.6%)

Table 10.1: Summary of performance figures for the standard, LI, and RF variable sets. Uncertainties on $\hat{\mu}$ are quoted stat., syst. In the case of the latter two, % differences are given where relevant. Differences in errors on μ are on full systematics and total error, respectively.

2011 Critical work remains to be done refining and extending the treatment of both the LI and RF
 2012 techniques in $VH(b\bar{b})$ analyses and their fit models, and completely independent techniques, like
 2013 the use of multiple event interpretations addressed in Appendix B promise further improvements
 2014 still.
 2015 No one can say for certain what the future of the energy frontier of experimental particle physics
 2016 may hold, but more nuanced treatments of the information in collision events born of meaningful
 2017 physical insight are sure to light the way.

If it's stupid but it works, it isn't stupid.

Conventional Wisdom

A

2018

2019

Micromegas Trigger Processor Simulation

2020 IN ORDER TO PRESERVE key physics functionality by maintaining the ability to trigger on low p_T
2021 muons, the Phase I Upgrade to ATLAS includes a New Small Wheel (NSW) that will supply muon
2022 track segments to the Level 1 trigger. These NSW trigger segments will combine segments from the
2023 sTGC and Micromegas (MM) trigger processors (TP). This note will focus in particular on the algo-

2024 rithm for the MMTP, described in detail with initial studies in ⁴¹. The goal of this note is to describe
2025 the MMTP algorithm performance under a variety of algorithm settings with both nominal and
2026 misaligned chamber positions, as well as addressing a number of performance issues.

2027 This note is organized as follows: the algorithm and its outputs are briefly described in Section
2028 A.1; Monte Carlo samples used are in Section B.1; nominal algorithm performance and certain quan-
2029 tities of interest are described in Section A.3; algorithm performance under misalignment, misalign-
2030 ment corrections, and corrected performance are shown in Section A.9; and conclusions are pre-
2031 sented in Section A.24.

2032 **A.1 ALGORITHM OVERVIEW**

2033 The MMTP algorithm is shown schematically in Figure A.1, taken from ⁴¹, where a more detailed
2034 description may be found. The algorithm begins by reading in hits, which are converted to slopes.
2035 These slopes are calculated under the assumption that the hit originates from the IP; slopes calcu-
2036 lated under this assumption are denoted by a superscript g for global in order to distinguish them
2037 from local slopes calculated using only hits in the wedge. In the algorithm simulation, events are
2038 screened at truth level to make sure they pass certain requirements. The track's truth-level coor-
2039 dinates must place it with the wedge since some generated tracks do not reach the wedge. These
2040 hits are stored in a buffer two bunch crossings (BCs) in time deep that separates the wedge into so-
2041 called "slope-roads." If any given slope-road has sufficient hits to pass what is known as a coinci-
2042 dence threshold, a fit proceeds. A coincidence threshold is a requirement for an event expressed as
2043 $aX+bUV$, which means that an slope-road must have at least a hits in horizontal (X) planes and at

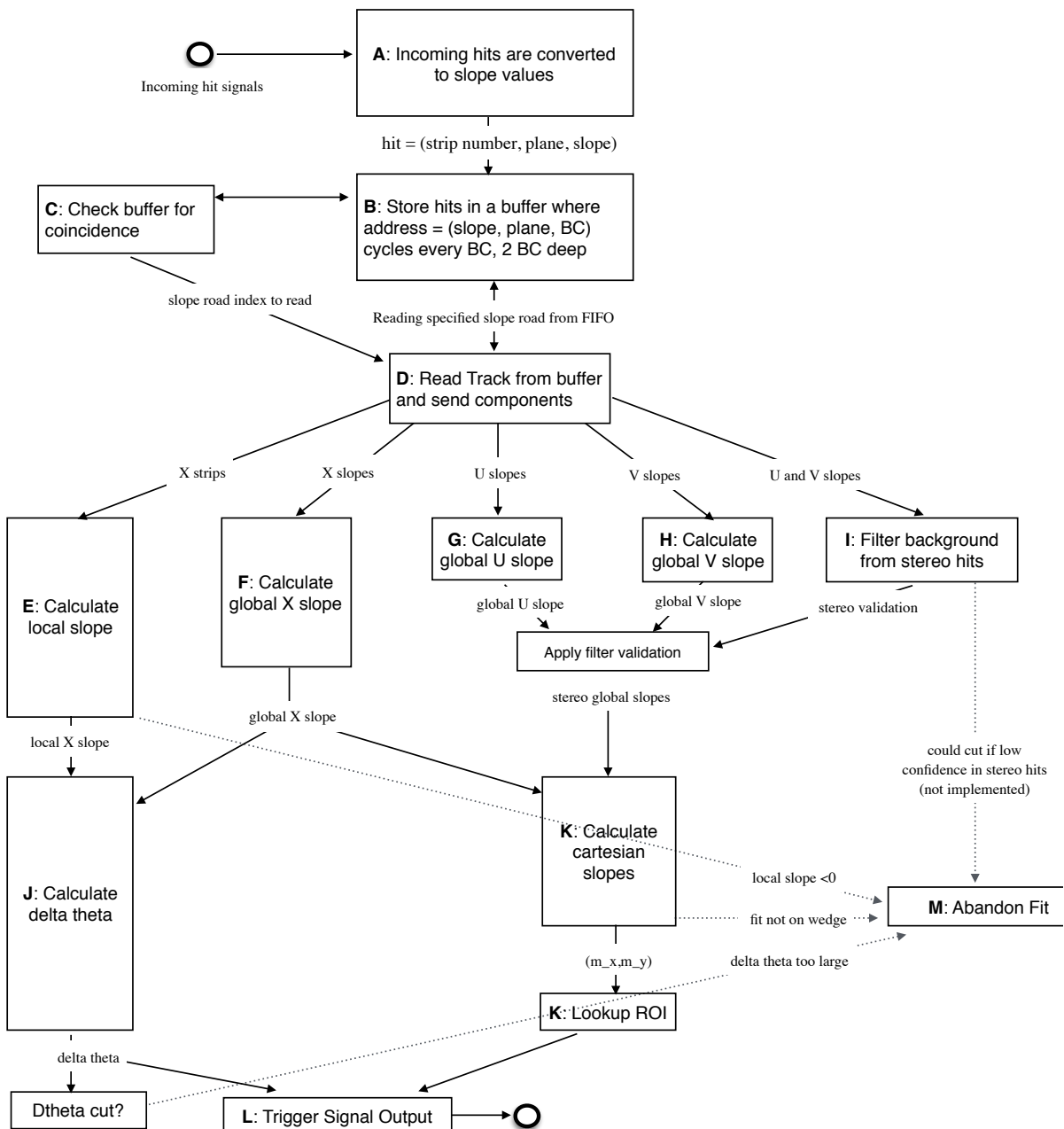


Figure A.1: A flow chart describing the algorithm steps, taken from⁴¹.

2044 least b hits in stereo (U or V (corresponding to positive and negative stereo rotations)) planes. For
 2045 coincidence thresholds with a $2X$ hit requirement there is the extra requirement that, in the case of
 2046 only $2X$ hits, one be on each quadruplet in order to ensure an adequate lever arm for the $\Delta\theta$ calcu-
 2047 lation. Note that less stringent (lower hit) coincidence thresholds are inclusive; i.e. a slope-road pass-
 2048 ing a $4X+4UV$ cut automatically passes $2X+1UV$. The coincidence threshold, size of the slope-roads
 2049 (denoted b), and the number of slope-roads into which each horizontal and stereo hits get written
 2050 centered upon their nominal value are configurable parameters of the algorithm.

2051 An individual hit's slope is calculated as shown in Equation A.1, where y_{base} is the local y coordi-
 2052 nate (orthogonal to the beamline and direction of the horizontal strips) of a station's base, w_{str} is the
 2053 strip pitch, n_{str} is the hit's strip number, and z_{plane} is the location of the hit's plane along the beam-
 2054 line.

$$M_{hit} = \frac{y}{z} = \frac{y_{base}}{z_{plane}} + \frac{w_{str}}{z_{plane}} \times n_{str} \quad (\text{A.1})$$

2055 In the fit, individual hit slopes in a slope-road are used to calculate global slopes associated with each
 2056 plane type, which are averages (e.g. M_X^{ℓ} for the average slope of horizontal planes). These in turn are
 2057 used to calculate the three composite slopes: slopes associated with the horizontal (m_x) and vertical
 2058 coordinates (m_y) and the local slope of hits in the horizontal planes (M_X^l), all of which are shown in
 2059 Equation A.4. Note that the expression for M_X^l differs but is equivalent to the expression given in ⁴¹.
 2060 This is due to a procedural change in the algorithm. The local X slope is expressed in ⁴¹ as:

$$M_X^{local} = A_k \sum_i y_i z_i - B_k \sum_i y_i, \quad B_k = \frac{1}{n} \sum_i z_i A_k = \bar{z} A_k \quad (\text{A.2})$$

2061 Procedurally, this entails doing the sums over y_i and $y_i z_i$, multiplying the sums by A_k , B_k , and then
 2062 subtracting both of these numbers, $\mathcal{O}(10^3)$, to get local slopes, $\mathcal{O}(10^{-1})$, while requiring preci-
 2063 sion on these numbers on the order of $\mathcal{O}(10^{-3})$. This requires precision in the sums $\mathcal{O}(10^{-7})$,
 2064 and with 32 bit fixed point numbers, there are deviations with respect to the floating point calcula-
 2065 tions at the level of $\mathcal{O}(10^{-5})$, which is enough to introduce a significant bias in the $\Delta\theta$ calculation.

2066 In order to prevent these errors, we do the subtraction first

$$M_X^{local} = A_k \sum_i y_i z_i - B_k \sum_i y_i = A_k \sum_i (y_i z_i - y_i \bar{z}) = B_k \sum_i y_i \left(\frac{z_i}{\bar{z}} - 1 \right) \quad (\text{A.3})$$

2067 Thus, we change the order of operations and store $1/\bar{z}$ instead of A_k in addition to B_k . We also
 2068 change the units of y_i and z_i in the calculation by dividing the millimeter lengths by 8192.* With
 2069 these changes, a 32 bit fixed point based algorithm has essentially identical performance to that of an
 2070 algorithm based on the usual C++ 32 floating point numbers. Future work includes converting the
 2071 32 bit fixed point arithmetic to 16 bit where possible in the algorithm. While introducing 16 bit num-
 2072 bers uniformly might seem preferable, since simple 16-bit operations in the firmware can be done in
 2073 a single clock tick, and a larger number of bits increases the algorithm latency, some numbers in the
 2074 algorithm will require a larger number of bits, in particular in the local slope calculation, which is
 2075 the single calculation in the algorithm requiring the largest numeric range.

2076 In Equation A.4, θ_{st} is the stereo angle of 1.5 degrees; the sums are over relevant planes; \bar{z} is the
 2077 average position in z of the horizontal planes; and y_i and z_i in the local slope expression refer to the y

*Chosen since it is a perfect power of 2 and of order the length scale of z in millimeters

2078 and z coordinates of hits in X planes.

$$m_x = \frac{1}{2} \cot \theta_{st} (\mathcal{M}_U^g - \mathcal{M}_V^g), \quad m_y = \mathcal{M}_X^g, \quad \mathcal{M}_X^l = \frac{\bar{z}}{\sum_i z_i^2 - 1/n (\sum_i z_i)^2} \sum_i y_i \left(\frac{z_i}{\bar{z}} - 1 \right) \quad (\text{A.4})$$

2079 From these composite slopes, the familiar expressions for the fit quantities θ (the zenith), ϕ (the az-
2080 imuth[†]), and $\Delta\theta$ (the difference in θ between the direction of the segment extrapolated back to the
2081 interaction point and its direction when entering the detector region; the following is an approxima-
2082 tion) may be calculated, as noted in⁴¹:

$$\theta = \arctan \left(\sqrt{m_x^2 + m_y^2} \right), \quad \phi = \arctan \left(\frac{m_x}{m_y} \right), \quad \Delta\theta = \frac{\mathcal{M}_X^l - \mathcal{M}_X^g}{1 + \mathcal{M}_X^l \mathcal{M}_X^g} \quad (\text{A.5})$$

2083 Looking at Equations A.4 and A.5, the dependence of fit quantities on input hit information be-
2084 comes clear. $\Delta\theta$ relies exclusively on information from the horizontal (X) planes. Both θ and ϕ rely
2085 on both horizontal and stereo slope information. However, the sum in quadrature of m_x and m_y in
2086 the arctangent for θ means that θ is less sensitive to errors in stereo hit information than ϕ . Given
2087 that θ_{st} is small, $\cot \theta_{st}$ is large (~ 38), so m_x multiplies small differences in \mathcal{M}_U and \mathcal{M}_V , where m_y
2088 is simply an average over slopes. This means that while errors in horizontal hit information will af-
2089 fect all three fit quantities, comparable errors in stereo hits will have a proportionately larger effect
2090 on θ and particularly on ϕ . The $\Delta\theta$ cut after step J in Figure A.1 has been implemented, requiring
2091 all fits to have $|\Delta\theta| < 16$ mrad. This requirement ensures good quality fits but also slightly reduces

[†]Defined with respect to the center (y) axis and *not* the axis of the strips (x) as is sometimes typical, so a hit along the center of the wedge has $\phi = 0$

2092 algorithm efficiency.

2093 A.2 MONTE CARLO SAMPLES

2094 The Monte Carlo (MC) samples used for these studies were generated in Athena release 20.1.0.2 us-
2095 ing simulation layout ATLAS-R2-2015-01-01-00 with muon GeoModel override version MuonSpectrometer-
2096 R.07.00-NSW and modifications to have two modules per multiplet and xxuvuvxx geometry with a
2097 stereo angle of 1.5 degrees. Muons of a single p_T were generated around the nominal IP with a smear-
2098 ing of 50 mm along the beam line and 0.015 mm orthogonal to it; these muons were pointed toward
2099 a single, large sector of the NSW. Each event consists of one muon fired towards the single NSW
2100 wedge separated by effectively infinite time from other events.

2101 A.3 NOMINAL PERFORMANCE

2102 In order to evaluate algorithm performance, a number of quantities are evaluated, including the fit
2103 quantities θ , ϕ , and $\Delta\theta$ as well as algorithm efficiency. Unless otherwise stated, that algorithm is
2104 run with a 4X+4UV coincidence threshold, slope-road size of 0.0009, an X tolerance of two slope-
2105 roads (i.e. hits in horizontal planes are written into the two slope-roads closest to the hits' value),
2106 a UV tolerance of four slope-roads[†], and a charge threshold requirement on hits of 1 (measured in
2107 units of electron charge) for a sample of 30 000 events with a muon p_T of 100 GeV. Samples were
2108 also generated for p_T values of 10 GeV, 20 GeV, 30 GeV, 50 GeV, and 200 GeV, which were used in

[†]The larger tolerance on stereo hits takes into account the particulars of the m_x calculation mentioned in Section A.1.

2109 some of the following studies.

2110 A.4 FIT QUANTITIES

2111 In order to evaluate the performance of the algorithm’s fit quantities θ , ϕ , and $\Delta\theta$, fit values are com-
2112 pared to truth-level MC values. The residual of the three fit quantities, $\theta_{fit} - \theta_{tru}$, $\phi_{fit} - \phi_{tru}$, and
2113 $\Delta\theta_{fit} - \Delta\theta_{tru}$, are recorded for every fitted track. The distributions of these quantities, in particular
2114 their biases and standard deviations, are then used to evaluate performance. In most cases, follow-
2115 ing⁴¹, the mean and standard deviation of a 3σ Gaussian fit are quoted, as they capture the main
2116 features of the algorithm and generally behave like the raw mean and rms. Nevertheless, discussion
2117 of the raw quantities will be included when their behavior deviates markedly from that of the 3σ fit
2118 quantities.

2119 The truth-level quantities used in residual distribution are taken from information in the MC.

2120 These come directly from the MC for θ , ϕ , and $\Delta\theta$. These quantities, along with the geometry of
2121 the (large) wedge, are then in turn used to calculate truth-level values for any intermediate quantities
2122 used in the algorithm. $m_{x,tru}$, for instance, is given by $\tan \theta_{tru} \sin \phi_{tru}$.

2123 Residual distributions for fit quantities under the previously described default settings of the al-
2124 gorithm are shown in Figure A.2. Both the $\theta_{fit} - \theta_{tru}$ and $\Delta\theta_{fit} - \Delta\theta_{tru}$ distributions feature a
2125 mostly Gaussian shape with more pronounced tails. The mean bias for these distributions is negligi-
2126 ble at under one tenth of a milliradian, and the fitted (raw) rms values are 0.349 (0.614) mrad for θ
2127 and 1.03 (2.55) mrad for $\Delta\theta$. The case of the $\phi_{fit} - \phi_{tru}$ distribution is less straightforward, with both
2128 the shape and bias arising from the xxuvuvxx geometry and relatively large extent of one of the two

²¹²⁹ η -stations, as explained in Appendix B of³⁸. The fitted (raw) rms for the ϕ distribution is 8.67 (16.6)
²¹³⁰ mrad.

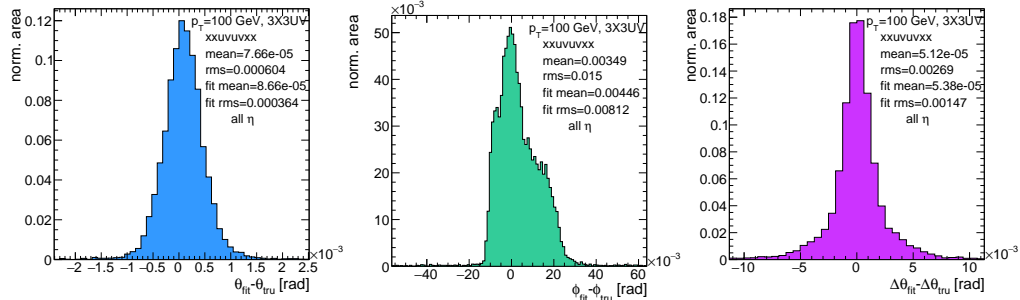


Figure A.2: Nominal residual plots; $\theta, \phi, \Delta\theta$ for $p_T = 100 \text{ GeV}$ muons

²¹³¹ Both increasing muon p_T and increasing muon η for a fixed p_T imply increasing muon energy. As
²¹³² muons become more energetic, two effects compete in affecting the quality of fit. On the one hand,
²¹³³ higher energy muons are deflected less by the ATLAS magnetic field, which should tend to improve
²¹³⁴ the quality of the fit, since the fitted θ (upon which $\Delta\theta$ also relies) and ϕ values are calculated under
²¹³⁵ the infinite momentum muon (straight track) assumption. However, as muon energy increases, the
²¹³⁶ likelihood that the muon will create additional secondaries increases, which creates extra hits that
²¹³⁷ degrade the quality of the fit. While the geometry of the multiplet is such that there is very good res-
²¹³⁸ olution in the direction orthogonal to the horizontal strip direction, the shallow stereo angle of 1.5
²¹³⁹ degrees means that early hits caused by secondaries can have an outsize impact on m_x . $\Delta\theta$, which
²¹⁴⁰ does not rely upon stereo information should feel the effect of secondaries the least and benefit from
²¹⁴¹ straighter tracks the most and hence benefit from higher muon energies; ϕ , relying upon stereo in-
²¹⁴² formation the most, would be most susceptible to secondaries and benefit the least from straighter

2143 tracks and hence least likely to benefit from higher muon energy; θ relies upon both horizontal and
 2144 vertical slope information, though small errors are less likely to seriously affect the calculation, so the
 2145 two effects are most likely to be in conflict for this fit quantity.

2146 The interplay of these effects on the residual standard deviations can be seen in their dependen-
 2147 cies on η (Figure A.3; note that the final point in each of these plots is the rms of the distribution
 2148 overall η) and p_T (Figure A.4). For $p_T = 100$ GeV muons, $\Delta\theta$ performance increases with η (en-
 2149 ergy), and ϕ performance decreases, as expected;[§] for θ , the two effects appear to compete, with per-
 2150 formance first increasing with η until the effects of secondaries begins to dominate. Integrated over
 2151 all η , the effects are less clearly delineated. Both $\Delta\theta$ and θ performance increases with increasing p_T ,
 2152 suggesting straighter tracks with increasing energy are the dominant effect for these quantities, while
 2153 ϕ performance appears to improve and then deteriorate (the slight improvement at high p_T is due to
 2154 the addition of the $\Delta\theta$ cut into the algorithm, which filters out very poor quality fits).

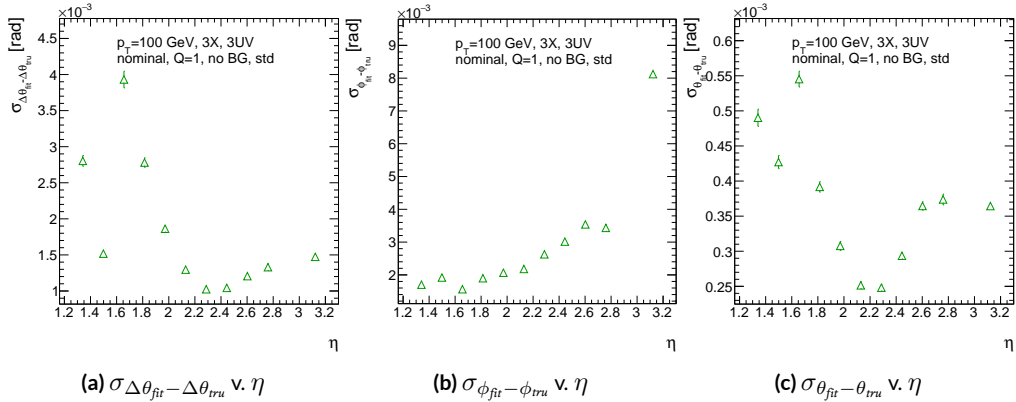


Figure A.3: The rms distributions of $\Delta\theta$, ϕ , and θ as a function of η for $p_T = 100$ GeV; the final point in each plot is the rms obtained from a fit to the full distribution including all η bins.

[§]The much worse overall performance for ϕ is due to the η dependent bias and other effects

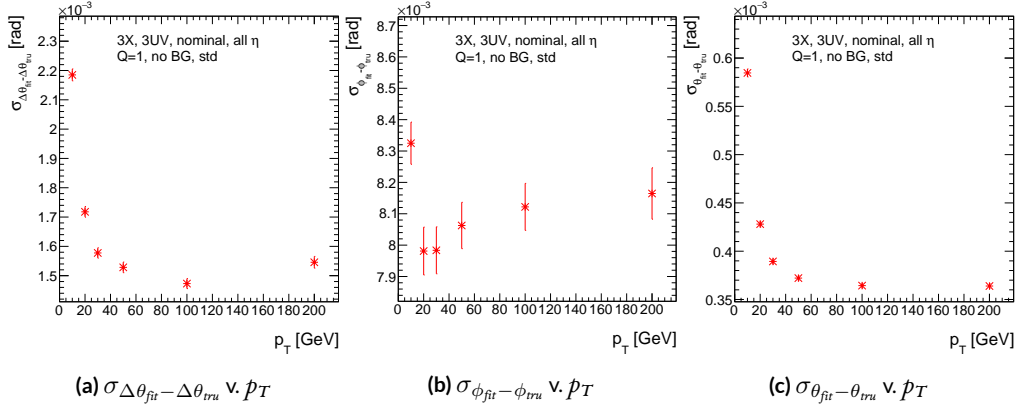


Figure A.4: The rms distributions of $\Delta\theta$, ϕ , and θ as a function of p_T .

2155 The rms of the three benchmark quantities as a function of algorithm set (i.e. slope-road) coinci-
 2156 dence threshold are shown in Figure A.5 using Gaussian fits and in Figure A.6 for the raw quantities.
 2157 The fitted σ 's for θ and ϕ are fairly stable across coincidence threshold. $\Delta\theta$, on the other hand, per-
 2158 forms better particularly for the most stringent coincidence threshold; this is a result of the fact that
 2159 additional information for more hits greatly improves the quality of the local slope fit calculation.
 2160 The raw rms is a different story. Naïvely, one would expect the performance to get better with more
 2161 stringent coincidence threshold, but this is not the case in Figure A.6. As the coincidence thresh-
 2162 old gets more stringent, fewer and fewer tracks are allowed to be fit. When moving from 2X hits to
 2163 3X hits, the tracks that get vetoed populate the tails of the distribution outside the 3σ fit range but
 2164 are not in the very extremes of the distribution. While tracks with 2X hits are of lower quality than
 2165 those with 3 and 4 X hits, tracks with the very worst fit values pass even the most stringent coinci-
 2166 dence threshold requirements (e.g. as a result of many hits arising from a shower of secondaries).
 2167 This is best illustrated when comparing the 2X+1UV $\Delta\theta$ residual distribution with the 4X+4UV

distribution in Figure A.7. As both the overlayed normalized curves and ratio distribution show,
 while the most central regions are fairly similar, the $\omega X + 1$ UV distribution is much more prominent
 in the tails but not the extreme tails, which means that, though the overall $\omega X + 1$ UV raw rms goes
 down, the overall quality of algorithm fits is worse.

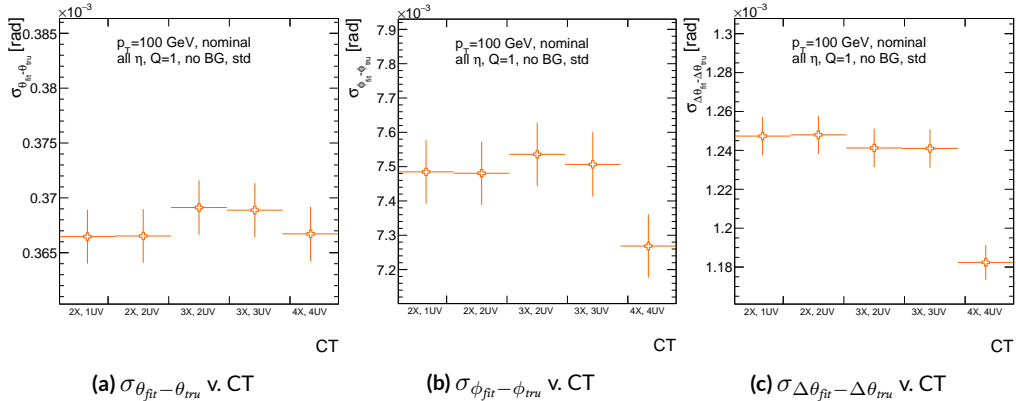


Figure A.5: The fitted rms of residual distributions for θ , ϕ , and $\Delta\theta$ as a function of coincidence threshold for $p_T = 100$ GeV.

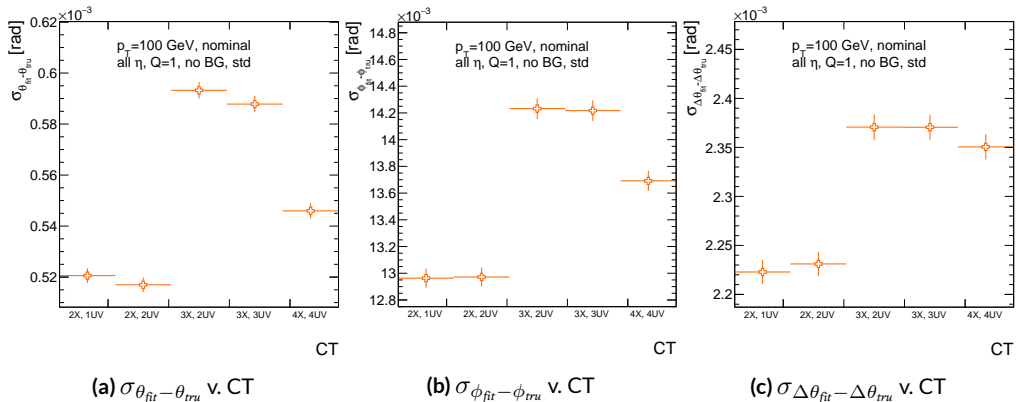


Figure A.6: The raw rms of residual distributions for θ , ϕ , and $\Delta\theta$ as a function of coincidence threshold for $p_T = 100$ GeV.

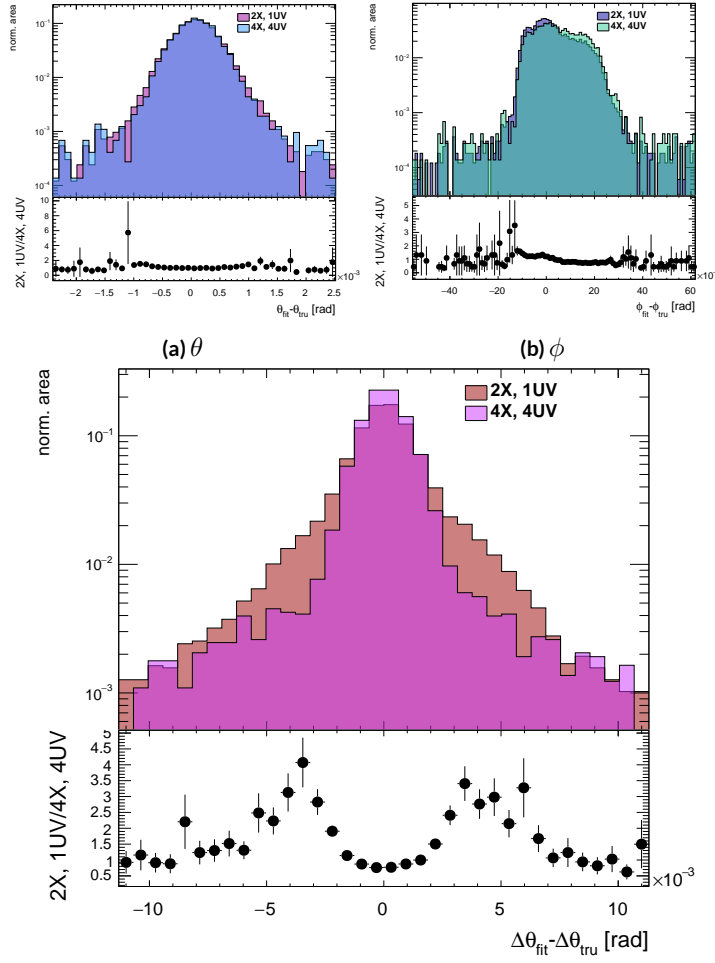


Figure A.7: Nominal $\Delta\theta$ residual distribution for $p_T = 100$ GeV muons with coincidence thresholds 2X+1UV and 4X+4UV normalized to the same area and plotted together (top) as well as the ratio of the 2X+1UV distribution and the 4X+4UV per bin.

2172 A.5 EFFICIENCIES

2173 Two general efficiencies have been formulated to study the performance of the MMTP algorithm.

2174 The first, denoted ε_{alg} , is the fraction of tracks that pass some (slope-road) coincidence threshold

2175 configuration that are successfully fit. An event that passes a slope-road coincidence but does not fit

2176 fails because some of the hits included are of sufficiently poor quality to throw off the fit. This effi-

2177 ciency answers the question of how often the algorithm performs fits when technically possible, giv-

2178 ing a measure of overall algorithm performance for a given configuration. For example, $\varepsilon = 95\%$ for

2179 $3X+2UV$ means that 95% of tracks that produce at least $3X$ hits and $2UV$ hits in at least one slope-

2180 road will be successfully fitted 95% of the time. The performance of this efficiency as a function of

2181 coincidence threshold, η (with the final point once again being the efficiency integrated over all η),

2182 and p_T is shown in Figure A.8. ε_{alg} is fairly constant in η and decreases with increased p_T , which can

2183 be attributed to the increased likelihood of secondaries introducing lower quality hits that cause the

2184 fit to fail.

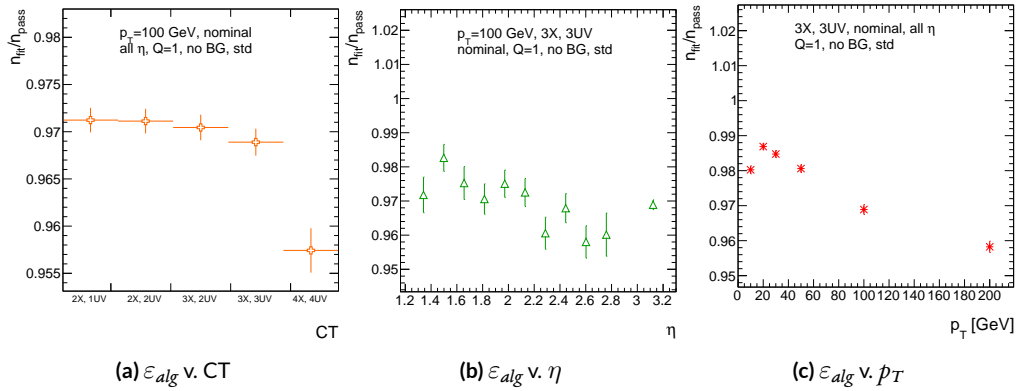


Figure A.8: ε_{alg} and as a function of coincidence threshold, η (final point is ε_{alg} integrated over all η), and p_T .

2185 The second efficiency type, denoted ε_{fit} , is the fraction of tracks that enter the wedge whose fits
 2186 (if any) satisfy a given coincidence threshold. This efficiency can be used to help establish an optimal
 2187 coincidence threshold setting in the algorithm, balancing the improved overall fit quality of higher
 2188 thresholds with the greater number of fits for lower thresholds. Hence, an ε_{fit} of 95% at 3X+2UV
 2189 means that 95% of tracks entering the wedge are fit and that these fits include at least 3X and 2UV
 2190 hits. ε_{fit} as a function of coincidence threshold is shown in Figure A.9 (a), which shows that the ma-
 2191 jority of fits having at most 3X+3UV hits. That there is a marked drop to 4X+4UV is not surpris-
 2192 ing, as there is a substantial population outside the 4X+4UV bin in Figure A.10. The behavior of
 2193 ε_{fit} with η in Figure A.9 (b) (with the final point once again being the efficiency integrated over all
 2194 η) is much more varied, with geometric effects of detector acceptance coming into play. The per-
 2195 formance of ε_{fit} as a function of p_T , shown in Figure A.9 (c), is similar to that of ε_{alg} coincidence
 2196 threshold, again consistent with the effects of secondaries at higher energies.

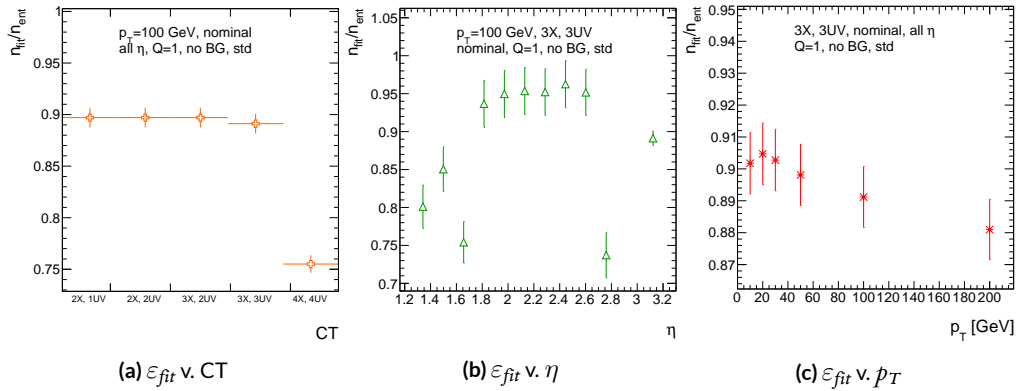


Figure A.9: ε_{fit} and as a function of coincidence threshold, η (final point is ε_{fit} integrated over all η), and p_T .

2197 In order to better understand efficiency behavior with coincidence threshold, the distribution of

2198 highest slope-road coincidence thresholds in events is shown in Figure A.10, with the o,o bin con-
 2199 taining events that did not meet requirements for the minimum $2X+1UV$ coincidence threshold for
 2200 a fit to occur. That the efficiency is lower at higher coincidence threshold suggests that most of the
 2201 fits that fail have high hit multiplicity (i.e. a similar number fails in each of the coincidence thresh-
 2202 old bins in Figure A.8 (a)), which is consistent with the interpretation that the primary source of fit
 2203 failures is bad hits originating from secondaries created by higher energy muons.

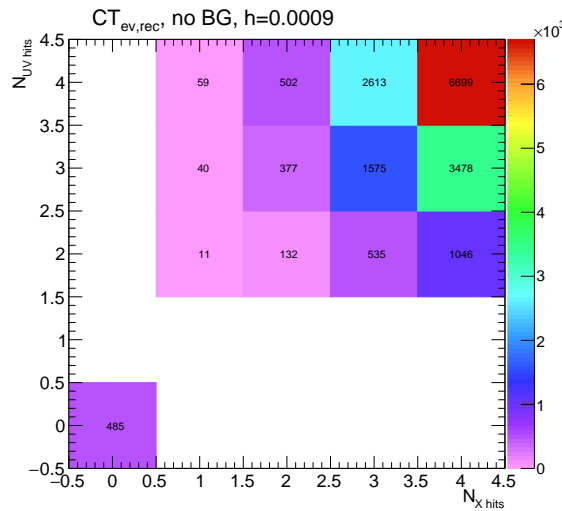


Figure A.10: The distribution of highest slope-road coincidence thresholds in events; the 0,0 bin is the number of events passing selection requirements that fail to form the minimum $2X+1UV$ coincidence threshold necessary for a fit.

2204 A.6 INCOHERENT BACKGROUND

2205 The default slope-road size and tolerances associated with horizontal and stereo hits used in the
2206 above studies were configured to optimize algorithm performance, similar to studies in ⁴¹. In order
2207 to evaluate algorithm performance under conditions with more limited resources, as might be ex-
2208 pected at run-time, additional studies were conducted with the slope-road size and hit tolerances set
2209 equivalent to the sensitive area of a single VMM chip[¶] both with and without generation of incoher-
2210 ent background.

2211 Incoherent background is generated based on the assumption that the intensity only varies as a
2212 function of the distance from a point to the beamline, r . The number of hits per unit area per unit
2213 time as a function of r is given in Equation A.6 and taken from ⁴¹.

$$I = I_0 (r/r_0)^{-2.125} \quad (\text{A.6})$$

2214 where $r_0 = 1000$ mm and $I_0 = 0.141$ kHz/mm²

2215 Background generation happens per event as follows:

- 2216 1. Determine the total number of hits to be generated in this event according to a Poisson distri-
2217 bution
- 2218 2. Assign a time to hits uniformly in $[t_{\text{start}} - t_{\text{VMM}}, t_{\text{end}}]$ where start and end are for the event
2219 clock and t_{VMM} is the VMM chip deadtime (100 ns)
- 2220 3. Assign a plane to hits uniformly
- 2221 4. Assign a ϕ value to hits uniformly

[¶]One VMM is assumed to cover 64 MM strips at 0.445 mm each.

2222 5. Assign an r to hits according to Equation A.6

2223 6. Calculate hit information according to these values.

2224 The expectation value for the Poisson distribution is determined by integrating Equation A.6

2225 over the surface area of the wedge to get the total hit rate for the wedge, Γ , and then multiplying this

2226 by the length of the time window over which hits may be generated. With $H = 982$ mm, $b_1 =$

2227 3665 mm, and $\theta_w = 33\pi/180$, we find^{||}:

$$\Gamma = 2I_0 r_0^{2.125} \int_0^{\theta_w/2} d\phi \int_{H \sec \phi}^{(H+b_1) \sec \phi} r dr r^{-2.125} = 98.6657 \text{ MHz} \quad (\text{A.7})$$

2228 In this case, we have taken the nominal values of the MM sector geometry for H (wedge base), b_1

2229 (the wedge height), and θ_w (the wedge opening angle).

2230 The effects of incoherent background and larger slope road size are summarized in Figure A.11 for

2231 efficiencies and in Figure A.13 and Table A.1 for residual of fit quantities.

2232 Figure A.11 show the effect of both wider slope-roads and the introduction of background on ef-

2233 ficiencies. The introduction of wider slope-roads increases the chance that an early errant hit (either

2234 from secondaries/ionization or background) will be introduced into the fit, and the presence of in-

2235 coherent background greatly increases the number of such errant hits. Both wider slope-roads and

2236 background drive down the number of fits (numerator) in both efficiencies, and background can

2237 artificially inflate the denominator of ε_{alg} , a reco-level, slope-road coincidence threshold. The shape

2238 of the ε_{fit} versus coincidence threshold distributions remains fairly constant with each complicat-

^{||}Using Mathematica and the extra factor of r from the volume element

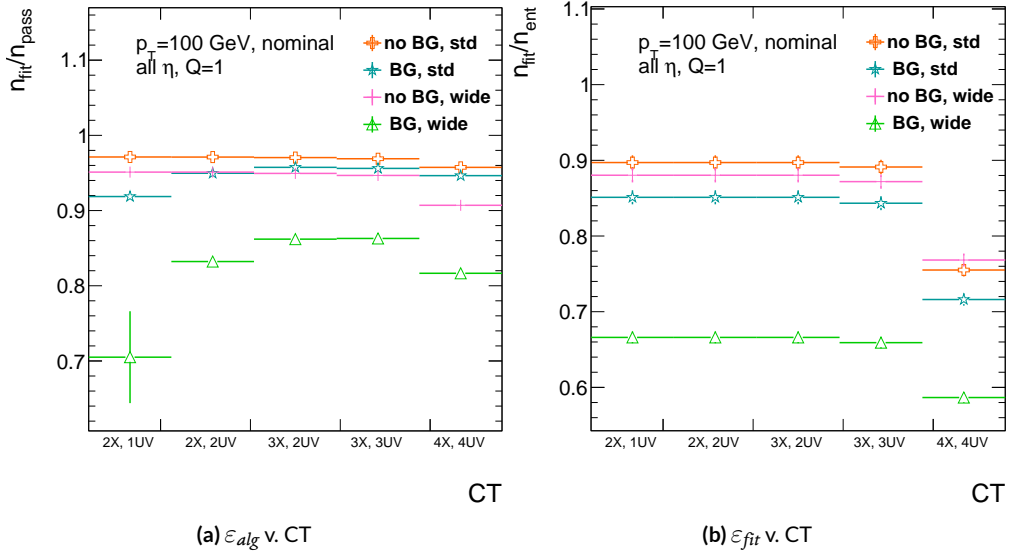


Figure A.11: The algorithm and total efficiencies as a function of coincidence threshold for different background settings and slope-road sizes (standard and wide (one slope road as 1 VMM chip)).

ing factor (standard, wider slope-roads, background, both wider slope-roads and background), suggesting many muons will simply not be fit with any number of hits; ε_{fit} does not take into account the coincidence threshold of tracks that are not fit, so the effect appears uniform across coincidence threshold. The effects seen for ε_{alg} , which are not uniform across coincidence threshold can be better understood when examining the distribution of event highest coincidence thresholds, shown for wide slope-roads both without and with background in Figure A.12. Take, for example the 2X+1UV case. The 2X+1UV bin in particular has a marked increase when background is introduced. No new good tracks are introduced between the no background and background cases, so the increase is entirely due to bad, background hits; hence, these events do not (and should not) fit, causing the particularly pronounced drop in this bin between these two cases in Figure A.11.

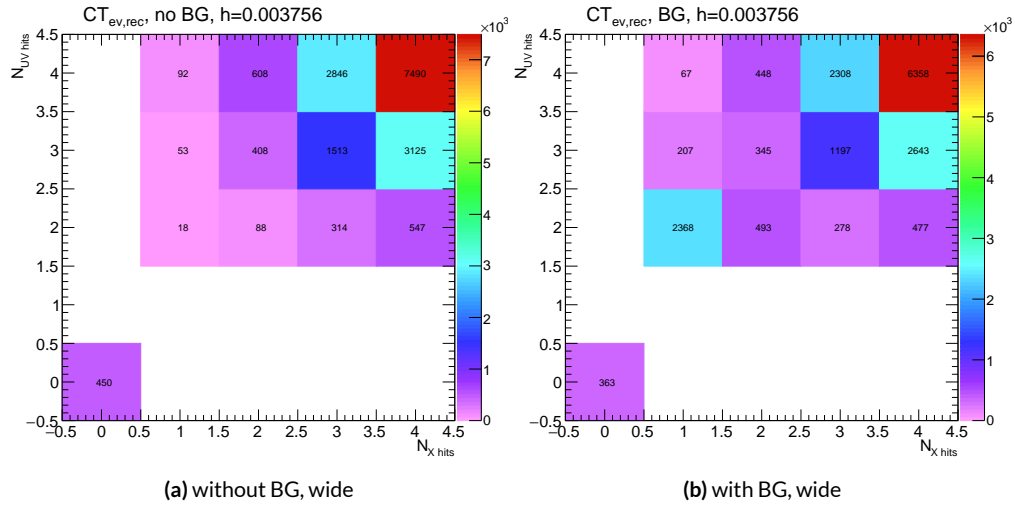


Figure A.12: The distribution of highest slope-road coincidence thresholds in events for the algorithm with wide slope-roads (width of 1 VMM) both without (a) and with (b) incoherent background; the 0,0 bin is the number of events passing selection requirements that fail to form the minimum $2X+1UV$ coincidence threshold necessary for a fit.

The effect of increasing slope-road size and incoherent background on fit quantity residual rms values as a function of p_T is shown in Figure A.13. As the figure shows, the fitted rms values are fairly robust against increased slope-road size and background. This does not hold for all of the raw rms values, however, as shown in Table A.1. Just as with the efficiencies, the introduction of background has a larger effect than that of increased slope-road size, which does not seem to have an overly large impact on any of the fit quantities on its own. While $\Delta\theta$ remains robust to both increased slope-road size and background (likely due to the $\Delta\theta$ cut of 16 mrad built into the algorithm), θ shows some degradation in performance, and the ϕ residual raw rms shows a very large increase upon the introduction of background. Nevertheless, the contrasting behavior of the fitted and raw rms values suggests that tracks that drive up the raw rms values already had very poor fit quality even before the introduction of background, so the impact on fit quantities should remain fairly limited.

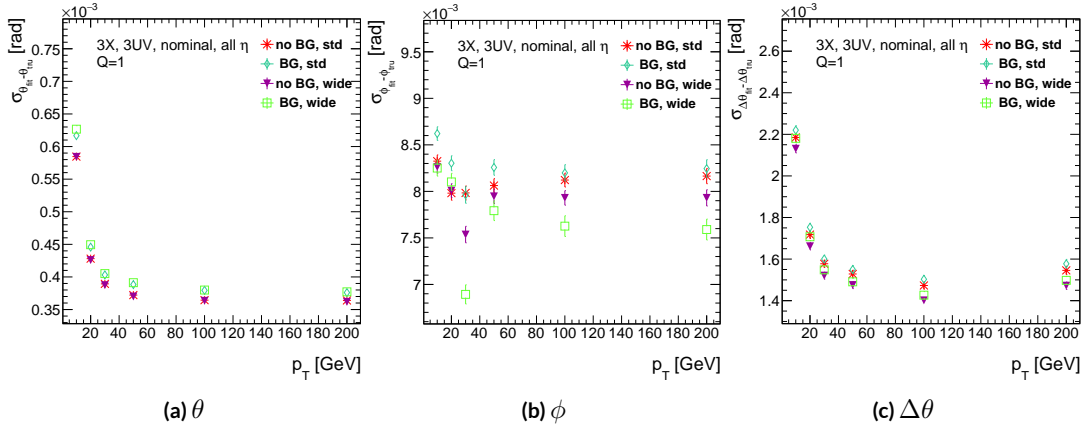


Figure A.13: The three fit quantity residual rms values as a function of p_T for different background settings and slope-road sizes (standard and wide (one slope road as 1 VMM chip)).

	No BG, std	No BG, wide	BG, std	BG, wide
θ	0.364 (0.604)	0.363 (0.542)	0.379 (0.886)	0.380 (1.07)
ϕ	8.12 (15.0)	7.93 (13.2)	8.20 (24.6)	7.63 (24.8)
$\Delta\theta$	1.47 (2.69)	1.40 (2.66)	1.50 (2.89)	1.43 (2.90)

Table A.1: The fitted (absolute) σ of fit quantity residuals in mrad under different algorithm settings.

2260 As Table A.1 shows, rms values appear to be robust to an increase in slope-road size. Neverthe-
2261 less, though the fitted σ residual values are also fairly robust to the introduction of background, the
2262 raw rms values are not. While the raw $\Delta\theta$ rms stays stable, both θ and ϕ suffer noticeable degra-
2263 dation, which suggests that the introduction of background has a detrimental effect on horizontal
2264 slope residual (i.e. on stereo strips in particular). This level of degradation is likely acceptable for θ ,
2265 though further steps may need to be taken to address ϕ .

2266 **A.7 BCID**

2267 A fitted track's BCID is determined by the most common BCID associated with its hits. Concerns
2268 were raised that this might cause incorrect BCID association for fitted tracks. In order to address
2269 this, the rate of successful BCID association for fitted tracks was recorded. Figure A.14 shows the
2270 dependence of this success rate as a function of p_T and coincidence threshold in the different back-
2271 ground and resource conditions used in the previous section. The successful BCID identification
2272 rate is always over 99.5%, demonstrating that this issue is not a concern with the state-of-the-art de-
2273 tector simulation.

2274 **A.8 CHARGE THRESHOLD**

2275 The MMTP uses the first hits registered passing a charge threshold requirement given in units of
2276 electron charge. In principle, it would be beneficial to be able to use any hits that are registered re-
2277 gardless of deposited charge, but in the high rate environment envisioned for the NSW, this require-
2278 ment might need to be raised. Nominal algorithm settings have this charge threshold requirement

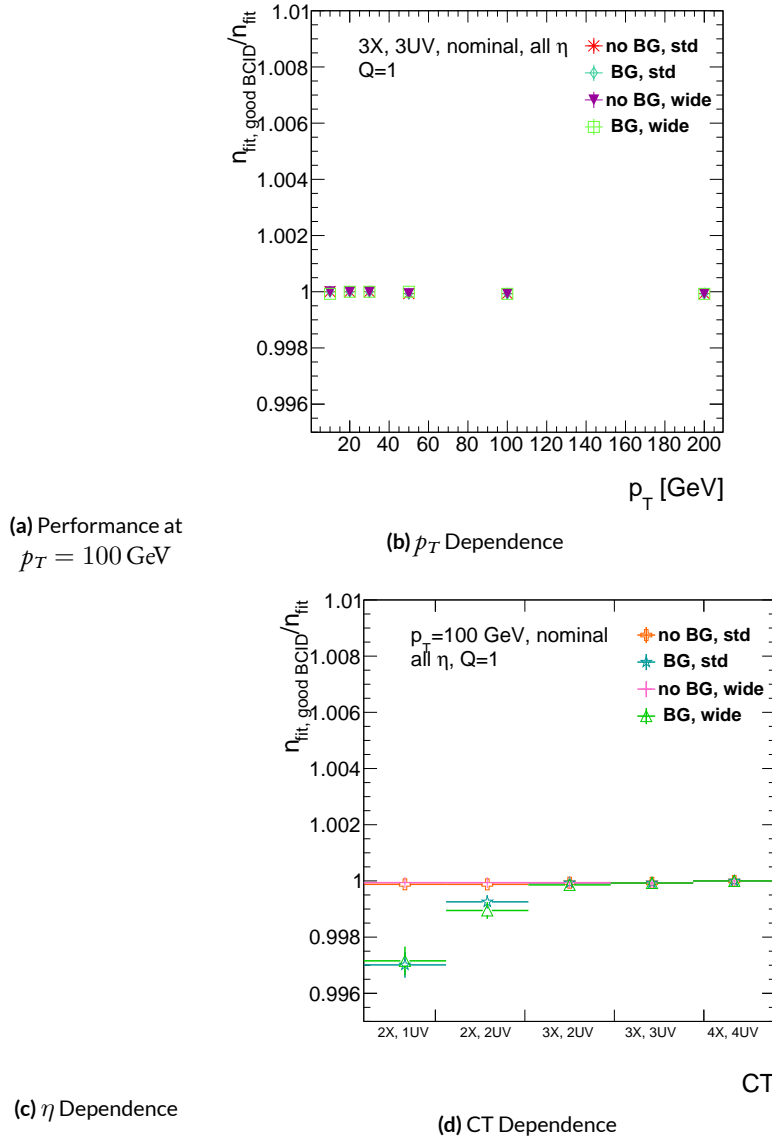


Figure A.14: The rate of good BCID association based majority hit BCID as a function of p_T and coincidence threshold.

2279 set to 1, and studies were conducted on algorithm performance for charge threshold values of 0, 1,
 2280 and 2. Efficiencies as a function of coincidence threshold for different charge thresholds are shown
 2281 in Figure A.15. Increasing the charge threshold lowers both efficiencies, particularly at high coinci-
 2282 dence threshold, which suggests that energetic muons with secondaries create both very many hits
 2283 and hits with higher charge. While the shapes of the fit quantity distributions as a function of p_T in
 2284 Figure A.16 are fairly constant across charge threshold, performance is not. θ and $\Delta\theta$ show some im-
 2285 provement with higher charge threshold, particularly at low p_T , suggesting that resolution improves
 2286 in the vertical direction, but ϕ shows degradation at higher charge threshold, which is a symptom
 2287 of more highly charged particles experiencing greater bending in the ATLAS magnetic field in the ϕ
 2288 direction.

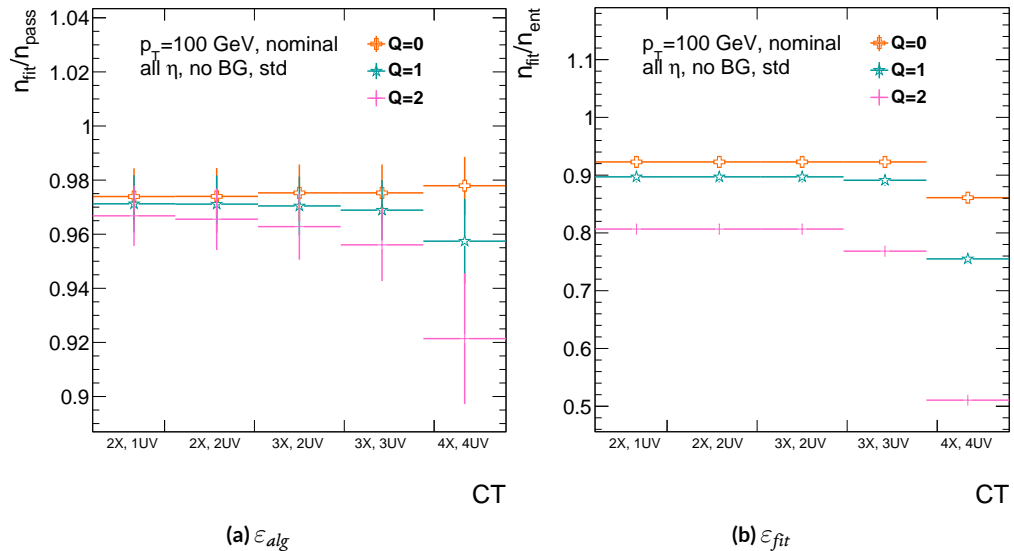


Figure A.15: The efficiencies as a function of coincidence threshold for charge thresholds of 0, 1, and 2.

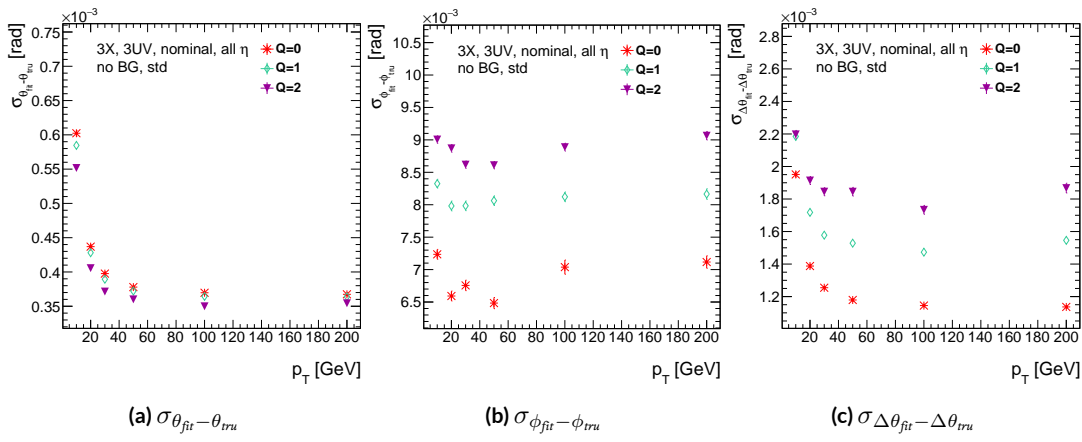


Figure A.16: The fit quantity residual rms values as a function of p_T for charge thresholds of 0, 1, and 2.

2289 A.9 MISALIGNMENTS AND CORRECTIONS

2290 The performance of the trigger algorithm under misalignment has been studied for each of the six
2291 alignment quantities (three translations and three rotations all along the principal axes) described
2292 in[?] and[?], whose convention we will follow here. For the simulated wedge studied here the local co-
2293 ordinates described in[?] are taken to be centered at the center of the base of the wedge^{**}, the local t
2294 axis corresponds to the axis of the beam line, the local z axis corresponds to the direction orthogo-
2295 nal to both the beam line and the horizontal strips, and the local s axis completes the right-handed
2296 coordinate system. The rotation angles α , β , and γ correspond to rotations around the local t , z ,
2297 and s axes, respectively. Note that the local s , z , and $-t$, axes correspond to the usual global x , y , and
2298 z axes. Misalignments were studied in twenty evenly spaced increments from nominal positions
2299 to misalignments of 1.5 mrad for the rotations (-1.5 mrad to +1.5 mrad for the γ case), and of 5 mm
2300 (a roughly corresponding linear shift) for the translations. In all cases, the front quadruplet is mis-
2301 aligned while the rear quadruplet remains in its nominal position. While only the front quadruplet
2302 of a single wedge is misaligned, the framework for misalignment presented below could be used to
2303 study generic local and global misalignments. The six misalignments are schematically represented
2304 in Figure A.17.

2305 Chamber misalignments manifest themselves as altered strips in algorithm input. In order to sim-
2306 ulate the effects of misalignment, the change in the local y coordinate—the distance from the bot-

**Not, as is sometimes the case, the centroid position for simplicity's sake, as the agreed upon geometry of the detector changed several times while studies were in progress; any transformation in a centroid-origin coordinate system can of course be formed by a combination of the six transformations examined.

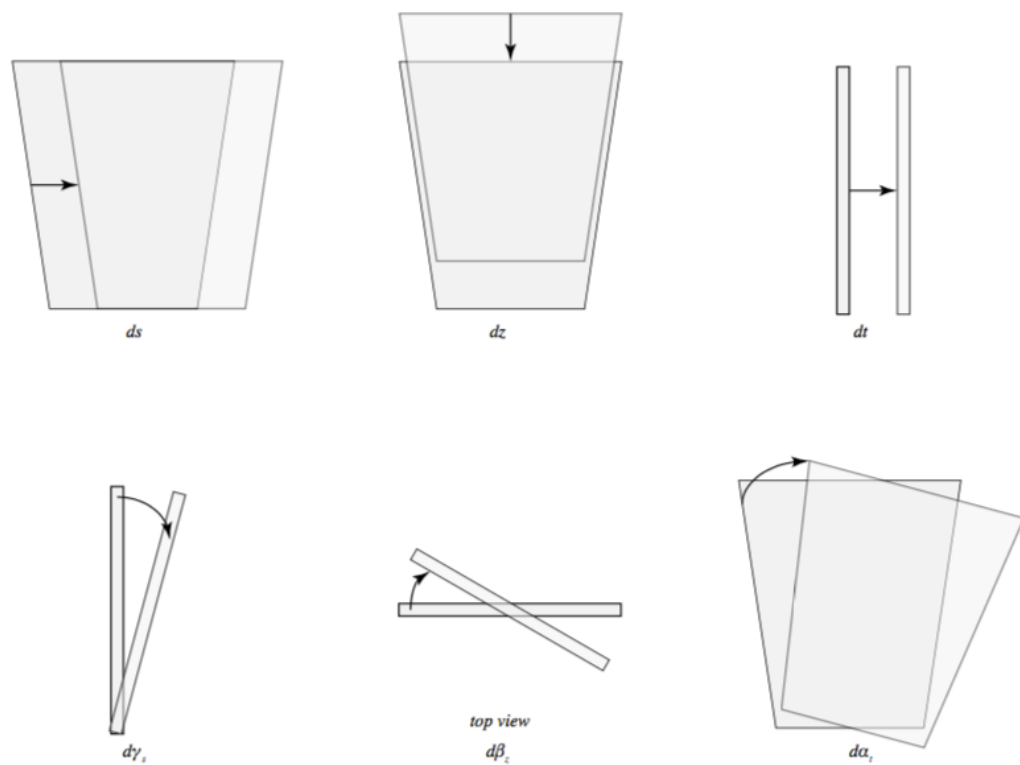


Figure A.17: The different misalignment cases as defined in the AMDB manual.

2307 tom wedge center in the direction perpendicular to both the beamline and the strip direction—is
 2308 calculated for a track coming straight from the interaction point defined by the truth-level θ and ϕ
 2309 angles for generic misalignment. This displacement in y is then added to input hit information and
 2310 the algorithm is then run normally.

2311 To understand how this displacement is calculated, some notation first needs to be described.

Table A.2: A summary of notation used in this section: note that non-AMDB notation is used in this section.

Symbol	Definition
s_x, s_y, s_z, \vec{s}	Position of the muon hit in ATLAS global coordinates; the infinite momentum muon track
\hat{n}	Vector normal to the plane; taken to be \hat{z} (the beamline) in the nominal case
$\vec{\mathcal{O}}_{IP}^{g,l}$	Position of the interaction point in ATLAS global (g) or wedge local (l) coordinates
$\vec{\mathcal{O}}_{base}^{g,l}$	Position of the plane base in ATLAS global (g) or wedge local (l) coordinates; $(0, y_{base}, z_{pl})$ ($(0, 0, 0)$) for the nominal case in global (local) coordinates
$\vec{\zeta}$	$\vec{s} - \vec{\mathcal{O}}_{base}$
primed quant.	quantities after misalignment

2312 Generically speaking, a hit is the intersection of a line (the muon track) with a plane (the individual plane in the multiplet). We assume the muon moves in a straight line defined by the origin and
 2313 the truth-level θ_{pos} and ϕ_{pos} (i.e. the infinite momentum limit) and that the MM plane is rigid and
 2314 defined by a point, which we take to be the center of the bottom edge of the plane, and a normal
 2315 vector, which we take to be the z axis in the nominal case.

2317 The coordinate axes x, y, z axes used here correspond to the usual AMDB $s, z, -t$ axes. Since the
 2318 direction does not really matter when studying misalignment or corrections thereof, the major dif-

²³¹⁹ ference is the choice of origin.

²³²⁰ The muon track we denote^{††} \vec{s} , the bottom point of the plane $\vec{\mathcal{O}}_{base}$, and the normal vector \hat{n} .

²³²¹ The muon track will always be given as (the wedge gets moved, not the muon):

$$\vec{s} = \mathcal{O}_{IP} + k\hat{s} \quad (\text{A.8})$$

$$\hat{s} = \sin \theta_{pos} \sin \phi_{pos} \hat{x} + \sin \theta_{pos} \cos \phi_{pos} \hat{y} + \cos \theta_{pos} \hat{z} \quad (\text{A.9})$$

$$\vec{s} = k\hat{s} = \frac{z_{pl}}{\cos \theta_{pos}} \hat{s} = z_{pl} (\tan \theta \sin \phi \hat{x} + \tan \theta \cos \phi \hat{y} + 1) \quad (\text{A.10})$$

²³²² where $k \in \mathbb{R}$, along with the unit vector \hat{s} , defines the point where the track intersects the wedge.

²³²³ Rotations are done before translations, according to the order prescribed in the AMDB guide for

²³²⁴ chamber alignment, so the axes the principal axes of the plane are rotated according to the following

²³²⁵ matrix (where s , c , and t are the obvious trigonometric substitutions)

$$\begin{aligned} & \begin{pmatrix} 1 & 0 & 0 \\ 0 & c\gamma & -s\gamma \\ 0 & s\gamma & c\gamma \end{pmatrix} \begin{pmatrix} c\beta & 0 & s\beta \\ 0 & 1 & 0 \\ -s\beta & 0 & c\beta \end{pmatrix} \begin{pmatrix} c\alpha & -s\alpha & 0 \\ s\alpha & c\alpha & 0 \\ 0 & 0 & 1 \end{pmatrix} = \begin{pmatrix} 1 & 0 & 0 \\ 0 & c\gamma & -s\gamma \\ 0 & s\gamma & c\gamma \end{pmatrix} \begin{pmatrix} c\alpha c\beta & -s\alpha c\beta & s\beta \\ s\alpha & c\alpha & 0 \\ -c\alpha s\beta & s\alpha s\beta & c\beta \end{pmatrix} \\ & = \boxed{\begin{pmatrix} c\alpha c\beta & -s\alpha c\beta & s\beta \\ s\alpha c\gamma + c\alpha s\beta s\gamma & c\alpha c\gamma - s\alpha s\beta s\gamma & -c\beta s\gamma \\ s\alpha s\gamma - c\alpha s\beta c\gamma & c\alpha s\gamma + s\alpha s\beta c\gamma & c\beta c\gamma \end{pmatrix}} = \mathcal{A} \end{aligned} \quad (\text{A.II})$$

^{††}Recall ϕ_{pos} is defined with respect to the y axis instead of the x axis, as might otherwise be typical.

2326 The thing that matters is what the new strip hit is—i.e. what the new y value is since this, along
 2327 with a plane number, is all that is fed into the algorithm. To find this, we must solve for the new
 2328 point of intersection with the rotated plane and then apply the effects of translations. The path con-
 2329 necting the base of the wedge with the intersection of the muon track will always be orthogonal to
 2330 the normal vector of the plane. Our quantities after misalignment, denoted by primed quantities,
 2331 will look like

$$\mathcal{O}_{base} \rightarrow \mathcal{O}_{base} + ds\hat{x} + dz\hat{y} + dt\hat{z} = \mathcal{O}'_{base}, \quad \hat{n} \rightarrow A\hat{n} = A\hat{z} = \hat{z}', \quad \vec{s} \rightarrow k'\hat{s} + \mathcal{O}_{IP} = \vec{s}' \quad (\text{A.12})$$

2332 so, moving to explicit, global coordinates in the last line so we can do the computation (relying on
 2333 the fact that any vector in the wedge, namely $\vec{\zeta} = \vec{s} - \mathcal{O}$ the local coordinates of the interaction
 2334 point, is necessarily orthogonal to \hat{n}):

$$0 = \hat{n} \cdot (\vec{\mathcal{O}}_{base} - \vec{s}) \rightarrow 0 = A\hat{z}' \cdot (\vec{\mathcal{O}}'_{base} - (k'\hat{s} + \vec{\mathcal{O}}_{IP})) \quad (\text{A.13})$$

$$\rightarrow k' = \frac{s\beta\vec{\mathcal{O}}'_{base-IP,x} - c\beta s\gamma\vec{\mathcal{O}}'_{base-IP,y} + c\beta c\gamma\vec{\mathcal{O}}'_{base-IP,z}}{\hat{s} \cdot \hat{z}'} \quad (\text{A.14})$$

$$= \frac{s\beta ds - c\beta s\gamma(y_{base} + dz) + c\beta c\gamma(z_{pl} + dt)}{s\beta s\theta s\phi - c\beta s\gamma s\theta c\phi + c\beta c\gamma c\theta} \quad (\text{A.15})$$

2335 To find our new y coordinate, we need to evaluate $s'_y = \hat{y}' \cdot k'\vec{s}$ to find the final correction of:

$$\Delta y = \vec{\zeta}' \cdot \hat{y}' - \vec{\zeta} \cdot \hat{y} = (k'\hat{s} - \vec{\mathcal{O}}'_{base}) \cdot \hat{y}' - (s_y - y_{base}) \quad (\text{A.16})$$

²³³⁶ The correction will be plane dependent since (denoting the stereo angle ω):

$$\hat{y}_x = \hat{y} \rightarrow \hat{y}'_x = -s\alpha c\beta \hat{x} + (\alpha c\gamma - s\alpha s\beta s\gamma) \hat{y} + (\alpha s\gamma + s\alpha s\beta c\gamma) \hat{z} \quad (\text{A.17})$$

²³³⁷ and

$$\begin{aligned} \hat{y}_{U,V} = & \pm s\omega \hat{x}' + \omega \hat{y}'_{U,V} = [\pm \alpha c\beta s\omega - s\alpha c\beta \omega] \hat{x} + [\pm (s\alpha c\gamma + s\alpha s\beta s\gamma) s\omega \\ & + (\alpha c\gamma - s\alpha s\beta s\gamma) \omega] \hat{y} + [\pm (s\alpha s\gamma - c\alpha s\beta c\gamma) s\omega + (\alpha s\gamma + s\alpha s\beta c\gamma) \omega] \hat{z} \end{aligned}$$

²³³⁸

²³³⁹ A.10 INDIVIDUAL CASES

²³⁴⁰ Currently we only study the cases where one misalignment parameter is not zero. We examine these
²³⁴¹ in detail below, calculating the most pertinent quantities in the misalignment calculation, k'/k and
²³⁴² the new horizontal and stereo y axes. Before setting out, we simplify the expressions for the trans-
²³⁴³ formed \hat{y}' 's, removing any terms with the product of two sines of misalignment angles, which will be
²³⁴⁴ zero.^{††}

$$\hat{y}'_x = -s\alpha c\beta \hat{x} + \alpha c\gamma \hat{y} + \alpha s\gamma \hat{z} \quad (\text{A.19})$$

²³⁴⁵

$$\hat{y}'_{U,V} = [\pm \alpha c\beta s\omega - s\alpha c\beta \omega] \hat{x} + [\pm s\alpha c\gamma s\omega + c\alpha c\gamma \omega] \hat{y} + [\mp c\alpha s\beta c\gamma s\omega + c\alpha s\gamma \omega] \hat{z} \quad (\text{A.20})$$

^{††}If only one misalignment parameter is non-zero, then two or more sines will contain at least one term will contain $\sin 0 = 0$.

2346 If the translations are zero,

$$k' = \frac{-c\beta s\gamma y_{base} + c\beta c\gamma z_{pl}}{s\beta s\theta s\phi - c\beta s\gamma s\theta c\phi + c\beta c\gamma \theta}, \quad k'/k = \frac{-c\beta s\gamma y_{base}/z_{pl} + c\beta c\gamma}{s\beta t\theta s\phi - c\beta s\gamma t\theta c\phi + c\beta c\gamma} \quad (\text{A.21})$$

2347 A.II $ds \neq 0$

2348 $k'/k = 1$ (the point of intersection does not move closer or further from the IP), and only the stereo
2349 planes are affected. Note that only relevant term in Equation A.16, for the stereo strip \hat{y} for $\vec{\mathcal{O}}'_{base} =$
2350 $d\hat{x}$ is:

$$\pm \sin \omega ds \approx \pm 0.0261 ds \quad (\text{A.22})$$

2351 meaning that a displacement in x of 17 mm, more than three times the range of misalignments stud-
2352 ied, would be necessary for a shift in the stereo planes corresponding to one strip width.

2353 A.12 $dz \neq 0$

2354 $k'/k = 1$ (the point of intersection does not move closer or further from the IP). This case is the
2355 trivial one (cf. Equation A.16 with $\vec{\mathcal{O}}'_{base} = dz\hat{y}$). y just gets moved in the opposite direction as the
2356 wedge. Correction is an additive constant.

2357 A.13 $dt \neq 0$

2358 $k'/k = (z_{pl} + dt) / z_{pl}$. y gets modified by a simple scale factor. Correct by storing changing defini-
2359 tions of plane positions in algorithm to match the misaligned values.

₂₃₆₀ A.14 $\alpha \neq 0$

₂₃₆₁ $k'/k = 1$ and

$$\hat{y}'_x = -s\alpha\hat{x} + c\alpha\hat{y} \quad (\text{A.23})$$

$$\hat{y}'_{U,V} = [\pm c\alpha s\omega - s\alpha c\omega] \hat{x} + [\pm s\alpha s\omega + c\omega] \hat{y} \quad (\text{A.24})$$

₂₃₆₂ A.15 $\beta \neq 0$

₂₃₆₃ We have $k'/k = (1 + \tan \beta \tan \theta \sin \phi)^{-1}$, and

$$\hat{y}'_x = \hat{y} \quad (\text{A.25})$$

$$\hat{y}'_{U,V} = \hat{y} \pm (c\beta\hat{x} - s\beta\hat{z}) s\omega \quad (\text{A.26})$$

₂₃₆₄ A.16 $\gamma \neq 0$

$$k'/k = \frac{1 - \tan \gamma \frac{y_{base}}{z_{pl}}}{1 - \tan \gamma \tan \theta \cos \phi} \quad (\text{A.27})$$

$$\hat{y}'_x = c\gamma\hat{y} + s\gamma\hat{z} \quad (\text{A.28})$$

$$\hat{y}'_{U,V} = \pm s\omega\hat{x} + c\omega\hat{y} - s\gamma c\omega\hat{z} \quad (\text{A.29})$$

₂₃₆₅ In order to evaluate algorithm performance under misalignment and corrections for misalign-

₂₃₆₆ ment, the absolute means and relative resolutions of the fit quantities θ , ϕ , and $\Delta\theta$ are measured as

2367 a function of misalignment. In the following, results will only be shown for which the effects of mis-
2368 alignment are significant. “Significant,” for misalignments of 1 mm (0.3 mrad) for translations (ro-
2369 tations) means more than a 5% degradation in rms and/or bias shifts in θ , ϕ , and $\Delta\theta$ of 0.01 mrad, 1
2370 mrad, and 0.1 mrad, respectively.

2371 While corrections are typically done on a case-by-base basis, they fall under two general cate-
2372 gories, analytic and simulation based. Analytic corrections rely upon specific knowledge of the mis-
2373 alignment, with each case being handled separately; as such, the additional resources required, both
2374 extra constants and operations, if any, vary accordingly. Simulation based corrections are all done in
2375 the same manner. The algorithm is run over a training MC sample (same setup but with $p_T = 200$
2376 GeV instead of the normal 100 GeV sample so as not to overtrain the corrections), and the mean bi-
2377 ases for θ , ϕ , and $\Delta\theta$ are saved for different, equally spaced regions in the $\eta - \phi$ plane over the wedge
2378 based on the fitted θ and ϕ values. Currently, these values are saved for 10 η and 10 ϕ bins (100 η, ϕ
2379 bins total), with the number of bins in each direction being a configurable parameter. When the al-
2380 gorithm runs with simulation based correction, this table of constant corrections is saved in a LUT
2381 before runtime, and corrections are added to final fit quantities based on the (uncorrected) θ and
2382 ϕ fit values. With the settings mentioned, this is 300 extra constants ($10\eta\text{-bins} \times 10\phi\text{-bins} \times 3$ fit
2383 quantities) and two extra operations (a lookup and addition for each quantity done in parallel). The
2384 simulation correction can, in principle, also be applied to the algorithm in nominal conditions with
2385 non-trivial improvements, as detailed below in Section A.17. Depending on the misalignment case in
2386 question, different approaches work better. A summary of correction methods, including resources
2387 necessary for the individual analytic cases, is shown in Table A.3.

	Δ_s	Δz	Δt	γ_s	β_z	α_t
Analytic Resources	yes+ 11c/2op	yes+ oc/oop	yes+ oc/oop	yes 56c/1op	no —	yes 400c/2n _X op, 32c/12n _X op
Simulation	yes+	no	no	no	yes+	yes+

Table A.3: A summary of corrections with additional constants/operations (written as $n_{const}c/n_{ops}op$; n_X is the number of X hits in a fit) necessary for analytic corrections. Yes means a correction exists but might not entirely remove misalignment effects, while yes+ means a quality of correction is only limited by knowledge of misalignment and memory

2388 A.17 SIMULATION CORRECTION OF THE ALGORITHM UNDER NOMINAL CONDITIONS

2389 In addition to using simulation based correction to counter the effects of several classes of misalign-
 2390 ment, the correction can be applied at to the algorithm under nominal conditions. The main effect
 2391 of this correction is to mitigate the effects of the bias in stereo strips. As such, the correction has a
 2392 larger effect on quantities that rely on the aggregate slope m_y , as can be seen in in Figure A.18, im-
 2393 proving $\sigma_{\theta_{fit} - \theta_{true}}$ resolution by about 25%, and reducing $\sigma_{\phi_{fit} - \phi_{true}}$ by over 50% and restoring a largely
 2394 Gaussian shape. The slight, apparent degradation in $\Delta\theta$ is due to a more mild version of the effect
 2395 seen in Figure A.7.

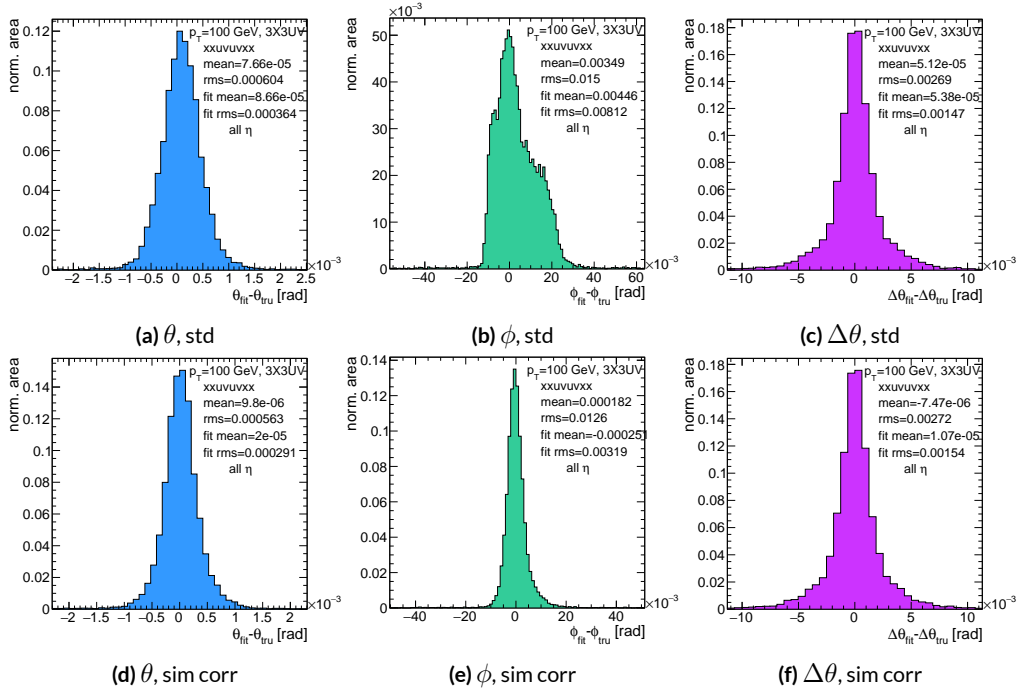


Figure A.18: Nominal residual plots for both uncorrected and simulation corrected cases; θ , ϕ , $\Delta\theta$ for $p_T = 100$ GeV muons

2396 As can be seen in Figure A.19, the simulation based correction also removes the η dependence to
 2397 fit quantity resolution distributions, as expected. One consequence of this is that simulation-based
 2398 corrections applied to the misalignment cases below will restore performance to the “sim” and not
 2399 the “std” distributions of Figure A.18. Hence, when making comparisons between simulation cor-
 2400 rected curves and the nominal performance point, simulation-corrected distributions of benchmark
 quantities versus misalignment will often look generally better.

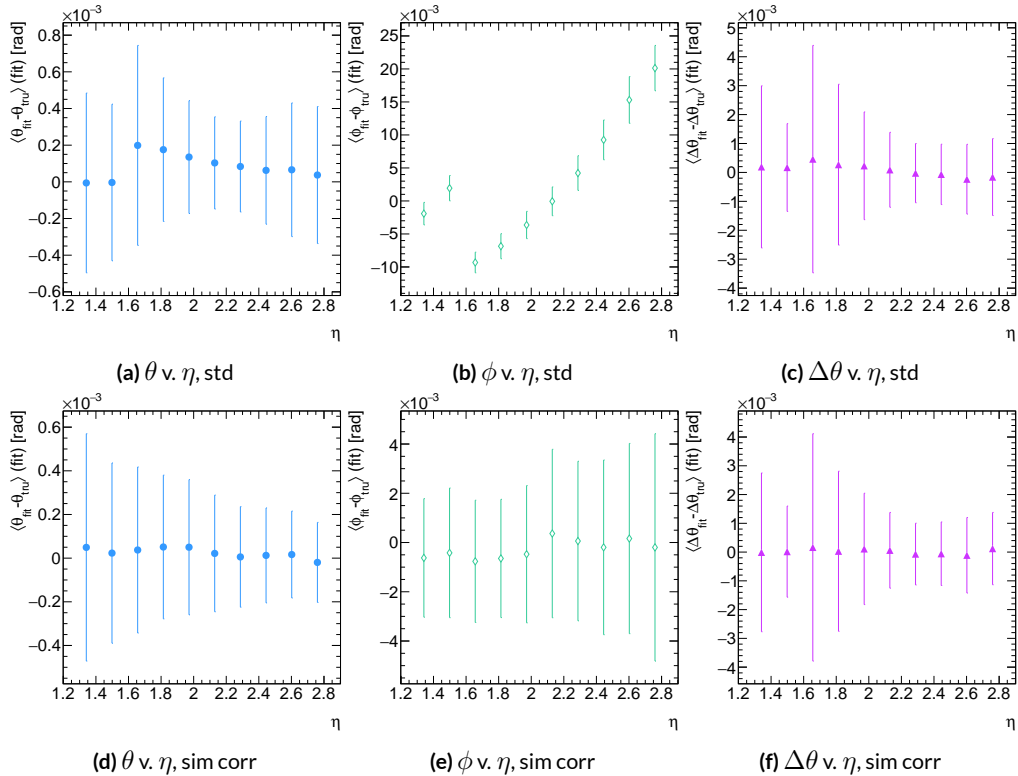


Figure A.19: Nominal residual plots as a function of η with points as means and error bars as rms values in each η bin for the angles $\theta, \phi, \Delta\theta$ for $p_T = 100$ GeV muons in the uncorrected and simulation corrected cases.

2401

2402 That the improvements from a simulation-based correction improve performance of the algo-

2403 rithm in nominal conditions most for the quantities that depend most on stereo information (ϕ and
 2404 θ) and remove the η dependence of fit quantity resolutions suggests that there could, in principle, be
 2405 analytic corrections that could be applied to the nominal algorithm. One possible solution is to in-
 2406 troduce an additional set of constants, having the y_{base} depend on the strip number, similar to the γ_s
 2407 correction for z_{plane} described in Section A.21, which would add a lookup per hit and $8 \times n_{bins,y}$ extra
 2408 constants that would be optimized as the γ_s correction was.

$$M_{hit} = \frac{\gamma}{z} = \frac{y_{base}}{z_{plane}} (n_{str}) + \frac{w_{str}}{z_{plane}} n_{str} \quad (\text{A.30})$$

2409 The simulation correction residual rms values suggest a limit on the quality of such correction
 2410 and could perhaps be implemented generically on their own regardless of misalignment for rms val-
 2411 ues on fit quantities of 0.291 mrad for θ , 3.19 mrad for ϕ , and 1.54 for $\Delta\theta$, which represent a 20%
 2412 improvement for θ , a 62% improvement for ϕ , and a slight degradation in $\Delta\theta$ of 4.7%, again owing
 2413 to an effect similar to the one in A.7.

2414 A.18 TRANSLATION MISALIGNMENTS ALONG THE HORIZONTAL STRIP DIRECTION (Δs)

2415 A translation in s (i.e. along the direction of a horizontal strip) only affects the stereo strips, and,
2416 since the stereo angle is small, a very large misalignment is necessary for effects to be noticeable (a
2417 misalignment of roughly 17 mm corresponds to one strip's misalignment in the stereo planes). The
2418 only quantity to show any meaningful deviation with misalignments with translations in s is the ϕ
2419 residual bias (a change of 0.4 mrad at $\Delta s = 1$ mm), as can be seen in the uncorrected curve of Figure
2420 A.20.

2421 A translation in s induces a constant shift in the calculated horizontal slope, m_x in Equation A.4.
2422 This constant shift should only depend on which stereo planes included in a fit are misaligned and
2423 how misaligned they are. Hence, the correction to m_x , for a sum over misaligned stereo planes i ,
2424 with their individual misalignments in s and plane positions in z is:

$$\Delta m_x = \frac{1}{N_{\text{stereo}}} \sum_{i, \text{misal stereo}} \frac{\Delta s_i}{z_{i, \text{plane}}} \quad (\text{A.31})$$

2425 Given prior knowledge of misalignment, these corrections to m_x can be performed ahead of time
2426 and saved in a lookup table (LUT), similar to the LUT used for constants in the X local slope (M_x^l)
2427 calculation. The added overhead of this analytic correction is hence eleven constants in memory, a
2428 lookup, and one addition. The correction perfectly corrects the effects of misalignment, as can be
2429 seen in Figure A.20. The simulation based correction described above can also be used to correct
2430 for Δs misalignments, with the results of that correction also shown in Figure A.20. The apparent

2431 discrepancy between the simulated and analytic correction is a natural consequence of the fact that
 2432 the simulation correction, as previously mentioned, restores the ϕ residual distribution to an overall
 2433 more Gaussian shape.

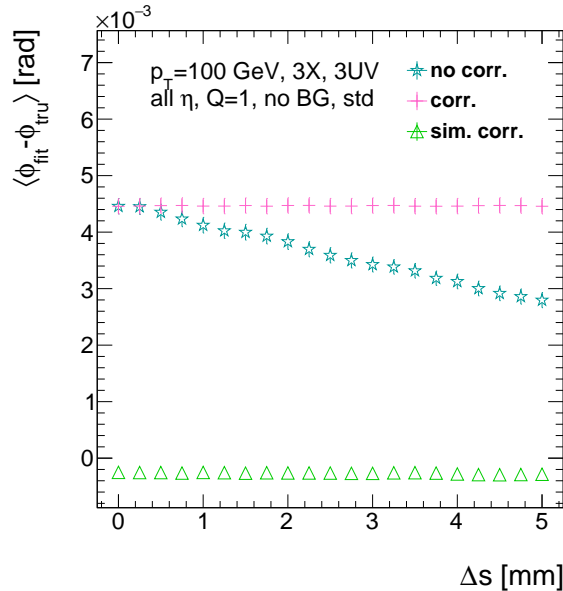


Figure A.20: The mean of the ϕ residual as a function of misalignment for the uncorrected case and the analytic and simulation correction cases.

2434 A.19 TRANSLATION MISALIGNMENTS ORTHOGONAL TO THE BEAMLINE AND HORIZON-
2435 TAL STRIP DIRECTION (Δz)

2436 A translation in AMDB z , the direction orthogonal to both the beamline and the horizontal strip
2437 direction, corresponds to a translation in the y of Equation A.1, affecting all slope calculations. This
2438 has a large impact on the θ residual bias and both the bias and rms of $\Delta\theta$ residual, as can be seen in
2439 Figures A.21 (a)–(c). The marked degradation and non-linear behavior in performance at very high
2440 levels of misalignments is a result of low statistics; there are fewer fits at high level of misalignments
2441 since for $\Delta z \gtrsim 3$ mm, most fits will fail the $\Delta\theta$ cut. The θ bias shifts by about 0.075 mrad at $\Delta z =$
2442 1 mm, and $\Delta\theta$ shifts by about 5 mrad for the same level of misalignment. While the fitted rms of the
2443 $\Delta\theta$ residual remains fairly stable for $\Delta z < 1$ mm or so, between $\Delta z = 2$ mm and $\Delta z = 3$ mm, the
2444 rms increases by 15% before the $\Delta\theta$ cut issue mentioned above intervenes.

2445 Fortunately, these misalignments are straightforward to correct with knowledge of the misalign-
2446 ment. The only modification necessary for this correction is to change the definitions of y_{base} in
2447 Equation A.1 for the individual hit slope addressing. This is done before runtime and adds no over-
2448 head to the algorithm, and the correction quality is only limited by knowledge of the misalignment.
2449 The results of this correction are also shown in Figures A.21 (a)–(c) and restore nominal perfor-
2450 mance.

Since $\Delta\theta = \frac{M_x^l - M_x^e}{1 + M_x^l M_x^e}$ and $M_x^l = B_k \sum y_i (z/\bar{z} - 1)$, a shift Δy translates (with typical slope values of ~ 0.3) to $5B_k (z_1 + z_2)/\bar{z}$ (with B_k in units of inverse mm); set equal to 16 mrad ($\Delta\theta$ is centered at zero), this corresponds to $\Delta y = 2.7$ mm

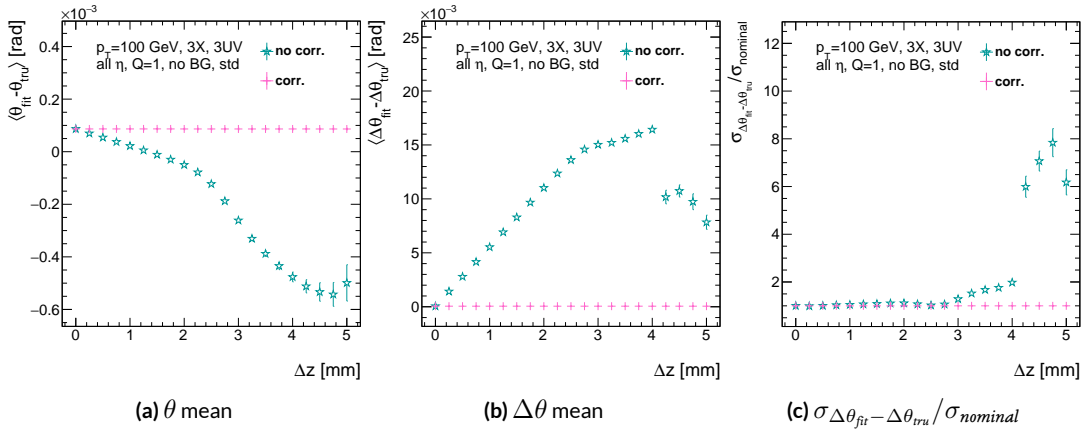


Figure A.21: The affected quantities of Δz misalignments: θ bias, $\Delta\theta$ bias, and $\sigma_{\Delta\theta_{\text{fit}} - \Delta\theta_{\text{tru}}} / \sigma_{\text{nominal}}$ for both the misaligned and corrected cases.

2451 A.20 TRANSLATION MISALIGNMENTS PARALLEL TO THE BEAMLINE (Δt)

2452 The effects of misalignment due to translations in t are very similar to those due to translations in
 2453 z without the complication of the $\Delta\theta$ cut, affecting the z instead of the y coordinate that enters
 2454 into hit slope calculations. Again, θ bias, $\Delta\theta$ bias, and $\sigma_{\Delta\theta_{fit}-\Delta\theta_{true}}$ are the primarily affected quan-
 2455 tities. For $\Delta t = 1$ mm, θ bias shifts by about 0.02 mrad, $\Delta\theta$ bias shifts by just under 2 mrad, and
 2456 $\sigma_{\Delta\theta_{fit}-\Delta\theta_{true}}$ degrades by about 20%. The correction for this misalignment once again costs no over-
 2457 head and consists of changing stored constants in the algorithm, in this case the positions along the
 2458 beamline of the misaligned planes, with results similarly limited by knowledge of the misalignment.
 2459 The slight improvement with correction to $\Delta\theta$ rms is due to the real effect of a larger lever arm.
 2460 Both the misaligned and corrected distributions of affected quantities of interest are shown in Fig-

ure A.22.

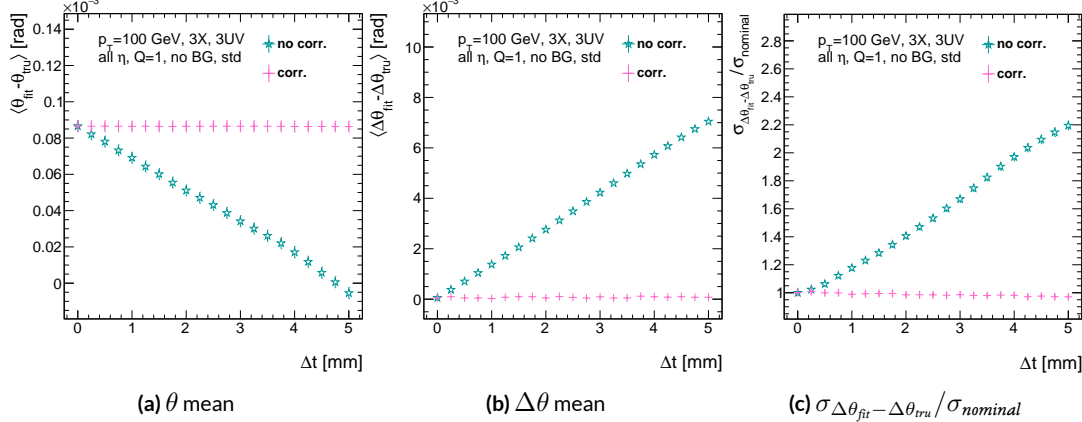


Figure A.22: The affected quantities of Δt misalignments: θ bias, $\Delta\theta$ bias, and $\sigma_{\Delta\theta_{fit}-\Delta\theta_{true}} / \sigma_{nominal}$ for both the misaligned and corrected cases.

2462 A.21 CHAMBER TILTS TOWARDS AND AWAY FROM THE IP (γ_s ROTATION)

2463 Chamber misalignment due to rotations around the s axis act effectively like a translation in t that
2464 depends on strip number. These rotations tilt misaligned chambers away from (towards) the IP for
2465 positive (negative) values of γ_s . Since, unlike for the other two rotation cases that will be studied,
2466 positive and negative rotation values are not symmetric, this misalignment is studied for both posi-
2467 tive and negative γ_s values. The divergent effect at the tails is a result of a large population of fits not
2468 having fit quantities within the cores, and so not appearing in the fit rms. Once again, affected quan-
2469 tities of interest θ bias, $\Delta\theta$ bias, and $\sigma_{\Delta\theta_{fit}-\Delta\theta_{tru}}$. The effects of misalignment can be seen in Figures
2470 A.23 (a)–(c). The relationship between biases and γ_s is roughly linear with $\Delta\gamma_s = 0.3$ mrad (the an-
2471 gular scale corresponding to linear shifts of ~ 1 mm) corresponding to 0.005 mrad (0.12 mrad) for θ
2472 ($\Delta\theta$). For $\sigma_{\Delta\theta_{fit}-\Delta\theta_{tru}}$, degradation is not symmetric. For negative (positive) γ_s , with the quadruplet
2473 tilted towards (away from) the IP, slope-roads are artificially expanded (shrunk), decreasing (increas-
2474 ing) the granularity of the trigger, explaining the asymmetry in Figure A.23 (c), with the degradation
2475 being a 10% (25%) effect for γ_s of $+(-)0.3$ mrad.

2476 Corrections are less simple in this case. In principle, corrections of the same accuracy of the trans-
2477 lations could be calculated per strip, but the overhead of one correction per strip (many thousands
2478 of constants) is prohibitive. Instead, each plane was divided into eight equal segments with a t value
2479 (z in the slope calculation) assigned to strips in each region to correct for the misalignment. This
2480 amounts to 56 extra constants and a 2D instead of a 1D LUT for z positions while the algorithm
2481 runs. The corrected distributions can also be seen in Figures A.23 (a)–(c). The corrections, while not

as effective as for the simple translation cases, are still very effective with the quoted misalignment values for bias shifts down to 0.001 mrad (0.25 mrad) for θ ($\Delta\theta$) and no more than a 2% degradation in $\sigma_{\Delta\theta_{fit}-\Delta\theta_{true}}$ for $|\gamma_s| = 0.3$ mrad.

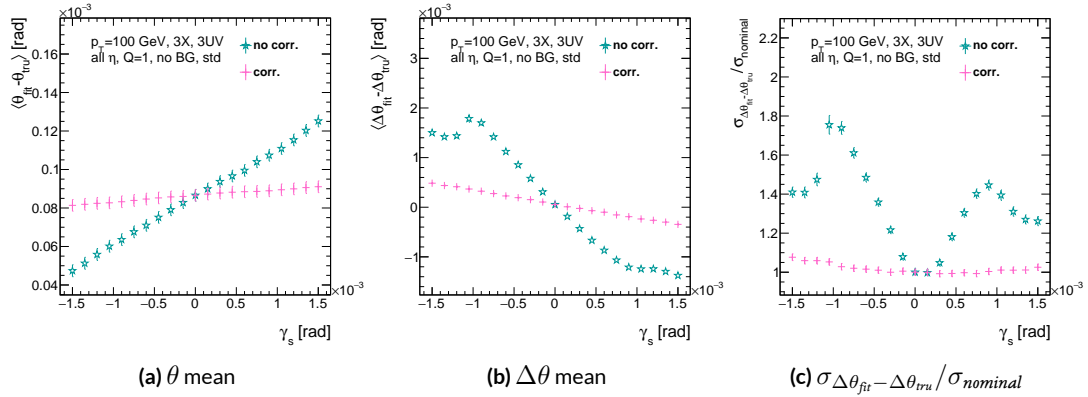


Figure A.23: The noticeable effects of rotations in the s axis and the behavior of these quantities (θ and $\Delta\theta$ bias shifts and $\sigma_{\Delta\theta_{fit}-\Delta\theta_{true}}/\sigma_{nominal}$) with and without misalignment correction.

2485 A.22 ROTATION MISALIGNMENTS AROUND THE WEDGE VERTICAL AXIS (β_z)

2486 While misalignments coming from rotations around the z axis (the direction orthogonal to both
 2487 the beamline and the horizontal strip direction) foreshorten the strips as seen from the IP and add
 2488 a deviation in t , the long lever arm largely washes out any effects of this misalignment. Only the
 2489 $\sigma_{\Delta\theta_{fit}-\Delta\theta_{tru}}$ is noticeably affected, though only at severe misalignments, with only about a 1% degra-
 2490 dation in performance at $\beta_z = 0.3$ mrad (corresponding to a linear shift of ~ 1 mm). A simulation
 2491 based correction works well to cancel out the effects of this misalignment, and the $\sigma_{\Delta\theta_{fit}-\Delta\theta_{tru}}$ as a
 2492 function of misalignment with and without corrections are shown in Figure A.24. The apparent
 2493 2% effect in the simulation corrected curve is a result of a more mild version of the effect shown in
 2494 Figure A.7.

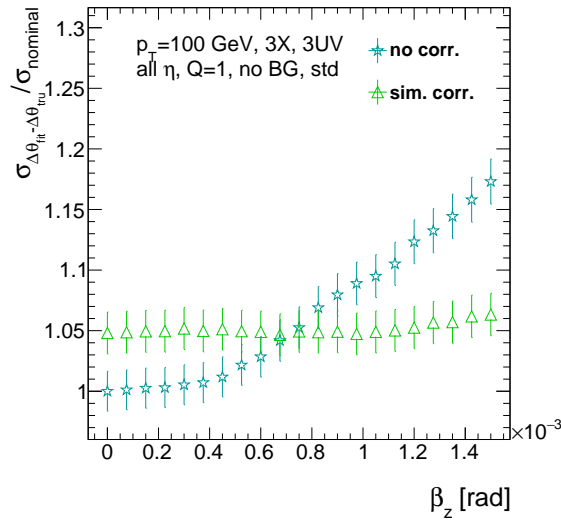


Figure A.24: The effects of rotations in the z axis on $\sigma_{\Delta\theta_{fit}-\Delta\theta_{tru}} / \sigma_{nominal}$ a function of β_z both with and without misalignment corrections.

2495 A.23 ROTATION MISALIGNMENTS AROUND THE AXIS PARALLEL TO THE BEAMLINE (α_t)

2496 Misalignments arising from rotations around the t axis (parallel to the beamline at the center of
2497 the base of the wedge) are essentially rotations in the ϕ direction. The quantities of interest most
2498 affected are the ϕ bias and $\sigma_{\Delta\theta_{fit}-\Delta\theta_{tru}}$, as shown in Figures A.25 (a) and (b), respectively, and cor-
2499 respond to a shift in ϕ bias of 0.2 mrad and a 10% degradation in $\sigma_{\Delta\theta_{fit}-\Delta\theta_{tru}}$ for $\alpha_t = 0.3$ mrad
2500 (corresponding to a linear shift of ~ 1 mm). The raw instead of fitted mean ϕ biases is used in Fig-
2501 ure A.25 (a) to better illustrate the effect of misalignment.

2502 Since the effect of misalignment is dependent on horizontal (along the strip direction, \hat{s}) in addi-
2503 tion to vertical information, corrections cannot be applied before a fit takes place. The ϕ bias shift is
2504 uniform over the entire wedge, so a constant additive correction to ϕ based on the level of misalign-
2505 ment can be applied to all fits depending on how many misaligned stereo planes enter in the fit. $\Delta\theta$
2506 is less straightforward, but corrections to the y and z information used in the local slope calculation
2507 in Equation A.4 can be applied once θ_{fit} and ϕ_{fit} are known. These corrections are calculated ahead
2508 of time in bins of uniform η and ϕ as with the simulation corrections using the same framework
2509 as the misalignment calculation. The results of both types of correction can be seen in Figure A.22.
2510 The apparent discrepancy between the simulation and analytic corrections in the ϕ bias happens for
2511 the same reason as in the Δs misalignment correction cases, as simulation correction restores a more
2512 Gaussian shape to the ϕ residual distribution opposed to the uncorrected nominal case, as discussed
2513 in Section A.17.

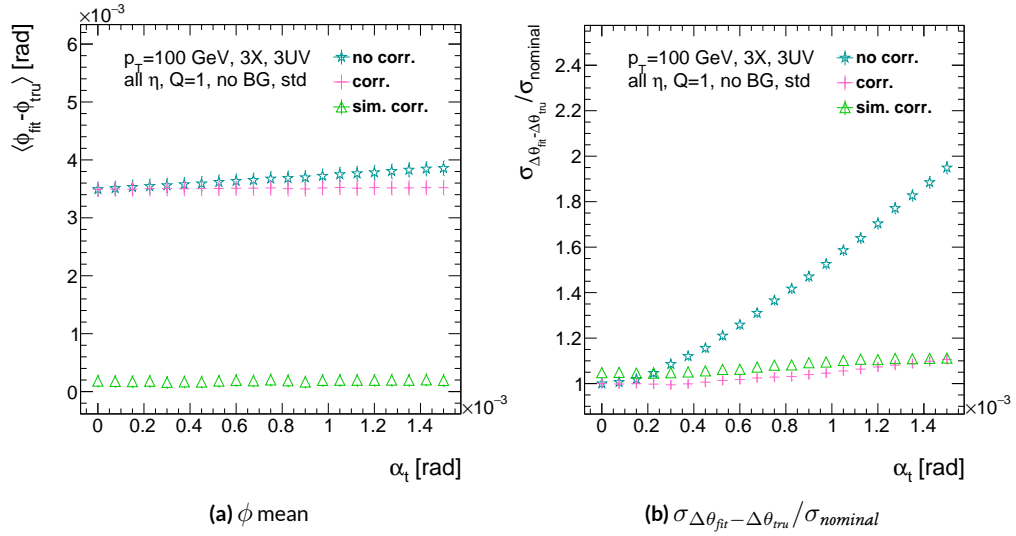


Figure A.25: The effects of rotation misalignments around the t axis for ϕ bias and $\sigma_{\Delta\theta_{\text{fit}} - \Delta\theta_{\text{true}}} / \sigma_{\text{nominal}}$ as a function of misalignment. The uncorrected and both the analytic and simulation correction cases are shown.

2514 A.24 CONCLUSION

2515 The algorithm for Micromegas detectors in the NSW Trigger Processor performs well in a variety of
2516 conditions and has proven robust to a number of effects to deliver measurements on muon tracks
2517 of the three angles θ , ϕ , $\Delta\theta$. Under nominal conditions, the rms values for the residuals of these
2518 quantities are 0.364 mrad for θ , 8.12 mrad for ϕ , and 1.47 mrad for $\Delta\theta$. Algorithm performance was
2519 found to be largely independent of the charge threshold setting, and a hit majority BCID associa-
2520 tion was found to provide proper timing information over 99.7% even in the most relaxed settings
2521 (2X+1UV coincidence threshold requirement+wide slope-road+background). The introduction of
2522 wide slope-roads to better mimic potentially limited algorithm resources at run time and the intro-
2523 duction of incoherent background was found to have a manageable effect on fit quantity residual
2524 rms values and on total algorithm efficiency for sufficiently stringent coincidence threshold. The ef-
2525 ffects of the three translation and three rotation misalignments specified by AMDB convention were
2526 studied, and correction methods for each of the six cases was developed. Simulation-based correc-
2527 tions were found to improve nominal algorithm performance to residual rms value of 0.291 mrad for
2528 θ , 3.19 mrad for ϕ , and 1.54 for $\Delta\theta$, which represent improvements of 20%, 62%, and -4.7%, respec-
2529 tively. Misalignment corrections were found to restore nominal performance for all but the rotation
2530 around the s axis, and a summary of tolerances may be found in Table A.4.

	No Correction	Correction
Δs	4 mm (ϕ bias)	> 5 mm
Δz	0.25 mm ($\Delta\theta$)	> 5 mm
Δt	0.25 mm ($\Delta\theta$)	> 5 mm
γ_s	0.15 mrad ($\Delta\theta$ bias)	0.75 mrad
β_z	0.9 mrad ($\Delta\theta$ rms)	> 1.5 mrad
α_t	0.375 mrad ($\Delta\theta$ rms)	> 1.5 mrad

Table A.4: A summary of levels of misalignment corresponding to a 10% degradation in any residual rms or, for biases shifts of 0.01 mrad for θ , 1 mrad for ϕ , and 0.25 mrad for $\Delta\theta$ for both the uncorrected and corrected cases; > 5 mm and > 1.5 mrad mean that such a degradation does not occur for the range of misalignment studied. Most affected quantity in parentheses.

Tod-Not-Brot

Old German Proverb

B

2531

2532

Telescoping Jets

2533 ANOTHER APPROACH TO IMPROVING $ZH \rightarrow \ell\ell b\bar{b}$ is the use of telescoping jets³⁶, which har-
2534 nesses the power of multiple event interpretations. The use of multiple event interpretations was
2535 originally developed with non-deterministic jet algorithms like the Q-jets (“quantum” jets) algo-
2536 rithm⁶⁹. When a traditional or “classical” algorithm, such as the Cambridge-Aachen⁸⁰ and anti- k_t ⁶³

algorithms, is applied to an event, it produces one set of jets for that event, i.e. a single interpretation of that event. With multiple event interpretations, each event is instead given an ensemble of interpretations. In the case of Q-jets, this ensemble is created through a non-deterministic clustering process for an anti- k_t jet algorithm. With telescoping jets, multiple jet cone radii (the characteristic size parameter, R) around a set of points in the pseudorapidity-azimuth ($\eta - \phi$) plane are used to generate a series of jet collections. Instead of an event passing or not-passing a given set of cuts, a fraction (called the cut-weight, z) of interpretations will pass these cuts. This cut-weight allows for enhanced background suppression and increased significance of observed quantities for a given data set, as detailed in Ref. ⁴⁷. The telescoping jets algorithm provides the benefits of multiple event interpretations without the significant computational overhead of a non-deterministic algorithm like the Q-jets algorithm, and its multiple cone sizes are particularly suited to studying processes like associated production, which suffers from a pronounced low tail in the dijet invariant mass distribution due to final state radiation (FSR) “leaking” outside the relatively narrow jets used for object reconstruction.

MONTE CARLO SIMULATION

The MC simulated samples used in this study are the same as in Ref.[?]. The signal sample used is generated in PYTHIA8⁷⁶ with the CTEQ6L1 parton distributions functions (PDFs) and AU2 tune^{55,2,3} for the ZH process with $m_H = 125$ GeV (henceforth, $ZH125$). The primary background processes examined in this study were Z +jets with massive b and c quarks. These samples are generated with version 1.4.1 of the SHERPA generator⁷⁸.

2557 B.2 JET RECONSTRUCTION AND CALIBRATION

2558 In order to construct telescoping jets, jet axes must first be found around which to “telescope.” In
2559 the reconstructed-level analysis, the anti- k_t algorithm with $R = 0.4$ is used to reconstruct jets from
2560 topological clusters in the calorimeters. The four vectors of these anti- k_t algorithm with $R = 0.4$ jets
2561 are calibrated to match truth information obtained from simulation and validated in data. To take
2562 into account the effect of pile-up interactions, jet energies are corrected using a jet-area based tech-
2563 nique³², and each jet with $p_T < 50$ GeV and $|\eta| < 2.4$ is subject to a requirement that at least 50% of
2564 the scalar sum of the p_T of tracks matched to this jet be composed of tracks also associated with the
2565 primary vertex. Jet energies are also calibrated using p_T and η -dependent correction factors¹¹. Fur-
2566 thermore, at least two jets must have $|\eta| < 2.5$ in order to be b -tagged. The MV1 algorithm^{43???}
2567 is used for b -tagging. Once jets are reconstructed and b -tag weights have been calculated, the two
2568 hardest, b -tagged jets are used as the telescoping jet axes. Additional details can be found in Ref.¹².

2569 After the telescoping jet axes have been established, telescoping jets are constructed using topolog-
2570 ical clusters in the calorimeters at a variety of jet cone sizes. Including the original anti- k_t jets used for
2571 the $R = 0.4$ case, twelve total sets of jets of cone sizes ranging from $R = 0.4\text{--}1.5$ are constructed,
2572 with each successive size having a radius 0.1 larger than the preceding set. For each jet axis, telescop-
2573 ing jets consist of any topological cluster lying within R of the axis. In the event of overlap, clusters
2574 are assigned to the closer jet axis. If a given cluster is equidistant from the two jet axes, the cluster
2575 is assigned to whichever jet axis is associated with the anti- k_t jet with higher p_T . Calibration for the
2576 telescoping jets is conducted using corrections for anti- k_t calorimeter topological cluster jets; the

2577 $R = 0.4$ corrections are used for telescoping $R = 0.5$, and the $R = 0.6$ corrections are used
2578 for telescoping $R \geq 0.6$ (cf. Sec. B.4). The telescoping cone jets ($R \geq 0.5$) at reconstructed level
2579 are trimmed using Cambridge-Aachen jets with $R = 0.3$ and $f_{cut} = 0.05$ with respect to the
2580 untrimmed jet p_T^{48} . Since these jets are trimmed, the active area correction is not applied. In the
2581 event a Z candidate electron falls within R of the axis of a telescoping jet, its 4-momentum is sub-
2582 tracted from that of the jet vectorially.

2583 A similar process is used to construct telescoping jets in the truth-level analysis below. Instead of
2584 the two hardest b -tagged anti- k_t with $R = 0.4$ jets reconstructed with calorimeter topological clus-
2585 ters, the two hardest truth b -jets in an event are used. Instead of making a cut on b -tagging weight
2586 to b -tag, truth jets are examined to see whether a b -hadron with $p_T > 5$ GeV is contained within
2587 $\Delta R < 0.4$ of the jet axis; the presence of a b -hadron is used to b -tag truth-level jets. These two jets
2588 again provide the jets for the $R = 0.4$ case and the axes around which telescoping takes place. Stable
2589 truth particles, not including muons and neutrinos, are used in place of calorimeter topological clus-
2590 ters. Z candidate electron-telescoping jet overlap removal is performed at truth level, too. Missing E_T
2591 is calculated using the vector sum of the four momenta of stable truth-level neutrinos. Since there
2592 are no pileup particles stored at truth level, truth-level telescoping jets are not trimmed.

2593 B.3 EVENT RECONSTRUCTION AND SELECTION

2594 Events are selected on the basis of a combination of leptonic, jet, and missing E_T requirements,
2595 which are outlined in Table B.1. Leptons are categorized by three sets of increasingly stringent qual-
2596 ity requirements, which include lower limits on E_T , upper limits on $|\eta|$, impact-parameter require-

2597 ments, and track-based isolation criteria. The requirements differ for electrons⁵ and muons¹. Events
2598 are selected with a combination of single lepton, dielectron, and dimuon requirements. Each event
2599 must contain at least one lepton passing medium requirements and at least one other lepton pass-
2600 ing loose requirements. These leptons are used to create a dilepton invariant mass cut to ensure the
2601 presence of a Z boson and suppress multijet backgrounds.

2602 Event selection requirements are also imposed on the anti- k_t with $R = 0.4$ jets. There must be at
2603 least two b -tagged jets in a given event. The p_T of the harder b -tagged jet must be at least 45 GeV, and
2604 the second b -tagged jet must have p_T of at least 20 GeV. There are further topological cuts on the
2605 separation of the two jets $\Delta R(b, \bar{b})$, the distance between the two jets in the (η, ϕ) plane, according
2606 to the transverse momentum of the Z boson, p_T^Z . These are shown in Table B.2.

2607 The truth-level analysis has the same missing E_T , jet p_T , m_{ll} , and additional topological selection
2608 criteria, but the use of truth-level information simplifies the other requirements. Instead of lepton
2609 quality requirements, Z boson candidate leptons' statuses and MC record barcodes are checked to
2610 ensure the leptons are stable.

2611 In the jet calibration validation, the reconstructed level analysis lepton and m_{ll} requirements are
2612 imposed, but neither the missing E_T nor the jet selection requirements are applied so as not to bias
2613 the validation.

2614 B.4 VALIDATION OF JET CALIBRATION

2615 In order to validate the jet energy scale and resolution of jets constructed with this telescoping-jets
2616 algorithm, values of p_T^{rec}/p_T^{tru} are studied for each value of R for the $Z+jets$ MC sample. In a given

Table B.1: A summary of basic event selection requirements. Truth-level b -tagging is done with truth-level information.

Requirement	Reconstructed	Truth	Validation
Leptons	1 medium + 1 loose lepton	2 produced by Z boson	1 medium + 1 loose lepton
b -jet	2 b -tags	2 b -jets	—
p_T jet 1 (jet 2)		$> 45 \text{ GeV} (> 20) \text{ GeV}$	—
Missing E_T		$E_T^{\text{miss}} < 60 \text{ GeV}$	—
Z boson		$83 < m_{ll} < 99 \text{ GeV}$	

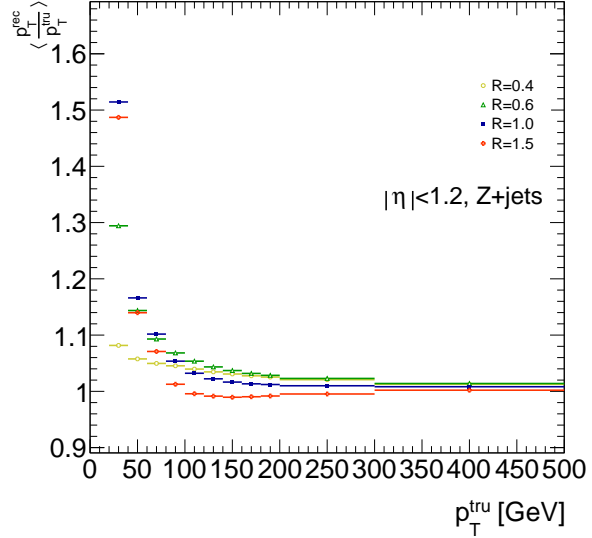
Table B.2: Topological requirements of the event selection.

$p_T^Z [\text{GeV}]$	$\Delta R(b, b)$
0–90	0.7–3.4
90–120	0.7–3.0
120–160	0.7–2.3
160–200	0.7–1.8
> 200	< 1.4

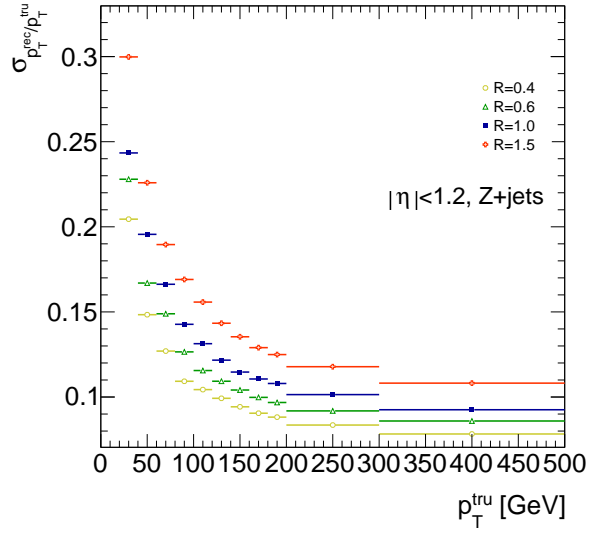
2617 event, all jets, not just the two hardest b -tagged jets, are telescoped. These jets are constructed in the
 2618 same way as in the reconstructed and truth-level analyses; reconstructed-level jets are made from
 2619 calorimeter topological clusters within R of the anti- k_t with $R = 0.4$ jet axes and then trimmed,
 2620 and truth-level jets are made from stable truth particles within R of the anti- k_t with $R = 0.4$ jet axes.
 2621 The reconstructed and truth-level telescoping jet ensembles are matched according to the separation
 2622 in the (η, ϕ) plane of their corresponding anti- k_t with $R = 0.4$ jets used as seeds. Only jets with
 2623 $|\eta| < 1.2$ are examined here, and the results of studies on the $ZH125$, ZZ , and $t\bar{t}$ samples, as well as
 2624 over other $|\eta|$ ranges, are outlined in³⁶. Any reconstructed jets not within $\Delta R = 0.3$ of a truth jet
 2625 are discarded. In the event that multiple reconstructed jets are the same distance away from a given
 2626 truth jet, the reconstructed jet with the highest p_T gets matched. Matching is retained for all R values
 2627 (i.e. telescoping seeds are matched, and telescoping jets are assumed to match if the anti- k_t jets from
 2628 which their seeds are derived match).

2629 Once anti- k_t with $R = 0.4$ reconstructed and truth jets are matched, response functions are cre-
 2630 ated by generating a series of distributions of p_T^{rec}/p_T^{tru} in 20 GeV bins of p_T^{tru} from 20–200 GeV, one
 2631 bin for 200–300 GeV, and one bin for 300–500 GeV for each R , with bins chosen for purposes of
 2632 statistics. Ensembles with $p_T^{tru} < 20$ GeV are ignored since no calibration exists for jets with trans-
 2633 verse momentum below this value. The values of $\langle p_T^{rec}/p_T^{tru} \rangle$ in each p_T^{tru} bin are calculated by doing
 2634 a two sigma gaussian fit on the distribution of p_T^{rec}/p_T^{tru} in that bin and taking the mean of that fit,
 2635 and the error on the mean is taken from the error of this parameter in the fit. The resolutions are the
 2636 values of the square root of the variance on this fit. As the total response distributions in Figure B.1
 2637 show, performance is best for low R values and high values of p_T^{tru} . Figure B.1 shows the $R = 0.4$

2638 (anti k_t) case to show a baseline for performance, $R = 0.6$ to show the deviations with “correct”
2639 calibrations, and $R = 1.0, 1.5$ to show how big those deviations get with larger R jets. The resolu-
2640 tions, $\sigma_{p_T^{rec}}/p_T^{tru}$, as a function of p_T^{tru} are shown in Figure B.1(b). For $p_T^{tru} > 60$ GeV, response is fairly
2641 consistent over various R values. Resolution, as might naïvely be expected, is worse for increasingly
2642 larger values of R . For $p_T^{tru} < 60$ GeV, resolution degrades, and response degrades in particular for
2643 increasing R ; this is likely a result from residual pileup effects.



(a)



(b)

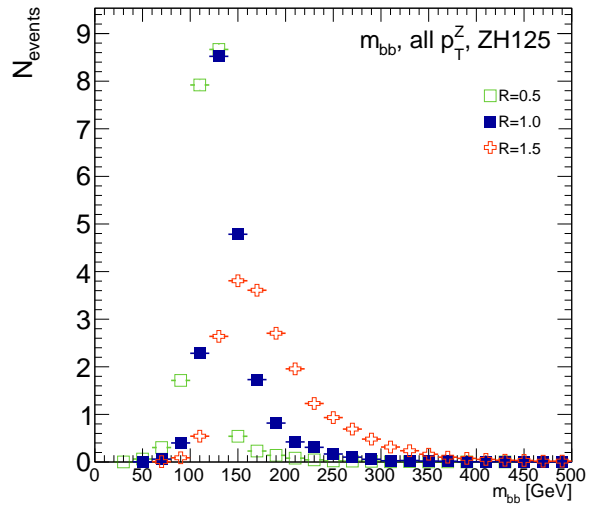
Figure B.1: The mean and resolution of p_T^{rec}/p_T^{tru} for the background $Z+jets$ sample for $|\eta| < 1.2$ and for $R = 0.4, 0.6, 1.0$, and 1.5 in 20 GeV bins of p_T^{tru} for $20\text{--}200\text{ GeV}$, one bin for $200\text{--}300\text{ GeV}$, and one bin for $300\text{--}500\text{ GeV}$, with bins chosen for purposes of statistics.

2644 B.5 TRUTH-LEVEL ANALYSIS

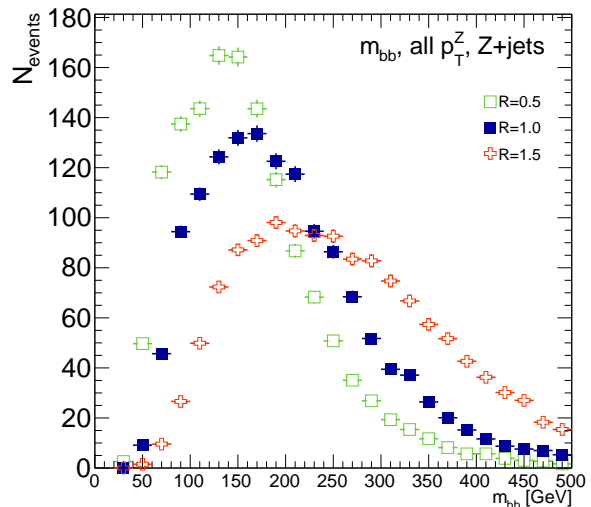
2645 To understand the limits and sources of any potential improvements, a truth-level analysis was con-
2646 ducted on MC samples with a ZH_{125} signal sample and a $Z+jets$ background sample. Distributions
2647 for the dijet invariant mass, m_{bb} , were made for each telescoping radius. Both signal and background
2648 samples develop more pronounced tails in the high m_{bb} region as R increases, as shown in Figure
2649 B.2. N_{events} is normalized to expected values in data.

2650 One way to take advantage of this information is to make a cut on m_{bb} for two different radii.
2651 This is graphically depicted in Figure B.3 for the optimized combination of $m_{bb,R=0.9}$ (telescoping
2652 cone jets constructed as outlined in Sec. B.2) vs. $m_{bb,R=0.4}$ (anti- k_t jets). At truth-level, the majority
2653 of events in the signal ZH_{125} sample are concentrated in relatively narrow region of parameter space,
2654 where this is certainly not the case for the more diffuse $Z+jets$ background sample.

2655 Another way to take advantage of multiple event interpretations is to make use of an event's cut-
2656 weight, denoted z and defined as the fraction of interpretations in a given event that pass a certain set
2657 of cuts (in this note, a cut on m_{bb}). The distribution of cut-weights for a sample of events is denoted
2658 $\rho(z)$. To enhance the significance of a cut-based analysis, events can be weighted by the cut-weight
2659 or any function $t(z)$ of the cut-weight. Weighting events by $t(z)$ modifies the usual $S/\delta B$ formula
2660 used to calculate significances. In this note, δB is based on Poissonian statistics and is taken as $0.5 +$
2661 $\sqrt{0.25 + N_B}$, where N_B is the number of background events.

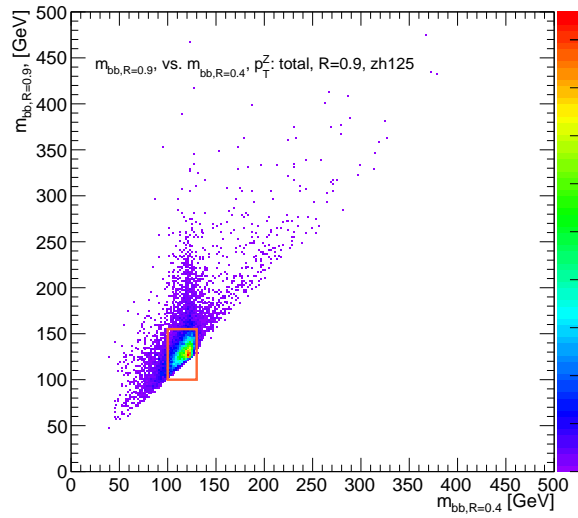


(a)

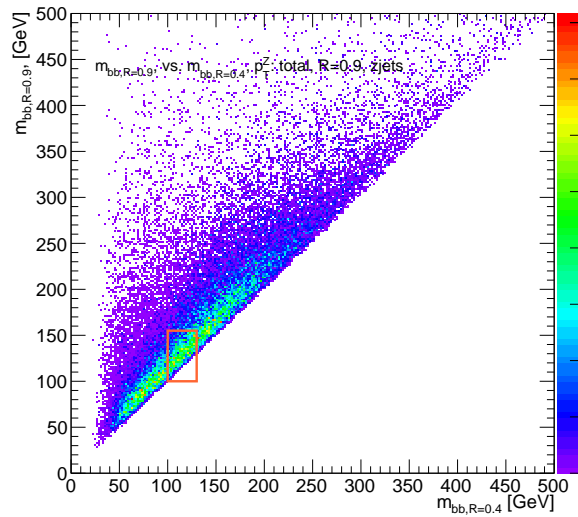


(b)

Figure B.2: The m_{bb} distribution for the telescoping jets with $R = 0.5, 1.0$, and 1.5 truth-level jets is shown for the signal and background samples in (a) and (b), respectively.



(a)



(b)

Figure B.3: The 2D distribution of $m_{bb,R=0.9}$ vs. $m_{bb,R=0.4}$ is shown for signal and background truth-level samples in (a) and (b), respectively. The region chosen for the double m_{bb} cut is outlined in orange.

2662 B.6 ERRORS ON TELESCOPING SIGNIFICANCES

2663 Significances of measurements are quoted in units of expected background fluctuations, schemati-
2664 cally, $S/\delta B$. For counting experiments with high numbers of events, we can use Gaussian statistics
2665 and express this as S/\sqrt{B} , which we here denote as \mathcal{S} . However, with lower statistics, it becomes
2666 more appropriate to use Poissonian statistics, and

$$\mathcal{S}_{gaus} = \frac{S}{\sqrt{B}} \rightarrow \mathcal{S}_{pois} = \frac{S}{0.5 + \sqrt{0.25 + B}} \quad (\text{B.1})$$

2667 where $0.5 + \sqrt{0.25 + B}$ is the characteristic upward fluctuation expected in a Poissonian data set
2668 using the Pearson chi-square test⁷⁸.

2669 B.7 COUNTING

2670 The significance is given as above, where $S = N_S$ and $B = N_B$. That is, the signal and background
2671 are just the number of events in signal and background that pass some cuts. The error for the Guas-
2672 sian case is the standard:

$$\Delta \mathcal{S}_{gaus} = \frac{1}{\sqrt{B}} \Delta S \oplus \frac{S}{2B^{3/2}} \Delta B \quad (\text{B.2})$$

2673 The error for the Poissonian case is:

$$\Delta \mathcal{S}_{pois} = \frac{1}{0.5 + \sqrt{0.25 + B}} \Delta S \oplus \frac{S}{2(0.5 + \sqrt{0.25 + B})^2 \sqrt{0.25 + B}} \Delta B \quad (\text{B.3})$$

²⁶⁷⁴ where \oplus denotes addition in quadrature, and $\Delta S(B)$ is the error on signal (background).

²⁶⁷⁵ B.8 MULTIPLE EVENT INTERPRETATIONS

²⁶⁷⁶ Using multiple event interpretations changes the formulae used in with simple counting. That is, S

²⁶⁷⁷ is not necessarily merely N_S , the number of events passing some signal cuts, and similarly for B and

²⁶⁷⁸ N_B . Using an event weighting by some function of the cut-weight, z , denoted $t(z)$, $S = N_S \langle t \rangle_{\rho_S}$

²⁶⁷⁹ and $B = N_B \langle t^2 \rangle_{\rho_B}$. So

$$\mathcal{S}_{t,gaus} = \frac{N_S \langle t \rangle_{\rho_S}}{\sqrt{N_B \langle t^2 \rangle_{\rho_B}}} \rightarrow \mathcal{S}_{t,pois} = \frac{N_S \langle t \rangle_{\rho_S}}{0.5 + \sqrt{0.25 + N_B \langle t^2 \rangle_{\rho_B}}} = \frac{N_S \int_0^1 dz t(z) \rho_S(z)}{0.5 + \sqrt{0.25 + N_B \int_0^1 dz t^2(z) \rho_B(z)}} \quad (\text{B.4})$$

For histograms, everything is done bin-wise. The notation used below is as follows: ρ_i is the value of $\rho(z)$ at bin i (where the bins run from 0 to n_{tel} , where n_{tel} is the total number of telescoping radii). $t_i = t_i(\rho_{S,i}, \rho_{B,i}, i/n_{tel})$ is the value of $t(z)$ at bin i , which can depend, in principle, on $\rho_{S,i}$, $\rho_{B,i}$, and i/n_{tel} (the last of which is z in bin i). Explicitly,

$$N = \sum_{i=0}^{n_{tel}} \rho_i, \quad \int_0^1 dz t(z) \rho_S(z) = \sum_{i=0}^{n_{tel}} t_i \rho_{S,i}, \quad \int_0^1 dz t^2(z) \rho_B(z) = \sum_{i=0}^{n_{tel}} t_i^2 \rho_{B,i}$$

²⁶⁸⁰ For the calculations that follow, let $\xi = \sum_{i=0}^{n_{tel}} t_i \rho_{S,i}$, $\psi = 0.5 + \sqrt{0.25 + N_B \sum_{i=0}^{n_{tel}} t_i^2 \rho_{B,i}}$,
²⁶⁸¹ $\partial_S = \frac{\partial}{\partial \rho_{S,i}}$ (and similarly for B), so $\mathcal{S}_t = N_S \xi / \psi$

2682 Some partial derivatives:

$$\begin{aligned}
 \partial_S N_S &= 1, & \partial_{B,i} N_B &= 1 \\
 \partial_S \xi &= t_i + (\partial_S t_i) \rho_{S,i}, & \partial_B \xi &= (\partial_B t_i) \rho_{B,i} \\
 \partial_S \psi &= \frac{N_B t_i (\partial_S t_i) \rho_{B,i}}{\sqrt{0.25 + N_B \sum_{i=0}^{n_{tel}} t_i^2 \rho_{B,i}}}, & \partial_B \psi &= \frac{\sum_{i=0}^{n_{tel}} t_i^2 \rho_{B,i} + N_B (t_i^2 + 2t_i (\partial_B t_i) \rho_{B,i})}{2\sqrt{0.25 + N_B \sum_{i=0}^{n_{tel}} t_i^2 \rho_{B,i}}} \\
 \partial_S \mathcal{S}_t &= \frac{\xi}{\psi} + \frac{N_S}{\psi} \partial_S \xi - \frac{N_S \xi}{\psi^2} \partial_S \psi, & \partial_B \mathcal{S}_t &= N_S \left(\frac{1}{\psi} \partial_B \xi - \frac{\xi}{\psi^2} \partial_B \psi \right)
 \end{aligned}$$

2683 Thus,

$$\Delta \mathcal{S}_{t,i} = \left[\frac{\xi}{\psi} + \frac{N_S}{\psi} \partial_S \xi - \frac{N_S \xi}{\psi^2} \partial_S \psi \right] \Delta \rho_{S,i} \oplus N_S \left[\frac{1}{\psi} \partial_B \xi - \frac{\xi}{\psi^2} \partial_B \psi \right] \Delta \rho_{B,i} \quad (\text{B.5})$$

2684 and the total error is given by the sum in quadrature over all bins i of $\Delta \mathcal{S}_{t,i}$.

2685 B.9 $t(z) = z$

2686 With $t(z) = z$, $t_i = i/n_{tel}$, so $\partial_S t_i = \partial_B t_i = 0$. So:

$$\begin{aligned}
 \partial_S \psi &= \partial_B \xi = 0 \\
 \partial_S \xi &= \frac{i}{n_{tel}} \\
 \partial_B \psi &= \frac{\sum_i i^2 \rho_{B,i} + N_B t^2}{n_{tel} \sqrt{n_{tel}^2 + N_B \sum_i i^2 \rho_{B,i}}}
 \end{aligned}$$

²⁶⁸⁷ so $\Delta\mathcal{S}_{z,i}$ reduces to

$$\Delta\mathcal{S}_{t,i} = \left[\frac{\xi + N_S t_i}{\psi} \right] \Delta\rho_{S,i} \oplus \left[\frac{N_S \xi}{\psi^2} \partial_B \psi \right] \Delta\rho_{B,i} \quad (\text{B.6})$$

²⁶⁸⁸ B.10 $t(z) = \rho_S(z) / \rho_B(z)$

²⁶⁸⁹ With the likelihood optimized* $t^*(z) = \rho_S(z) / \rho_B(z)$, $t_i = \rho_{S,i} / \rho_{B,i}$, so $\partial_S t_i = 1 / \rho_{B,i}$ and $\partial_B t_i =$

²⁶⁹⁰ $-\rho_{S,i} / \rho_{B,i}^2$. So:

$$\begin{aligned} \partial_S \xi &= 2 \frac{\rho_{S,i}}{\rho_{B,i}} = 2t_i \\ \partial_B \xi &= -\frac{\rho_{S,i}}{\rho_{B,i}} = -t_i \\ \partial_S \psi &= \frac{N_B t_i}{\sqrt{0.25 + N_B \sum_i \rho_{S,i}^2 / \rho_{B,i}}} \\ \partial_B \psi &= \frac{\sum_i \rho_{S,i}^2 / \rho_{B,i} - N_B (\rho_{S,i} / \rho_{B,i})^2}{\sqrt{1 + 4N_B \sum_i \rho_{S,i}^2 / \rho_{B,i}}} \end{aligned}$$

²⁶⁹¹ simplifying somewhat the terms in the per bin error in Equation B.6.

²⁶⁹² The new significance figure using multiple event interpretations becomes, with ρ_S and ρ_B denot-

²⁶⁹³ ing the cut-weight distributions in signal and background, respectively

$$\frac{S}{\delta B} = \frac{N_S \langle t \rangle_{\rho_S}}{0.5 + \sqrt{0.25 + N_B \langle t^2 \rangle_{\rho_B}}} \quad (\text{B.7})$$

*for the Gaussian statistics case

²⁶⁹⁴ Of particular interest is the likelihood optimized $t(z)$,[†] $t^*(z) = \rho_S(z)/\rho_B(z)$. m_{bb} windows are
²⁶⁹⁵ chosen separately for each scheme studied to maximize total significances and are summarized in
²⁶⁹⁶ Table B.3.

$$\left(\frac{S}{\delta B}\right)_z = \frac{N_S \epsilon_S}{0.5 + \sqrt{0.25 + N_B (\epsilon_B^2 + \sigma_B^2)}} \quad (B.8)$$

²⁶⁹⁷

$$\left(\frac{S}{\delta B}\right)_{t^*(z)} = \frac{N_S \int_0^1 dz \frac{\rho_S^2(z)}{\rho_B(z)}}{0.5 + \sqrt{0.25 + N_B \int_0^1 dz \frac{\rho_S^2(z)}{\rho_B(z)}}} \quad (B.9)$$

²⁶⁹⁸ where $\epsilon_{S,B}$ are the means of $\rho_{S,B}(z)$ and σ_B^2 is the variance of $\rho_B(z)$. Further details can be found in
²⁶⁹⁹ Refs.^{36,47} and Appendix B.6.

Table B.3: m_{bb} windows studied. These windows were chosen to optimize significances over all p_T^Z .

Analysis Type	$S/\delta B$ Type	Optimal m_{bb} Window
Reconstructed	$\text{anti-}k_t R = 0.4$ $t(z) = z$ $t(z) = \rho_S(z)/\rho_B(z)$ $\text{anti-}k_t R = 0.4$, telescoping $R = 0.6$	$90\text{--}140 \text{ GeV}$ $110\text{--}155 \text{ GeV}$ $110\text{--}155 \text{ GeV}$ $95\text{--}140 \text{ GeV} (R = 0.4), 105\text{--}160 \text{ GeV} (R = 0.6)$
Truth	$\text{anti-}k_t R = 0.4$ $t(z) = z$ $t(z) = \rho_S(z)/\rho_B(z)$ $\text{anti-}k_t R = 0.4$, telescoping $R = 0.9$	$100\text{--}130 \text{ GeV}$ $115\text{--}140 \text{ GeV}$ $120\text{--}135 \text{ GeV}$ $100\text{--}130 \text{ GeV} (R = 0.4), 100\text{--}155 \text{ GeV} (R = 0.9)$

²⁷⁰⁰ The truth-level distributions $\rho_S(z)$, $\rho_B(z)$, and $\rho_S(z)/\rho_B(z)$ are shown for the m_{bb} window
²⁷⁰¹ that optimizes $(S/\delta B)_{t^*(z)}$ in Figure B.4, and significance improvements as a function of p_T^Z are
²⁷⁰² summarized in Figure B.5. Uncertainties in Figures B.5 and B.9 are statistical uncertainties. JES sys-

[†]Derived under the assumption of Gaussian statistics in Ref⁴⁷

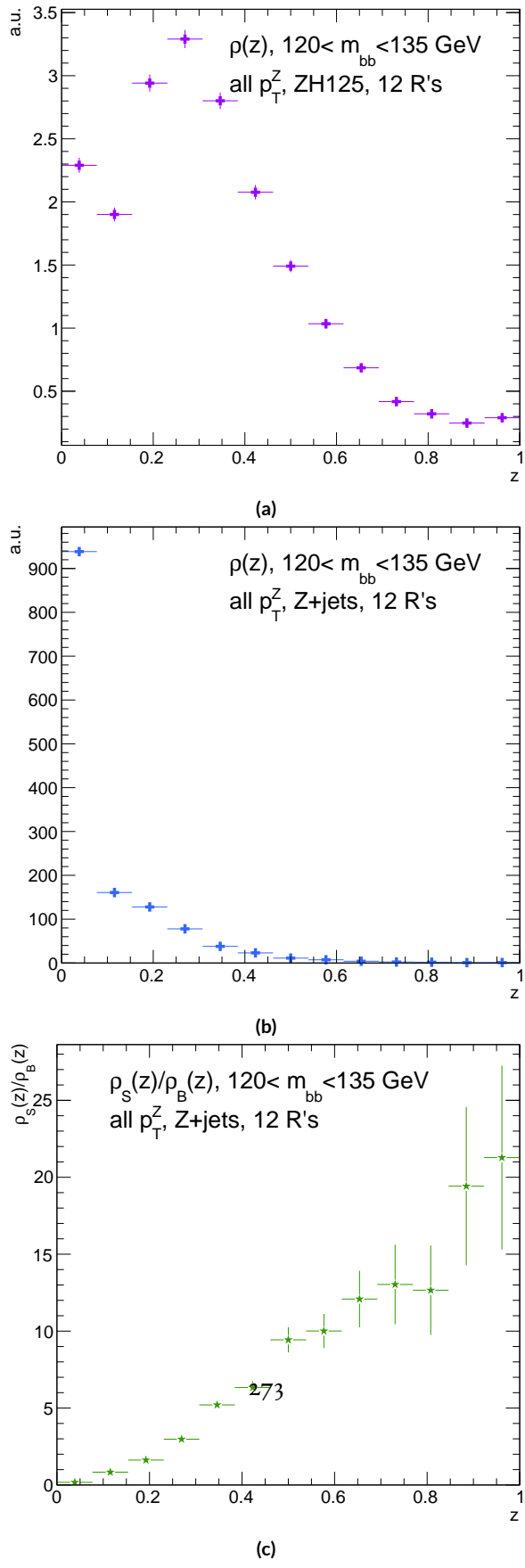


Figure B.4: Truth-level $\rho(z)$ distributions for the m_{bb} window optimizing $(S/\delta B)_{t^*(z)}$. $\rho_S(z)$ for the signal $ZH125$ sample is shown in (a), and $\rho_B(z)$ for the background $Z+jets$ sample is shown in (b). The distribution of $\rho_S(z) / \rho_B(z)$

2703 tematics will need to be evaluated for different R 's, as modeling uncertainties is an outstanding is-
 2704 sue, but these systematics will likely be strongly correlated for the different R 's and are not antici-
 2705 pated to be a very large contribution to total uncertainties. While the two dimensional m_{bb} cut and
 2706 $t(z) = z$ schemes only showed marginal improvement at truth level at 2.87%[‡] and 1.45%, respec-
 2707 tively, the likelihood optimized $t^*(z)$ showed a more substantial 40.7% improvement overall, with
 2708 a steady increase in improvement with increasing p_T^Z . Figure B.5 (d) summarizes the improvements
 2709 with respect to p_T^Z for the $t^*(z)$ event weight for five, seven, and twelve telescoping radii (interpreta-
 2710 tions) per event. Improvements increase with a greater number of interpretations and are more pro-
 2711 nounced at higher p_T^Z for this scheme. The optimal $120 < m_{bb} < 135$ GeV window for $t^*(z)$ case
 2712 is among the smallest studied. The benefits of this window's narrowness are suggested in Figure B.4.
 2713 While the background cut-weight distribution, $\rho_B(z)$ in Figure B.4 (b) behaves as one might with
 2714 a marked peak at $z = 0$, the signal $\rho_S(z)$ distribution peaks at a relatively modest $z = 0.3$, which
 2715 indicates that much of the gain at truth level comes from background rejection. This is possible at
 2716 truth level since there is both truth-level information available and no smearing and since ρ_S/ρ_B is
 2717 the relevant quantity (as shown in Figure B.4 (c)).

[‡]The limited improvement is provably due to the simplified treatment of the 2D case; better performance with a more sophisticated treatment has been observed in Ref.³⁹.

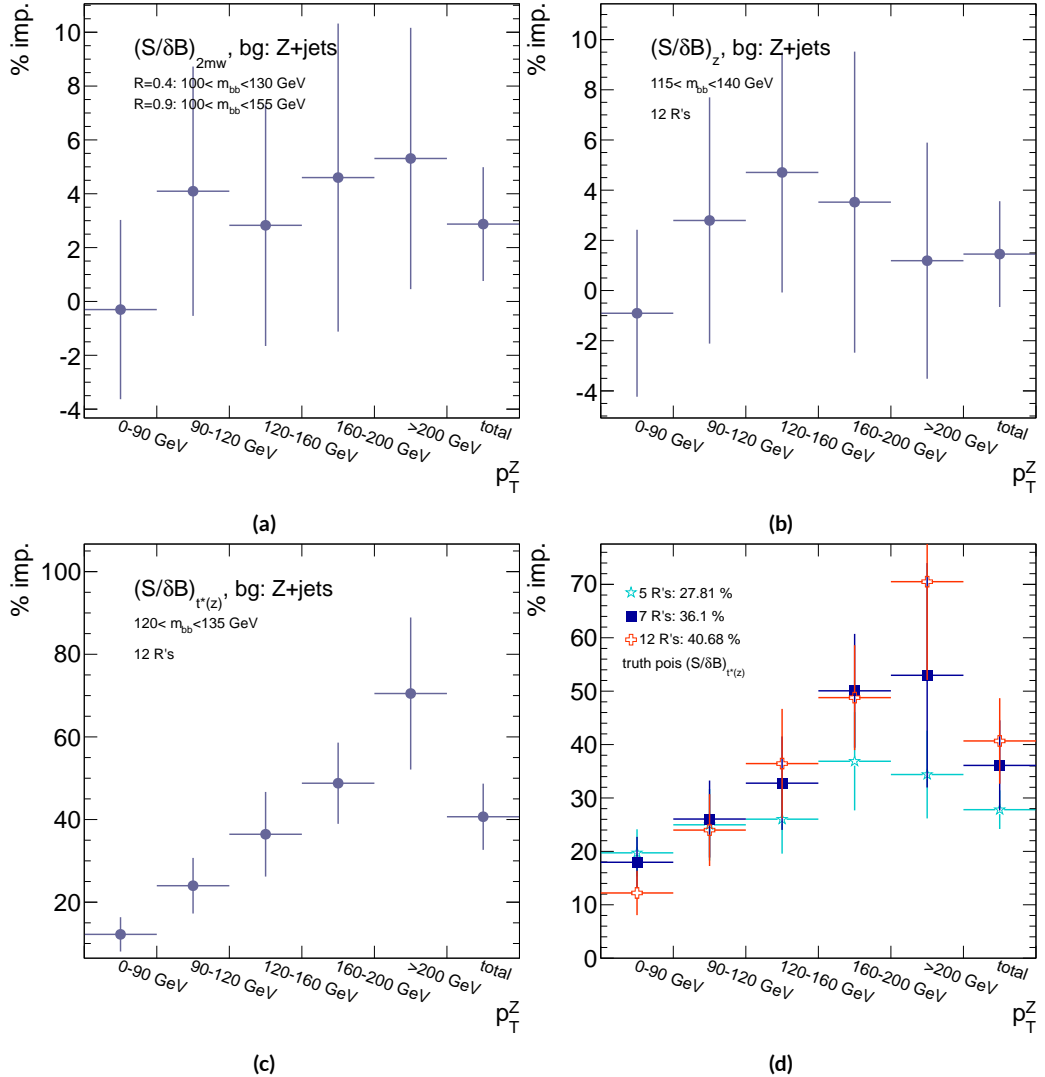


Figure B.5: A summary of the improvements for different truth-level telescoping jet cuts and weights is shown in bins of p_T^Z . The final bin is the total improvement over all p_T^Z . Shown are improvements for the 2D m_{bb} cut (a), $t(z) = z$ (b), $t(z) = t^*(z)$ with 12 radii (c), and $t(z) = t^*(z)$ for various radii (d).

2718 B.II RECONSTRUCTED-LEVEL ANALYSIS

2719 At reconstructed level, the same overall effect of introducing a high tail in m_{bb} distributions with
2720 increasing R is evident in comparing Figures B.2 and B.6. The optimal m_{bb} windows, however, grow
2721 larger, due to the lack of truth-level information.

2722 Total significance gains at reconstructed level for the two dimensional m_{bb} cut and the $t(z) = z$
2723 case are similar, at 2.87% and 1.45%, respectively. The optimal two-dimensional m_{bb} cut at recon-
2724 structed level is $95 < m_{bb,R=0.4} < 140 \text{ GeV}$, $105 < m_{bb,R=0.6} < 160 \text{ GeV}$. Just as at truth level,
2725 the $R = 0.4$ m_{bb} cut is comparable to the optimal single $R = 0.4$ m_{bb} cut, and the second m_{bb} cut is
2726 at similar values (cf. Table B.3 and Figures B.3 and B.7). However, the optimal second telescoping ra-
2727 dius is markedly smaller at $R = 0.6$ versus the optimal truth-level second radius of $R = 0.9$, which
2728 suggests that effects like pileup at reconstructed level obscure correlations between the $R = 0.4$
2729 interpretations and limit the usefulness of larger R interpretations in this particular scheme. The
2730 $t(z) = z$ case has a wider optimal window and yields about half the improvement it does at truth
2731 level.

2732 The optimal m_{bb} window for the $t^*(z)$ case is also markedly wider at reconstructed level, at $110 <$
2733 $m_{bb} < 155 \text{ GeV}$ in comparison to the truth-level optimal $120 < m_{bb} < 135 \text{ GeV}$. The $\rho(z)$ dis-
2734 tributions for the signal $ZH125$ and background $Z+\text{jets}$ as well as the $\rho_S(z) / \rho_B(z)$ in this window
2735 are shown in Figure B.8. Compared with the truth-level distributions in Figure B.4, both the sig-
2736 nal and background optimal $\rho(z)$ distributions have higher values at higher z . The peak in $\rho_S(z)$ at
2737 $z = 1$ suggests that at reconstructed level, maximizing the number of more “signal-like” events is

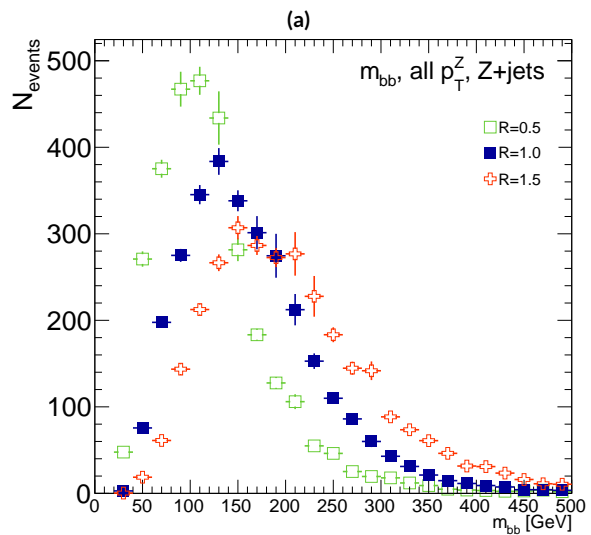
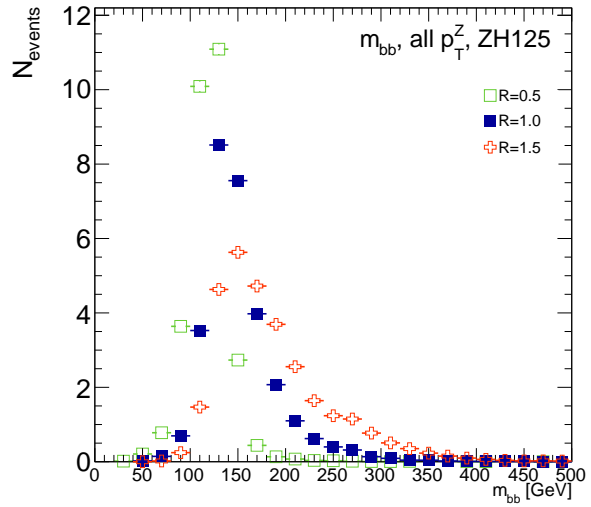


Figure B.6: The m_{bb} distribution for the telescoping jets with $R = 0.5$, $R = 1.0$, and $R = 1.5$ reconstructed-level jets is shown for the signal and background samples in (a) and (b), respectively.

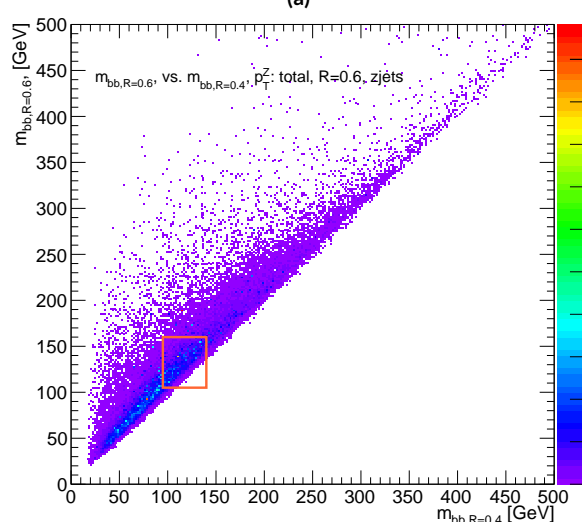
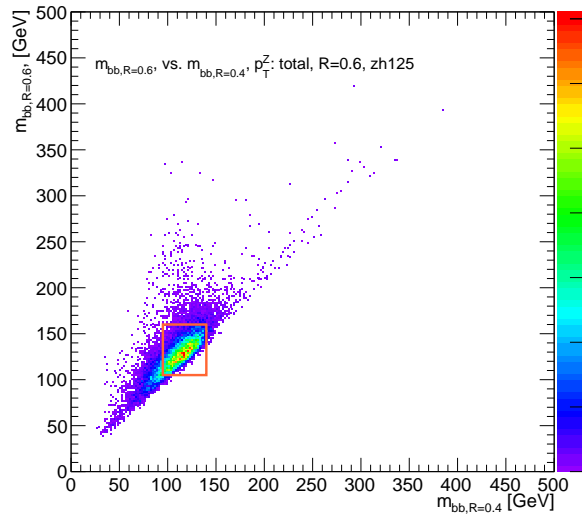


Figure B.7: The 2D distribution of $m_{bb,R=0.8}$ vs. $m_{bb,R=0.4}$ is shown for signal and background reconstructed-level samples in (a) and (b), respectively. The region chosen for the double m_{bb} cut is outlined in orange.

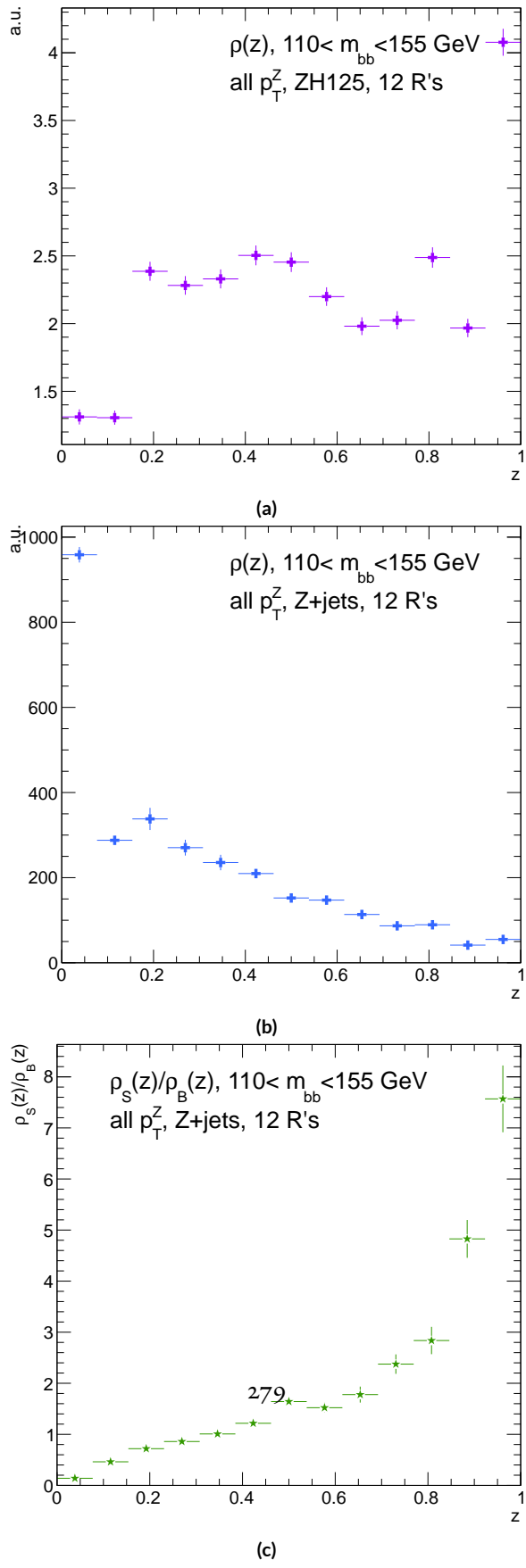


Figure B.8: Reconstructed-level $\rho(z)$ distributions for the m_{bb} window optimizing $(S/\delta B)_{t^*(z)} \cdot \rho_S(z)$ for the signal ZH125 sample is shown in (a), and $\rho_B(z)$ for the background Z+jets sample is shown in (b). The distribution of $\rho_s(z)/\rho_B(z)$ for these samples is shown in (c).

2738 the key to optimizing significances, as opposed to the optimal, background suppressing $\rho(z)$ distri-
 2739 butions at truth level. The use of a greater number of interpretations per event (telescoping radii)
 2740 does appear to result in overall greater improvement as at truth level, as twelve radii performed bet-
 2741 ter than five, but this is less clear at reconstructed level, as shown in Figure B.9 (d). The improve-
 2742 ment at reconstructed level using an event weight of $t^*(z)$ is 20.5%, just over half the improvement
 2743 at truth level but still quite significant. Summaries of improvements as a function of p_T^Z for all three
 2744 cases studied and for the $t^*(z)$ case for different numbers of telescoping radii are shown in Figure
 2745 B.9.

Table B.4: A summary of significances for different weighting schemes and cuts and for reconstructed and truth jets for a luminosity of 20.3 fb^{-1} .

Type	0–90 GeV	90–120 GeV	120–160 GeV	160–200 GeV	> 200 GeV	total
anti- k_t , $R = 0.4_{rec}$	0.47492	0.28214	0.28339	0.25748	0.37337	0.76887
anti- k_t , $R = 0.4_{tru}$	0.57414	0.30655	0.37309	0.35042	0.53569	0.98619
$2 m_{bb,rec}$	0.48903	0.2858	0.28812	0.25972	0.38297	0.78611
$2 m_{bb,tru}$	0.5724	0.3191	0.38364	0.36655	0.56414	1.0145
z_{rec}	0.50698	0.27962	0.29937	0.25688	0.36846	0.79158
z_{tru}	0.56894	0.31511	0.39065	0.36277	0.54206	1.0005
$t^*(z)_{rec}$	0.55085	0.29931	0.33367	0.30107	0.51321	0.92649
$t^*(z)_{tru}$	0.64425	0.38008	0.50904	0.5214	0.91337	1.3873

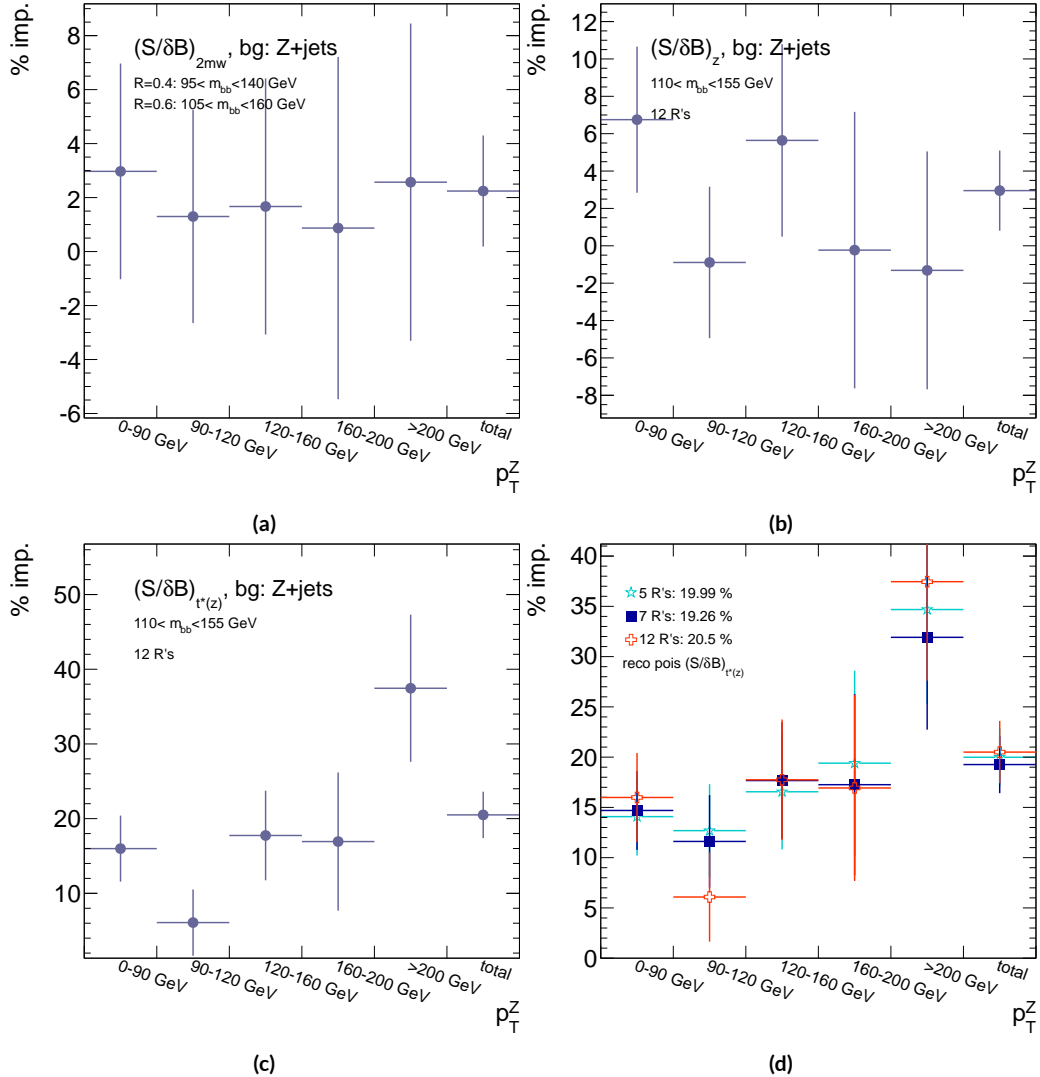


Figure B.9: A summary of the improvements for different reconstructed-level telescoping jet cuts and weights is shown in bins of p_T^Z . The final bin is the total improvement over all p_T^Z . Shown are improvements for the 2D m_{bb} cut (a), $t(z) = z$ (b), $t(z) = t^*(z)$ with 12 radii (c), and $t(z) = t^*(z)$ for various radii (d).

2746 B.12 CONCLUSIONS AND PROSPECTS

2747 The use of telescoping jets to provide multiple event interpretations shows promise as an avenue to
2748 increase significances in the $H \rightarrow b\bar{b}$ search in ATLAS and make an observation in the systematics-
2749 limited environment of early Run 2. A preliminary study using the telescoping jets algorithm with
2750 12 telescoping radii to build 12 event interpretations on 2012 Monte Carlo based on the full, cut-
2751 based Run 1 analysis yielded a 20.5% improvement in $S/\delta B$ over using anti- k_t with $R = 0.4$ alone
2752 at reconstructed level using a likelihood maximized event weighting to study the $ZH \rightarrow llb\bar{b}$ pro-
2753 cess. The jets used in this note at reconstructed level were trimmed in order to guarantee reasonable
2754 resolution in the large- R interpretations. The algorithm, in particular, showed discriminating power
2755 at high p_T^Z , so better performance can be expected in Run 2 with a higher \sqrt{s} and higher numbers of
2756 events with large p_T^Z . Additionally, the many simplifying assumptions regarding jet calibration and
2757 the relatively basic use of information[§] from multiple invariant masses in this note suggest that even
2758 further improvements than those quoted are possible. While this note did not explore the correla-
2759 tions between multiple event interpretations and the variables used in the BDT of the latest multi-
2760 variate version of the $H \rightarrow b\bar{b}$ analysis²⁰, new phenomenological studies suggest that such correla-
2761 tions are not strong³⁹. The corresponding reconstructed-level study, using a BDT, is left for future
2762 work. Also left for future work are better understanding the effects of jet trimming and which inter-
2763 pretations are the most useful.

[§]For examples of more sophisticated treatments compared to the treatment in this note, see Ref³⁹.

Ah, peut on être heureux?

Quand on forme des autres voeux?

J. P. Rameau, Forêts Paisibles

2764

C

2765

Progress in Particle Physics and Existential

2766

Threats to the American World Order

2767 INTERNATIONAL COLLABORATIONS with thousands of scientists like those at CERN's (the Euro-

2768 pean Organisation for Nuclear Research) 27 km circumference Large Hadron Collider (LHC) are

2769 fast becoming the norm in many fields of science, making the past seven decades of discovery in par-
2770 ticle physics seem a natural part of history's long march of progress. Seemingly arcane terms like dark
2771 matter and the Higgs boson (the infamous "God particle") even pop up in blockbuster movies and
2772 primetime television. All of this, however, would have been impossible without the fascist and then
2773 communist existential threats to the American world order throughout the 20th century.

2774 The Manhattan Project and its atomic arsenal were a direct response to the threat of global fas-
2775 cism in World War II. They both secured the United States' position as a world power at the end of
2776 the war and laid the foundations for many particle physics developments for the following three
2777 decades. High ranking American officials were well aware that this would have been impossible
2778 without the contributions of particle physicists. Some of these physicists, like Enrico Fermi and
2779 Arthur Compton, were already Nobel laureates and luminaries in the field. Others, like Richard
2780 Feynman and Owen Chamberlain, would go on to make their marks in the decades following the
2781 war. Though a few of these physicists, most notably Edward Teller, would continue their work on
2782 nuclear weapons, most of these physicists would return to basic science research as the nation turned
2783 towards the uneasy peace time of the Cold War.

2784 Particle physicists' service and connections made during the war would serve them well in the
2785 decades to come as the military-controlled Manhattan Project transitioned to the civilian-led Atomic
2786 Energy Commission (AEC). The AEC was founded in 1946 to oversee the nuclear arsenal, the devel-
2787 opment of atomic power, and related fundamental research in the United States. Many of those on
2788 AEC board were former Manhattan Project particle physicists, including Glenn Seaborg, the AEC
2789 chairman from 1961-1971. Congressional oversight for AEC funding consisted of a single committee,

2790 the Joint Committee on Atomic Energy (JCAE), whose deliberations often took place behind closed
2791 doors owing to the AEC's sensitive national security mission. Elementary particle physics research
2792 was clearly central to the AEC mission at its founding, as nuclear fission was the bleeding edge of par-
2793 ticle physics at the beginning of World War II and represented the culmination of decades of highly
2794 specialized research that had no immediately obvious practical application. Furthermore, particle ac-
2795 celerator technology, the main workhorse then as now for basic science research in particle physics
2796 and the most expensive item on any particle physicist's wish list, had been crucial to many of these
2797 discoveries. The anticipation of future windfalls as momentous as the power of the atom and the ex-
2798 emplary performance of particle physicists during the war ensured that experimental particle physics
2799 and particle accelerators would remain the crown jewel of AEC research throughout the organiza-
2800 tion's existence.

2801 The AEC's sizable budget (thanks to its crucial mission of securing the nation's nuclear arsenal)
2802 and lavish support were the biggest contributing factors to the development of particle physics in
2803 the mid 20th century through its funding of accelerator facilities. Particle accelerators use powerful
2804 electromagnetic fields to take beams of subatomic particles, usually protons or electrons, as close to
2805 the speed of light as possible before colliding them into either fixed targets or other beams to pro-
2806 duce high energy collisions. Physicists use these collisions to test models of the universe that predict
2807 behavior in these extreme regimes. Without more energetic collisions, progress becomes function-
2808 ally impossible. While the first such accelerator was smaller than the average human hand, studying
2809 more complete models of the universe called for more energetic collisions and hence bigger, more
2810 powerful, and more expensive accelerators.

2811 Soon, these experiments became too big and expensive for individual universities to operate on
2812 their own. Progress in American particle physics became entirely dependent on the AEC, and hence
2813 on the continued threat of nuclear annihilation. National laboratories, all under AEC stewardship,
2814 became regional centers of research for particle physicists. By the late 1960's, Brookhaven National
2815 Laboratory, Lawrence Berkeley National Laboratory, and the Stanford Linear Accelerator Center
2816 hosted the majority of cutting edge accelerator facilities in the country alongside a dwindling num-
2817 ber of single university accelerators. By the decade's end Cornell hosted the only such university op-
2818 erated facility. The competitive rivalry among these different institutions fostered American success
2819 and dominance in experimental particle physics through the 1970's. The culmination of AEC pa-
2820 tronage was the National Accelerator Laboratory (now Fermilab), which began operations in 1967.
2821 Fermilab's construction was not a foregone conclusion given the economically challenging backdrop
2822 of the Vietnam War, but an emphasis on cost effective plans for both the laboratory and accelerator
2823 backed by the full support of the AEC secured Fermilab's funding. Fermilab would ultimately be-
2824 come home to the Tevatron, the final particle accelerator in the United States to claim the title of the
2825 world's most powerful.

2826 Particle physics only became more dependent on the existence of a Soviet threat with the end of
2827 the AEC. Due to budgetary pressures, the AEC was abolished in 1975, and its duties were eventually
2828 reorganized into the Department of Energy (DOE). Under DOE administration, proposed parti-
2829 cle physics experiments now had to compete against research projects from the entire range of fields
2830 germane to American energy instead of only other nuclear and particle physics projects. Moreover,
2831 DOE leadership had far fewer officials with track records of supporting particle physics research

2832 projects above all others. Nevertheless, there remained one last, great effort to promote collider
2833 physics in the United States, the Superconducting Supercollider (SSC). The SSC was an incredibly
2834 ambitious design: a 50 mile ring under the Waxahachie desert with superconducting magnets to ac-
2835 celerate protons and antiprotons to energies more than three times higher than the LHC's current
2836 world record. The project was conceived during the Reagan administration and billed as a megapro-
2837 ject to reassert American dominance as the president took a more aggressive approach to the Soviet
2838 threat. Unfortunately, the project was perhaps too ambitious and suffered from management prob-
2839 lems. It is not surprising, then, that the end of the Cold War spelled the end of the SSC. With no
2840 external threat to American global dominance, there was little impetus to continue funding such an
2841 expensive and over-budget project. There has not been a single initiative since for the United States
2842 to recapture its once commanding lead over efforts in Western Europe.

2843 Western Europe was the only other serious center of 20th century particle physics, and successes
2844 there also depended upon five decades of existential threat to the United States, though in a less di-
2845 rect fashion. Most obviously, American institutions and physicists have been essential to the devel-
2846 opment of European particle physics, just as European physicists were crucial to the success of the
2847 Manhattan Project. Seven of the ten Cold War era CERN Directors General were either educated
2848 or did research at American universities, and every major particle physics discovery since the end of
2849 World War II has relied on both American and European talent and infrastructure. Furthermore,
2850 the European approach to experimental particle physics, epitomized by CERN, emphasized consen-
2851 sus and cooperation and was emblematic of larger geopolitical currents on the European continent
2852 in the latter half of the 20th century. Such a culture and its success would have been impossible with-

2853 out the same threats that facilitated American success in particle physics. While limited resources of
2854 member states were no doubt contributing factors in CERN's genesis, the collaborative culture of
2855 CERN and other pan-European organizations was a reaction to centuries of competition for conti-
2856 nental dominance. After the total destruction of the world wars, enough was enough. The relatively
2857 peaceful prosperity on the Western side of the Iron Curtain made European cooperation possible,
2858 while the threat at Western Europe's doorstep only heightened the urgency of pan-European desires.
2859 Hence, the symbolic importance of European unity during the Cold War is hard to underestimate, and
2860 CERN-facilitated European cooperation made it a forerunner to organizations like the European
2861 Union and a model to the world. Every major achievement in particle physics after 1940 therefore
2862 relies on facilities and institutions on both sides of the Atlantic that would never have been formed
2863 without the back to back threats of global fascism and Soviet Communism.

2864 With the cancellation of the SSC in 1993 and the closing of Fermilab's Tevatron in 2011, CERN
2865 and its LHC remain the lone laboratory and experiment at the energy frontier. The United States
2866 is now a mere "observer state" at CERN: American talent and funding are essential to CERN and
2867 its mission, but the United States does not have a seat on CERN's governing council. It remains
2868 to be seen whether a legacy of over six decades of international cooperation will provide sufficient
2869 motivation for particle physics to continue at CERN after the LHC without guarantee of any dis-
2870 covery at the next experiment. Current nuclear threats, while attention grabbing, are far from exis-
2871 tential and unlikely to reignite any initiative for distinctly American science megaprojects. The only
2872 other prospect for a future collider at the energy frontier is China, whose nationalistic desire for su-
2873 perpower status may prove a sufficiently powerful and lasting motivator for the next generation of

²⁸⁷⁴ collider.

References

- [1] (2010). Measurement of the $w \rightarrow l\nu$ and $z/\gamma^* \rightarrow ll$ production cross sections in proton-proton collisions at $\sqrt{s} = 7$ TeV with the atlas detector. *JHEP*, 1012.
- [2] (2011a). *ATLAS tunes of PYTHIA 6 and Pythia 8 for MCII*. Technical Report ATL-PHYS-PUB-2011-009, CERN, Geneva.
- [3] (2011b). *New ATLAS event generator tunes to 2010 data*. Technical Report ATL-PHYS-PUB-2011-008, CERN, Geneva.
- [4] (2012a). *b-jet tagging calibration on c-jets containing D^{*+} mesons*. Technical Report ATLAS-CONF-2012-039, CERN, Geneva.
- [5] (2012b). Electron performance measurements with the atlas detector using the 2010 lhc proton-proton collision data. *Eur. Phys. J.*, C72.
- [6] (2012a). Observation of a new boson at a mass of 125 GeV with the CMS experiment at the LHC. *Phys.Lett.*, B716, 30–61.
- [7] (2012b). Observation of a new particle in the search for the Standard Model Higgs boson with the ATLAS detector at the LHC. *Phys.Lett.*, B716, 1–29.
- [8] (2012). The Proton Synchrotron.
- [9] (2012). The Proton Synchrotron Booster.
- [10] (2012). The Super Proton Synchrotron.
- [11] (2013a). Jet energy measurement with the atlas detector in proton-proton collisions at $\sqrt{s} = 7$ TeV *Eur. Phys. J.*, C73.
- [12] (2013b). *Search for the bb decay of the Standard Model Higgs boson in associated W/ZH production with the ATLAS detector*. Technical Report ATLAS-CONF-2013-079, CERN, Geneva.

- 2898 [13] (2014). *ATLAS Run 1 Pythia8 tunes*. Technical Report ATL-PHYS-PUB-2014-021, CERN,
 2899 Geneva.
- 2900 [14] (2014). *Electron efficiency measurements with the ATLAS detector using the 2012 LHC*
 2901 *proton-proton collision data*. Technical Report ATLAS-CONF-2014-032, CERN, Geneva.
- 2902 [15] (2015). *Expected performance of the ATLAS b-tagging algorithms in Run-2*. Technical Report
 2903 ATL-PHYS-PUB-2015-022, CERN, Geneva.
- 2904 [16] (2015). *Jet Calibration and Systematic Uncertainties for Jets Reconstructed in the ATLAS*
 2905 *Detector at $\sqrt{s} = 13 \text{ TeV}$* . Technical Report ATL-PHYS-PUB-2015-015, CERN, Geneva.
- 2906 [17] (2015). *Muon reconstruction performance in early $\sqrt{s}=13 \text{ TeV}$ data*. Technical Report ATL-
 2907 PHYS-PUB-2015-037, CERN, Geneva.
- 2908 [18] A. L. Read (2002). Presentation of search results: the CL_s technique. *J. Phys. G*, 28, 2693–
 2909 2704.
- 2910 [19] Aad, G. et al. (2014). Measurement of the Z/γ^* boson transverse momentum distribution in
 2911 pp collisions at $\sqrt{s} = 7 \text{ TeV}$ with the ATLAS detector. *JHEP*, 09, 145.
- 2912 [20] Ahmadov, F., Alio, L., Allbrooke, B., Bristow, T., Buescher, D., Buzatu, A., Coadou, Y.,
 2913 Debenedetti, C., Enari, Y., Facini, G., Fisher, W., Francavilla, P., Gaycken, G., Gentil, J.,
 2914 Goncalo, R., Gonzalez Parra, G., Grivaz, J., Gwilliam, C., Hageboeck, S., Halladjian, G., Jack-
 2915 son, M., Jamin, D., Jansky, R., Kiuchi, K., Kostyukhin, V., Lohwasser, K., & Lopez Mateos,
 2916 D, e. a. (2014). *Supporting Document for the Search for the bb decay of the Standard Model*
 2917 *Higgs boson in associated (W/Z)H production with the ATLAS detector*. Technical Report
 2918 ATL-COM-PHYS-2014-051, CERN, Geneva.
- 2919 [21] Aliev, M., Lacker, H., Langenfeld, U., Moch, S., Uwer, P., et al. (2011). HATHOR: Hadronic
 2920 Top and Heavy quarks cross section calculator. *Comput.Phys.Commun.*, 182, 1034–1046.
- 2921 [22] Alwall, J., Frederix, R., Frixione, S., Hirschi, V., Maltoni, F., Mattelaer, O., Shao, H. S.,
 2922 Stelzer, T., Torrielli, P., & Zaro, M. (2014). The automated computation of tree-level and
 2923 next-to-leading order differential cross sections, and their matching to parton shower simula-
 2924 tions. *JHEP*, 07, 079.
- 2925 [23] Alwall, J., Herquet, M., Maltoni, F., Mattelaer, O., & Stelzer, T. (2011). Madgraph 5 : Going
 2926 beyond.

- 2927 [24] ATLAS Collaboration (2014). *Tagging and suppression of pileup jets with the ATLAS detector*. Technical Report ATLAS-CONF-2014-018, CERN, Geneva.
- 2928
- 2929 [25] ATLAS Collaboration (2015a). MCPAnalysisGuidelinesMC15.
- 2930 <https://twiki.cern.ch/twiki/bin/view/AtlasProtected/MCPAnalysisGuidelinesMC15>.
- 2931 [26] ATLAS Collaboration (2015b). *Performance of missing transverse momentum reconstruction for the ATLAS detector in the first proton-proton collisions at at $\sqrt{s} = 13 \text{ TeV}$* . Technical Report ATL-PHYS-PUB-2015-027, CERN, Geneva.
- 2932
- 2933
- 2934 [27] Ball, R. D. et al. (2013). Parton distributions with LHC data. *Nucl. Phys.*, B867, 244–289.
- 2935 [28] Ball, R. D. et al. (2015). Parton distributions for the LHC Run II. *JHEP*, 04, 040.
- 2936 [29] Botje, M. et al. (2011). The PDF4LHC Working Group Interim Recommendations.
- 2937 [30] Buckley, A., Butterworth, J., Grellscheid, D., Hoeth, H., Lonnblad, L., Monk, J., Schulz, H.,
2938 & Siegert, F. (2010). Rivet user manual.
- 2939 [31] Buzatu, A. & Wang, W. (2016). *Object selections for SM Higgs boson produced in association with a vector boson in which $H \rightarrow b\bar{b}$ and V decays leptonically with Run-2 data: Object support note for $VH(bb)$ 2015+2016 dataset publication*. Technical Report ATL-COM-PHYS-
2940 2016-1674, CERN, Geneva. This is a support note for the $VH(bb)$ SM publication using the
2941 2015+2016 datasets.
- 2942
- 2943
- 2944 [32] Cacciari, M., G. P. Salam, M. C., & Salam, G. P. (2008). Pileup subtraction using jet areas.
2945 *Phys. Lett.*, B659.
- 2946 [33] Campbell, J. M. & Ellis, R. K. (2010). MCFM for the Tevatron and the LHC. *Nucl. Phys.*
2947 *Proc. Suppl.*, 205-206, 10–15.
- 2948 [34] Capeans, M., Darbo, G., Einsweiller, K., Elsing, M., Flick, T., Garcia-Sciveres, M., Gemme,
2949 C., Pernegger, H., Rohne, O., & Vuillermet, R. (2010). *ATLAS Insertable B-Layer Technical
2950 Design Report*. Technical Report CERN-LHCC-2010-013, ATLAS-TDR-19.
- 2951 [35] CERN (2008). LHC first beam: a day to remember.
- 2952 [36] Chan, S., Huth, J., Lopez Mateos, D., & Mercurio, K. (2015a). *ZH → llb̄ Analysis with
2953 Telescoping Jets*. Technical Report ATL-PHYS-INT-2015-002, CERN, Geneva.

- 2954 [37] Chan, S. K.-w. & Huth, J. (2017). *Variations on MVA Variables in the SM ZH → ℓℓ $b\bar{b}$ Search*. Technical Report ATL-COM-PHYS-2017-1318, CERN, Geneva.
- 2955
- 2956 [38] Chan, S. K.-w., Lopez Mateos, D., & Huth, J. (2015b). *Micromegas Trigger Processor Algo-*
2957 *rithm Performance in Nominal, Misaligned, and Corrected Misalignment Conditions*. Tech-
2958 nical Report ATL-COM-UPGRADE-2015-033, CERN, Geneva.
- 2959 [39] Chien, Y.-T., Farhi, D., Krohn, D., Marantan, A., Mateos, D. L., & Schwartz, M. (2014).
2960 Quantifying the power of multiple event interpretations.
- 2961 [40] Ciccolini, M., Dittmaier, S., & Kramer, M. (2003). Electroweak radiative corrections to asso-
2962 ciated WH and ZH production at hadron colliders. *Phys. Rev.*, D68, 073003.
- 2963 [41] Clark, B., Lopez Mateos, D., Felt, N., Huth, J., & Oliver, J. (2014). *An Algorithm for Mi-*
2964 *cromegas Segment Reconstruction in the Level-1 Trigger of the New Small Wheel*. Technical
2965 Report ATL-UPGRADE-INT-2014-001, CERN, Geneva.
- 2966 [42] Collaboration, A. (2017a). Evidence for the $h \rightarrow b\bar{b}$ decay with the atlas detector.
- 2967 [43] Collaboration, A. (2017b). Study of the material of the atlas inner detector for run 2 of the
2968 lhc.
- 2969 [44] Collaboration, T. A., Aad, G., Abat, E., Abdallah, J., & A A Abdelalim, e. a. (2008). The atlas
2970 experiment at the cern large hadron collider. *Journal of Instrumentation*, 3(08), S08003.
- 2971 [45] Cowan, G., Cranmer, K., Gross, E., & Vitells, O. (2011). Asymptotic formulae for likelihood-
2972 based tests of new physics. *Eur. Phys. J. C*, 71, 1554.
- 2973 [46] Czakon, M., Fiedler, P., & Mitov, A. (2013). Total Top-Quark Pair-Production Cross Section
2974 at Hadron Colliders Through $\alpha(\frac{4}{5})$. *Phys. Rev. Lett.*, 110, 252004.
- 2975 [47] D. Kahawala, D. Kahawala, D. K. & Schwartz, M. D. (2013). Jet sampling: Improving event
2976 reconstruction through multiple interpretations.
- 2977 [48] D. Krohn, D. Krohn, J. T. L. W. (2009). Jet trimming.
- 2978 [49] Delmastro, M., Gleyzer, S., Hengler, C., Jimenez, M., Koffas, T., Kuna, M., Liu, K., Liu, Y.,
2979 Marchiori, G., Petit, E., Pitt, M., Soldatov, E., & Tackmann, K. (2014). *Photon identification*
2980 *efficiency measurements with the ATLAS detector using LHC Run 1 data*. Technical Report
2981 ATL-COM-PHYS-2014-949, CERN, Geneva.

- 2982 [50] Evans, L. & Bryant, P. (2008). Lhc machine. *Journal of Instrumentation*, 3(08), S08001.
- 2983 [51] Gleisberg, T. et al. (2009a). Event generation with SHERPA 1.1. *JHEP*, 02, 007.
- 2984 [52] Gleisberg, T., Höche, S., Krauss, F., Schönherr, M., Schumann, S., Siegert, F., & Winter, J.
2985 (2009b). Event generation with sherpa 1.1. *Journal of High Energy Physics*, 2009(02), 007.
- 2986 [53] Hagebock, S. (CERN, Geneva, 2017). Lorentz Invariant Observables for Measurements of
2987 Hbb Decays with ATLAS.
- 2988 [54] Heinemann, B., Hirsch, F., & Strandberg, S. (2010). *Performance of the ATLAS Secondary
2989 Vertex b-tagging Algorithm in 7 TeV Collision Data*. Technical Report ATLAS-COM-CONF-
2990 2010-042, CERN, Geneva. (Was originally 'ATL-COM-PHYS-2010-274').
- 2991 [55] J. Pumplin, J. Pumplin, D. S. J. H. H. L. P. M. N. e. a. (2002). New generation of parton
2992 distributions with unvertainties from global qcd analysis. *JEGP*, 0207.
- 2993 [56] Jackson, P. & Rogan, C. (2017). Recursive jigsaw reconstruction: Hep event analysis in the
2994 presence of kinematic and combinatoric ambiguities.
- 2995 [57] Kant, P., Kind, O., Kintscher, T., Lohse, T., Martini, T., Molbitz, S., Rieck, P., & Uwer, P.
2996 (2015). Hathor for single top-quark production: Updated predictions and uncertainty esti-
2997 mates for single top-quark production in hadronic collisions. *Computer Physics Communica-
2998 tions*, 191, 74 – 89.
- 2999 [58] Lampl, W., Laplace, S., Lelas, D., Loch, P., Ma, H., Menke, S., Rajagopalan, S., Rousseau,
3000 D., Snyder, S., & Unal, G. (2008). *Calorimeter Clustering Algorithms: Description and Per-
3001 formance*. Technical Report ATL-LARG-PUB-2008-002. ATL-COM-LARG-2008-003,
3002 CERN, Geneva.
- 3003 [59] Lavesson, N. & Lonnblad, L. (2005). W+jets matrix elements and the dipole cascade.
- 3004 [60] LHC Higgs Cross Section Working Group, Dittmaier, S., Mariotti, C., Passarino, G., &
3005 Tanaka (Eds.), R. (CERN, Geneva, 2011). Handbook of LHC Higgs Cross Sections: 1. In-
3006 clusiv Observables. *CERN-2011-002*.
- 3007 [61] Loch, Peter and Lefebve, Michel (2007). Introduction to Hadronic Calibration in ATLAS.

- 3008 [62] Luisoni, G., Nason, P., Oleari, C., & Tramontano, F. (2013). H_w ±/h_z + o and 1 jet at nlo
 3009 with the powheg box interfaced to gosam and their merging within minlo. *Journal of High*
 3010 *Energy Physics*, 2013(10), 83.
- 3011 [63] M. Cacciari, M. Cacciari, G. P. S. & Soyez, G. (2008). The anti- k_t jet clustering algorithm.
 3012 *JHEP*, 0804.
- 3013 [64] Marcastel, F. (2013). CERN's Accelerator Complex. La chaîne des accélérateurs du CERN.
 3014 General Photo.
- 3015 [65] Masubuchi, T., Benitez, J., Bell, A. S., Argyropoulos, S., Arnold, H., Amaral Coutinho, Y.,
 3016 Sanchez Pineda, A. R., Buzatu, A., Calderini, G., & Chan, Stephen Kam-wah, e. a. (2016).
 3017 *Search for a Standard Model Higgs boson produced in association with a vector boson and de-*
 3018 *caying to a pair of b-quarks*. Technical Report ATL-COM-PHYS-2016-1724, CERN, Geneva.
- 3019 [66] Patrignani, C. et al. (2016). Review of Particle Physics. *Chin. Phys.*, C40(10), 100001.
- 3020 [67] Robson, A., Piacquadio, G., & Schopf, E. (2016). *Signal and Background Modelling Stud-*
 3021 *ies for the Standard Model VH, H → b̄b and Related Searches: Modelling support note*
 3022 *for VH(b̄b) 2015+2016 dataset publication*. Technical Report ATL-COM-PHYS-2016-1747,
 3023 CERN, Geneva. This is a support note for the VH(b̄b) SM publication using the 2015+2016
 3024 datasets.
- 3025 [68] S. Alioli et al. (2009). NLO Higgs boson production via gluon fusion matched with shower
 3026 in POWHEG. *JHEP*, 0904, 002.
- 3027 [69] S. D. Ellis, S. D. Ellis, A. H. T. S. R. D. K. & Schwartz, M. D. (2012). Qjets: A non-
 3028 deterministic approach to tree-based jet substructure. *Phys. Rev. Lett.*, 108.
- 3029 [70] Salam, G. P. (2009). Towards jetography.
- 3030 [71] Sjostrand, T., Mrenna, S., & Skands, P. Z. (2008). A Brief Introduction to PYTHIA 8.1.
 3031 *Comput.Phys.Commun.*, 178, 852–867.
- 3032 [72] Stancari, G., Previtali, V., Valishev, A., Bruce, R., Redaelli, S., Rossi, A., & Salvachua Fer-
 3033 rando, B. (2014). *Conceptual design of hollow electron lenses for beam halo control in the*
 3034 *Large Hadron Collider*. Technical Report FERMILAB-TM-2572-APC. FERMILAB-TM-
 3035 2572-APC, CERN, Geneva. Comments: 23 pages, 1 table, 10 figures.

- 3036 [73] Stewart, I. W. & Tackmann, F. J. (2011). Theory uncertainties for higgs and other searches
3037 using jet bins.
- 3038 [74] Symmetry Magazine (2015). The Standard Model of Particle Physics.
- 3039 [75] T. Gleisberg et al., T. G. e. a. (2009). Event generation with sherpa 1.1. *JHEP*, 02.
- 3040 [76] T. Sjöstrand, T. Sjöstrand, S. M. & Sands, P. Z. (2008). A brief introduction to pythia 8.1.
3041 *Comput. Phys. Commun.*, 178.
- 3042 [77] Tully, C. C. (2011). *Elementary particle physics in a nutshell*. Princeton, NJ: Princeton Univ.
3043 Press.
- 3044 [78] Verkerke, W. & Kirkby, D. (2003). The RooFit toolkit for data modeling. In *2003 Computing
3045 in High Energy and Nuclear Physics, CHEP03*.
- 3046 [79] Watts, G., Filthaut, F., & Piacquadio, G. (2015). *Extrapolating Errors for b-tagging*. Technical
3047 Report ATL-COM-PHYS-2015-711, CERN, Geneva. This is for internal information only, no
3048 approval to ever be seen outside of ATLAS.
- 3049 [80] Y. L. Dokshitzer, Y. L. Dokshitzer, G. D. L. S. M. & Webber, B. R. (1997). Better jet cluster-
3050 ing algorithms. *JHEP*, 9708.